TROPOSPHERIC PRECIPITATION MICROSTRUCTURE AND ITS INFLUENCE ON ELECTROMAGNETIC WAVE PROPAGATION

MARZUKI MARZUKI

Institute of Broadband Communication

Graz University of Technology

A thesis submitted for the degree of

Doctor of Engineering Sciences (Dr. techn.)

February 2011

Examiner:

  Ao.Univ.Prof. Dr.techn. Walter L. RANDEU (Supervisor)

  Assoc.Prof. Ondrej FISER Ph.D. (Czech Academy of Sciences)

Date of the oral examination: 28 February 2011

Dedicated to

My parent, my sisters and brothers,

My beloved wife (Febri) and my son (Daffa)

Acknowledgements

If we would count the favours of Allah (God) we could not compute them, verily Allah is Merciful. This has proven true during my doctoral program. Therefore, my profuse thanks are due both to God and to the people who made these last three and a half years a rewarding and enjoyable.

This doctoral thesis would never have come to pass without the support, encouragement and guidance of my supervisor, Prof. Walter L. Randeu. It all started in January 2007 with a letter to him. At that time, I was looking for a recommendation letter from a professor, as a requirement to apply the Asian-European Academic University Partnership Network (ASEA-UNINET) scholarship. Three and a half years latter, I am writing the last line of my thesis, and thinking back to my first contact and discussion with Prof. Walter L. Randeu. I most appreciated his creativity, thoroughness, and infinite interest in wave propagation study particularly in radar meteorology. It was exciting time without being stressful. Thank you.

When I first came to Graz I was extensively guided by Dr. Franz Teschl. I greatly appreciate his help manage everything regarding my accommodations and also his guidance in studying the electromagnetic scattering and rainwater complex permittivity. Many thanks also go to other members of Radar and Microwave Propagation Research Group, and Optikom Group as well as all staffs of Institute of Broadband Communication. I also thank Dr. Michael Schönhuber and Dipl.-Ing.(FH) Günter Lammer for helpful discussions on 2DVD performance. Special thanks to Prof. Toshiaki Kozu and Dr. Toyoshi Shimomai of Shimane University, Japan; Dr. Hiroyuki Hashiguchi of

Abstract

Precipitation microstructure, which is characterized by raindrop size distribution (DSD) has become crucial in many applications especially, in radar meteorology and telecommunication service. Precipitation is highly variable in space and time and it is directly linked to the DSD variability. Natural variation of DSDs substantially limits the accuracy of radar-derived rainfall estimates. This thesis was devoted to elucidating the natural variations of raindrop axis ratio, falling velocity and size distribution in equatorial Indonesia, particularly at Kototabang (KT), West Sumatra, Indonesia (0.20^oS, 100.32^oE, 864 m above sea level). The data from 2D-Video Distrometer (2DVD) observation were analyzed. Before that, two possible bias sources in estimating the DSD parameters were examined, namely the bias in the moment method (MM) and bin width selection of 2DVD data. It was found that the sensitivity to the moment estimator and bin width selection by which DSDs are modeled should be kept in mind when comparing the DSDs and integral rainfall parameters from various studies, all of which may have different order moment estimators and bin sizes for DSD quantization. The biases of MM were larger than those of maximum likelihood method (ML) and L-moment method (LM). The biases of MM were significantly influenced by the total number of drops and the moment estimator used. The MM might provide the results of sufficient accuracy even very close to those of the LM and the ML methods if very large samples of drops were available. In general, the DSD parameters obtained by the MM were larger than those of the underlying DSD from which the samples were taken. For bin width selection, using the midsize of bin (bin size of

0.20-0.30 mm) as the representative value for the class (bin) of binned data may be the best choice because the DSD parameters of these bin widths are very close to those obtained from drop-by-drop data.

The dependence of raindrop falling velocity and axis ratio on rainfall type were not clearly visible. The rainfall type was classified into stratiform, mixed convective/stratiform, deep convective and shallow convective, through 1.3-GHz wind profiler observation. Measured raindrop fall velocities were in so good agreement with Gunn-Kinzer's data that air density correction for KT (864 m above sea level) brings the terminal velocities much larger than the observed values. On the other hand, the raindrop axis ratio at KT is more spherical than that of artificial rain and equilibrium axis ratio, and close to the values reported in the turbulent high shear zone of the Earth's surface layer. Of some natural DSD variations investigated, the dependence of DSD on rainfall rate and rainfall type as well as diurnal variation were clearly visible. A striking contrast between stratiform and convective rain events is that the size distributions from the stratiform (convective) rains tend to narrow (broaden) with increasing rain rates. For rain rate $R < 10$ mm/h, the size distribution of stratiform was broader than that of convective. On the other hand, at higher rainfall rate more large-sized drops were found in convective rain. During convective type of rain, very large-sized drops were found mainly at the very start of rain event. During stratiform type of rain, very large-sized drops were found to be associated with the strong bright band. On a diurnal basis, the DSDs in the morning were narrower than those in the evening hours which was indicated by a smaller mass-weighted mean diameter (D_m) values in the morning than their counterparts in the evening hours. Consistent with a previous study, seasonal variation of DSD at KT was not clearly observed since significant local convective and orographic effects in this region may be dominant throughout the year. However, D_m values in our result were larger than D_m considered as orographic rain ($D_m < 1$ mm).

Rainfall type dependence and diurnal variation of DSD lead to variation of $Z - R$ relations. Consequently, usage of a single fixed $Z - R$ relation to convert Z observed by weather radar into rainfall rate R will underestimate at one time and overestimate at other times. Before evaluating the effect of DSD variability on the modeling of rain attenuation, the complex permittivity of real rainwater, as collected in nature, was determined. It was found that a slight difference in the complex permittivity between the measurement and model results exhibits very small biases in the Mie extinction coefficients. Thus, the existing models are generally acceptable for rainwater. We found some discrepancies of the International Telecommunication Union-Radiocommunication Sector (ITU-R) models to predict the rain attenuation for Sumatra which was partially due to the natural variation of precipitation in this region. The effect of diurnal variation of the DSD on the specific rain attenuation (γ) was obvious for convective rain in which the largest rain attenuation occurs when rain events occur in the first half of the day. Measured rain attenuation for stratiform rain events was in good agreement with the values obtained by the DSD and $\gamma - R$ relationship through Simple Attenuation Model (SAM) and the ITU-R. However, the agreement for convective rain, especially for shallow convective, was not good. Some assumption on the models such as rain height and spatial distribution of shallow convective rain for Sumatra need to be characterized in future studies.

Zusammenfassung

Die Niederschlags-Mikrostruktur, die durch die Regentropfen-Größen-Verteilung (Drop Size Distribution, DSD) charakterisiert wird, ist entscheidend in vielen Anwendungen mit Bezug zur Ausbreitung elektromagnetischer Wellen in der Troposphäre, besonders in der Radarmeteorologie und Telekommunikation. Niederschlag ist in Raum und Zeit hoch variabel und steht in direkter Verbindung zur DSD-Veränderlichkeit. Die natürliche Variation der DSD beschränkt wesentlich die Genauigkeit von radarabgeleiteten Niederschlags-Schätzungen. Diese Arbeit behandelt die natürliche Variation des Regentropfen-Achsen-Verhältnisses, Fallgeschwindigkeits- und Größen-Verteilung im äquatorialen Indonesien, besonders in Kototabang (KT), Westliches Sumatra, Indonesien (0.20ºS, 100.32ºE, 864 m über dem Meeresspiegel). Umfangreiche Messdaten vom 2D-Video-Distrometer (2DVD) wurden analysiert. Davor wurden zwei mögliche Fehlerquellen bei der Schätzung der DSD Parameter, nämlich der Fehler in der Momenten-Methode (MM) und Durchmesser-Quantisierung an 2DVD-Daten untersucht. Es stellte sich heraus, dass die Empfindlichkeit der Moment-Schätzfunktion und Quantisierungs-Auswahl berücksichtigt werden müssen wenn DSD- und integrierte Niederschlags-Parameter von verschiedenen Studien mit verschiedenen Ordnungsmoment-Schätzfunktionen und DSD-Quantisierungen miteinander verglichen werden. Fehler der Momenten-Methode (MM) waren größer als diejenigen der maximalen Wahrscheinlichkeitsmethode (ML) und L-Moment-Methode (LM). Die Fehler bei MM sind maßgeblich von der Totalzahl von Regentropfen und der Moment-Schätzfunktion abhängig. Die MM könnte Ergebnisse genügender Genauigkeit, ja sogar bis in die Nähe

von derjenigen der LM- und der ML-Methoden bringen, wenn sehr große Proben von Regentropfen verfügbar sind. Im Allgemeinen waren die DSD Parameter zufolge MM größer als diejenigen der zu Grunde liegenden DSD, von der die Proben genommen wurden. Für die Quantisierung ist der Mittelwert eines Bin die beste Wahl für den repräsentativen Durchmesser (oder die Klasse) von quantisierten Daten, weil die DSD-Parameter von diesen Bins sehr nahe denjenigen kommen, welche sich ohne Quantisierung ergeben.

Die Abhängigkeit der Regentropfengröße, der Geschwindigkeit und des Achsenveerhältnisses vom Niederschlags-Typ fällt, war nicht deutlich sichtbar. Der Niederschlags-Typ wurde in stratiform, gemischt convective/stratiform, deep convective und shallow convective, mit Hilfe von 1.3-GHz Wind-Profiler Beobachtungen klassifiziert. Gemessene Regentropfen-Fall-Geschwindigkeiten waren in so guter Übereinstimmung mit Gunn-Kinzer Modell-Daten, dass die Luftdichte-Korrektur für KT (864 m über dem Meeresspiegel) die Endgeschwindigkeiten viel größer macht als die beobachteten Werte. Andererseits ist das Regentropfen-Achsen-Verhöltnis in KT mehr kugelförmig als jenes von Modellen aus der Literatur. Von allen untersuchten natürlichen DSD-Variationen war die Abhängigkeit der DSD von der Niederschlags-Rate und dem Niederschlags-Typ, sowie von der Tageszeit deutlich sichtbar. Ein bemerkenswerter Unterschied zwischen stratiformen und konvektiven Regenereignissen ist, dass die Größenverteilung von stratiformem (konvektivem) Regen dazu neigt mit zunehmender Regenrate schmäler (breiter) zu werden. Für die Regenrate $R < 10$ mm/h war die Größenverteilung von stratiformem Regen breiter als die von konvektivem Regen. Andererseits wurden bei höheren Niederschlagsraten mehr große Regentropfen im konvektiven Regen beobachtet. Während Regen des konvektiven Typs wurden sehr große Regentropfen hauptsächlich am Anfang des Regenereignisses gefunden. Während des stratiformen Regens, wurden sehr große Regentropfen im starken hellen Band (bright band) beobachtet. Auf einer tageszeitlichen Basis war die DSD am Morgen schmäler als diejenige in den Abendstunden,

charakterisiert durch kleinere massengewichtete Mitteldurchmesser (D_m) am Morgen. Übereinstimmend mit einer früheren Studie wurde die saisonale Variation der DSD in KT außer einem bedeutenden lokalen konvektiven Ereignis nicht deutlich beobachtet, Orographie-Wirkungen in diesem Gebiet können im Laufe des Jahres dominierend sein. Jedoch waren D_m-Werte in unserem Ergebnis größer als jene die üblicher Weise zu orographischem Regen gehören ($D_m < 1$ mm).

Die Abhängigkeit vom Niederschlags-Typ und die tägliche und tageszeitliche Variation der DSD führen zu Schwankung der $Z-R$ Beziehung. Folglich führt der Gebrauch einer einzigen, starren $Z-R$-Beziehung für die Konversion von Z (gemessen mit dem Wetterradar) in die Niederschlags-Rate R einmal zur Unterschätzung, ein anderes Mal zur Überschätzung des tatsächlich fallenden Regens. Vor Auswertung der Wirkung der DSD-Veränderlichkeit auf die Modellierung der Regendämpfung, wurde die komplexe Dielektrizitätszahl von natürlichem Regenwasser - wie in der Natur gesammelt - gemessen. Es ergab sich zwar ein kleiner Unterschied zu destilliertem Wasser, jedoch mit einer vernachlässigbaren Wirkung auf die Streu- und Auslöschungskoeffizienten von Regentropfen bei üblichen Radarfrequenzen. So sind die vorhandenen Modelle, berechnet mit destilliertem Wasser, auch für Regenwasser allgemein annehmbar. Wir fanden, dass einige Diskrepanzen mit den ITU-R-Modellen für die Voraussage der Regendämpfung in Sumatra existieren, welche teilweise auf die natürliche Variation des Niederschlags in diesem Gebiet zurück zu führen ist. Die Wirkung der täglichen Variation der DSD auf die spezifische Regendämpfung (γ) orientiert sich offensichtlich am konvektiven Regen, in dem die größte Regendämpfung vorkommt, wenn Regenereignisse in der ersten Tageshälfte auftreten. Die gemessene Regendämpfung für Stratiform-Regenereignisse war in guter Übereinstimmung mit den Werten erhalten aus der DSD und $\gamma - R$ Beziehung, dem Einfachen Verdünnungsmodell (SAM) und der ITU-R. Jedoch war die Übereinstimmung für den konvektiven Regen, besonders für shallow convective, nicht gut. Eine Verfeinerung der Modelle für die Regenhöhe

und die räumliche Verteilung des Regentyps Shallow Convective für Sumatra muss in zukünftigen Studien charakterisiert werden.

Contents

List of Figures

List of Tables

Chapter 1

Introduction

"See you not that Allah (God) drives the clouds gently,
then joins them together, then makes them into a heap of layers,
and you see the rain come forth from between them;
and He sends down from the sky, from mountains in it of ice, and strikes
therewith whom He wills, and averts it from whom He wills.
The vivid flash of its (clouds) lightning nearly blinds the sight"
[Quran, Chapter 24, Verse 43].

As one of the most important atmospheric phenomena and a key component
of the hydrologic cycle, knowledge of precipitation is critical for understanding
the Earth's climate. Precipitation formation releases about 70 to 80 percent of
latent heat received by the global atmosphere (e.g., Simpson *et al.*, 1996; Tokay
and Short, 1996). In addition, precipitation processes occur over scales smaller
than typical model grid sizes, then these processes need to be parameterized
in global climate models (Rotstayn, 1997). Over the last few decades, increasing
effort has been devoted to improve the accuracy of remote sensing of precipitation
(Tokay and Short, 1996) and parameterization of precipitation processes in global
climate models (Rotstayn, 1997). Great progress has been made in both areas as
a result.

This work deals with liquid precipitation which is commonly known as rain.
Understanding the rainfall microstructure is essential to characterize the rain-

fall and its property, which will lead us to a better knowledge and prediction of natural phenomena that can be caused by the rainfall such as floods, microwave attenuation (e.g., Oguchi, 1983), soil erosion (e.g., Coutinho and Toms, 1995), etc. The rainfall microstructure is characterized by the way the rainwater distributed in the air. The most complete way to study the distribution of the drops is through drop size distribution (DSD). Despite the great progress has been made in the DSD measurements (e.g., Donnadieu, 1980; Hauser *et al.*, 1984; Joss and Waldvogel, 1969; Löffler-Mang and Joss, 2000; Schönhuber, 1998) and parameterization (e.g., Feingold and Levin, 1986; Kozu and Nakamura, 1991; Marshall and Palmer, 1948; Testud *et al.*, 2001; Ulbrich, 1983), both areas still suffer from large uncertainties, and much remains to be done.

In the following sections we will start with a brief review of the previous work done in the DSD and our motivation. Afterwards, the objectives of this thesis will be described. And finally in the last Section the outlines of the following Chapters of this thesis will be presented.

1.1   Literature Review and Motivation

The rainfall process are often characterized by different macroscopic quantities, such as radar reflectivity factor, rainfall rate, liquid water content, median volume diameter and mass-weighted mean diameter. These descriptors can be obtained from moments of DSD. Hence, the moment method is widely used to govern analytical expressions to describe the measured DSD. Kozu and Nakamura (1991) used the third, fourth and sixth moments (referred to as M_3, M_4 and M_6, respectively) while Ulbrich and Atlas (1998) used moments M_2, M_4 and M_6. Recently, Caracciolo *et al.* (2006) used higher moments, i.e. M_4, M_5 and M_6, to parameterize the measured DSD. Smith and Kliche (2005) have demonstrated the bias in moment estimators from a hypothetical exponential DSD for several selected moments. The bias can provide a significant impact to draw inference about the characteristics of the DSD being sampled. The expected value of the fitted parameters may differ from the parameters of the underlying raindrop populations. It is very difficult to criticize any given set of results based on moment method because 'true' DSD parameters in nature are unknown. However, study on the bias

in the moment method is necessary when comparing the DSD parameters from various studies or when taking conclusion of precipitation microphysics from the DSD parameters, all of which may have different moment criteria for evaluating the DSDs.

Some in situ measurements of DSD have been conducted by using various techniques from the early study of this field (e.g., Donnadieu, 1980; Hauser *et al.*, 1984; Joss and Waldvogel, 1969; Löffler-Mang and Joss, 2000; Schönhuber, 1998). A mechanical impact device, which is well known as Joss and Waldvogel Disdrometer, hereinafter JWD, seems to be the most widely used instrument in scientific research. The raw data set of JWD is organized in 127 size bins. In order to get statistically meaningful samples and to reduce the amount of data, the firmware of the JWD reduces the number of classes to 20 ranging from 0.3 to about 5.0-5.5 mm (interval sizes and averaging periods may vary depending on the user). The widths of the 20 intervals are not uniform and increase as drop size increases (0.1 - 0.5 mm). Like the JWD, a rather new optical instrument (Parsivel) also operates with non-uniform bin sizes (Löffler-Mang and Joss, 2000). 2D - Video Distrometer (2DVD) has been employed in recent field studies of ice and raindrop physics (e.g., Kozu *et al.*, 2005). The 2DVD has twice the sampling area of the JWD and can measure the size of the drops with a nominal accuracy of ± 0.2 mm. The 2DVD is capable of measuring not only DSD and fall velocity, but also the shape of hydrometeors. Unlike the JWD and the Parsivel, the 2DVD provides the DSD with uniform bin size.

All instruments listed above provide DSDs at nominal drop diameters that correspond to the mean of the bin sizes. Selection of bin width may influence the shape of raindrop spectra. If we choose a too large bin size, the binned data would not represent the shape of the underlying distribution (Shimazaki and Shinomoto, 2007). In this study, we used a 2DVD to obtain the DSD. Some previous investigators have analyzed the raindrop spectra of 2DVD binned at different sizes (e.g., Kozu *et al.*, 2005; Tokay *et al.*, 2001). Neither Tokay *et al.* (2001) nor Kozu *et al.* (2005) dealt with ice and raindrop physics. Selection of bin width may not significantly influence the conclusion in ice and raindrop physics study, but it may be important when we are dealing with ground validation of radar and other remote sensing techniques.

Precipitation is highly variable in space and time and such variability is directly linked to the variability of DSD (Ulbrich, 1983). Therefore, rainfall properties estimated from the DSD show great variability due to climatological, physical and instrumental factors (Uijlenhoet *et al.*, 2006). It is accordingly worthwhile to study and model the DSD for different climatic environments. The Indonesian maritime continent which is surrounded by the warm sea water is characterized by a huge amount of rainfall throughout the year due to the convective clouds frequently generated over this region (Renggono *et al.*, 2001). The rainfall microstructure, however, have not yet been clearly identified because of the sparseness of observational data from that region. Through a research project called Coupling Processes in the Equatorial Atmosphere (CPEA), which is a collaborative research project between Japanese and Indonesian institutions, it is possible to study the atmospheric phenomena in the equatorial atmosphere with the 47 MHz Equatorial Atmosphere Radar (EAR) at Kototabang, west Sumatra, Indonesia (0.20^{o}S, 100.32^{o}E, 865 m above mean sea level) as the key facility. A 1.3 GHz Wind Profiler, X-Band Radar, the 2DVD, Optical Rain Gauge (ORG) and Mobile Automatic Weather Station (MAWS) are among the supporting instruments (Fukao, 2006; Fukao *et al.*, 2003). Topographic map of Sumatra is provided in Fig. 1.1. By taking advantage of the aforementioned facilities, it is possible to figure out the DSD characteristics of tropical precipitation over Sumatra, Indonesia especially at Kototabang.

Propagation of millimeter waves in the atmosphere would be seriously affected by rain. Therefore, rain attenuation models are based on the properties of raindrops and interaction between raindrops and electromagnetic waves. To deal with interaction of electromagnetic waves with raindrops, the rainwater complex dielectric constant is one of the crucial parameters. Ray (1972) developed a regression model which is applicable over a wide spectral and temperature range (-20 ^{o}C to 50 ^{o}C) by subjectively weighting the experimental data. Ray's model needs more than 30 coefficients. Then Liebe *et al.* (1991) carefully examined the existing data in the frequency range 5 - 410 GHz and also obtained an empirical model of the complex refractive index of pure liquid water. Liebe's model is actually an update of Ray's model by using some new experimental data. These two empirical models are widely used for modeling wave propagation in rain.

However, some data used in Ray (1972) and Liebe *et al.* (1991) come from pure water (e.g., Cook, 1952; Grant and Shack, 1967) or an unspecified type of water (e.g., Collie *et al.*, 1948; Grant *et al.*, 1957; Sandus and Lubitz, 1961). The composition of rainwater may not be the same as pure water or distilled water because of multiple inputs from the atmosphere, sea-spray and continental dust (e.g., Mphepya *et al.*, 2006; Puxbaum *et al.*, 1998). One contribution of this work is also the measurement of the complex dielectric constant of real rainwater, as collected in nature.
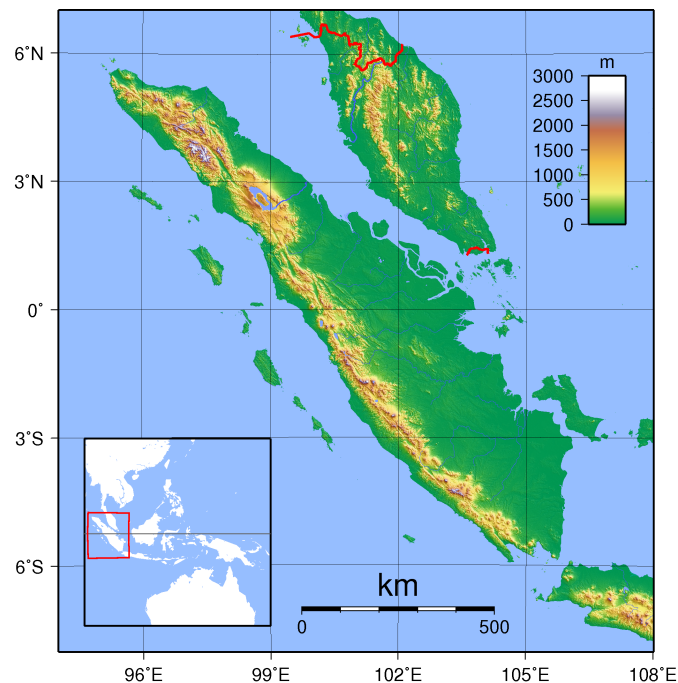
Figure 1.1: Topographic map of Sumatra produced by Generic Mapping Tools (GMT) from the Shuttle Radar Topography Mission (SRTM) data (http://commons.wikimedia.org). The position of Kototabang is 0.20^{o}S, 100.32^{o}E, 865 m above mean sea level.

Although the Indonesian maritime continent receives a huge amount of rainfall throughout the year, this region has not yet been covered by a weather radar network. However, in the period 2006-2009, Meteorology, Climatology and Geophysics Agency of Indonesia (BMKG) plan to install several weather radars at

21 locations in the frame of the Meteorological Early Warning System (MEWS) program (B. Suhardi, BMKG, 2009, private communication). At present, 12 radars have been put in operation at Biak, Pontianak, Bandar Lampung, Denpasar dan Tangerang (EEC DWSR-2501C type), Semarang dan Kupang (Baron-C Band type), Banda Aceh, Padang, Surabaya, Manado dan Batam (Gematronik Meteor-500C type). In the near future, one radar will be installed at Pondok Betung (DWSR-2000X type). Kototabang is very close to Padang ($\approx$ 90 km). Hence, the instruments at Kototabang will be worthwhile to increase the Quantitative Precipitation Estimation (QPE) which pursues to improve the precipitation estimates and enhance the reliability of flood prediction, by means of MEWS especially the Meteor-500C radar installed at Padang. In the use of weather radar, a relationship between rainfall rate (R) and the radar reflectivity factor (Z) obtained traditionally from DSD measurements has been widely used to convert the radar reflectivity to rainfall parameters. However, it is commonly recognized that this classical rain estimation is highly variable and has many sources of error. One of them is the sensitivity of $Z - R$ relations with respect to the natural variations of DSD (Maki *et al.*, 2005).

1.2 Objectives

The goal of this work is to investigate the bias on the estimation of the DSD parameters by applying different moment methods and bin sizes of the underlying simulated and measured DSD. The sensitivity to the moment estimators and the bin sizes selection by which the DSDs are determined should be kept in mind when comparing the DSD parameters from various studies or when taking conclusion on precipitation microphysics from the DSD parameters, all of which may have different criteria for evaluating the DSDs. The second goal of this work is to characterize the natural variation of the DSDs at Kototabang. The DSD data are still sparse in the equatorial region, particularly in the Indonesian maritime continent. Therefore, this work will increase the confidence of the information about the DSDs and the radar parameters estimated from the DSD in the equatorial region. Finally, this work includes rain attenuation modeling, based on DSD measurements, for Kototabang, in comparison with the International

Telecommunication Union-Radiocommunication Sector (ITU-R) model. Prior to studying the interaction of electromagnetic waves and raindrops, the complex dielectric constant of rainwater will be investigated and compared with some commonly used models.

1.3 Outlines of Following Chapters

In Chapter 2, a review of basic knowledge on precipitation formation, microphysical property of raindrop, observation of precipitation using radar and attenuation by rain are provided.

Chapter 3 presents an overview of the instrumentation. The 2DVD is the main instrument in this work. Therefore, the performance of this instrument is described in more detail than other instrumentation. It is well known that noise can be introduced in 2DVD measurements, and several techniques have been developed to filter them out. In this chapter, the noises due to the 2DVD's standard matching in comparison with that of re-matching algorithm and due to limited sampling size of the 2DVD are discussed. Afterwards, we reviewed on Sequential Intensity Filtering Technique (SIFT) and the Sorting and Averaging Based on Two Parameters (SATP) approach. These approaches are commonly used to minimize the effect on the spurious variability of 2DVD data.

The following two chapters (Chapters 4, 5) are devoted to analyze the bias in moment estimators and bin width selection of 2DVD data. The theoretical background concerning the functional forms of the DSD and integrals rainfall parameters (IRPs) are first reviewed. Because the DSD parameters in nature are inherently unknown, two types of data were used, i.e., simulated and measured DSD. First, we studied the bias by examining their ability to recover known parameters of simulated DSD. Second, real DSD collected by the 2DVD at Kototabang were analyzed. The 2DVD also provides data on drop-by-drop basis. Hence, we compared the DSD parameters calculated from binned data with those calculated from drop-by-drop data basis.

In Chapter 6, the characteristics distribution of drop size, shape and and falling velocity at Kototabang with the help of 2DVD observations are described. Some natural variations of the DSD parameters (e.g., the dependence of the DSD

with the precipitation type, diurnal and intraseasonal variation) and its impact on the $Z - R$ relation are also provided.

Chapter 7 is devoted to analyze the complex dielectric constant of real rainwater, as collected in nature. Afterwards, rain attenuation modeling for Sumatra are analyzed in Chapter 8. Analysis of rain rate cumulative distribution and rain attenuation values estimated from the experimentally observed DSD in comparison with the ITU-R model and real attenuation data of a satellite link was described. Finally the last chapter is devoted to present the final conclusions.

Chapter 2

Theoretical Background

2.1 Precipitation Formation

There are several books working on cloud physics. The two books that are referred in this section are those of Houze (1993) and Roger and Yau (1996).

Precipitation is water that falls from a cloud and reaches the ground. It can be in liquid or solid form such as rain, snow, hail and sleet. Precipitation formation changes water from one phase to another. Condensation, evaporation, freezing, melting, deposition and sublimation are among the phase changes of water involved in the precipitation formation. To remind the reader, the phase changes of water is simply defined below:

- Condensation is the change of water from gaseous form (water vapor) into liquid water and the opposite of condensation is evaporation.

- Freezing is the change of liquid water into solid water. The opposite of freezing is melting.

- Finally, deposition is water moving from a vapor to a solid state and the opposite process is sublimation.

Saturation that can be inferred from the relative humidity (RH) is a necessary condition to the precipitation formation. Air becomes saturated if RH equals 100 % and becomes supersaturated if RH is larger than 100 %. RH is defined as

$$RH = \frac{e_a}{e_s}, \tag{2.1}$$

where e_a is the actual water vapor pressure defined by

$$e_a = \frac{\rho_v R_d T}{0.622},\tag{2.2}$$

where ρ_v is the water vapor density, R_d is the gas constant of dry air (287.04 Jkg^{-1}K^{-1}) and T is the absolute temperature (K). Furthermore, e_s is the saturation vapor pressure which is defined by the Clausius-Clapeyron equation and can be approximated by

$$e_s = 0.611\exp\left(\frac{17.502T_c}{T_c + 240.91}\right),\tag{2.3}$$

where T_c is the air temperature (^{o}C). Figure 2.1 shows the relationship between e_s and T_c.
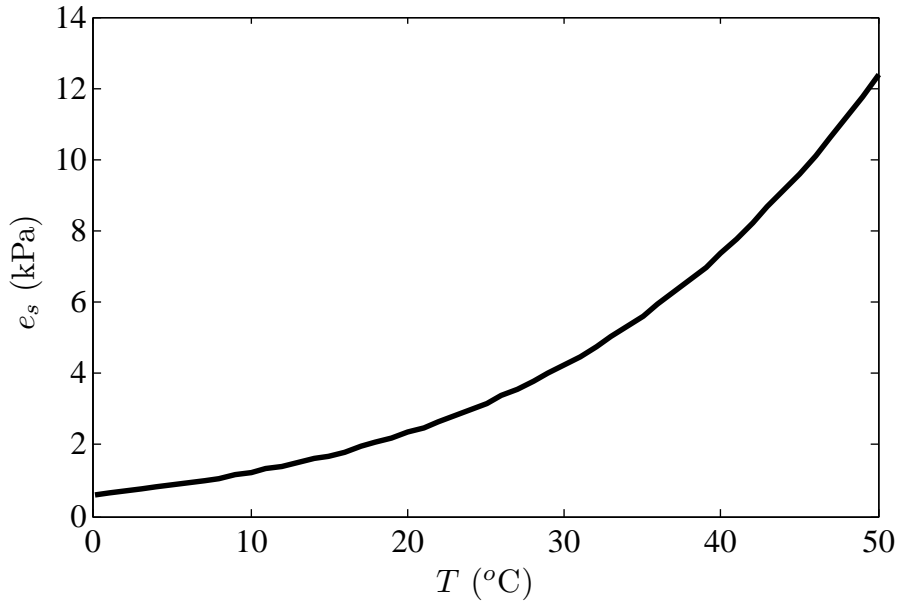
Figure 2.1: Relationship between saturation vapor pressure versus the air temperature.

From (2.2) and (2.3) as well as Fig. 2.1, saturation or supersaturation can be achieved when ρ_v increases (for a fixed temperature) or when temperature decreases. One mechanism to decrease temperature is lifting the parcel of air to a higher altitude. As the air is lifted to a higher altitude, it becomes cooler.

Consequently, e_s will be smaller. Clouds will form at altitude at which e_s equals e_a. Orographic, frontal surface and convective lifting are the mechanisms that are commonly known to lift air.

The precipitation formation begins with the nucleation process that are deposition, freezing or condensation of water vapor in free air onto condensation nuclei. As in aforementioned discussion, RH of the air around the condensation nuclei will determine the drop growth. Under normal circumstances, drop growth by condensation or deposition will only occur when the environment is supersaturated. This condition is seldom achieved. Therefore, some condensation nuclei attract water molecules to continue growing.

Condensation and deposition process alone will be slower than routine observations to produce a precipitation particle, which is heavy enough to fall to the surface. Therefore, there are other processes involved to produce the precipitation particles that work much faster, namely the collision and coalescence process, and the ice crystal process (Roger and Yau, 1996).

2.1.1 Collision and Coalescence Process

Collision and coalescence process involve interaction between liquid water droplets. Therefore, this process applies to warm clouds that commonly form in the tropic. However, it is also effective in some mid-latitude cumulus clouds whose mass lies above the freezing level.

Not all droplets that collide will merge (coalescence). Size variation of condensation nuclei in the atmosphere is one crucial factor to form precipitation under this model. Large sized condensation nuclei will create large water droplets and so contrary to the small condensation nuclei. Droplets have to be heavy enough to fall to the surface, to overcome the resistance imposed by upwardly rising air that is fueling the development of the cloud. The smaller and lighter droplets are easily suspended in the updrafts of air. On the other hand, the larger heavy collector droplets fall and collide with the smaller ones. On collision, the droplets coalesce into a bigger droplet. With enough collisions, the droplet achieves a size sufficient to fall to the surface. Resistance by the air can also flatten the droplet to the point where it becomes unstable and breaks apart. If the air underneath

the cloud is moist, the droplets will reach the ground as drizzle. Moreover, if the cloud is extremely high above the ground, the droplets will evaporate before reaching the surface. Electric charge of droplet, cloud thickness, updrafts of the cloud and turbulence may also influence the collision and coalescence process (Roger and Yau, 1996).

2.1.2   Ice Crystal Process

The ice crystal process involves interaction between ice particles, super cooled water and water vapor. This model applies to cold clouds that commonly form in the middle and high latitudes. Cold clouds primarily exist when the temperatures are below the freezing level. In cold clouds, water still exists in its liquid phase even though the temperatures are cold enough to freeze it. This water is called supercooled water.

Besides supercooled water droplets, ice crystals are also found in cold clouds. Many supercooled droplets will surround the ice crystals. The difference in vapor pressure between them causes water vapor molecules to move from the liquid droplets to the ice crystals that will reduces the vapor pressure above the droplet. This condition causes the droplets are not in the equilibrium with its surrounding and the droplets will evaporate to replace the supply of water vapor above it. This process provides a constant source of moisture for the ice crystals to absorb. Thus, the ice crystals grow by deposition process. As the ice crystals grow, they will be heavy enough to keep afloat on the air from the updrafts of the cloud. Therefore, these ice crystals will fall through the sky.

In some clouds, ice crystals will collide with supercooled droplets on the descent. This collision and coalescence process causes the droplets to freeze on contact with the ice crystal, which is known as riming process. Graupel is the particles that are formed by this process. The graupel tends to splinter up into tiny ice particles as it collides with other cloud droplets during their fall. These then themselves turn into more graupel, and these again splinter and the process continues. For a colder clouds, ice crystals may collide with other crystals and fracture into smaller ice particles. As the numerous amounts of ice crystals fall, they may collide or stick to one another forming a collection of ice crystals called

a snowflake. If the snowflake melts before reaching the ground, it is called as rain.

2.2 Convective-Stratiform Precipitation

Convective and stratiform precipitation are two main classes of precipitation in the tropical region. The classification is based on the growth processes of precipitation particles and the vertical distribution of latent heating associated with the precipitation processes (Houze, 1997).

Convective precipitation is characterized by strong vertical air motions (in the order of ms^{-1}), high rainfall rates, small horizontal dimension and intense radar echo. Mass collection processes (i.e., coalescence and riming) are the dominant microphysical mechanisms to grow the precipitation particles (Houze, 1993). Convective precipitation is then categorized into shallow and deep convective. Shallow convective is associated with clouds with limited vertical development, small droplets generated by condensation and followed by collision and coalescence for larger drops. In the tropical region, cold cloud processes are typically observed when the cloud has significant vertical extent above the freezing level (Zipser and Lutz, 1994). Hence, deep precipitation involves cold cloud processes such as aggregation, riming and deposition, though warm cloud processes may still operate in the above-freezing portions of the deep convective cloud.

Stratiform precipitation is characterized by less active convection (weaker vertical air motions) and mass of precipitation particles increase primarily through vapor deposition. Most stratiform precipitation falls from clouds that reach well above the 0 ^{o}C level, and ice particles in the upper levels of the cloud play an important role in the precipitation process. From this definition, the stratiform region must contain ice. The stratiform precipitation is commonly characterized by radar bright band in horizontal layer about 0.5 km depth just below the 0 ^{o}C level. The radar bright band reflects the layer where the large snowflakes melt. Airborne Doppler radar has shown that the convective regions distribute heating throughout the depth of the troposphere and stratiform regions, heat the upper troposphere and cool the lower troposphere (Houze, 1997).

2.3 Microphysical Properties of Raindrops

As a consequence of the variety of microphysical processes involved in the precipitation formation, several types of hydrometeor exist in the atmosphere such as raindrop, snow, graupel and hail. In this work, we study the tropical precipitation in the equatorial region where precipitation at the ground comes only from rain. Therefore, the following two sections are only devoted to review the microphysical properties of raindrops.

2.3.1 Raindrop Size Distribution

Raindrop size distribution (DSD) is not a distribution in the probabilistic sense but a function $N(D)$ in unit of $\text{m}^{-3}\text{mm}^{-1}$, such that $N(D)dD$ is the number of drops of diameter D to $D + dD$ mm per unit volume (m^3) of air. One of the pioneering studies of DSD was carried on by Marshall and Palmer (1948). They approximated the DSD with exponential function that can be written as

$$N(D) = N_0 e^{-\Lambda D}, \tag{2.4}$$

with $N_0 = 8000$ $\text{m}^{-3}\text{mm}^{-1}$ and $\Lambda = 4.1R^{-0.21}$ (Λ in mm^{-1}, R in mmh^{-1}). N_0 and Λ are widely known as intercept and slope parameter of the distribution function, respectively. Marshall-Palmer distribution fails to parameterize the observed instantaneous spectra (Joss and Gori, 1978). Therefore, some authors have preferred the two-parameters exponential distribution that did not assume N_0 as a fixed value. By substituting Λ as $4/D_m$, (2.4) is also written as

$$N(D) = N_0 e^{-4D/D_m}. \tag{2.5}$$

where D_m is the mass-weighted mean diameter.

Ulbrich (1983) parameterized the DSD in the form of a modified gamma distribution as

$$N(D) = N_0 D^\mu e^{-\Lambda D}, \tag{2.6}$$

with N_0 $(\text{m}^{-3}\text{mm}^{-1-\mu})$, Λ and μ as parameters. By substituting Λ as $(\mu+4)/D_m$ and defining $D^\mu = (D/D_m)^\mu D_m^\mu$, (2.6) is also written as

$$n(D) = N_0 D_m^\mu (D/D_m)^\mu e^{-(\mu+4)D/D_m}. \tag{2.7}$$

14

The advantages of the modified gamma distribution are that it is possible for DSD spectra with various shapes including those which are either concave upward or downward on a logarithmic plot of $N(D)$ versus D. In addition, the gamma distribution reduces to the exponential distribution for $\mu = 0$.

An alternative function, which has been widely used, is the lognormal function having the form

$$N(D) = \frac{N_T}{\sqrt{2\pi}\sigma D} e^{-(\ln D - m)^2/2\sigma^2}, \tag{2.8}$$

where N_T (m^{-3}) is the total number of drops per unit volume, m is the natural logarithm of geometric mean of drop diameter and σ (mm) is the standard deviation of the DSD about the geometric mean diameter (Feingold and Levin, 1986; Kozu and Nakamura, 1991). The Weibull distribution is also sometimes used to parameterize the DSD (Sekine *et al.*, 1987).

Different models of the DSD such as exponential, lognormal and gamma distribution have their own limitations. The exponential distribution has been widely used to parameterize the DSD for a long time. However, semilogarithmic plots of the observed DSD often exhibit deviations from the exponential function (e.g., fewer drops at small diameter end). Although the lognormal function approximates drop size distributions well, it does not allow for as broad spectrum of DSD shapes as other representations and does not reduce to the exponential function as a special case. On the other hand, the coefficient N_0 of gamma distribution no longer has the simple units as the equivalent coefficient in the exponential distribution and, in fact, include the parameter μ. As a result N_0 and μ are strongly correlated, as shown by Ulbrich (1983). This correlation as demonstrated by Chandrasekar and Bringi (1987) do not imply any physical basis. To overcome this problem, they defined (2.6) in another format as

$$N(D) = \frac{N_T \Lambda^{\mu+1}}{\Gamma(\mu+1)} D^\mu e^{-\Lambda D}, \tag{2.9}$$

where N_T is related to N_0 as

$$N_0 = \frac{N_T \Lambda^{\mu+1}}{\Gamma(\mu+1)}. \tag{2.10}$$

Some formulations to remove the dependence of DSD's equation on N_0 and Λ are also proposed by other authors. Sekhon and Srivastava (1971) normalized (2.4)

using liquid water content (LWC) and median volume diameter (D_0). On the other hand, Willis (1984) and Testud *et al.* (2000) normalized (2.6) using LWC and D_m. Recently, Testud *et al.* (2001) proposed a normalization procedure of the DSD without any assumption on its shape, given by

$$N(D) = N_w f(D/D_m),\tag{2.11}$$

where N_w is the scaling parameter for drop concentration. For gamma distribution, $f(D/D_m)$ and N_w are defined by

$$f(D/D_m) = \frac{6}{4^4} \frac{(4+\mu)^{(\mu+4)}}{\Gamma(\mu+4)} \left(\frac{D}{D_m}\right)^\mu e^{-(4+\mu)\left(\frac{D}{D_m}\right)},\tag{2.12}$$

$$N_w = \frac{4^4}{\pi \rho_w} \frac{LWC}{D_m^4},\tag{2.13}$$

where ρ_w is the water density. Normalization procedure compares the shape of two spectra that have not the same LWC and/or D_m. The concept of normalization can be used to describe the intrinsic shape of raindrop spectra because it normalizes the diameters and the $N(D)$ in order to treat all the data together, without any separation (Testud *et al.*, 2001). Doing this, the parameters could be estimated more robustly independently of R because we do not group the measurements into classes of R as done in other methods.

The methods that are widely used to estimate the DSD parameters is described in Chapter 4.

2.3.2 Raindrop Shape

Small-sized drops are generally spherical in shape. As the size of the drop increases, a raindrop would have more of a spheroidical shape (i.e., an oblate spheroid). The drag force on the falling drop may mainly cause the drop to be flattened. Other key factors commonly affect the raindrop shape are surface tension, hydrostatic pressure, aerodynamic pressure, internal circulation and electric stress (e.g., Beard and Chuang, 1987; Beard *et al.*, 1989; Pruppacher and Pitter, 1971; Spilhaus, 1948) .

Magono (1954) began the modern experimental research on raindrop shape with the wind tunnel. Pruppacher and Beard (1970) and Pruppacher and Pitter

(1971) have provided more detailed information on the axis ratio as a function of raindrop size. The wind tunnel measurements of Pruppacher and Beard (1970) provided an empirical formula, in terms of the axial ratio (b/a) between the vertical (b) and the horizontal axis (a) of the raindrop with the diameter $D > 0.5$ mm ($b/a = 1$ for $D < 0.5$ mm) , as

$$b/a = 1.030 - 0.062D, \tag{2.14}$$

where D is in mm. Some authors used equivolumetric drop diameter (D_{eq}) for nonspherical drops. D_{eq} is the diameter of the sphere of the same volume as the drop and for spherical drops, $D_{eq} = D$.

Spilhaus (1948) provided the theoretical estimate of raindrop shape and suggested that the flattened drops are due to aerodynamics pressure. More extensive theoretical approaches were proposed later by other authors (e.g., Green, 1975; Pruppacher and Pitter, 1971). A more complete model for the raindrop shape falling at their terminal velocities was proposed by Beard and Chuang (1987). This model is commonly referred as the equilibrium model of axis ratio. It described the shape of a rain drop as a 10th order cosine distortion of a sphere :

$$r(\theta) = a(1 + \sum_{n=1}^{10} c_n cos(n\theta)), \tag{2.15}$$

where, a is the radius of the undistorted sphere, $c_1...c_{10}$ are the coefficients that depend on the radius of the drop and θ is the polar nadir angle. $\theta = 0$ corresponds to the direction of the fall. Raindrop shapes of various sizes (0.5-2.5 mm) are shown in Fig. 2.2. Chuang and Beard (1990) provided an empirical fit of the axis ratio computed by the equilibrium model for $1 < D < 9$ mm, given by

$$b/a = 1.0048 + 0.00057D - 0.02628D^2 + 0.003682D^3 - 0.0001677D^4. \tag{2.16}$$

Some laboratory measurements shown the difference in the axis ratio from the equilibrium model, especially for medium and large-sized drops. For example, Kubesh and Beard (1993) showed that raindrops with diameters between 2.0 and 2.5 mm exhibited a mean axis ratio larger than that obtained by the model. Andsager *et al.* (1999) extended the laboratory measurements of Kubesh and
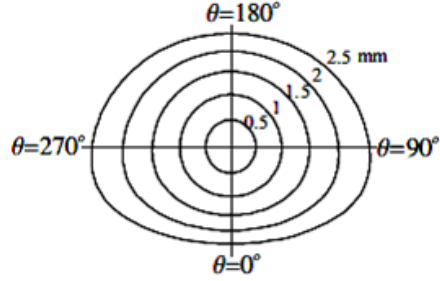
Figure 2.2: Shapes of rain drops of various sizes (0.5 - 2.5 mm) based on Beard and Chuang (1987). Large drops are clearly distorted, while smaller drops are almost spherical.

Beard (1993) to larger sizes (2.5-4.0 mm) and obtained a second order polynomial fit explaining the generally higher average axis ratio of the raindrops as

$$b/a = 1.012 - 0.0144D - 0.0103D^2. \tag{2.17}$$

A predicted phenomenon that causes the raindrop axis ratio differing from equilibrium shape is drop oscillation. Raindrops with diameters larger than $D = 1$ mm continuously oscillate in response to vortex shedding. Instead of using axis ratio relationship in the aforementioned discussion, Keenan *et al.* (2001) used a relationship, which is obtained from several laboratory measurements and theoretical estimates, given as

$$b/a = 0.9939 + 0.00736D - 0.018485D^2 + 0.001456D^3. \tag{2.18}$$

In another report, Brandes and Vivekanandan (2002) also determined an axis ratio relationship representing more spherical drop shapes by combining different existing equations as

$$b/a = 0.9951 + 0.02510D - 0.03644D^2 + 0.005030D^3 - 0.0002492D^4. \tag{2.19}$$

In a recent work, observation of water drops artificially generated from water source on an 80 m high bridge using a 2DVD, shows that the raindrop shape with diameters between 1.5 to 9 mm is in agreement with the equilibrium shape (Thurai and Bringi, 2005). Moreover, they found that the predominant oscillation mode is the oblateprolate axisymmetric mode. Thurai *et al.* (2006) governed

the empirical fits of the axis ratio based on the data in Thurai and Bringi (2005) and other existing equations, as

$D < 0.7$ mm

$$b/a = 1, \qquad (2.20)$$

$0.7 \leq D \leq 1.5$ mm

$$b/a = 1.17 - 0.516D + 0.47D^2 - 0.132D^3 - 0.0085D^4, \qquad (2.21)$$

$D > 1.5$ mm

$$b/a = 1.065 - 0.0625D - 0.00399D^2 + 0.000766D^3 - 0.00004095D^4. \qquad (2.22)$$
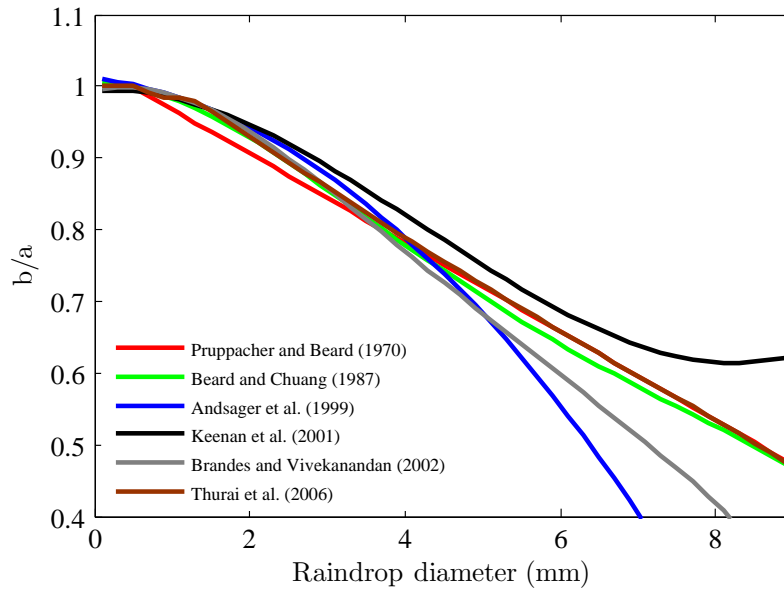
Figure 2.3: Axis ratio of oblate drops (b/a) as a function of equivalent volume diameter from several references.

Figure 2.3 shows the raindrop axis ratio calculated from several aforementioned publications. The equation from Brandes and Vivekanandan (2002) yields axis ratios that are significantly more spherical than that of Pruppacher and Beard (1970), particularly for drops with diameters between 1 to 4 mm, and

agrees quite well with the result of Andsager *et al.* (1999) for $D < 3$ mm. For large-sized drop ($D > 4$ mm), with the exception of Beard and Chuang (1987) and Thurai *et al.* (2006), all axis ratios differ much from Pruppacher and Beard (1970).

2.3.3 Raindrop Falling Velocity

Knowledge of the raindrop falling velocity is important in cloud physics, interpreting the Doppler radar and soil erosion study. As a raindrop falls, it attains a constant velocity, called the terminal velocity. Experimental work of the terminal falling velocity of distilled water drops under sea-level conditions (1013 millibars and 20 ^{o}C) was made by Gunn and Kinzer (1949). Another measurement was conducted by Beard and Pruppacher (1969).

Several statistical approximations that describe the terminal velocity in function of raindrop diameter have been published by several authors. The power law relations, $v(D) = aD^b$, (e.g., Atlas and Ulbrich, 1977; Sekhon and Srivastava, 1971) are mostly inaccurate especially for small and large-sized drops. Atlas *et al.* (1973) fitted the results in Gunn and Kinzer (1949) to yield

$$v(D) = 9.65 - 10.3e^{(-0.6D)}, \tag{2.23}$$

where $v(D)$ is the terminal falling velocity of raindrop in still air (ms^{-1}) and D is the drop diameter (mm). Maitra and Gibbins (1995) proposed another equation as

$$v(D) = 9.65 - 10.3e^{(-0.6D)} + 0.65e^{(-7D)}. \tag{2.24}$$

Brandes and Vivekanandan (2002) obtained a polynomial fit to the laboratory measurements of Gunn and Kinzer (1949) and Pruppacher and Pitter (1971) as

$$v(D) = 0.9951 + 0.02510D - 0.03644D^2 + 0.005030D^3 - 0.0002492D^4. \tag{2.25}$$

Figure 2.4 shows the terminal velocities of raindrop calculated from several references along with the laboratory measurements of Gunn and Kinzer (1949). For many applications it is important to have reliable estimates at altitude higher than sea level. Therefore, the above equations are frequently multiplied by air density correction as $(\rho/\rho_0)^{0.4}$, where ρ and ρ_0 are the air densities at altitude and sea level, respectively.
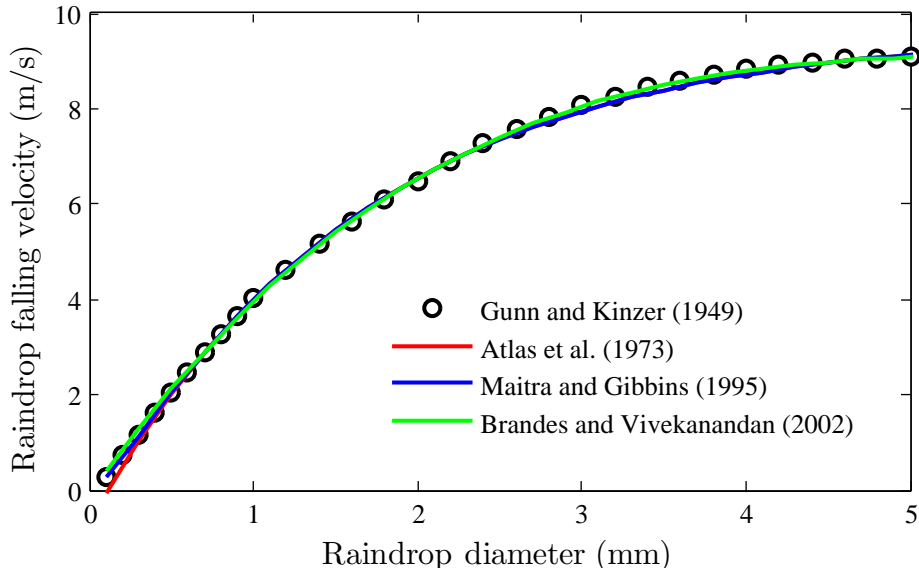
Figure 2.4: Terminal velocities of raindrop calculated from several references along with the laboratory measurements of Gunn and Kinzer (1949).

2.3.4 Canting Angle of Raindrops

In the presence of significant vertical gradient of horizontal wind, drops can cant out of the vertical (e.g., Beard and Jameson, 1983; Brussaard, 1974, 1976; Howard and Gerogiokas, 1982). Holt (1984) defined the canting angle as the angle between the projection of the drop's symmetry axis on the polarization plane and the projection of the local vertical direction on this same plane.

The distribution of canting angle (θ) can be assumed as a Gaussian distribution with probability density function as

$$p(\theta) = \frac{1}{\sqrt{2\pi}\sigma}\exp(-\frac{(\theta - \theta_0)^2}{2\sigma^2}), \tag{2.26}$$

where θ_0 is the mean canting angle and σ is the standard deviation. Beard and Jameson (1983) found small canting angles with $\theta_0 \approx 0^0$ and $\sigma \leq 5^0$, respectively. Field measurements using the 2DVD (Schonhuber *et al.*, 2000), have shown that the canting angle histograms of all drops with $D \geq 2$ mm are peaked at 0^0 with

a mean value of 0^0 and a standard deviation of 7^0, respectively (Thurai *et al.*, 2007).

2.4 Observation of Precipitation Using Radar

Since the late 1940's, radar has been used to track weather systems. Because of its ability to observe and measure precipitation quickly, accurately, and from great distance, radar has become essential in cloud physics study and in observation and forecasting of cloud and precipitation. There are many excellent and comprehensive books on weather radar (e.g., Battan, 1973; Bringi and Chandrasekar, 2001; Doviak and Zrnic, 1984; Illingworth, 2004; Raghavan, 2003). We refer the readers to these books for detailed analysis and derivation of the weather radar that will simply quote.

2.4.1 Simple Radar Equations

The radar equation expresses the relationship between the returned power and the characteristics of the radar and the target. In this section we provide a simple equation of pulse weather radar. Suppose the radar transmits a peak power P_t to a point target. Most of targets do not scatter the power isotropically, therefore, as a convenient artifice the radar backscattering cross section of the target (σ_s) is introduced. The power returned to an antenna with the gain G from a point target can be simply written as

$$P_r = \frac{P_t G^2 \lambda^2}{(4\pi)^3 r^4} \sigma_s. \tag{2.27}$$

λ is the wavelength of the radar and r is the distance to the scanned target. Table 2.1 shows the frequency of interest for various applications in meteorology.

Raindrops, snowflakes, and cloud droplets are examples of an important class of radar targets known as distributed targets. The observation volume of the radar can be approximated as

$$V = \pi (r\frac{\Theta}{2})(r\frac{\Phi}{2})\frac{c\tau}{2}, \tag{2.28}$$

Table 2.1: Radar frequencies for various meteorological applications (Raghavan, 2003)

Band	Frequency	Wavelengths	Applications
VHF	30-300 MHz	10-1 m	Observation of clear air phenomena in
			troposphere and stratosphere, wind-profiling,
UHF	0.3-1 GHz	1-0.3 m	turbulence, refractive index structure
L	1-2 GHz	30-15 cm	Clear air and precipitation phenomena
S	2-4 GHz	15-7.5 cm	Precipitation measurement, tropical cyclone
			observation, local severe storms, radio wave
			propagation
C	4-8 GHz	7.5-3.75 cm	Precipitation measurement, tropical cyclone
			observation, local severe storms, radio wave
			propagation, use on aircraft
X	8-12 GHz	3.75-2.5 cm	Thunderstorm and gust front detection, radio
			wave propagation, use on aircraft
Ku	12-18 GHz	2.5-1.7 cm	Cloud physics, ceilometers, air- and space
			borne radar, Synthetic-Aperture Radar (SAR)
Ka	27-40 GHz	1.1-0.75 cm	for sea surface studies, Precipitation
			measurement from attenuation, tornado
			observation
milli	40-300 GHz	7.5-1 mm	Ceilometers, cloud microphysics and
W	94 GHz	3.2 mm	dynamics, tornado observation
F	140 GHz	2.14 mm	
G	220 GHz	1.30 mm	

where Θ (Φ) is the horizontal (vertical) width of the radar beam, c is the light speed and τ is the pulse duration. Finally, by using the Gaussian antenna assumption the mean received power from a distributed target can be simply written as (Battan, 1973)

$$P_r = \frac{P_t G^2 \lambda^2 \Theta \Phi c \tau}{1024.\ln(2)\pi^2 r^2} \frac{\sum_{Vol} \sigma_s}{V}. \tag{2.29}$$

2.4.2 Scattering by Spherical Raindrops

Rayleigh and Mie scattering are two theoretical frameworks in light scattering study. Rayleigh scattering theory (after Lord Rayleigh) is, strictly speaking as originally formulated, applicable to small, dielectric (non-absorbing), spherical particles. On the other hand, Mie scattering theory (after Gustav Mie) encompasses the general spherical scattering solution (absorbing or non-absorbing) without a particular bound on particle size. Mie scattering theory has no size limitations and converges to the limit of geometric optics for large particles. Therefore, Mie theory may be used for describing most spherical particle scattering systems, including Rayleigh scattering. However, Rayleigh scattering theory is generally preferred if applicable, due to the complexity of the Mie scattering formulation.

A collection of books related to light scattering theory have been published by several authors. In this section, we follows primarily the treatment and notation of Bohren and Huffman (1983). For the readers who are interesting in the development of light scattering theory, we recommend the following two books, namely Bohren and Huffman (1983) and van de Hulst (1957). Recently, Mishchenko *et al.* (2000) described a comprehensive analysis of light scattering for nonspherical particles.

Maxwell's equations, which are based on the Faraday's law and Ampere's law, are the key point to determine how electromagnetic wave propagates through a material and it is given by

$$\nabla \mathrm{x} \mathbf{E} = -\frac{\partial \mathbf{B}}{\partial t}, \tag{2.30}$$

$$\nabla \mathrm{x} \mathbf{H} = \frac{\partial \mathbf{D}}{\partial t} + \mathbf{J}, \tag{2.31}$$

$$\nabla \bullet \mathbf{D} = \rho, \tag{2.32}$$

$$\nabla \bullet \mathbf{B} = 0, \tag{2.33}$$

where $\mathbf{D} = \epsilon_0 \mathbf{E} + \mathbf{P}$, $\mathbf{H} = \frac{\mathbf{B}}{\mu_0} - \mathbf{M}$, $\mathbf{J}$ is the current density, $\mathbf{E}$ is the electric field intensity, $\mathbf{D}$ is the electric displacement, $\mathbf{H}$ is the magnetic field intensity, $\mathbf{B}$ is the magnetic field, $\mathbf{P}$ is the electric polarization, $\mathbf{M}$ is magnetization, ρ is the charge density, ϵ_0 and μ_0 are the permittivity and permeability of free space, respectively. Equations (2.30)-(2.33) must be supplemented by

$$\mathbf{J} = \sigma \mathbf{E}, \tag{2.34}$$

$$\mathbf{B} = \mu\mathbf{H}, \tag{2.35}$$

$$\mathbf{P} = \epsilon_0\chi\mathbf{E}, \tag{2.36}$$

where σ is conductivity, μ is permeability, and χ is the electric susceptibility.

Bohren and Huffman (1983) assumed the incident field as plane harmonic wave given by

$$\mathbf{E}_i = \mathbf{E}_0\exp(i\mathbf{k}.\mathbf{x} - i\omega t), \tag{2.37}$$

$$\mathbf{H}_i = \mathbf{H}_0\exp(i\mathbf{k}.\mathbf{x} - i\omega t) \tag{2.38}$$

where the wave vector ($\mathbf{k}$) is a complex number as $\mathbf{k} = \mathbf{k}' + i\mathbf{k}''$. The fundamental task in solving the scattering-absorption problem is to construct the Maxwell equation of $\mathbf{E}$ and $\mathbf{H}$, both inside and outside the particle, that satisfies the boundary condition between the particle and surrounding medium. It can be done by superposing fundamental solutions.

When electromagnetic radiation meets a raindrop, its energy induces oscillating electric and magnetic dipoles within the raindrop. Part of the energy is absorbed by the drop as heat, and another part is reradiated as a scattered electromagnetic field. The induced oscillating dipole moment is manifest as a source of electromagnetic radiation, thereby resulting scattered light. Hence, total of energy intercepted by the sphere is

$$W_{ext} = W_s + W_a \tag{2.39}$$

where W_s and W_a are the rate at which energy is scattered and absorbed, respectively. If the incident irradiance is assumed as I_i (irradiance is often called as intensity and its dimensions are energy per unit area and time), another formulation of (2.39) can be introduced as

$$C_{ext} = C_s + C_a \tag{2.40}$$

where C_{ext}, C_a and C_s are the extinction, absorption and scattering cross section, respectively, which are defined by

$$C_{ext} = \frac{W_{ext}}{I_i}, C_a = \frac{W_a}{I_i}, C_s = \frac{W_s}{I_i}. \tag{2.41}$$

Efficiency factors for extinction, scattering and absorption are also sometimes used, given by

$$Q_{ext} = \frac{C_{ext}}{G}, Q_a = \frac{C_a}{G}, Q_s = \frac{C_s}{G} \qquad (2.42)$$

where G is the particle cross-sectional area projected onto a plane perpendicular to the incident beam in which for a spherical drop with radius a the value is $G = \pi a^2$.

According to the Mie's theory, Q_{ext} and Q_s are given by

$$Q_{ext} = \frac{2}{x^2} \cdot \sum_{n=1}^{\infty} (2n+1) \text{Re}(a_n + b_n), \qquad (2.43)$$

$$Q_s = \frac{2}{x^2} \cdot \sum_{n=1}^{\infty} (2n+1)(|a_n|^2 + |b_n|^2), \qquad (2.44)$$

where a_n and b_n are the Mie scattering coefficients, and x is the size parameter ($x = ka$). The coefficients a_n and b_n represent the amplitude of the field distribution on the sphere due to the magnetic multipoles (e.g., dipoles, quadrupoles, etc.) and electric multipoles (e.g., dipoles, quadrupoles, etc.) that are induced by the incident wave. Hence, the letter n represents the number of the terms in the expansions of describing the amplitude of a_n and b_n. The quantities of a_n and b_n can be expressed in terms of spherical Bessel and Hankel functions of the second kind with the given arguments, the size parameter and the refractive index with respect to the ambient medium (m), as

$$a_n = \frac{m^2 j_n(mx)[xj_n(x)]' - \mu_1 j_n(x)[mxj_n(mx)]'}{m^2 j_n(mx)[xh_n^{(1)}(x)]' - \mu_1 h_n^{(1)}(x)[mxj_n(mx)]'}, \qquad (2.45)$$

$$b_n = \frac{\mu_1 j_n(mx)[xj_n(x)]' - j_n(x)[mxj_n(mx)]'}{\mu_1 j_n(mx)[xh_n^{(1)}(x)]' - h_n^{(1)}(x)[mxj_n(mx)]'}, \qquad (2.46)$$

where $j_n(z)$ and $h_n^{(1)}(z)$ are spherical Bessel functions of order n, and μ_1 is the permeability of the sphere.

In radar meteorological studies or other fields of wave propagation, it is also common to use backscattering cross section (σ) as in (2.29) instead of C_s in (2.40). When a is small in comparison with λ, only the first term of b_1 (electric dipole)

needs to be considered. Hence, the backscattering cross section of a single particle becomes

$$\sigma_s = \frac{\lambda^2}{\pi} x^6 \left| \frac{m^2 - 1}{m^2 + 2} \right|^2. \tag{2.47}$$

By substituting the size parameter as $x = 2\pi a/\lambda$ and drop diameter as $a = D/2$, the above equation can be written as

$$\sigma_s = \frac{\pi^5 D^6}{\lambda^4} \left| \frac{m^2 - 1}{m^2 + 2} \right|^2. \tag{2.48}$$

This equation represents the Rayleigh approximation of the backscattering cross section because of its similarity to the Rayleigh scattering formula. In this work, calculation of the Mie scattering coefficient follows Bohren and Huffman (1983), which was then coded in MATLAB by Mätzler (2002).

2.4.2.1 $Z - R$ Relations

The average returned power as in (2.29) can be calculated by knowing the backscattering cross section of individual spherical particles. In simple, (2.29) can be written as

$$P_r = \frac{C \left| \frac{m^2-1}{m^2+2} \right|^2 Z}{r^2}, \tag{2.49}$$

where C is a constant depending on the radar instrument characteristics given by

$$C = \frac{P_t G^2 \pi^3 \Theta \Phi c \tau}{1024.\ln(2)\lambda^2}, \tag{2.50}$$

and Z is the reflectivity factor given as $\sum_{vol} D_i^6$. In terms of Rayleigh scattering, Z which is a function of raindrop size (D) and the DSD can be written as

$$Z = \int_0^\infty D^6 N(D) dD. \tag{2.51}$$

It can be seen that weather radar measures only an indirect variable Z. On the other hand, the variable of interest in many applications is the rainfall rate (R). Therefore, a transformation between rainfall rate and radar reflectivity is needed. The rainfall rate is a function of the DSD as

$$R = 6\pi.10^{-4} \int_0^\infty v(D) D^3 N(D) dD, \tag{2.52}$$

where $v(D)$ is the raindrop fall speed in still air (see Section 2.3.3). Hence, analytical formulation of the DSD can provide a relation between Z and R that is widely written as

$$Z = AR^b \quad \text{or} \quad R = A^{-1/b}Z^{1/b}, \tag{2.53}$$

where A and b are the parameters obtained from linear regression or other methods. There is no single $Z - R$ relationship that can be applied in every part of the world. For example, there are 69 $Z - R$ relationships in Battan (1973) because of the DSD variability. It emphasizes the importance of studying the DSD variability, for different climatological regions, different storms and seasons, and within different regimes of a storm, to improve the $Z - R$ conversion required to estimate rainfall rate from a weather radar.

2.4.3 Scattering by Nonspherical Raindrops

The real shape of raindrop is not spherical (see Section 2.4.2). A comprehensive description of light scattering by nonspherical particles can be found in Mishchenko *et al.* (2000). In this section, the scattering of nonspherical drops will be simply quoted from Seliga and Bringi (1976).

Seliga and Bringi (1976) provided the calculation of the backscattering cross section for nonspherical drops at a non-attenuating wavelength ($\lambda = 10$ cm). Assuming a small drop with major axis horizontal and with zero canting angle (i.e., their minor axis remains vertical), the backscattering cross section for an oblate spheroid can be written as

$$\sigma_H = \frac{16}{9} \frac{\pi^7}{\lambda^4} D_{eq}^6 \left| \frac{m^2 - 1}{[4\pi + (m^2 - 1)P']} \right|^2, \tag{2.54}$$

$$\sigma_V = \frac{16}{9} \frac{\pi^7}{\lambda^4} D_{eq}^6 \left| \frac{m^2 - 1}{[4\pi + (m^2 - 1)P]} \right|^2, \tag{2.55}$$

where P and P' are geometrical factors in function of eccentricity of the principal elliptical cross section ($e^2 = (a^2 - b^2)/a^2$), given by

$$P = 4\pi - 2P' = \frac{4\pi}{e^2} \left(1 - \sqrt{\frac{1 - e^2}{e^2}} \text{arc sin} e \right). \tag{2.56}$$

The value of σ_H and σ_V in (2.54) and (2.55) are the horizontal (vertical) backscattering cross section at horizontal (vertical) polarization, respectively. The scattered field of a horizontally (vertically) polarized incident wave is generated by the induction of an electric dipole aligned a long the major (minor) axis of the oblate spheroid. Seliga and Bringi (1976) defined the semi-minor axis as a, semi-major axis as b and consequently the axis ratio of oblate spherical as a/b. Moreover, they used the unit of $\sigma_{H,V}$ in cm^2. For spherical drops, we assume $D_{eq} = D$ and $P = P' = 4\pi/3$, hence, (2.54) and (2.55) are reduced to (2.48).

Many investigators have developed methods to calculate the backscattering cross section of nonspherical particles. To review the performance of the methods, the readers can refer to Wriedt (1998). In this work, the calculation of scattering coefficients for nonspherical drop used the point matching technique which was developed by Schönhuber (1987).

As was mentioned above, the use of reflectivity factor (Z) has been the most important parameter to estimate precipitation with weather radar. However, there are many ambiguities and uncertainties using only Z that can be minimized by using dual-polarization techniques. Dual-polarization radars are also common as polarimetric radars. Comprehensive explanation on polarimetric radar can be found in Bringi and Chandrasekar (2001). In the following section, some polarimetric radar parameters will be discussed.

2.4.3.1 Differential Reflectivity

The reflectivity factors at horizontal and vertical polarization are given by

$$Z_{HH,VV} = \frac{\lambda^4}{\pi^5} |K|^2 \int_0^\infty \sigma_{H,V} N(D) dD. \tag{2.57}$$

and $K = (m^2 - 1)/(m^2 + 2)$. The ratio of radar reflectivities at horizontal and vertical polarization is called as the differential reflectivity (Z_{DR}), given by (Seliga and Bringi, 1976)

$$Z_{DR} = 10\log \left| \frac{Z_{HH}}{Z_{VV}} \right|. \tag{2.58}$$

Z_{DR} is sensitive to the flattening of raindrops and increases with drop size in which the values for meteorological echoes typically range between -2 dB and

7 dB. If hydrometeors in the volume are horizontally oriented, a horizontally-polarized radar pulse will, therefore, be backscattered more than a vertically-polarized one. Consequently, returned signal for the horizontal pulse is more than the vertical one. In this case, Z_{DR} value is positive and the values above 2 dB are commonly observed in rain. On the other hand, if hydrometeors are vertically oriented such as some graupel and hail hydrometeors with a conical shape, their Z_{DR} will be negative. Z_{DR} near zero indicates the hydrometeors in the volume have a nearly spherical shape such as hailstones. The height of the melting level is indicated by the altitude at which positive Z_{DR} values begin to appear in the stratiform region.

2.4.3.2 Specific Differential Phase

An electromagnetic wave experiences a phase sift when propagating through the precipitation medium. The differential propagation phase (ϕ_{DP}) is simply defined as the difference in phase between the horizontally (ϕ_H)- and vertically (ϕ_V)-polarized pulses at a given distance along the propagation path, given by

$$\phi_{DP} = \phi_H - \phi_V. \tag{2.59}$$

On the other hand, the specific differential phase is the rate change of ϕ_{DP} along the propagation path for a given distance, written as

$$K_{DP} = \frac{\phi_{DP}(r_2) - \phi_{DP}(r_1)}{2(r_2 - r_1)}. \tag{2.60}$$

The number of "2" in the denominator appears since there is a phase shift on the outbound and return trip. If the falling raindrops are oblate, the electric field will encounter more water content in the horizontal direction than in the vertical one. Therefore, the horizontally polarized pulse will be more affected by water than the vertically polarized one in which it will travels more slowly than the vertically polarized pulse because electromagnetic waves travel more slowly through water than through air.

2.4.3.3 Linear Depolarization Ratio

Linear depolarization ratio (LDR) is a ratio of the power that has been backscattered into the cross-polarization sense (Z_{VH}, Z_{HV}) to the co-polar received signal power (Z_{HH}, Z_{VV}). Cross-polarization is when the transmit and receive polarizations are orthogonal (HV or VH) and on the other hand, co-polarization is when the transmit and receive polarizations are the same (HH or VV). LDR is defined as

$$LDR_H = 10log\frac{Z_{HV}}{Z_{HH}}, \tag{2.61}$$

$$LDR_V = 10log\frac{Z_{VH}}{Z_{VV}}. \tag{2.62}$$

LDR is mainly influenced by the shape, canting angle and phase of the particles. Strong LDR is generally best realized when wet-surfaced, irregularly shaped ice particles are present. The highest value of LDR (about -15 dB) is found in the region of brightband which is associated with the melting snowflakes (Illingworth, 2004). Conversely, LDR is minimized when only spherical particles, like drizzle drops, are present. Straka *et al.* (2000) found the lowest values of LDR for the CSU-CHILL polarimetric radar to be in the order of -30 dB.

2.4.4 Problems of Precipitation Observation Using Radar

Estimation of precipitation using weather radar has many sources of error. As was previously discussed in other sections that converting the radar variables (e.g., Z, Z_{dr}, K_{dp}) to rainfall rate R needs a knowledge on the DSD because the $Z - R$ relationship that is required to convert the radar variables is obtained from the DSD measurement. It is well known that great variability of the DSD due to climatological, physical and instrumental factors (Uijlenhoet *et al.*, 2006) results a great variability of $Z - R$ relationship. Thus, using single $Z - R$ relation such as the MP model may generate large deviation of rainfall rate estimation from reflectivity measurement. Atlas *et al.* (1984) and Doviak and Zrnic (1984) pointed out the error due to the DSD variability about 33% and 30-35%, respectively. Therefore, it is important to measure the DSD for the environments where the weather radar is located.

Variation of vertical profile of reflectivity (VPR) may also be crucial source of error in weather radar. The height of radar measurement increases with increasing range of measurement. Therefore, the hydrometeor intercepted by the radar beam may be composed of raindrops, melting snowflakes, snowflakes, hail, etc. Because of the variability of scatterers in the radar beam, reflectivity measurements may not be fully representative of the rainfall rate at the ground. Joss and Waldvogel (1990) found the error due to the melting snowflakes being up to a factor of 5. Some investigators have proposed algorithms to correct the variation of VPR (e.g., Gray *et al.*, 2002; Kitchen *et al.*, 1994).

Partial blockage of the beam is a major problem when radars are situated near mountains. The echoes from nearby mountains can be misinterpreted as heavy precipitation. Drastic reductions in the sampled volume by blockage have been illustrated in Switzerland by Joss and Waldvogel (1990). The problem may be mitigated by installing the radar on a peak. However, if the top of mountain is very high, the lowest elevation slices of the scanned volume are so high above ground that near-surface precipitation is sometimes not seen.

At frequencies higher than 3 GHz such as C-band and X-Band, attenuation due to precipitation is another source of error. The attenuation increases with increasing rainfall rate. Bringi and Chandrasekar (2001) proposed a correction of the attenuation of polarimetric radar by using the specific differential phase.

2.5 Complex Refractive Index of Water

The complex refractive index has been mentioned several times in the previous sections when we defined the electromagnetic scattering and polarimetric radar quantities. It is a ratio of the speed of light in a vacuum c to the speed of light in the medium v, and described in form of $n = n' + in''$. If $\exp(i\omega t)$ was chosen in the plane electromagnetic wave equation, $n = n' - in''$ is used (Bohren and Huffman, 1983). Relative permeability of most of materials are close to 1 at optical frequencies. Hence, the complex refractive index is related to complex permittivity as $n = \sqrt{\epsilon}$. The Real part of n describes the propagation of the electromagnetic wave in the medium while the imaginary part gives the absorption

coefficient of the medium. Detailed discussion about the complex permittivity of rainwater are given in Chapter 7.

2.6 Attenuation by Rain

Raindrops can absorb and scatter electromagnetic energy. Thus, attenuation of electromagnetic waves by hydrometeors may come from absorption and scattering, depending on their size, shape and composition. In this section, only the attenuation due to raindrops is discussed. Oguchi (1983) has reviewed and summarized the attenuation due to raindrop, snow and other particles in the atmosphere.

Besides being a problem for weather radar, rain attenuation of microwave signals is a common problem faced by telecommunication service providers all over the world. Link budgeting must be fine-tuned to achieve optimum use of resources. On the other hand, level of service quality and outage must be controlled to meet customers requirements.

For a plane wave propagating in a rain medium, the variation of wave intensity I along propagation direction z can be written as (Oguchi, 1983)

$$\frac{dI}{dz} = -(\Sigma \sigma_{ext})I.$$ (2.63)

where $\Sigma \sigma_{ext}$ is the sum of extinction cross section of all raindrops in a unit volume. It can be seen that the rate of decrease of wave intensity in a thin slab of thickness dz is proportional to the energy absorbed in, and scattered from, the raindrops in the slab. It is common to write the attenuation due to rain as a function of the DSD, given by

$$\gamma[\text{dB/km}] = 4.343.10^{-3} \int_0^\infty \sigma_{ext} N(D) dD.$$ (2.64)

For distorted raindrops, the extinction cross section, σ_{ext}, depends on polarization, thus the attenuation γ is polarization dependent. The specific attenuation coefficient (γ) is approximately related to rainfall rate (R) as

$$\gamma[\text{dB/km}] = AR^b,$$ (2.65)

where A and b are constants. The theoretical explanation of this form has been described by Olsen *et al.* (1978).

As was discussed above, rain is the principal limitation of millimeter-wave link availability or link distance. Once the rain availability requirement is determined, rain models can be used to determine the fade depth that will not be exceeded with that probability. Rainfall rate is most often used for rain fade characterization. There are some models available today such as Crane (Crane, 1980) and the ITU model (e.g., ITU-Recommendations, 2001, 2002).

The ITU models make use of the specific attenuation due to rain that is computed from the ITU data library. The specific attenuation is determined by using regression coefficients and the rainfall rate of interest. The models differ in the values for rainfall rate and in the modeling equations used, but they share the same regression coefficients for the specific attenuation. The coefficients are frequency and polarization dependent. Characteristics of precipitation for propagation models can be found in ITU-Recommendations (2001). These models are based on geographical regions.

The Crane global model is divided into two segments based on distance and the rainfall rate. Like the ITU model, the Crane model also uses the rain region concept. However, although the Crane rain regions are also labeled alphabetically, but they do not correspond to the ITU regions.

Although studies of rain attenuation of microwave signals have been conducted in many locations in the world, it is now common knowledge that the rain-attenuation and DSD models are highly regionalized, if not localized. Moreover, many studies also pointed to the inaccuracy of the aforementioned prediction models for use outside Europe and North America. Therefore, it is worthwhile to develop rain-attenuation and DSD models for different climatic environments.

Chapter 3

Instrumentation

This thesis is based upon the data obtained by several instruments. The following sections are devoted to explain the specifications and performance of the instruments such as a rain gauge, a 2D-Video-Distrometer (2DVD), three radars, and an Agilent Technologies 85070E dielectric probe kit. The properties of the radars are shortly summarized without giving a detailed overview on their principles. The 2DVD is the main instrument in this thesis, its performance is therefore described more detail than others.

3.1 Optical Rain Gauge

Optical Rain Gauge (ORG) is a precipitation gauge, working on the basis of scintillation technique. It has been developed by Optical Scientific Inc. (OSi), United States. Detailed specifications of this instrument can be found at the manufacturer's website (http://www.opticalscientific.com). In March 2002, the ORG was installed at Kototabang. The instrument is ORG-815 sampling rain rate every 1 minute. Height of the sensor is 3 m from the ground and 3 m westward to avoid the splashes by the roof of the observatory.

3.2 2D-Video Distrometer

The 2DVD is a precipitation gauge, working on the basis of video cameras. It has been developed by Joanneum Research (Graz, Austria), in cooperation with the

European Space Agency/European Space and Technology Center (ESA/ESTEC). The 2DVD is a new instrument, capable of measuring not only drop size and fall velocity but also drop shape of hydrometeors. The 2DVD at Kototabang was installed in March 2002; therefore, it is a first generation version in which two video cameras are enclosed in a large box. Moreover, our 2DVD is about 4 m away from a building.
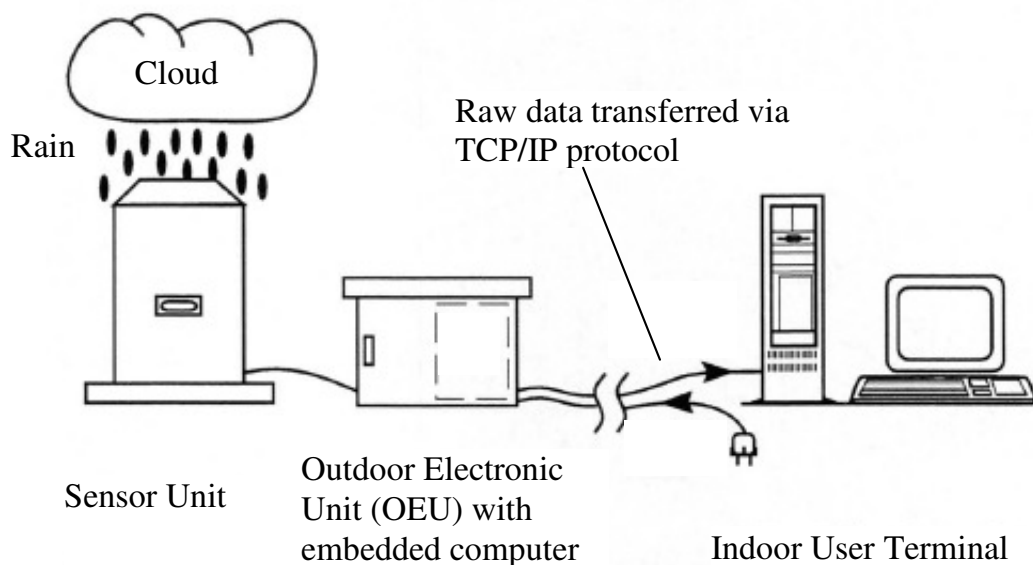
Figure 3.1: Schematic diagram of the 2DVD equipment arrangement (after Schönhuber *et al.* 1997).

Figure 3.1 provides a principle drawing of the system components of the 2DVD. The instrument consists of three main parts, the sensor unit, the outdoor electronics unit (OEU) and the indoor user terminal. The sensor unit houses the optics and line-scan cameras, with a square base of about 0.5 m and 1.1 m tall. The OEU contains an embedded computer that controls the camera and records the slit images. The third component is the indoor PC which is connected to the OEU via the standard Internet TCP/IP protocol.

Figure 3.2 is a schematic drawing illustrating the operating principle of the sensor unit. A light source generates a light sheet that is projected onto a line-scan camera. The manufacturer uses white light. Line-scan cameras have a single line

of photodetectors. The 2DVD uses two line-scan cameras, vertically offset from each other by ≈ 6.2 mm, and are directed towards the opening of the illumination devices. The optical system is designed in such a way that the slit of the illumination device appears as a relatively evenly illuminated background of extreme brightness. The light sheets are quite bright and particles falling through them cast shadows on the photodetectors. The two orthogonal projections provide, in principle, three-dimensional raindrop shape information. Shape information allows computation of the drop volume and equivalent drop diameter, as well as the oblateness. Hydrometeor images are recorded with both cameras and have to be matched later. Only if the image of a hydrometeor from camera A is matched to an image from camera B the fall velocity of a particle can be derived. The 2DVD sofware matches the particles' shadow and measures the time it takes for the particles to move 6.2 mm vertically, and obtains their vertical velocity. Table 3.1 provides a summary of the specifications of the 2DVD. A detailed description of the 2DVD could be found in Kruger and Krajewski (2001).
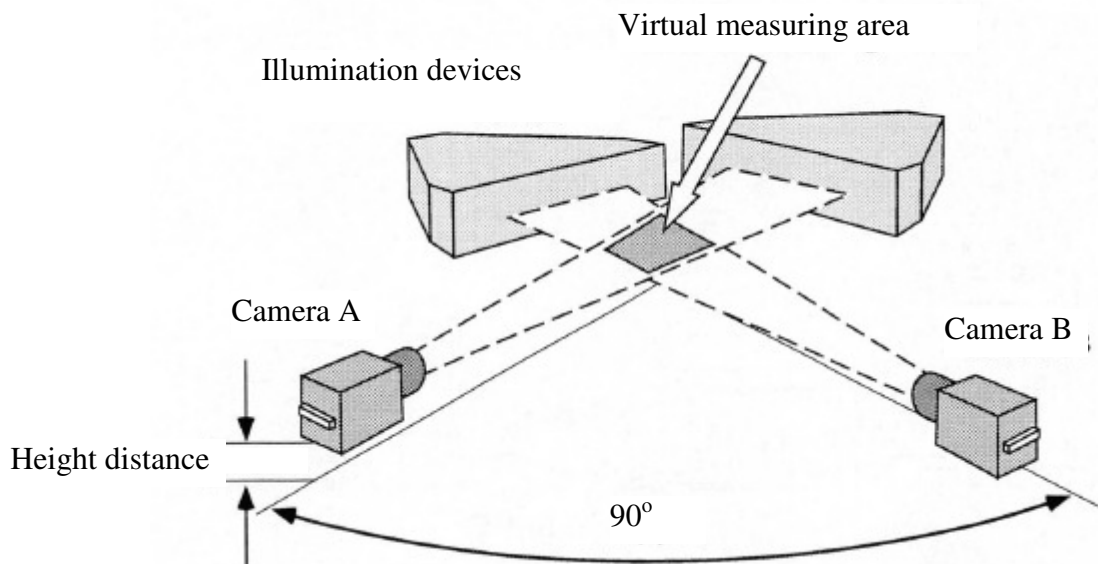
Figure 3.2: Intersection of the two orthogonal, horizontal light sheets determines the virtual measuring area of the 2DVD. The virtual measuring area is nominally 10 x 10 cm and the height distance of plane separation is 6.2 mm (after Schönhuber *et al.* 1997).

Table 3.1: Summary of some properties of the 2DVD (after Schönhuber *et al.* 1997)

Parameters	values
Horizontal resolution	better than 0.2 mm
Vertical resolution	better than 0.3 mm
Vertical velocity accuracy	better than 5%
Sampling area	≈ 100 x 100 mm^2

The DSDs of the 2DVD in unit of m^{-3}mm^{-1} are given by (Schönhuber, 1998):

$$N(D_i) = \frac{1}{\Delta t \Delta D} \cdot \sum_{j=1}^{m_i} \frac{1}{A_j v_j}, \tag{3.1}$$

where Δt is the time interval in seconds, i is the particular drop size class, j is the particular drop within size class D_i, m_i is the number of drops within size class i, D_i is the mean diameter of class i, ΔD is the width of drop size class (mm), A_j is the effective measuring area for drop j (m^2) and v_j is the fall velocity of drop j (ms^{-1}). The user can adjust ΔD in the software provided by the manufacturer, based on their preferences (e.g., Kozu *et al.*, 2005; Tokay *et al.*, 2001). The rainfall rate in 2DVD software is calculated by the following equation

$$R = 3600 \cdot \frac{1}{\Delta t} \cdot \sum_{i=1}^{n} \frac{V_i}{A_i}, \tag{3.2}$$

where Δt is the time interval, i is the drop number, n is the total number of fully visible drops measured in time interval Δt; V_i is the volume of drop i in mm^3 and A_i is the effective measuring area for drop i in mm^2.

3.2.1 Standard Matching and Re-matching Algorithm Performance

As described above, the 2DVD works on the basis of two orthogonal video cameras. Therefore, matching particle's shadows in the upper light sheet with those

in the lower sheet is very important. The following is a description of the matching procedure in the 2DVD standard matching algorithm. If there is a plausible element recorded by camera B, each drop in camera A will be tested. Plausibility is based on comparisons of heights and widths of such particle records. This test is carried out for a certain time window. The first plausible match is accepted and entered into V*.HYD (M. Schönhuber, Joanneum Research, 2007, personal communication).

Tokay *et al.* (2001) and Marzuki *et al.* (2006) predicted that the 2DVD occasionally records spurious small drops especially, in heavy rainfall. The reason is in windy condition, small drops may pass the observing area at low angles without falling into the container. These spurious drops resulted in false terminal fall speeds. To overcome this problem, they adopted a threshold of fall speed to filter out the spurious drops using the results of Gunn and Kinzer (1949), as also proposed in the previous studies (e.g., Donnadieu, 1980; Hauser *et al.*, 1984). Tokay *et al.* (2001) retained the drops within 50% of GK observations that eliminated 18% of the observation drops. On the other hand, Marzuki *et al.* (2006) used the same threshold as Tokay *et al.* (2001), excluding 38% of the drops. The shortcoming of such a filtering procedure is that the 2DVD mostly underestimated the rain totals, due mainly to the matched drops that have been eliminated trough the velocity threshold mentioned above. Both Tokay *et al.* (2001) and Marzuki *et al.* (2006) analyzed the raindrop derived by the 2DVD standard matching algorithm. The shortcoming of such a matching procedure in the 2DVD standard matching algorithm is that the first plausible match is directly accepted without checking another plausible.

Some of spurious drops may be due to the mismatching problem between the front-and side-view camera images in the 2DVD especially, for small-sized drops. The manufacturer of 2DVD (Joanneum Research) realized the shortcoming of such a matching procedure in the 2DVD standard algorithm and then developed a new re-matching algorithm. Instead accepting the first plausible match, in re-matching algorithm all plausible matches are examined and then they are ranked according to their height and width ratios. In re-matching procedure, literature models for raindrops are also considered. By appropriate programming techniques

the best matches are found and entered into V*.HYD (M. Schönhuber, Joanneum Research, 2007, personal communication).
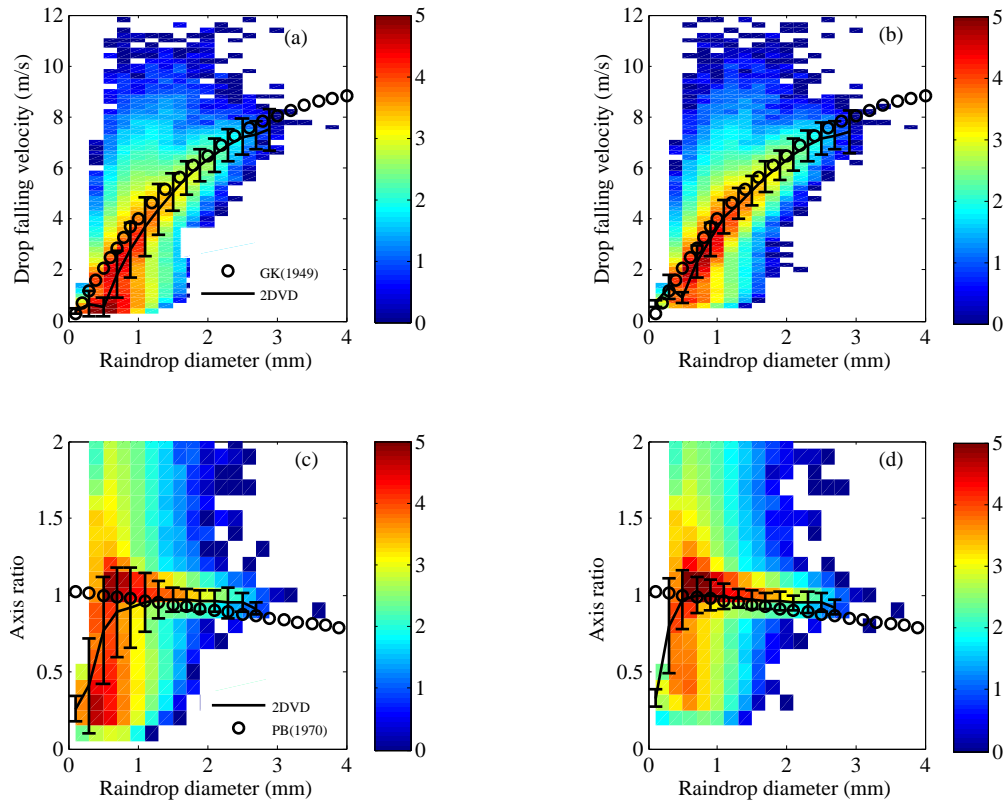
Figure 3.3: Distribution of raindrop falling velocity and oblateness (axis ratio) derived by using 2DVD standard matching (a and c) and re-matching algorithm (b and d) for rain event on 23 March 2006 at Kototabang, west Sumatera, Indonesia. GK denotes the observation results from Gunn and Kinzer (1949) and PB denotes the oblateness relationship from Pruppacher and Beard (1970). Solid line and error bars are the average value and its standard deviation. Color scale represents $\log_{10}$ of the number of raindrops for a given drop diameter, falling velocity and axis ratio.

Figure 3.3 shows the hydrometeor velocities and axis ratio of precipitation on 23 March 2006 at Kototabang derived by using standard (Figs. 3.3a and c) and re-matching algorithm (Figs. 3.3b and d). Solid line and error bars denote the averaged value and its standard deviation. Prior to averaging, the outliers are

first filtered out by identifying the outliers as the values more than three times of standard deviation. It is observed that the distribution of raindrop falling velocity derived from re-matching algorithm is closer to the results of Gunn and Kinzer (1949) than that from standard matching. For $D > 1$ mm, Fig. 3.3c (re-matching) shows that the raindrop falling velocity in good agreement with Gunn and Kinzer (1949). However, for $D < 1$ mm, raindrop falling velocity produced by re-matching algorithm are much smaller compared to the data of Gunn and Kinzer (1949). Employing re-matching algorithm also produces better axis ratio distribution than the standard matching algorithm. The mean axis ratios obtained by the re-matching algorithm lie close to the axis ratio from Pruppacher and Beard (1970), at least for raindrop diameter bigger than 0.75 mm (Fig. 3.3d). Figure 3.4 shows the histogram of axis ratio for several diameters from two years observation period (2006-2007). It can be seen that the axis ratios for drops smaller than 0.4 mm is not reliable because their value is mostly smaller than 1. This condition occurs not only at heavy rain but also at light rain (Fig. 3.4). Therefore, we will hereafter exclude drops that are smaller in diameter than 0.4 mm.
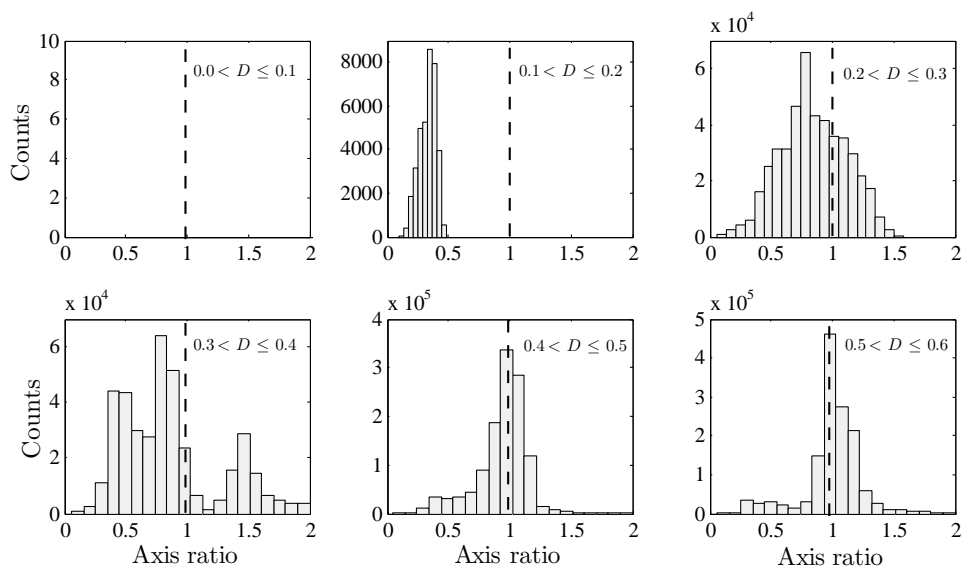
Figure 3.4: Histogram of axis ratio for several diameters. Dashed line denotes the axis ratio = 1 which is commonly known for small sized drops ($D < 1$ mm).
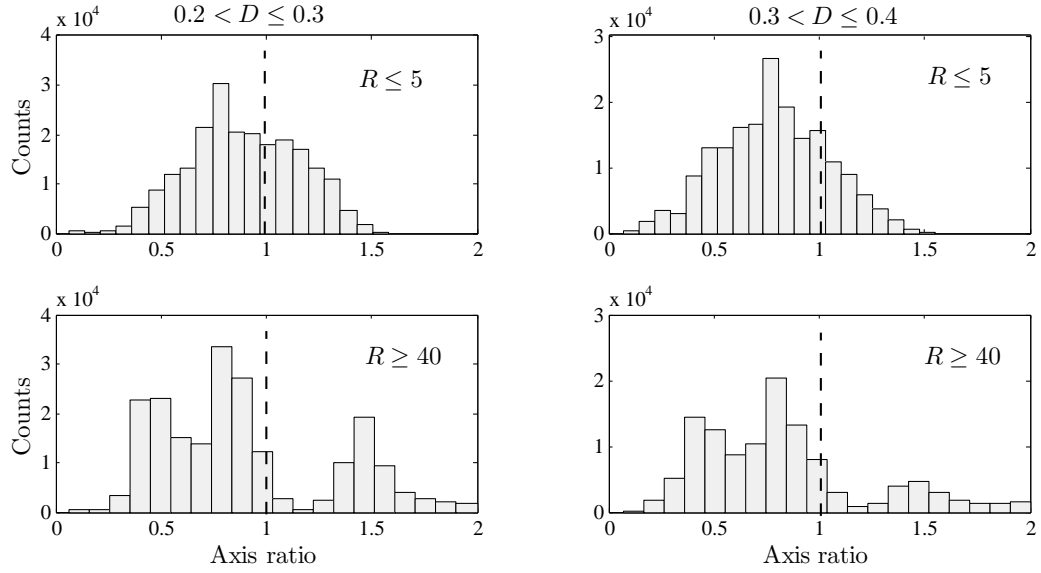
Figure 3.5: Same as Fig. 3.4 but for two diameter classes that are classified into two rainfall rates.
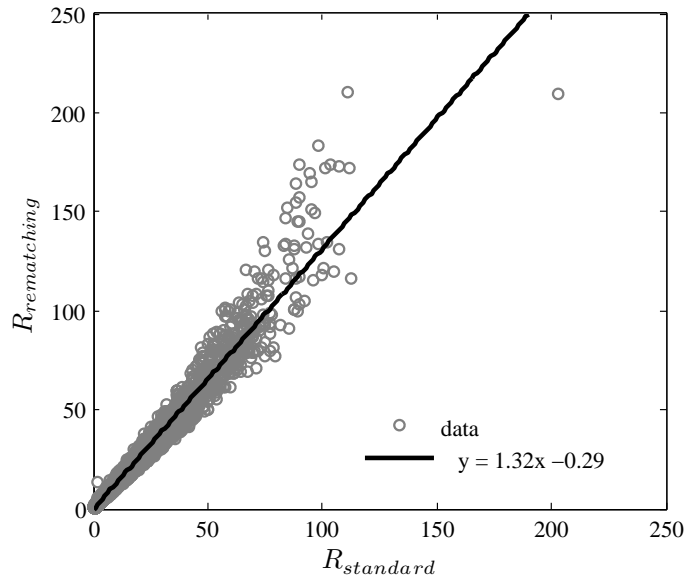
Figure 3.6: Comparison of rainfall rate measured by 2DVD standard matching with that obtained by re-matching algorithm.

The re-matching algorithm reduces the number of raindrops in the spectra. However, the rainfall rate measured by the re-matching algorithm is higher than that of the standard matching. From two years observation period (2006-2007), the linear regression of R between these two algorithms is $R_{rematching} = 1.32R_{standard} - 0.29$, with the correlation coefficient of 0.99 (Fig. 3.6). Moreover, R from re-matching also shows better comparison with ORG than standard matching. The linear regression equation (correlation coefficient) for this two matching procedure are $R_{standard} = 0.80R_{ORG} + 0.55(0.97)$, $R_{rematching} = 1.10R_{ORG} + 0.09(0.98)$, respectively.

Rainfall rates are significantly influenced by the concentration of medium and large-sized drops. The re-matching algorithm adequately results in a higher concentration of medium and large-size drops than the standard matching, which in course contributes to higher precipitation parameters such as rainfall rate. Figure 3.7 shows the distribution of $\Delta N(D)/N(D)_{standard}$ for several rain classes. $\Delta N(D)$ is defined as the difference between $N(D)$ produced by the re-matching and the standard matching algorithm $(\Delta N(D) = N(D)_{rematching} - N(D)_{standard})$. In general, the re-matching algorithm reduces the concentration of small-sized drops in the standard matching algorithm as indicated by negative value of $\Delta N(D)/N(D)_{standard}$. It is also found that the difference in the DSD produced by two matching methods is rainfall rate-dependent. For light rain (Fig. 3.7a), the differences between the two methods are small enough. However, the differences become significant as the rainfall rate increases. Thus, from this comparative analysis, in this thesis, the re-matching algorithm is used to reduce the small drops mismatch produced by the standard matching software of 2DVD.

3.2.2 Wind Effect

Besides the small drops mismatch problem, the 2DVD measurements could be affected by another source of uncertainty due to the small sampling volume (statistical undersampling noise), drop sorting (observational noise), and instrumental uncertainty (instrumental noise). The instrumental uncertainties of disdrometers are poorly known. The effect of strong winds, calibration errors, are among the sources of instrumental noise. The 2DVD at Kototabang is a first generation
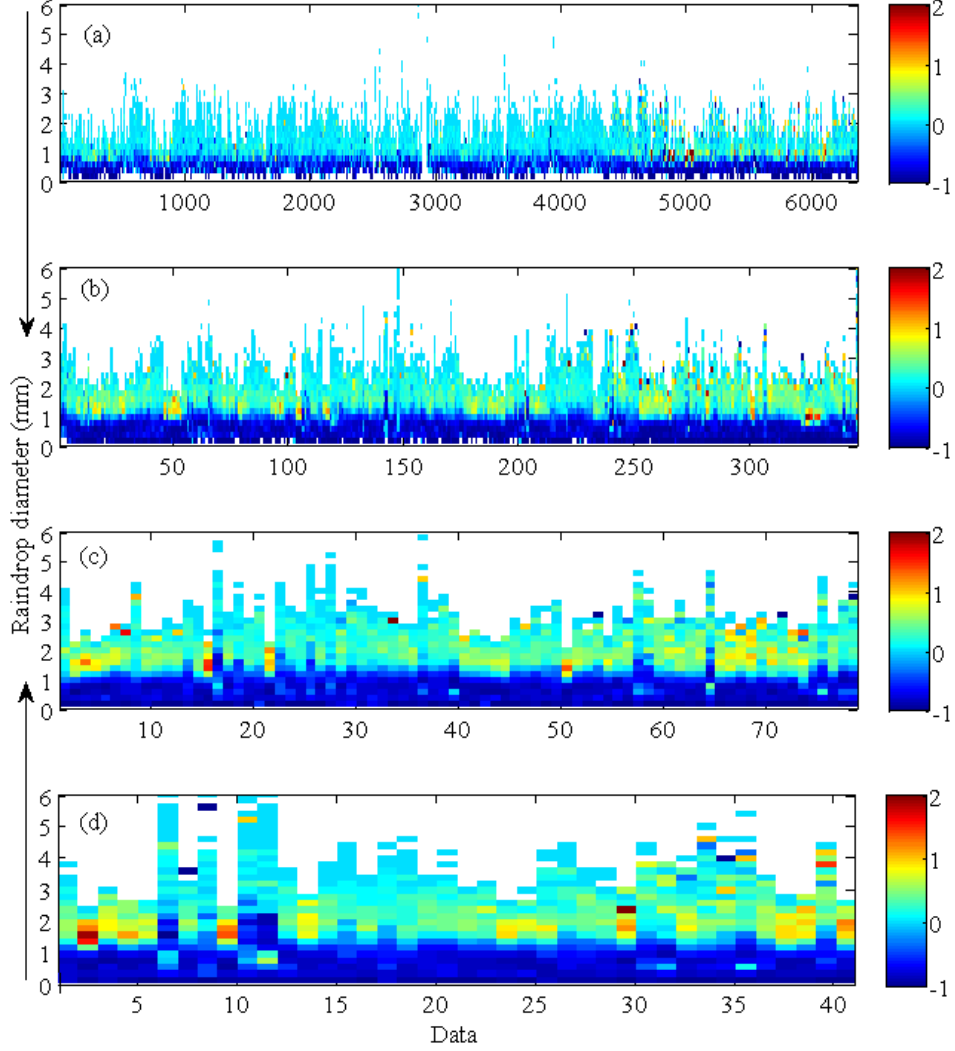
Figure 3.7: Distribution of $\Delta N(D)/N(D)_{standard}$ per drop size for rainfall rate classes of $1\leq R <2$ mm h^{-1} (a), $9\leq R <10$ mm h^{-1} (b), $19\leq R <20$ mm h^{-1} (c), and $29\leq R <30$ mm h^{-1} (d). $\Delta N(D)$ is defined as the difference between $N(D)$ produced by re-matching and that by the standard matching algorithm ($\Delta N(D) = N(D)_{rematching} - N(D)_{standard}$). The x axis shows the number of plotted data, while the y axis is the raindrop diameter. Color scale represents the value of $\log_{10}[\Delta N(D)/N(D)_{standard}]$. Data on horizontal axis denotes time (1-min. resolution for each rainfall rate class)

version in which two video cameras are enclosed in a large box. Nešpor *et al.* (2000) pointed out the box modifies the air flow, and this in turn affects the drop trajectories, causing some of the drops to miss the virtual measuring area in the instruments opening. Consequently, the shape of the enclosure of the instrument generates errors in the detection of the small drops. Moreover, the 2DVD at Kototabang is installed beside a building ($\approx$ 4 m). Wind that comes toward the building may generate turbulence that could distort the spatial distribution of drops in the measuring area. In this study, however, the possible wind effect on the estimated DSD is still not considered.

3.2.3 Sampling Size Errors

Joss and Waldvogel (1969) investigated the standard deviation of the rainfall rate and the reflectivity factor due to limited sampling size. They argued that some variabilities of the DSD and $Z - R$ relationship found in several references could be due to the statistical undersampling noise, besides because of a change in the meteorological situation. One difficulty to relate discrete measuring instruments to constant volume instruments, such as radars, is that the sample volume of surface disdrometer is diameter dependent with larger raindrops having larger sampling volumes because they travel further distances during a fixed observational dwell times. Schuur *et al.* (2001) and Lee and Zawadzki (2005) investigated the undersampling effect in the 2DVD and in a Precipitation Occurrence Sensor System (POSS), respectively, by using the methodology proposed by Joss and Waldvogel (1969). Schuur *et al.* (2001) used an empirical distribution (Marshall-Palmer and biexponential distribution) in their calculation. In this section we used the measured DSD to demonstrate the significance of the undersampling effect in the 2DVD.

Rainfall rate (instead of (3.2)) and radar reflectivity factor from the 2DVD data can be estimated using the following equations (Schuur *et al.*, 2001)

$$R = 6 \text{x} 10^{-4} . \pi . \sum_{i=1}^{n} v(D_i) D_i^3 \frac{n_i}{V_i}, \qquad [\text{mm/h}] \qquad (3.3)$$

$$Z = \sum_{i=1}^{n} D_i^6 \frac{n_i}{V_i}, \qquad [\text{mm}^6/\text{m}^3] \qquad (3.4)$$
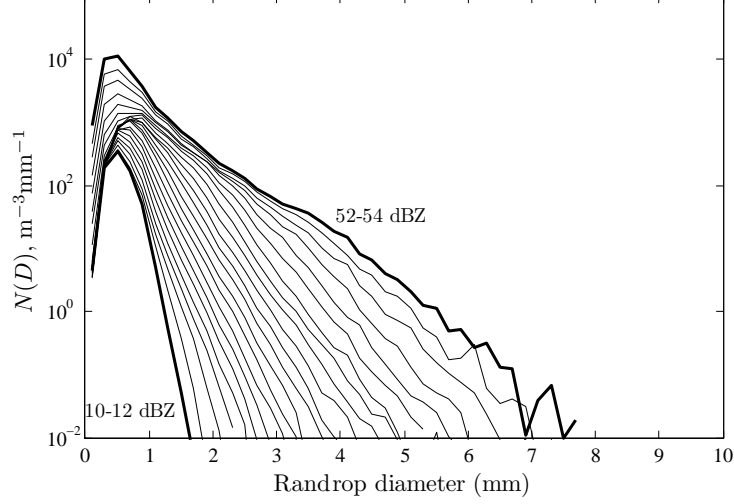
Figure 3.8: Average of 2 years of 1-min DSDs at 2-dBZ reflectivity intervals, with 1-min rainfall-rate threshold of 0.1 mm h^{-1}. The first solid line curve is for 10-12 dBZ and the last one for 52-54 dBZ. Total number of 1-min samples is 45415.

where i denotes the ith interval of drop diameters, n_i is the number of drops within this size interval, D_i (mm) is the equivolume sphere diameter of a drop, $v(D_i)$ the terminal fall velocity of a drop with diameter D_i, and V_i(m^3) is the sampling volume of drops in the ith size category. In this calculation, V_i is calculated as $V_i(D) = v(D_i)AT$ with A(m^2) being the exposure area of 2DVD (0.01 m^2 in our assumption) and T(s) is the accumulation time (60 s in our calculation). For simplification, it is assumed that the total number of drops n_i in a given diameter interval dD_i(mm) counted in different volumes of the same size, are distributed according to the Poisson distribution:

$$p(n_i) = \frac{\overline{n_i}}{n_i!}e^{-\overline{n_i}}. \tag{3.5}$$

Note that the diameter interval of the 2DVD is uniform (i.e., $dD_i = dD_{i+1} = dD$). Assuming the Poison distribution with the mean value $\overline{n_i}$, the fractional standard deviation (FSD) of R and Z due to Poisson undersampling can be estimated by

$$\text{FSD(R)} = (AT)^{-1/2}\frac{\sqrt{\int_{D_{min}}^{D_{max}} v(D)N(D)D^6 dD}}{\int_{D_{min}}^{D_{max}} v(D)N(D)D^3 dD}, \tag{3.6}$$

$$\text{FSD(Z)} = (AT)^{-1/2} \frac{\sqrt{\int_{D_{min}}^{D_{max}} v(D)N(D)D^{12}dD}}{\int_{D_{min}}^{D_{max}} N(D)D^6 dD}, \tag{3.7}$$

where $v(D)$ is the terminal fall velocity of a drop in still air according to Atlas *et al.* (1973). Lee and Zawadzki (2005) called (3.6) and (3.7) as the relative standard deviation. Detailed derivation of (3.6) and (3.7) can be found in Schuur *et al.* (2001) or in Lee and Zawadzki (2005).
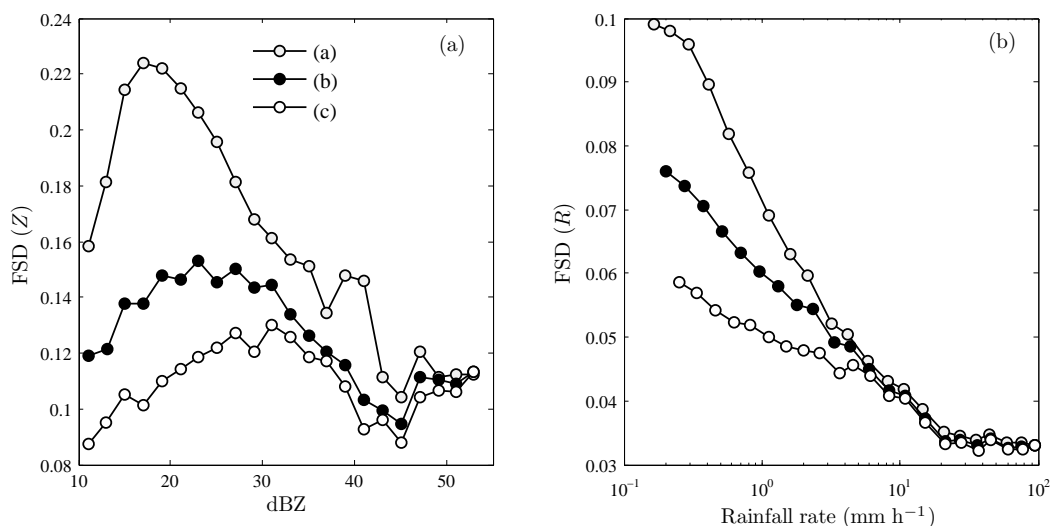
Figure 3.9: FSD in Z (a) and R (b) due to the statistical undersampling for 1-min DSDs obtained from the DSD in Fig. 3.8 by assuming a Poisson distribution is assumed. Lines which are symbolized by (a), (b) and (c) denote the FSD estimated from Fig. 3.8 (without the number of drops threshold), average DSDs with a 1-min number of drops threshold of 100 ($N_T > 100$) and average DSDs with a 1-min number of drops threshold of 200 ($N_T > 200$), respectively. N_T is total number of drops in the DSD.

The value of n_i decreases with increasing diameter and can be zero for very large-sized drops. Hence, large errors of R and Z from the 2DVD data have to be expected if (a) the total concentration of particles is small (small $\overline{n_i}$ in all size bins) or (b) larger drops are in excess and small drops are in deficit. As was mentioned above, the Marshall-Palmer and biexponential distribution were used in Schuur *et al.* (2001). In this work, the measured DSD is used, instead of any empirical

47

distribution. Figure 3.8 shows average DSDs at 2-dBZ reflectivity intervals from 2 years of 2DVD data at Kototabang, with a 1-min rainfall-rate threshold of 0.1 mm h^{-1}. The first solid line curve is for 10-12 dBZ and the last one for 52-54 dBZ. These average DSDs are not affected by undersampling because they are averages of numerous 1-min DSDs (Lee and Zawadzki, 2005). Williams (2008) described that biases and uncertainties of Z calculated from Joss-Waldvogel Distrometer, JWD (e.g., Joss and Waldvogel, 1969) data are decreasing with increasing number of sampled raindrops, with at least 300 raindrops needed to reduce the reflectivity bias and uncertainty below 1 and 0.8 dBZ, respectively. The 2DVD has twice the sampling area of the JWD. Therefore, for comparison, we also calculated FSD(R) and FSD(Z) for 1-min number of drops exceeding a threshold of 100 (fulled black circle in Fig. 3.9) and 200 (empty circle in Fig. 3.9), respectively. It can be seen from Fig. 3.9 that the errors in estimating R are relatively small (< 10 %) for all rain intensities. On the other hand, the standard errors of Z are more serious. It can be also observed that the uncertainties of R and Z decrease with increasing number of raindrops. A 1-min number of drops threshold of 200 ($N_T > 200$) provides the smallest bias. However, this threshold eliminates 40% of the data. Therefore, in the next analysis in this thesis, a 1-min number of drops threshold of 100 ($N_T > 100$) are used, in addition to a 1-min rainfall-rate threshold of 0.1 mm h^{-1}.

3.2.4 Sequential Intensity Filtering Technique (SIFT)

Because of small sampling volume of instrument used, the observed DSDs at the ground are affected by the drop sorting through turbulent air motion and the statistical variability. Lee and Zawadzki (2005) proposed the sequential intensity filtering technique (SIFT) to minimize the effect of spurious variability on disdrometric data. The SIFT approach filters out the observational noise concentrating on the stability of the $Z - R$ relationship during a physically uniform situation. The basic steps of a SIFT procedure can be summarized as follows:

- Z (or R) is calculated from 1-min DSDs for a time window.

- DSDs are ordered in increasing Z (or R). A moving average of M consecutive ordered DSDs is performed to derive filtered DSDs.
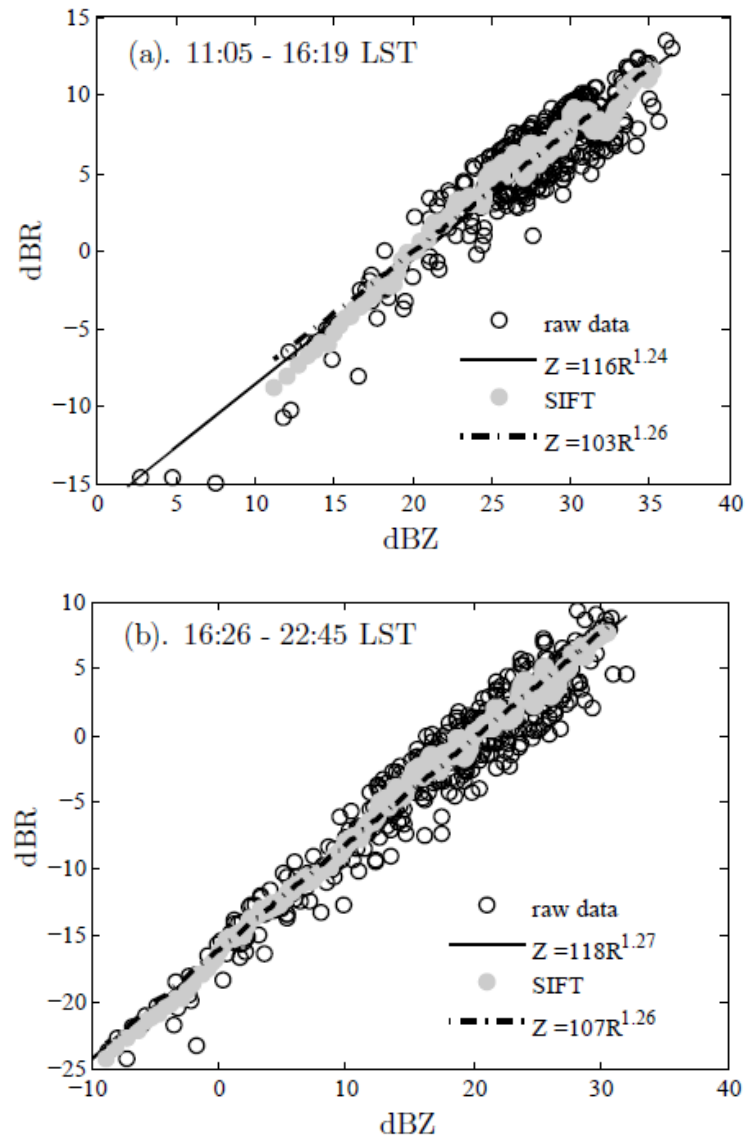
Figure 3.10: Scatter plot of $R - Z$ relationships for raw 1-min data for two rain events on 3 January 2007 where dBZ and dBR denote $10\log(Z)$ and $10\log(R)$, respectively. The size of the moving average within a window (rain event) is fixed at M = 10 1-min DSDs

- Z and R are calculated from filtered DSDs.

Figure 3.10 shows the $R - Z$ scattergram before and after applying SIFT on 2DVD data for rain event 3 January 2007 with a time window W of the whole event. We will average groups of 10 DSDs samples of sequential intensity taken within the event. Hence, the averaging size is fixed as M=10 1-min DSDs. It is clear that the uncertainty is greatly reduced by SIFT and that the $R - Z$ relationship is almost deterministic. Lee and Zawadzki (2005) proposed to use a one hour time window. However, if only one time window is taken over the entire event for SIFT, a similar $R - Z$ relationship would be obtained.

The SIFT technique may be acceptable to reduce the variability of the $R - Z$ relation. However, it will reduce the temporal variation of the DSD that is also important in cloud physics study. Cao *et al.* (2008) modified the SIFT approach by averaging the DSDs based on two parameters (sorting and averaging based on two parameters, SATP). Unlike the SIFT method, SATP is applied to a whole dataset rather than a single event. With SATP, two parameters are used to characterize the DSD, and physical variability is therefore preserved much better than with SIFT. The basic steps of a SATP procedure can be summarized as follows:

- Select two characteristic parameters to build two dimensional grids.

- Calculate both characteristic parameters based on 1-min DSD measurements.

- Sort the whole dataset and find DSDs with similar physical characteristics according to their two characteristic parameters.

- Average the observed DSDs located in the same grid to obtain a new DSD, and

- Process the averaged DSDs (i.e., fit them to a gamma distribution) to develop $R - Z$ or other relations.

Cao *et al.* (2008) sorted their rain data based on rainfal rate R (step 10%) and median volume diameter D_0 (step 0.05 mm). If we parameterize the DSD with

the gamma function, D_0 is a function of μ and Λ. Errors of D_0 estimates depend on the measurement errors of μ and Λ that depends on the moments of DSD used. In general, the high moments, which have relatively larger measurement errors, and the low moments, which are determined by small drops and susceptible to disdrometer measurement uncertainty, do not represent rain physics well (see Chapter 4). Therefore, it may be better to use the mass-weighted mean diameter (D_m) than D_0. If the size of the dataset is big enough, sorting based on more than two parameters is of course much better. Moreover, two parameters are not accurate enough to characterize some extreme cases (e.g., nongamma distributions).
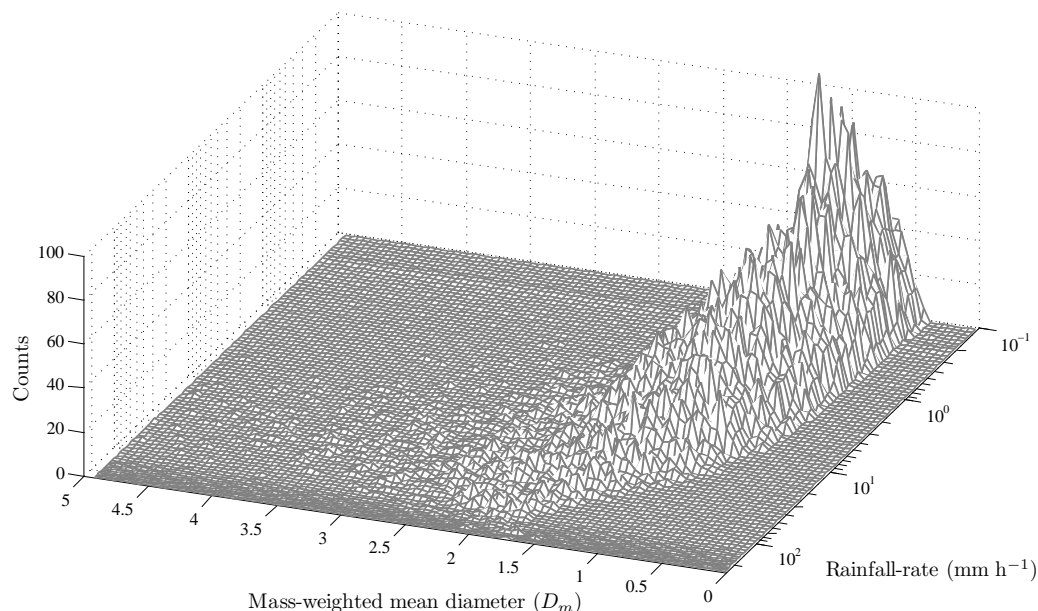
Figure 3.11: Frequency distribution of sorted rain data based on rain rate (step 10% for $R < 100$ mm h^{-1} and step of 10 mm h^{-1} for $R > 100$ mm h^{-1}) and mass-weighted mean diameter D_m (step 0.05 mm). Each pixel of the $R - D_m$ plane represents a specific DSD. The bar over the pixel denotes the number of observed DSDs sorted for one specific DSD. Observed DSDs within a pixel are averaged to obtain the specific DSD.

Figure 3.11 shows an example of SATP application for 2 years of 1-min DSDs collected at Kototabang. Each grid in the $R - D_m$ plane is defined by variations

of $\pm 5\%$ for R and $\pm$ 0.025 mm for D_m. Averaging the DSDs may reduce the physical variation if the grid pixels are not small enough. Therefore, for very extreme rain ($R > 100$ mm h^{-1}), the step of R is 10 mm h^{-1}. The bar length indicates the number of observed DSDs. The DSDs within each grid pixel are characterized by small variations of R and D_m and are assumed to represent similar rain physics.

The SIFT and the SATP method will reduce the temporal variation of the DSD. It is well known that the DSD in the early stage of the precipitation is different from that in the end stage. Therefore, the SIFT and SATP approaches will be used only when we deal with the relationship of the DSD parameters (e.g., μ, Λ) with the integral rainfall parameters (e.g., R, Z).

3.3 Radars

There are three radars providing data being used in this thesis. However, a detailed description of these radars will not be devoted here, because the radars are only used in a small function of this thesis.

Table 3.2 summarizes the system specifications of two radars used in this study. The 1.3 GHz wind profiler is a UHF-band wind profiler which is designed for observing wind in the lower troposphere (Gage *et al.*, 1994). The wind profiler used here is located at the Global Atmosphere Watch (GAW) observatory of Indonesian Meteorology and Geophysics Agency (BMG), about 300 m away from the 2DVD site. The wind profiler can provide information on the atmospheric motion in clear air by the Doppler principle (Carter *et al.*, 1995; Gage *et al.*, 1994). Because the backscatter signal from the precipitation particles is much larger than that from the atmospheric turbulence (when rain passes over the radar site), the wind profiler can be also used to study precipitation (Williams *et al.*, 1995). The wind profiler echoes were considered as echoes from precipitation, if rain at the ground surface was detected by the 2DVD. To ensure that both instruments (the 2DVD and the wind profiler) were simultaneously observing rain, the observations were screened to require that the profiler had reflectivities greater than 18 dBZ and mean downward Doppler velocities greater than 3 ms^{-1}, while the surface disdrometer was required to have observed at least 0.1 mmh^{-1} rainfall rate in the

Table 3.2: Radar specifications

Radar Parameters	BLR	EAR
Radar system	Pulse Doppler radar	Pulse Doppler radar
Operating frequency	1.3 GHz	47.0 MHz
Transmit power	1.1 kW	100 kW
Antenna	5.9 m^2	110 m in diameter
Beam width	4.1^o	3.4^o
Range resolution	150 m	150 m

minute sample. The sensitivity of these thresholds has been examined in detail by Renggono *et al.* (2001). The wind profiler observations are used to classify the type of precipitation.

Equatorial Atmosphere Radar (EAR) is a very high frequency (VHF) atmospheric radar system with an active phased-array antenna system. The characteristics and performance of the EAR are described in detail by Fukao *et al.* (2003). This radar is designed to have some capabilities to study the atmospheric activities at the troposphere and the lower stratosphere. However, sensitive VHF Doppler radars can detect the precipitation echoes simultaneously with the echoes from ambient atmosphere (e.g., Fukao *et al.*, 1985; Wakasugi *et al.*, 1986). Techniques for retrieving the DSD using the VHF Doppler radar have been developed over the past decades (e.g., Sato *et al.*, 1990; Wakasugi *et al.*, 1986). Hence, the EAR data is used to study the vertical structure of DSD over Kototabang. However, only the data during April-May 2004 (first campaign of Coupling Process in the Equatorial Atmosphere; CPEA) are available for this study.

Another radar, which is also used in this work, is an X-band meteorological radar. This radar is belong to the Shimane University of Japan. The operational frequency and peak transmission power of this radar are 9.74 GHz and 40 kW, respectively. The antenna is an off-set 1.2 m parabolic dish and the range resolution and the maximum range of observation are 100 m and 30 km. The horizontal beam scanning rate of the radar is 2 rpm, and it can present Constant Altitude Plan Position Indicator (CAPPI) and Range Height Indicator (RHI)

displays every 10 min using 16 elevation angles.

3.4   Agilent 85070E Dielectric Probe Kit

The Agilent 85070E Dielectric Probe Kit, used with an Agilent N5242A-400 Vector Network Analyzer (VNA), determines the intrinsic electromagnetic properties of many dielectric materials. It is based on an open-ended coaxial probe. A Detailed description of this instrument could be found in Agilent (2008). In this thesis, this instrument was used to investigate the complex dielectric constant of real rainwater, as collected in nature. Rainwater samples were collected at Graz, Austria (47.04ºN, 15.26ºE, 353 m above mean sea level), and Kototabang.

Chapter 4

Bias in Moment Method to Estimate Parameters of Raindrop Size Distribution

4.1 Introduction

It is well known that almost all integral rainfall parameters (IRPs) of interest can be represented by a moment of the raindrop size distribution (DSD). In terms of the gamma distribution as in (2.6), it is given by

$$M_n = \int_0^\infty D^n N(D)\, dD = N_0 \Gamma(n + \mu + 1)/\Lambda^{n+\mu+1}, \tag{4.1}$$

where $\Gamma(y)$ is the complete gamma function. The DSD moment for the exponential distribution can be derived from (4.1) by assuming $\mu = 0$. On the other hand, for the lognormal distribution as in (2.8) it is given by

$$M_n = \int_0^\infty D^n N(D)\, dD = N_T e^{nm + \frac{1}{2}n^2\sigma^2}. \tag{4.2}$$

Table 4.1 summarizes the various moments of the DSD for the exponential ($\mu = 0$) and gamma distribution ($\mu > 0$) in which complete gamma function is simply represented as factorial operation (Smith, 2003).

The moment method that uses combinations of moment of the DSD is widely used to estimate the DSD parameters. For example, Kozu and Nakamura (1991)

Table 4.1: Various moments of the DSD for the exponential and gamma distribution

n	Related IRPs	Exponential	Gamma
0	Total number of drops (N_T)	$N_0 D_m/4$	$N_0(\mu)![D_m/(\mu+4)]^{\mu+1}$
1	-	$N_0 D_m^2/16$	$N_0(\mu+1)![D_m/(\mu+4)]^{\mu+2}$
2	Total surface area	$N_0 D_m^3/32$	$N_0(\mu+2)![D_m/(\mu+4)]^{\mu+3}$
3	Liquid water content (LWC)	$3N_0 D_m^4/128$	$N_0(\mu+3)![D_m/(\mu+4)]^{\mu+4}$
4	Close to rain rate (R)	$3N_0 D_m^5/128$	$N_0(\mu+4)![D_m/(\mu+4)]^{\mu+5}$
5	-	$15N_0 D_m^6/512$	$N_0(\mu+5)![D_m/(\mu+4)]^{\mu+6}$
6	Reflectivity factor (Z)	$45N_0 D_m^7/1024$	$N_0(\mu+6)![D_m/(\mu+4)]^{\mu+7}$

used the third, fourth and sixth moments (referred to as M_3, M_4 and M_6, respectively) while Ulbrich and Atlas (1998) used moments M_2, M_4 and M_6. Recently, Caracciolo *et al.* (2006) used higher moments, i.e. M_4, M_5 and M_6, to parameterize the measured DSD. The moment method is simple and easy to be used. However, some authors have reported that this method is significantly biased (e.g., Kliche *et al.*, 2008; Smith and Kliche, 2005). Smith and Kliche (2005) have demonstrated the bias in moment estimators for the exponential DSD while Kliche *et al.* (2008) compared the bias involved in the procedure of L-moments (LM), moment method (MM), and maximum likelihood (ML), for the gamma distribution. Both authors concluded that the bias produced by the MM can provide significant impact to draw inference about the characteristics of DSD being sampled. In addition, Kliche *et al.* (2008) found that the drop truncation at the small drop end would give large errors when using the lowest moment combinations. Furthermore, the LM and ML method start to give more errors than MM when small drop truncation is allowed in the analysis.

In the following sections we will again visit the bias in the MM to retrieve the DSD parameters, not only for the exponential and the gamma but also for the lognormal distributions. Besides the MM, the ML and the LM will also be used. Because the parameters of the DSD in nature are inherently unknown, this work must be done by examining the ability of each method to recover the parameters

of known DSDs from which the samples are taken. To deal with the measured DSD, we analyze the data collected by the 2DVD at Kototabang during 2006-2007. Some points of this chapter may be a review of the previous work done. However, in this chapter we studied the bias in moment estimators, of all possible moments (e.g., 35 for gamma and 21 for exponential).

4.2 Governing Equations to Retrieve DSD Parameters of Binned Data (DSD)

The 2DVD also provides data on drop-by-drop basis. This section is devoted to derive the equations to retrieve the DSD Parameters of binned data while the equations for drop-by-drop data is given in Chapter 5.

4.2.1 Moment Method (MM)

Table 4.1 provides a wide range of possible ways for the two moments needed to fit the two parameters of the exponential distribution or the three moments needed for the gamma and lognormal distribution. There are 21 and 35 possibilities to choose two (Table 4.2) and three moments (Table 4.3) out of seven . Hence, there are 21 and 35 ways to calculate the DSD parameters of exponential, gamma and lognormal, respectively, using two (M_x, M_y) and three (M_x, M_y, M_z) out of the seven moments.

4.2.1.1 Exponential Distribution

As mentioned above, we will examine 21 possible moment estimators to calculate the parameters of exponential function. Parameters N_0 and D_m of each possible moment combination can be simply derived by taking two moments in Table 4.1. The following explanation, we devote, as an example, to the derivation of exponential parameters from M_3 and M_4.

From Table 4.1, $M_3 = 3N_0D_m^4/128$ and $M_4 = 3N_0D_m^5/128$, hence, D_m can be derived easily by calculating the ratio between M_4 and M_3 which can be written

Table 4.2: 21 ways to estimate the DSD parameters of exponential distribution

Moment	1	2	3	4	5	6	7	8	9	10	11	12	3	14	15
x	0	0	0	0	0	0	1	1	1	1	1	2	2	2	2
y	1	2	3	4	5	6	2	3	4	5	6	3	4	5	6
Moment	16	17	18	19	20	21									
x	3	3	3	4	4	5									
y	4	5	6	5	6	6									

as

$$D_m = M_4/M_3. \tag{4.3}$$

By substituting D_m in M_4, the equation for N_0 is given by

$$N_0 = (128/3)M_3^5/M_4^4. \tag{4.4}$$

Finally, another parameter (Λ) for this moment estimator is derived from $\Lambda = 4/D_m$, given by

$$\Lambda = 4M_3/M_4. \tag{4.5}$$

Similarly, the equations for other moment estimators can be governed.

4.2.1.2   Gamma Distribution

Parameters of the gamma distribution (N_0, D_m and μ) can be calculated by taking three moments in Table 4.1. We will examine 35 possible moment estimators to calculate the parameters of gamma function. In the following example, we explain the derivation of MM using M_2, M_3 and M_4.

From Table 4.1, $M_2 = N_0(\mu + 2)![D_m/(\mu + 4)]^{\mu+3}$, $M_3 = N_0(\mu + 3)![D_m/(\mu + 4)]^{\mu+4}$ and $M_4 = N_0(\mu + 4)![D_m/(\mu + 4)]^{\mu+5}$ respectively; hence, D_m can be derived easily by calculating the ratio between M_4 and M_3, as in the exponential distribution, which can be written as

$$D_m = M_4/M_3 = \frac{(\mu + 4)M_3}{(\mu + 3)M_2}. \tag{4.6}$$

Table 4.3: 35 ways to estimate the DSD parameters of gamma and lognormal distribution

Moment	1	2	3	4	5	6	7	8	9	10	11	12	13	14	15
x	0	0	0	0	0	0	0	0	0	0	0	0	0	0	0
y	1	1	1	1	1	2	2	2	2	3	3	3	4	4	5
z	2	3	4	5	6	3	4	5	6	4	5	6	5	6	6
Moment	16	17	18	19	20	21	22	23	24	25	26	27	28	29	30
x	1	1	1	1	1	1	1	1	1	1	2	2	2	2	2
y	2	2	2	2	3	3	3	4	4	5	3	3	3	4	4
z	3	4	5	6	4	5	6	5	6	6	4	5	6	5	6
Moment	31	32	33	34	35										
x	2	3	3	3	4										
y	5	4	4	5	5										
z	6	5	6	6	6										

Next we form the ratio

$$\eta = \frac{M_3^2}{M_4 M_2} = \frac{\mu + 3}{\mu + 4}. \tag{4.7}$$

Equation (4.7), which is derived by substituting D_m in M_4, may be solved for μ to yield

$$\mu = \frac{3 - 4\eta}{\eta - 1}. \tag{4.8}$$

Λ for this moment estimator, is derived from $\Lambda = (\mu + 4)/D_m$, resulting in

$$\Lambda = M_2(\mu + 3)/M_3. \tag{4.9}$$

N_0 is determined from substituting of the values of μ and Λ for any of the three moments M_2, M_3, and M_4. Similarly, the equations for other moment estimators can be governed.

In general, we can calculate η, Λ and N_0 from three different moments (M_x, M_y, M_z) as

$$\eta = \frac{M_y^{\frac{z-x}{y-x}}}{M_x^{\frac{z-y}{y-x}} M_z}, \tag{4.10}$$

$$\Lambda = \frac{M_x}{M_y}\left(\frac{\Gamma(\mu+y+1)}{\Gamma(\mu+x+1)}\right)^{\frac{1}{y-x}}, \tag{4.11}$$

$$N_0 = M_z\frac{\Lambda^{\mu+z+1}}{\Gamma(\mu+z+1)}, \tag{4.12}$$

where $0 \leq x < y < z$. Several moment estimators will develop high order polynomial equations (e.g., quadratic, cubic) that have several solutions for μ in (4.7). The best μ value is chosen by selecting the one that provides the minimum difference between measured and calculated moment.

4.2.1.3 Lognormal Distribution

Like parameters of gamma distribution, the parameters of the lognormal distribution (N_T, m and σ) can also be derived by taking three moments. Assuming Ln_n is the natural logarithm of M_n, the parameters of lognormal distribution from M_3, M_4 and M_6, as an example, can be then obtained as,

$$N_T = \exp[(24Ln_3 - 27Ln_4 + 6Ln_6)/3], \tag{4.13}$$

$$m = (-10Ln_3 + 13.5Ln_4 - 3.5Ln_6)/3, \tag{4.14}$$

$$\sigma^2 = (2Ln_3 - 3Ln_4 + Ln_6)/3. \tag{4.15}$$

Similarly, the equations for other moment estimators can be governed.

4.2.2 Maximum Likelihood Estimation

In term of probability density function, $f(D|\theta)$, DSD can be written as a product of $f(D|\theta)$ with the total number of raindrops (N_T), given by

$$N(D) = N_T.f(D|\theta), \tag{4.16}$$

where $f(D|\theta)$ for gamma, exponential and lognormal distribution, respectively, are:

$$f(D|(\Lambda, \mu)) = \frac{\Lambda^{\mu+1}}{\Gamma(\mu+1)}D^\mu e^{-\Lambda D}, \tag{4.17}$$

$$f(D|(\Lambda)) = \Lambda e^{-\Lambda D}, \tag{4.18}$$

$$f(D|(\sigma, m)) = \frac{1}{\sqrt{2\pi}\sigma D}e^{-(\ln D - m)^2/2\sigma^2}. \tag{4.19}$$

Suppose there is a sample D_1, D_2, ... , D_n of n observations, coming from a distribution with a certain distribution. The idea behind the method of maximum likelihood (ML) is to first find the joint density function for all observations which is called likelihood function defined by

$$\varphi(\theta) = f(D_1|\theta).f(D_2|\theta)...f(D_n|\theta) = \prod_{n=1}^{n_{max}} f(D_n|\theta). \qquad (4.20)$$

Haddad *et al.* (1996) wrote the likelihood function in term of DSD as

$$\varphi(\theta) = \prod_{n=1}^{n_{max}} [f(D_n|\theta)]^{N(D_n)}. \qquad (4.21)$$

where $N(D_n)$ corresponding to the observed DSD (3.1). In practice it is always more convenient to work with the scaled logarithm of the likelihood function, called the log-likelihood. The ML method try to find θ that maximizes the likelihood function $\varphi(\theta)$ or log-likelihood $\ln \varphi(\theta)$. From (4.21), it can be seen that there is no ML estimator for the mean total number concentration parameter (N_T). In this work, N_T is estimated from the 0th moment of DSD.

4.2.2.1 Gamma Distribution

From (4.17), the likelihood function and log-log-likelihood of gamma distribution, respectively, to be maximized are

$$\varphi(\theta) = \prod_{n=1}^{n_{max}} \left[\frac{\Lambda^{\mu+1}}{\Gamma(\mu+1)} D_n^{\mu} e^{-\Lambda D_n} \right]^{N(D_n)}, \qquad (4.22)$$

$$\begin{aligned} \ln\varphi(\theta) \quad = \quad & (\mu+1)\ln\Lambda \sum_{n=1}^{n_{max}} N(D_n) - \ln\Gamma(\mu+1) \sum_{n=1}^{n_{max}} N(D_n) \\ + \quad & \mu \sum_{n=1}^{n_{max}} N(D_n)\ln D_n - \Lambda \sum_{n=1}^{n_{max}} N(D_n)D_n. \end{aligned}$$
$$(4.23)$$

The scale parameter (Λ) can be obtained by solving the derivative of (4.23), with respect to Λ, given by

$$\Lambda = \frac{(\mu+1) \sum_{n=1}^{n_{max}} N(D_n)}{\sum_{n=1}^{n_{max}} N(D_n)D_n}. \qquad (4.24)$$

Substituting (4.24) in (4.23), the shape parameter (μ) can be then determined numerically by solving the derivative of (4.23), with respect to μ, and yielding the following equation:

$$\ln(\mu+1) - \Psi(\mu+1) = -\frac{\sum_{n=1}^{n_{max}} N(D_n)\ln D_n}{\sum_{n=1}^{n_{max}} N(D_n)} + \ln \sum_{n=1}^{n_{max}} N(D_n)D_n - \ln \sum_{n=1}^{n_{max}} N(D_n),$$

(4.25)

where Ψ is the "psi" or "digamma" function defined by

$$\Psi(x) = \frac{d}{dx}\ln\Gamma(x) = \frac{\Gamma'(x)}{\Gamma(x)}.$$

(4.26)

Let α be as $\alpha = \mu + 1$, (4.25) can be solved by iteration using recursion as

$$\alpha_{j+1} = \alpha_j \frac{\ln(\alpha_j) - \Psi(\alpha_j)}{Y},$$

(4.27)

where

$$Y = -\frac{\sum_{n=1}^{n_{max}} N(D_n)\ln D_n}{\sum_{n=1}^{n_{max}} N(D_n)} + \ln \sum_{n=1}^{n_{max}} N(D_n)D_n - \ln \sum_{n=1}^{n_{max}} N(D_n),$$

(4.28)

$$\alpha_1 = \frac{1 + \sqrt{1 + 4\exp(Y)/3}}{4\exp(Y)}.$$

(4.29)

After getting α, the shape parameter is calculated by $\mu = \alpha - 1$.

4.2.2.2 Exponential Distribution

Derivation of ML method for exponential distribution is similar with that of gamma distribution because the modified gamma distribution reduces to the exponential distribution when $\mu = 0$. Hence, the scale parameter (Λ) of exponential distribution can be obtained from (4.24), given by

$$\Lambda = \frac{\sum_{n=1}^{n_{max}} N(D_n)}{\sum_{n=1}^{n_{max}} N(D_n)D_n}.$$

(4.30)

4.2.2.3 Lognormal Distribution

From (4.19), the likelihood function and log-log-likelihood of gamma distribution, respectively, to be maximized are

$$\varphi(\theta) = \prod_{n=1}^{n_{max}} \left[\frac{1}{\sqrt{2\pi}\sigma D_n}e^{-(\ln D_n - m)^2/2\sigma^2}\right]^{N(D_n)},$$

(4.31)

$$\ln\varphi(\theta) = -\ln(\sqrt{2\pi})\sum_{n=1}^{n_{max}} N(D_n) - \ln\sigma \sum_{n=1}^{n_{max}} N(D_n) - \ln \prod_{n=1}^{n_{max}} D_n^{N(D_n)}$$
$$- \frac{\sum_{n=1}^{n_{max}} N(D_n)(\ln D_n)^2}{2\sigma^2} + \frac{m \sum_{n=1}^{n_{max}} \ln D_n}{\sigma^2} - \frac{m^2 \sum_{n=1}^{n_{max}} N(D_n)}{2\sigma^2}.$$
$$(4.32)$$

The value of m can be obtained by solving the derivative of (4.32), with respect to m and given by

$$m = \frac{\sum_{n=1}^{n_{max}} N(D_n)\ln D}{\sum_{n=1}^{n_{max}} N(D_n)}. \tag{4.33}$$

Another parameter (σ^2) can be then determined numerically by solving the derivative of (4.32), with respect to σ, and yielding the following equation:

$$\sigma^2 = \frac{\sum_{n=1}^{n_{max}} N(D_n)(\ln D_n)^2}{\sum_{n=1}^{n_{max}} N(D_n)} - \frac{2m \sum_{n=1}^{n_{max}} N(D_n)\ln D_n}{\sum_{n=1}^{n_{max}} N(D_n)} + m^2. \tag{4.34}$$

4.2.3 L-Moment Estimation

L-moment (LM) estimators are "linear" combinations of the observations that do not require squaring or cubing of the observations. Therefore, they are less sensitive to the largest observations in a sample than product moment. L-moments are an alternative system of describing the shape of probability distributions.

Let $X_1, X_2, ..., X_N$ is a random sample of size N with cumulative distribution function $F(x)$ and quantile function $x(F)$. If the samples are sorted into ascending order, such that $X_{1:N} \leq X_{2:N}...X_{N:N}$, then rth L-moment of X is defined as (Hosking, 1990)

$$\lambda_r \equiv r^{-1} \sum_{k=0}^{r-1} (-1)^k \binom{r-1}{k} E\{X_{r-k:r}\}, \quad r = 1, 2, ... \tag{4.35}$$

where $E\{.\}$ is the expectation of an order statistic, given by

$$E\{X_{j:r}\} = \frac{r!}{(j-1)!(r-j)!} \int x\{F(x)\}^{j-1}\{1 - F(x)\}^{r-j}dF(x). \tag{4.36}$$

Since L-moments are the linear function of Probability Weighted Moments (PWMs) a simple description of L-moments can be expressed in terms of the PWMs (Hosking, 1990). Using order statistics, an unbiased estimate of sample PWMs can be

computed by

$$b_r = N^{-1} \sum_{i=1}^{N} \frac{(i-1)(i-2)...(i-r)}{(N-1)(N-2)...(N-r)} x_{i:N}. \tag{4.37}$$

Writing the L-moments in terms of PWMs we have

$$l_1 = b_0, \tag{4.38}$$

$$l_2 = 2b_1 - b_0, \tag{4.39}$$

$$l_3 = 6b_2 - 6b_1 + b_0, \tag{4.40}$$

$$l_4 = 20b_3 - 30b_2 + 12b_1 - b_0. \tag{4.41}$$

Let $D_1, D_2, ..., D_N$ be a random sample of drop size with total number of drops N, in order to calculate two parameters of distribution (4.17 and 4.19), we need only the first two L-moments, i.e., l_1 and l_2, where b_0 and b_1 are given by

$$b_0 = \frac{1}{N} \sum_{i=1}^{N} D_{i:N}, \tag{4.42}$$

$$b_1 = \frac{1}{N(N-1)} \sum_{i=1}^{N} (i-1) D_{i:N}. \tag{4.43}$$

Equations (4.42) and (4.43) are only applicable for the continuous data. However, this is not always possible because almost all of the instruments used to collect DSD provide the raindrop sizes grouped into classes. Assuming the number of DSD classes as n with the midsize of the bin width as D_n, (4.42) and (4.43) are modified for the DSD data as

$$b_0 = \frac{\sum_{n=1}^{n_{max}} N(D_n) D_n}{\sum_{n=1}^{n_{max}} N(D_n)}, \tag{4.44}$$

$$b_1 = \frac{1}{N(N-1)} \sum_{i=1}^{N} (i-1) D_n. \tag{4.45}$$

where i in (4.45) is the total number of raindrops in each class, which is obtained from $\sum_{n=1}^{n_{max}} N(D_n) \Delta D$.

4.2.3.1 Gamma Distribution

To calculate two parameters of the gamma distribution, we need only the first two L-moments, given by (Gupta and Kundu, 2003)

$$l_1 = \frac{\mu + 1}{\Lambda}, \tag{4.46}$$

$$l_2 = \frac{1}{\Lambda} \left[\frac{\mu + 1.5}{\Gamma(0.5)\Gamma(\mu + 1)} \right] \tag{4.47}$$

From the dimensionless ratio of l_2/l_1, we can estimate the shape parameter (μ) by using an iterative procedure. Once μ is determined, the scale parameter (Λ) is calculated from

$$\Lambda = \frac{\mu + 1}{l_1}. \tag{4.48}$$

4.2.3.2 Exponential Distribution

To calculate the parameter of the exponential distribution, we need only the first L-moment, given by

$$l_1 = \frac{1}{\Lambda}. \tag{4.49}$$

Hence, Λ can be simply calculated from

$$\Lambda = \frac{1}{l_1}. \tag{4.50}$$

4.2.3.3 Lognormal Distribution

The two L-moments of a lognormal distribution are (Kundu *et al.*, 2006)

$$l_1 = \theta e^{\frac{\sigma^2}{2}}, \tag{4.51}$$

$$l_2 = \theta e^{\frac{\sigma^2}{2}} \mathrm{erf}(\sigma/2), \tag{4.52}$$

where $\ln\theta$ denotes m in (4.19) and $\mathrm{erf}(x) = 2\Theta\sqrt{2x} - 1$ and $\Theta(x)$ is the standard normal distribution function. From the dimensionless ratio of l_2/l_1, we can estimate σ by using an iterative procedure. Once σ is determined, θ is calculated from (4.51).

4.3   Data Description

4.3.1   Simulation of Artificial Raindrops

As was described in Section 4.2.2, in terms of probability density function, $f(D|\theta)$, DSD can be written as a product of $f(D|\theta)$ with the total number of raindrops (N_T), given by

$$N(D) = N_T.f(D|\theta), \tag{4.53}$$

where $f(D|\theta)$ for the gamma, exponential and lognormal distributions are given by (4.17), (4.18) and (4.19), respectively and θ are the parameters of the aforementioned probability density functions.

The simulation was started by selecting N_T, θ, and assuming a 1 m^3 sampling volume (independent of the drop size). After that, drops of diameter D that follows the probability density function were generated. For gamma probability density function, the method proposed by Marsaglia and Tsang (2000) was used. Using (4.53) and the concept of $\int (\text{PDF})dD = 1$, we got

$$\int \frac{N(D)}{N_T} dD = 1. \tag{4.54}$$

For the total number of raindrops N_T, the probability of drops within the interval $D \pm (\Delta D/2)$ is C/N_T, where C is the number of drops in the mentioned interval. Therefore, if we relate this basic definition to (4.54), the DSD from the probability density function is obtained. Some investigators such as Moisseev and Chandrasekar (2007) and Smith *et al.* (2009) simulated the DSD with the drop sizes normalized to median volume diameter (D_0) and mass-weighted mean diameter (D_m), respectively. They also used the diameter-independent sampling volume. Besides investigating the bias due to moment selection, the goal of this study is also to investigate the effect of binning on the DSD parameters (see Chapter 5). For this purpose, it is important to keep the conservation of the drops in a given sample for all selected bin widths. Therefore, we simulated the drop sizes without any normalization procedure.

4.3.2   2DVD measurement

A detailed description of the 2DVD measurement is provided in Section 3.2. The DSD data for the present work is binned at 0.2 mm.

4.4   Results

The following section discusses the nature of the bias in the MM, ML, and LM methods by examining their ability to recover the parameters of known DSDs from which samples are taken. The variation of exponential, gamma and lognormal parameters calculated by different moments for real data collected by 2DVD, is also shown.

4.4.1   Exponential Distribution

Figure 4.1 shows the bias in the moment method for $\hat{\Lambda}$ and $\hat{N}_0$ based on 10^3 simulated spectra. The parameters of simulated exponential DSD (Λ, N_T), are 4 for Λ and (a-b) 10^2, (c-d) 10^3 for N_T, respectively. The value of N_0 is estimated from the equation $N_0 = N_T.\Lambda$, and yielding the values 4 x 10^2 and 4 x 10^3, respectively. Symbols with "^" indicate the estimated values. In Fig. 4.1a, the LM/ML method underestimated the value of $\hat{\Lambda}$ namely, more than 70 % of the data. The mean of $\hat{\Lambda}$ is 3.82. As was previously expected, the parameters obtained by the MM depend on the order moment. By using the lowest order moment (M_0M_1), more than 99 % of $\hat{\Lambda}$ are underestimated, and the mean of $\hat{\Lambda}$ is 3.09. Involving M_6 in the MM, generates higher bias. More than 88 % of $\hat{\Lambda}$ estimated by M_5M_6 are overestimated, and its mean is 5.74. M_3 and M_6, which were used in Waldvogel (1974), overestimated the value of $\hat{\Lambda}$ namely, more than 70 % of the data. The mean of $\hat{\Lambda}$ is 5.16. It can be observed that moment estimators tend to overestimate the parameter $\hat{\Lambda}$ and the biases are higher when higher moments are used in the procedure. Same behavior is also found for $\hat{N}_0$. It should be remembered that LM and ML methods use $\hat{M}_0$ to calculate N_0 because these methods do not provide an equation to calculate N_0. Low order moments (M_0M_x) underestimated the value of $\hat{N}_0$ namely, more than 99 % of the data both for $N_T = 10^2$ and $N_T = 10^3$. This characteristic, of course, is the same as that

Table 4.4: Average fractional errors (%) for several moments of DSD where the sample was drawn from the exponential DSD.

N_T	M_0	M_1	M_2	M_3	M_4	M_5	M_6
10^2	27.424	9.460	17.656	32.126	51.547	73.636	95.409
10^3	27.521	5.788	5.538	10.508	18.525	30.767	47.028

of the ML/LM method. For $N_0 = 4 \times 10^2$ ($\log 10 N_0 = 2.60$), the averages of $\hat{N}_0$ (in log10) for several estimators are 2.44 (LM/ML), 2.39 ($M_0 M_1$), 2.53 ($M_1 M_2$), 2.64 ($M_2 M_3$), 2.79 ($M_3 M_4$), 2.97 ($M_3 M_6$), 3.29 ($M_5 M_6$).

The bias of MM decreases with increasing number of raindrops. Figure 4.1c is the same as Fig. 4.1a but for $N_T = 10^3$. The averages of $\hat{\Lambda}$ calculated by several moment combinations are 3.07 ($M_0 M_1$), 3.76 ($M_1 M_2$), 3.97 ($M_2 M_3$), 4.09 ($M_3 M_4$), 4.26 ($M_3 M_6$), 4.47 ($M_5 M_6$), respectively. On the other hand, the averages of $\hat{\Lambda}$ calculated by the LM/ML method is 3.8. Moreover, the averages of $\hat{N}_0$ (the initial value in $\log 10 N_0 = 3.60$) calculated by several estimators are 3.44 (LM/ML), 3.35 ($M_0 M_1$), 3.52 ($M_1 M_2$), 3.59 ($M_2 M_3$), 3.63 ($M_3 M_4$), 3.70 ($M_3 M_6$), 3.83 ($M_5 M_6$), respectively. Thus, if the number of drops is large, the values derived by higher order moment are not different much from the initial value and close to that of ML/LM method.

The moment error is a key factor in accurately estimating the DSD parameters through the moment method. Table 4.4 lists the average fractional errors for several moments of DSD that are obtained by the following equations:

$$AFE = \frac{1}{n} \sum_{j=1}^{n} \frac{|x - \hat{x}|}{x}. \tag{4.55}$$

where n is the number of data points, $\hat{x}$ and x indicate the estimated and the truth (initial) value, respectively. The initial of M_x is calculated by (4.1). It can be observed that the degree of scatter increases with increasing the moment order. Hence, the higher the moment order, the larger the moment errors. The value of $\hat{M}_0$ is underestimated about 20 % that causes underestimating the DSD parameters calculated by this moment.
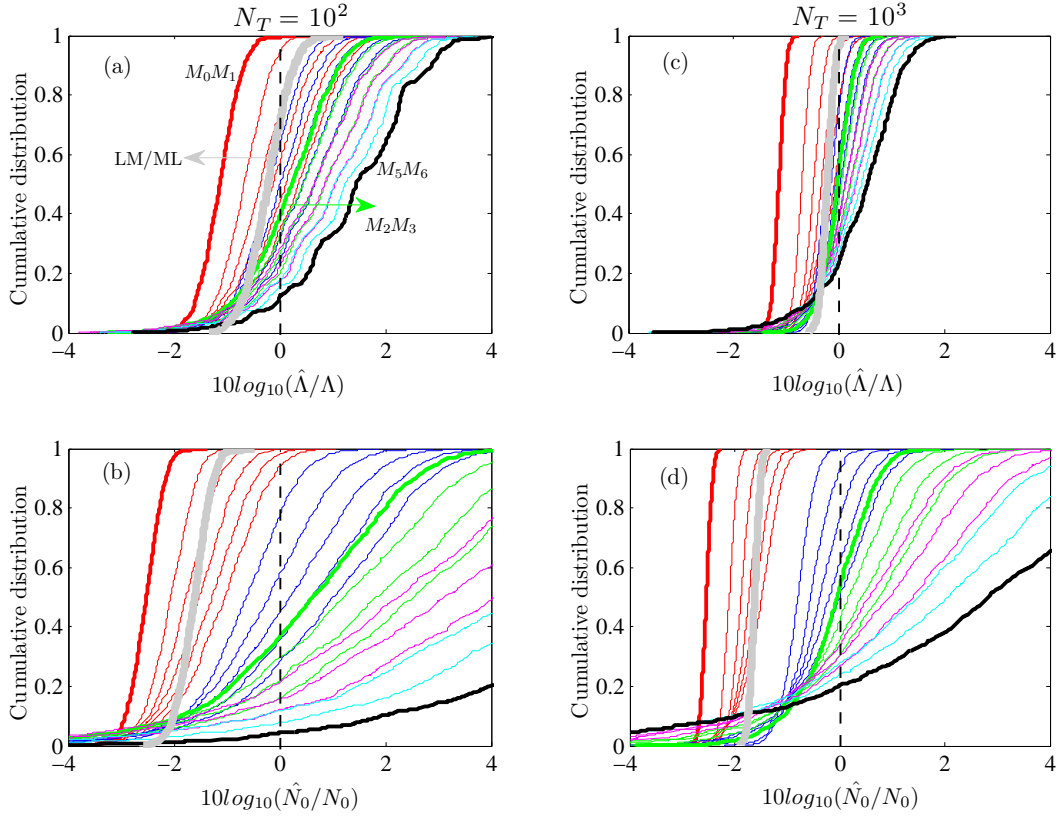
Figure 4.1: Cumulative distribution of ratio between estimated parameters ($\hat{\Lambda}$, $\hat{N}_0$) and initial values namely, $\Lambda = 4$ and $N_T = 10^2$ for (a-b) and $N_T = 10^3$ for (c-d). Different colors represent different moment estimators. Red lines denote the value from moment estimators involving zero moment ($M_0 M_x$), blue lines denote the value from $M_1 M_x$, green lines denote the value from $M_2 M_x$, magenta lines denote the value from $M_3 M_x$, cyan lines denote the value from $M_4 M_x$ and black line denotes the value from $M_5 M_x$ moment. Bold red line denotes the value from the lowest moment estimator ($M_0 M_1$), bold green line denotes the value from $M_2 M_3$, bold black line denotes the value from the highest moment estimator ($M_5 M_6$) and bold gray line denotes the value from ML and LM method. For the exponential distribution, the equation of ML and LM to calculate $\hat{\Lambda}$ is the same. Vertical dashed line denotes the population value.
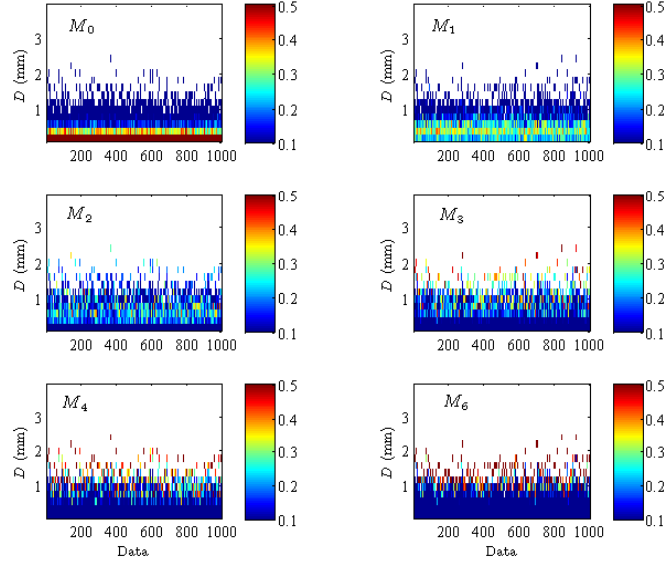
Figure 4.2: Fraction of the DSD moment (M_x) formed by raindrops within a particular diameter interval for initial values; $\Lambda = 4$ and $N_T = 10^2$. Color scale represents the value of $\frac{M_x(D)}{M_x}$. Data on horizontal axis denotes the sample number $(1...10^3)$.
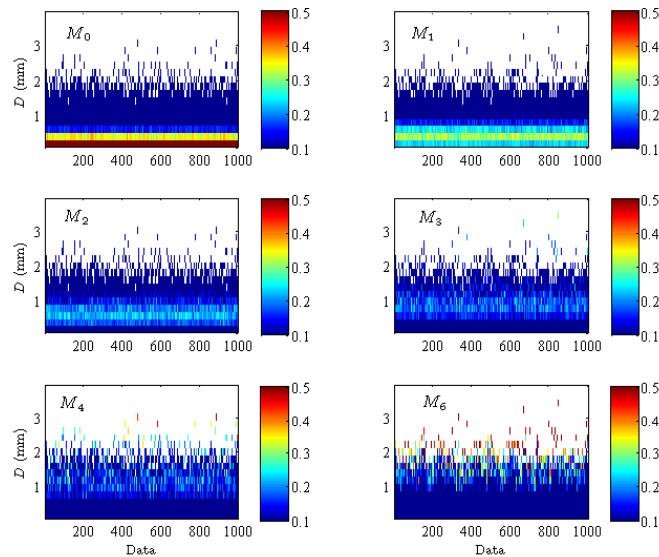
Figure 4.3: Same as Fig. 4.2 but for $N_T = 10^3$.

Figures 4.2 and 4.3 show the fraction of the DSD moment (M_x) formed by raindrops within a particular diameter interval for the following initial values; $\Lambda = 4$, $N_T = 10^2$, and $N_T = 10^3$. The exponential distribution is characterized by large concentration of small-sized drops. From the figures, it can be seen that the population of large-sized drops mainly influence the high order moments. On the other hand, the population of medium and small-sized drops are mainly influencing the low order moments.

From the above discussion, using the lowest moments (M_0 and M_1) is the best procedure of moment method because they provide the smallest bias of all. However, instrument responses to very small drops are highly variable and often suspect (Testud *et al.*, 2001). Calibration of the instrument is one of the problems. For example, in case of 2DVD, calibration is done by dropping balls with known diameter through the measuring area. Joanneum Research supplies calibration spheres in the range 0.5 - 8 mm. Thus, particles in size less than 0.5 mm are not well calibrated. As consequence, trying to use moments that are lower than M_2 would introduce another kind of uncertainty into the moment procedure. There may even be problems with using M_2 if the instrument does not adequately sense small drops. Table 4.5 compares the fitting performance between full-samples and truncated samples (truncated at 0.4 mm). As the accuracy test of fit, we used the normalized root mean squared error ($NRMSE$) as

$$NRMSE = \frac{\sqrt{\frac{\sum_{j=1}^{n}(N(D)_{fit} - N(D)_{observed})^2}{n}}}{\frac{\sum_{j=1}^{n} N(D)_{observed}}{n}}, \tag{4.56}$$

where j is the drop size class number. For full-samples, although the performance of the ML/LM method to calculate $\hat{\Lambda}$ is better than the MM method, the ability of ML/LM method to conserve the observed DSD is not much different from the lower order moments. This behavior of ML/LM method is due to the under-estimation of $\hat{N}_0$. For truncated samples, like M_{0x}, M_{1x} and M_{2x}, the ML and LM methods are very sensitive to the absence of small-sized drops. The ability of ML/LM method and lower order moments to conserve the observed DSD decrease as the samples are truncated. Moreover, M_{3x} estimators give better results than ML/LM and lower moment estimators in this case.

Table 4.5: Average $NRMSE$ of the simulated DSD ($\Lambda = 4$)

Estimators	$N_T = 10^2$		$N_T = 10^3$		Estimators	$N_T = 10^2$		$N_T = 10^3$	
	full	trunc.	full	trunc.		full	trunc.	full	trunc.
LM/ML	1.27	3.14	1.21	3.00	M_{16}	1.28	2.26	0.50	2.08
M_{01}	1.52	3.16	1.49	3.01	M_{23}	1.14	2.50	0.45	2.09
M_{02}	1.39	3.14	1.35	2.99	M_{24}	1.78	1.56	0.63	1.33
M_{03}	1.23	2.97	1.22	2.82	M_{25}	2.32	1.52	0.81	1.25
M_{04}	1.19	3.05	1.20	2.90	M_{26}	2.97	1.50	1.02	1.18
M_{05}	1.15	3.12	1.18	2.96	M_{34}	2.61	1.74	0.91	1.28
M_{06}	1.11	3.19	1.15	3.02	M_{35}	4.11	1.52	1.35	0.74
M_{12}	1.00	3.08	0.72	2.78	M_{36}	5.52	1.70	1.75	0.73
M_{13}	0.84	2.19	0.49	2.03	M_{45}	6.23	1.76	1.93	0.75
M_{14}	0.95	2.19	0.46	2.04	M_{46}	9.25	2.86	2.69	1.17
M_{15}	1.09	2.22	0.47	2.06	M_{56}	14.65	4.68	3.95	1.95

Table 4.6: Average $NRMSE$ of the observed DSD

Estimators	full	trunc.	Estimators	full	trunc.
LM/ML	3.01	2.78	M_{16}	11.62	2.48
M_{01}	3.01	2.79	M_{23}	11.41	2.58
M_{02}	3.35	2.78	M_{24}	16.75	2.81
M_{03}	3.63	2.58	M_{25}	20.56	3.11
M_{04}	3.95	2.70	M_{26}	24.49	3.38
M_{05}	4.21	2.82	M_{34}	24.45	3.25
M_{06}	4.43	2.92	M_{35}	34.80	4.62
M_{12}	5.36	2.82	M_{36}	43.68	5.27
M_{13}	7.55	2.10	M_{45}	51.30	5.65
M_{14}	8.99	2.23	M_{46}	70.52	7.76
M_{15}	10.34	2.36	M_{56}	107.01	10.82

Figure 4.4 shows the cumulative distribution of the exponential DSD parameters estimated from the DSD recorded by 2DVD at Kototabang during 2006-

2007. The plotted data are for rainfall rates more than 1 mm/h, and the DSD was binned at 0.2 mm. The DSD parameters estimated by using $M_5 M_6$ procedure are much higher than those estimated by using $M_0 M_1$. The parameters estimated by the ML/ML methods are close to that for $M_0 M_1$. However, when $NRMSE$ is used as a measure of goodness of fit, almost all estimators of exponential distribution do not demonstrate a good performance to fit the observed DSD, which are indicated by large values of $NRMSE$ (Table 4.6). The reason for this behavior has been previously found by Joss and Gori (1978) in which the observed DSD exhibit deviations from the exponential function (e.g., fewer drops at small diameter end). Comparison of several functional fits for Kototabang data will be devoted in the last part of this chapter.

4.4.2 Gamma Distribution

Figure 4.5 shows the bias in the moment method for the gamma distribution. The initial parameters of the simulated DSD are $\Lambda = 4$ and $\mu = 2$. The total number of raindrop (N_T) for the aforementioned parameters are 10^2 and 10^3, then the initial values of N_0 which are obtained from (2.10) are 3.2 x 10^3 and 3.2 x 10^4. Symbols with "ˆ" indicate the estimated parameters. Both for $N_T = 10^2$ and $N_T = 10^3$, the ML method underestimated the values of all parameters ($\hat{\mu}$, $\hat{\Lambda}$, $\hat{N}_0$) namely, 100 % of the data. For $N_T = 10^2$, average of $\hat{\mu}$, $\hat{\Lambda}$ and $\hat{N}_0$ (in log10 scale) are 1.84, 3.78, 3.39, respectively, while they are 1.84, 3.79, 4.39, respectively, for $N_T = 10^3$. It can be seen that the ML method provides the parameters which are very close to the initial parameters. Like the ML method, the LM method also provides the parameters which are close to the initial values. In case of $N_T = 10^2$, 99% of $\hat{\mu}$, 66% of $\hat{\Lambda}$ and 66% of $\hat{N}_0$ are underestimated and 93% of $\hat{\mu}$, 91% of $\hat{\Lambda}$ and 93% of $\hat{N}_0$ are underestimated for $N_T = 10^3$. Average of $\hat{\mu}$, $\hat{\Lambda}$ and $\hat{N}_0$ (in log10 scale) for $N_T = 10^2$ ($N_T = 10^3$) are 1.85 (1.80), 3.82 (3.74), 3.41 (4.38), respectively. From the above analysis we can observe that the ML and LM method are not significantly influenced by the sample size.

As perviously discussed in case of exponential distribution, the DSD parameters calculated by the MM depend on the order moment and more than 60% of all parameters are overestimated. For $N_T = 10^2$, average $\hat{\mu}$, $\hat{\Lambda}$ and $\hat{N}_0$ (in
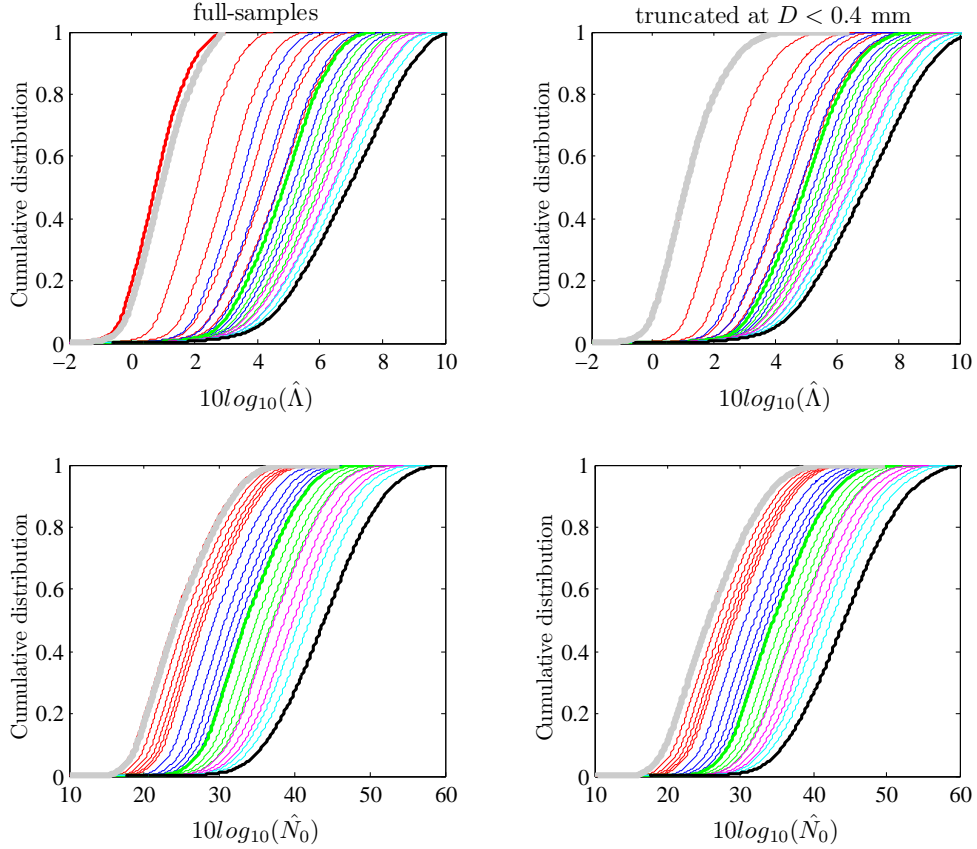
Figure 4.4: Cumulative distribution of exponential DSD parameters estimated from the actual DSD recorded by the 2DVD during 2006-2007 at Kototabang. Different colors represent different moment estimators. Red lines denote the value from moment estimators involving zero moment (M_0M_x), blue lines denote the value from M_1M_x, green lines denote the value from M_2M_x, magenta lines denote the value from M_3M_x, cyan lines denote the value from M_4M_x and black line denotes the value from M_5M_x moment. Bold red line denotes the value from the lowest moment estimator (M_0M_1), bold green line denotes the value from M_2M_3, bold black line denotes the value from the highest moment estimator (M_5M_6) and bold gray line denotes the value from the ML and LM method.

Table 4.7: Average fractional errors (%) for several moments of DSD where the sample was drawn from gamma DSD

μ	N_T	M_0	M_1	M_2	M_3	M_4	M_5	M_6
$\mu = 2$	$N_T = 10^2$	2.36	4.82	10.02	17.14	27.07	40.01	55.94
	$N_T = 10^3$	2.38	1.57	3.21	5.59	9.18	14.51	22.17
$\mu = 6$	$N_T = 10^2$	0.00	2.90	6.00	9.83	14.89	21.56	29.93
	$N_T = 10^3$	0.00	0.92	1.91	3.19	4.94	7.43	11.00
$\mu = 10$	$N_T = 10^2$	0.00	2.48	5.07	8.04	11.58	15.99	21.51
	$N_T = 10^3$	0.00	0.76	1.54	2.48	3.66	5.19	7.21

log10 scale) obtained from the lowest order moment ($M_0 M_1 M_2$) are 2.31, 4.34, 3.66, respectively, for $N_T = 10^2$, and 2.18, 4.15, 4.58, respectively, for $N_T = 10^3$. On the other hand, the highest order moment (M_4, M_5, M_6) which are also used by Caracciolo $et\ al.$ (2006) give the average $\hat{\mu}$, $\hat{\Lambda}$ and $\hat{N}_0$ (in log10 scale) being 7.13, 7.73, 5.09, respectively, for $N_T = 10^2$, and 3.34, 4.89, 4.87, respectively, for $N_T = 10^3$. Kozu and Nakamura (1991) used M_3, M_4 and M_6. For $N_T = 10^2$ ($N_T = 10^3$), average $\hat{\mu}$, $\hat{\Lambda}$ and $\hat{N}_0$ (in log10 scale) obtained from this estimator are 5.15 (2.61), 6.52 (4.46), 4.62 (4.70), respectively. Ulbrich and Atlas (1998) used moments M_2, M_4 and M_6. For $N_T = 10^2$ ($N_T = 10^3$), average $\hat{\mu}$, $\hat{\Lambda}$ and $\hat{N}_0$ (in log10 scale) obtained from this estimator are 4.37 (2.50), 6.04 (4.41), 4.44 (4.70), respectively. Some investigators proposed to use lower order moments. For example, Smith and Kliche (2005) and Kliche $et\ al.$ (2008) proposed to use M_2, M_3, and M_4. For $N_T = 10^2$ ($N_T = 10^3$), average $\hat{\mu}$, $\hat{\Lambda}$ and $\hat{N}_0$ (in log10 scale) obtained from this estimator are 3.12 (2.21), 5.07 (4.18), 4.00 (4.59), respectively. Thus, it again emphasizes that the MM of gamma distribution is significantly influenced by moment order and the sample size (N_T).

As was discussed in exponential case, the moment error is a key factor in accurately estimating the DSD parameters using the moment method. Table 4.7 lists the average fractional errors for several moments of DSD which are obtained by (4.55). For $\mu = 0$ (exponential case), the error of moments can be found in Table 4.4. It can be observed that the degree of scatter increases with
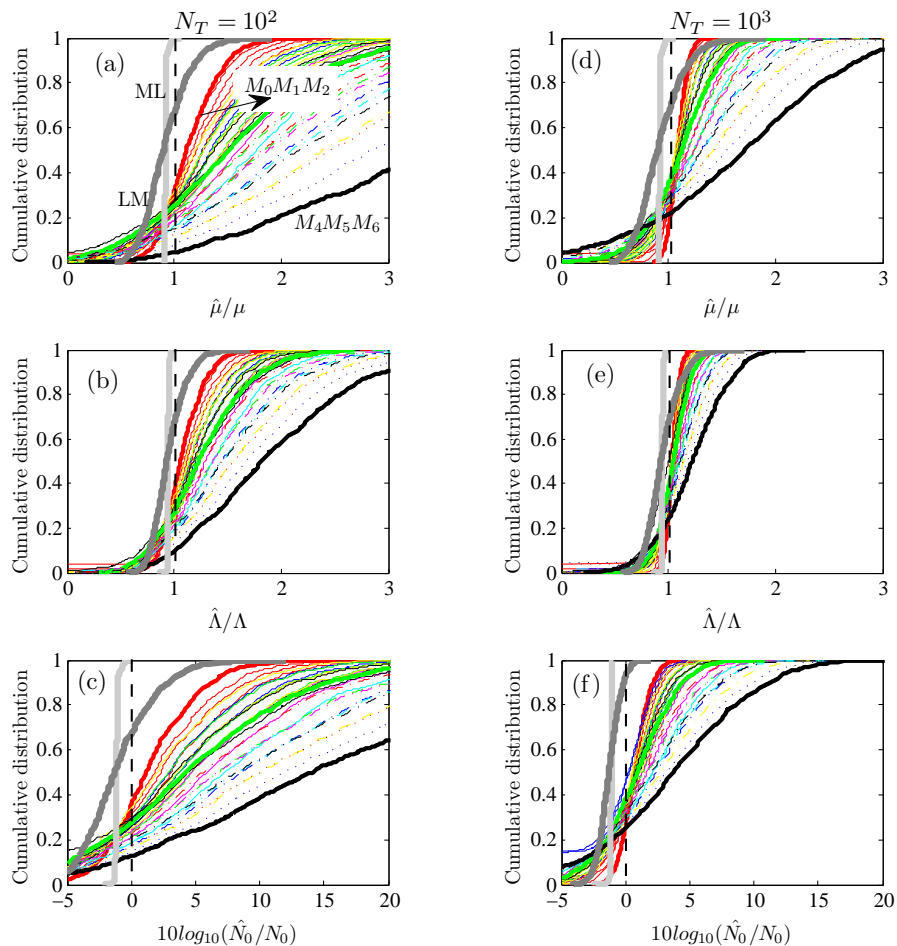
Figure 4.5: Cumulative distribution of ratio of estimated DSD parameters ($\hat{\mu}$, $\hat{\Lambda}$, $\hat{N_0}$) and those of initial value ($\mu = 2$, $\Lambda = 4$) for $N_T = 10^2$ (a-c) and $N_T = 10^3$ (d-f) for 35 possible moment estimators. Different colors and type of lines represent different moment estimators. Bold red line denotes the value from the lowest moment estimator ($M_0M_1M_2$), bold green dashed line denotes the value from $M_2M_3M_4$ and bold black dashed line denotes the value from the highest moment estimator ($M_4M_5M_6$). Bold gray lines denotes the value from the ML and LM method.

increasing the moment order and decreases with increasing N_T. Consequently, the bias of MM increases with increasing the moment order used and decreases with increasing N_T. For narrower DSD which is indicated by large value of μ, the moment error is smaller than that of broader DSD. Hence, the bias of MM to estimate the DSD parameters may be reduced when DSD is narrow.

Some investigators explained the relationship between the DSD parameters and IRPs (e.g., rainfall rate). Sauvageot and Laucaux (1995) found a systematic increase in intercept and a decrease in slope parameters of exponential distribution with increasing rainfall rate. Kozu and Nakamura (1991) concluded that shape parameter (μ) of gamma distribution decreases as the rainfall rate increases. On the other hand, Tokay and Short (1996) and Tokay *et al.* (2001) showed an increase in all three parameters of the gamma distribution with rainfall rate. The difference in the DSD characteristics may be partly due to regional difference in generating convective rainfall (high rain rate), and partly due to the use of different moments. As explained above, the moment error is a key factor in accurately estimating the DSD parameters through the moment method. The moment error increases with increasing the moment order and decreases with increasing N_T. Thus, when higher-order moments are used, the properties of large drops are reflected by μ, while using lower-order moments will reflect the DSD properties at small drop regions. Although it is very difficult to criticize in a quantitative manner any given set of results based on moment method because the parameters of 'true' raindrop spectra are unknown, we can offer some comments based on this bias study. As commonly known, the total number concentration of drops increases with increasing rainfall rate. Figure 4.6 shows the variation of averaged $\hat{\mu}$ and $\hat{\Lambda}$ with N_T. Although the tendency is not uniform, we can see the decrease of $\hat{\mu}$ and $\hat{\Lambda}$ with increasing N_T especially for high order moments. Therefore, the decrease of μ as reported by aforementioned authors may not fully reflect any physical meaning, but also be a consequence of an increasing number of raindrops as rainfall rate increases. The bias so decreases that shape parameter decreases. Unlike the MM method, it is again found that the ML and LM method are not significantly influenced by N_T.

According to the aforementioned discussion, using the lowest moments (M_0 and M_1) would be the best choice of moment method because this moment esti-
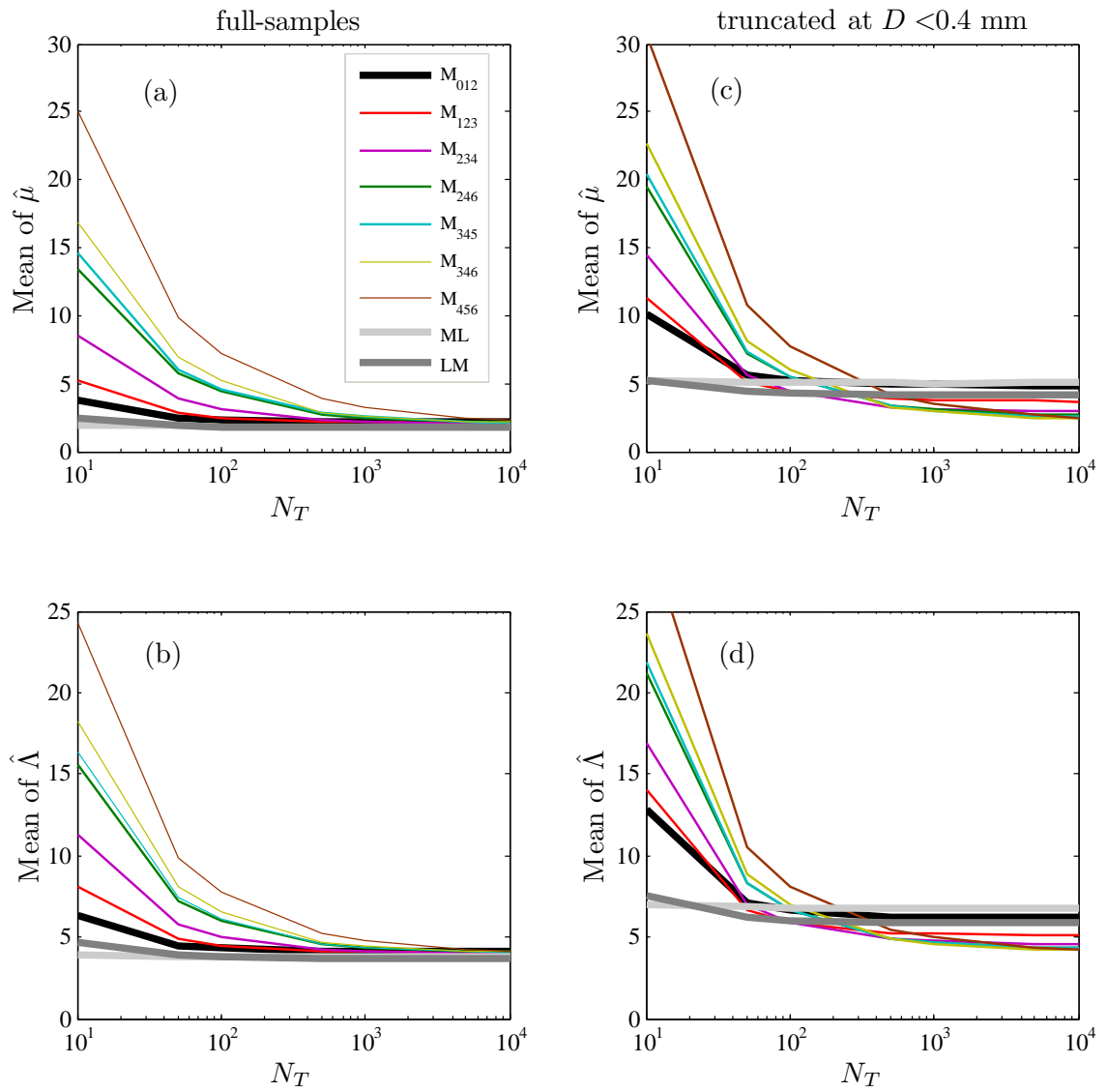
Figure 4.6: Variation of averaged $\hat{\mu}$ and $\hat{\Lambda}$ with N_T. Initial values are $\mu = 2$ and $\Lambda = 4$.

mator provides the smallest bias of all. However, it is very difficult for current instruments to measure small-sized drops accurately. Figures 4.6c-d show the variation of averaged $\hat{\mu}$ and $\hat{\Lambda}$ with N_T for the DSD spectra truncated at $D < 0.4$ mm. It can be seen that the performance of low order moments, ML and LM method decrease for the truncated data. Like for full-samples, the performance of the ML and LM method are not significantly influenced by the sample size. With the large number of drops, the bias and error in the MM method are smaller than those of LM and ML method, and the MM method gives the result sufficiently close to the population value. Because the moment error of narrow DSD is smaller than that of broad DSD, hence, the truncation procedure also significantly influences the broad DSD (Fig. 4.7).
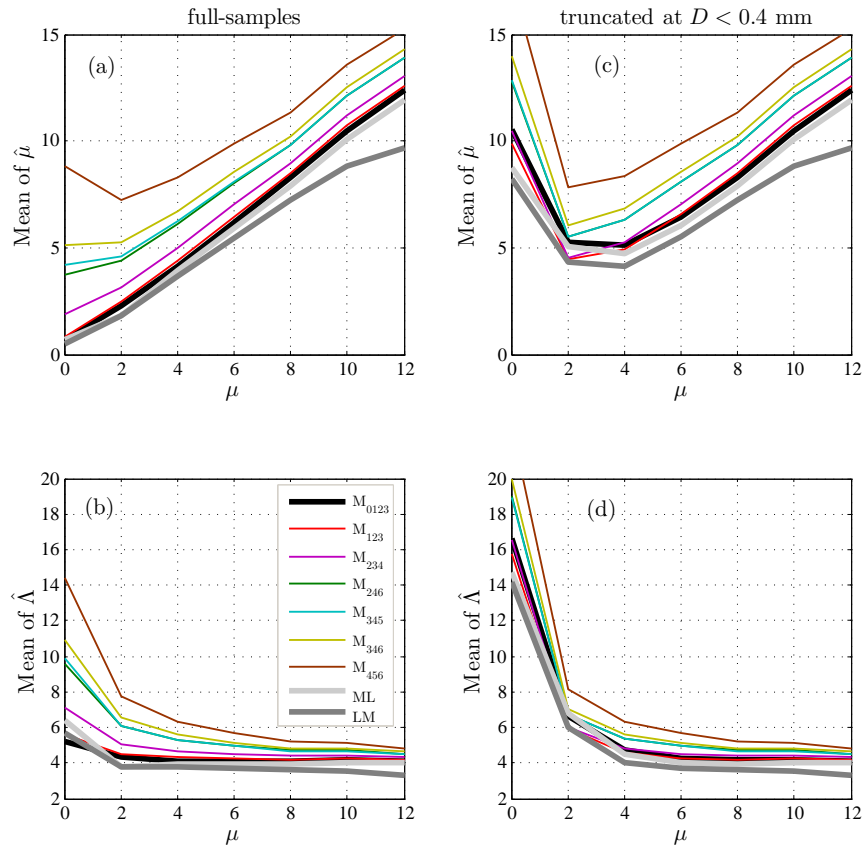
Figure 4.7: Variation of averaged $\hat{\mu}$ and $\hat{\Lambda}$ with μ. The initial parameters of the simulated DSD are $N_T = 10^2$ and $\Lambda = 4$.

4.4.3 Lognormal Distribution

The behaviour of the lognormal distribution is close to that of the gamma distribution in which the shape for the gamma distribution is determined by μ, while for the lognormal distribution it is determined by σ. For large values of σ and small values of m, the shape of the lognormal distribution is concave upward. It is the same as a gamma distribution with $\mu < 0$. Because its property is close to that of the gamma distribution, the bias of MM for the lognomal distribution would be close to that of the gamma distribution. Hence, we will not re-analyze the bias for all moment estimators, but we will study it for some selected estimators only.
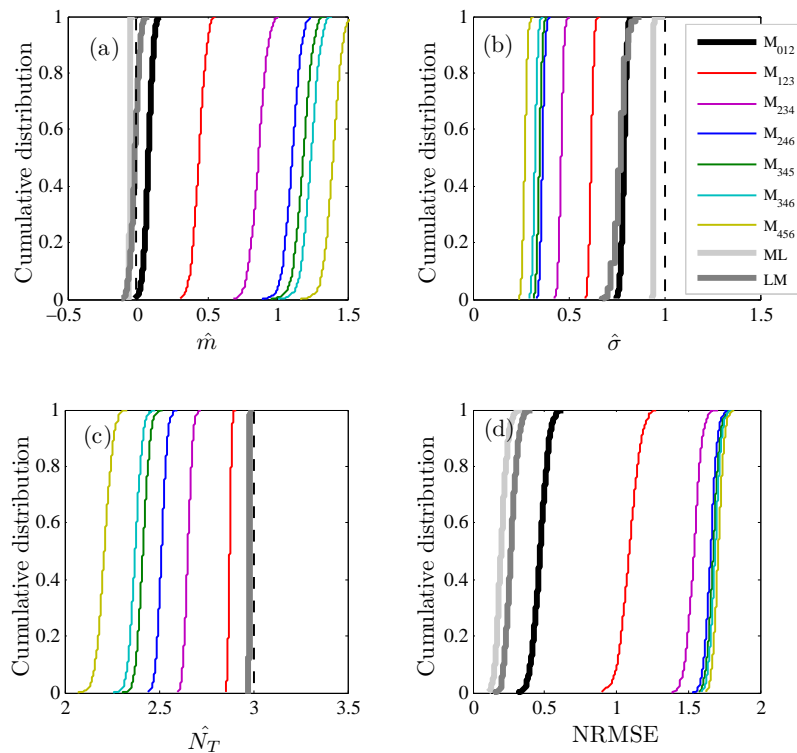
Figure 4.8: Cumulative distribution of the estimated parameters of the lognormal distribution ($\hat{m}$, $\hat{\sigma}$, $\hat{N_T}$) and that of initial values ($m = 0$, $\sigma = 1$, $N_T = 10^3$). Different colors represent different estimators. Vertical dashed line denotes the population value. N_T on horizontal axis is in logarithmic scale.

Figure 4.8 shows the bias in the moment method for lognormal distribution. The initial parameters of the simulated DSD are $m = 0$, $\sigma = 1$ and $N_T = 10^3$. It can be seen that the ML method provides the parameters which are very close to the initial parameters. Like the ML method, the LM method also provides the parameters close to the initial values. As a consequence, these two methods fit the distribution well indicated by the NRMSE. On the other hand, the values derived from the MM again depend on the order moment used. By using the lowest order moment (M_0, M_1, M_2), the parameters $(\hat{m}, \hat{\sigma}, \hat{N}_T)$ are close to the values obtained by the ML and LM methods. This moment estimator also fits the distribution well as indicated by the NRMSE. The deviation of the parameters from the initial value increases with increasing the moment order as previously observed in case of the exponential and gamma distribution.
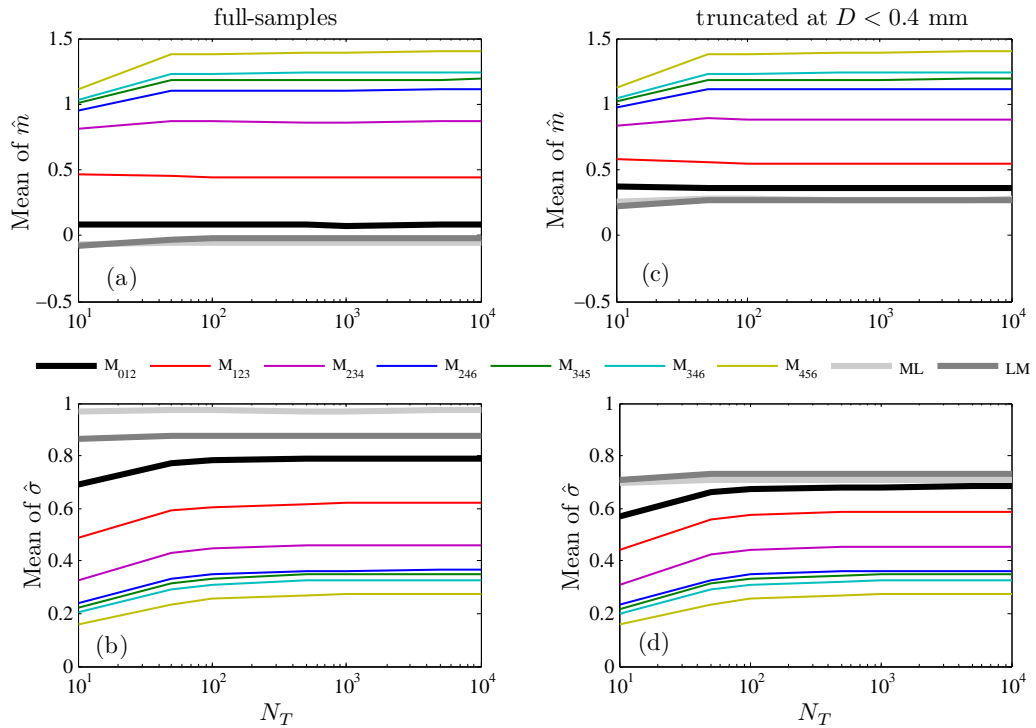
Figure 4.9: Lognormal distribution: variation of mean of $\hat{m}$, $\hat{\sigma}$ with N_T. The initial values are $m = 0$ and $\sigma = 1$.

For the exponential and gamma distribution, the MM method is significantly influenced by the number of raindrops (N_T) in which the bias decreases as N_T increases and even the parameters are very close to those of the ML and LM method for $N_T > 10^3$. However, these behaviors are not found in case of the lognormal distribution. Figure 4.9 shows the variation of averaged $\hat{m}$ and $\hat{\sigma}$ with N_T. ML, followed by LM and M_{012}, give the result being closest to the initial values. It can be seen that none of the estimators is significantly influenced by N_T. Moreover, moment estimators involving high order moments never reach the population values even for $N_T = 10^4$. Figures 4.9c-d show the variation of averaged $\hat{m}$ and $\hat{\sigma}$ with N_T for the DSD spectra truncated at $D < 0.4$ mm. The performance of low order moments, ML and LM methods decrease for the truncated data. However, their performance is still better than the MM method, even than the lowest order moment (M_{012}). Like for full-samples, the performance of all estimators are not significantly influenced by the sample size. The MM of lognormal distribution never gives better results than the ML and LM methods.
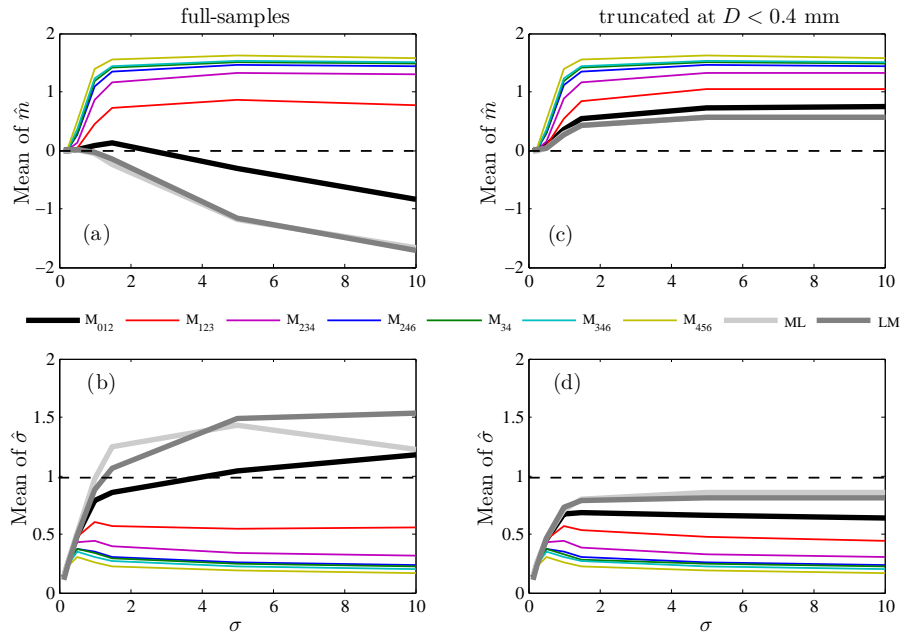
Figure 4.10: Lognormal distribution: variation of averaged $\hat{m}$, $\hat{\sigma}$ with σ. The initial values are $m = 0$ and $N_T = 10^2$.

In case of the lognormal distribution, the bias of narrow DSD is not much different from that of a broad DSD (Fig. 4.10). However, the biases of ML, LM and M_{012} estimators are significantly influenced by the shape of DSD and the truncation procedure. Hence, we can see the difference in the MM method performance among the exponential, gamma and lognormal distribution in which transforming the moment of DSD to logarithmic scale in the lognormal distribution may reduce the sensitivity of MM method to the number of drops and the shape of DSD. Moreover, the ratio of estimated to initial parameters $(\hat{x}/x)$ obtained by the MM method for the lognormal distribution is much better than that of gamma and exponential distribution particularly for small sample size. The difference between calculated and initial parameters for lognormal is much smaller than that of gamma and exponential distribution.

4.4.4 Comparison of Three Functional Fits

The bias of the DSD parameters estimation can be quite misleading when we do not select the correct fit (distribution) for the data. For example, if the data is actually exponential DSD, but we use the gamma distribution to fit the data. Figure 4.11 shows an example where a sample of 10^3 drops was drawn from an exponential (Fig. 4.11a) , gamma (Fig. 4.11b) and lognormal DSD (Fig. 4.11c). M_3, M_3 and M_6 are used to calculate the DSD parameters through the MM. It can be seen that using the exponential fit for exponential DSD, gamma fit for gamma DSD and lognormal fit for lognormal DSD will reveal that the underlying DSD is exponential, gamma and lognormal, respectively. This behavior is found for all estimators. Hence, using exponential fit for gamma and lognormal DSD will not correspond to the population from which the samples were drawn. Figure 4.12 shows the average NRMSE of DSD where a sample of 10^3 drops was drawn from an exponential (Fig. 4.12a) , gamma (Fig. 4.12b) and lognormal DSD (Fig. 4.12c). It is consistent with Fig. 4.11 in which the selection of correct fit/distribution is very important to get the fitting result that corresponds to the population from which the samples were drawn. Gamma distribution will reduce to the exponential distribution when $\mu = 0$, thus this distribution can be used to fit the exponential distribution. However, from Fig. 4.11a the exponential

distribution is better fitting the exponential DSD than the gamma and lognormal distribution.
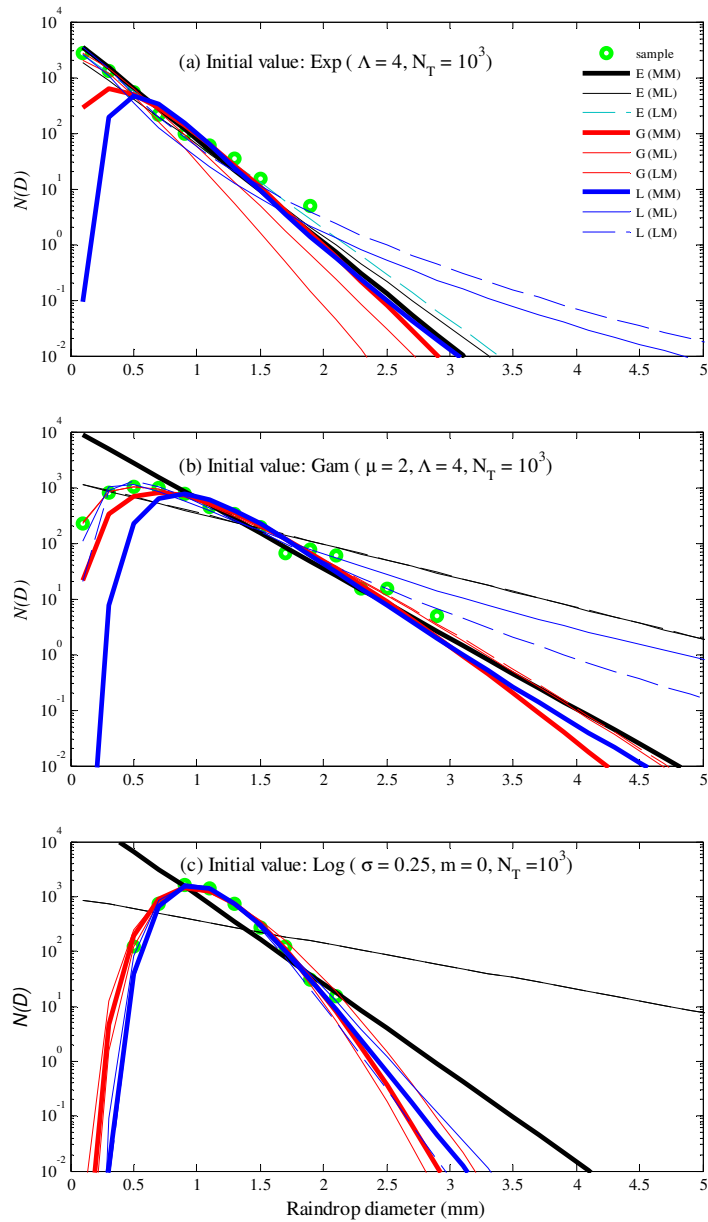
Figure 4.11: Sample of 10^3 drops drawn from exponential (a), gamma (b) and lognormal DSD (c). Different colors represent different estimators.
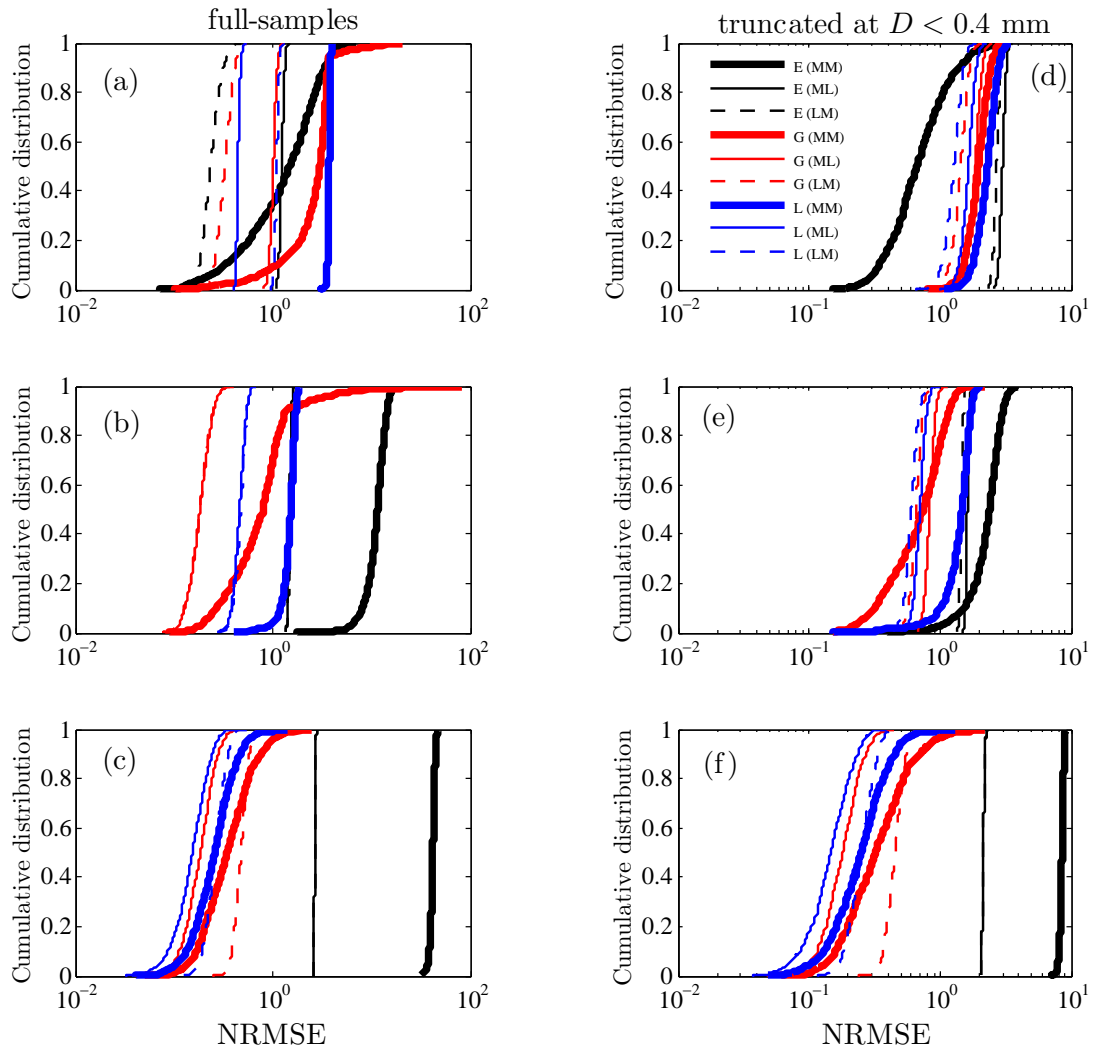
Figure 4.12: Cumulative distribution of NRMSE for 10^3 samples with the initial values as in Fig. 4.11.

Joss and Gori (1978) found that observed DSDs approach the exponential form as the sample size is increased by averaging more data. Figure 4.13 shows the average DSDs for several rainfall rate classes. It can be seen when the sampling time is sufficiently long (DSD averaging time), the DSD at Kototabang shows the exponential nature of the distribution, consistent with the result of Joss and Gori (1978). The three models are showing good fit to the average DSD. The model tends to overestimate (underestimate) the DSD at the smaller (larger) drop diameters. However, the difference is not significant. Observed instantaneous spectra are different from the average one. Moreover, the temporal variation of DSD reflects the physics of rain. Therefore, it would be worthwhile to study the performance of three functional fits from instantaneous spectra instead of average DSD.
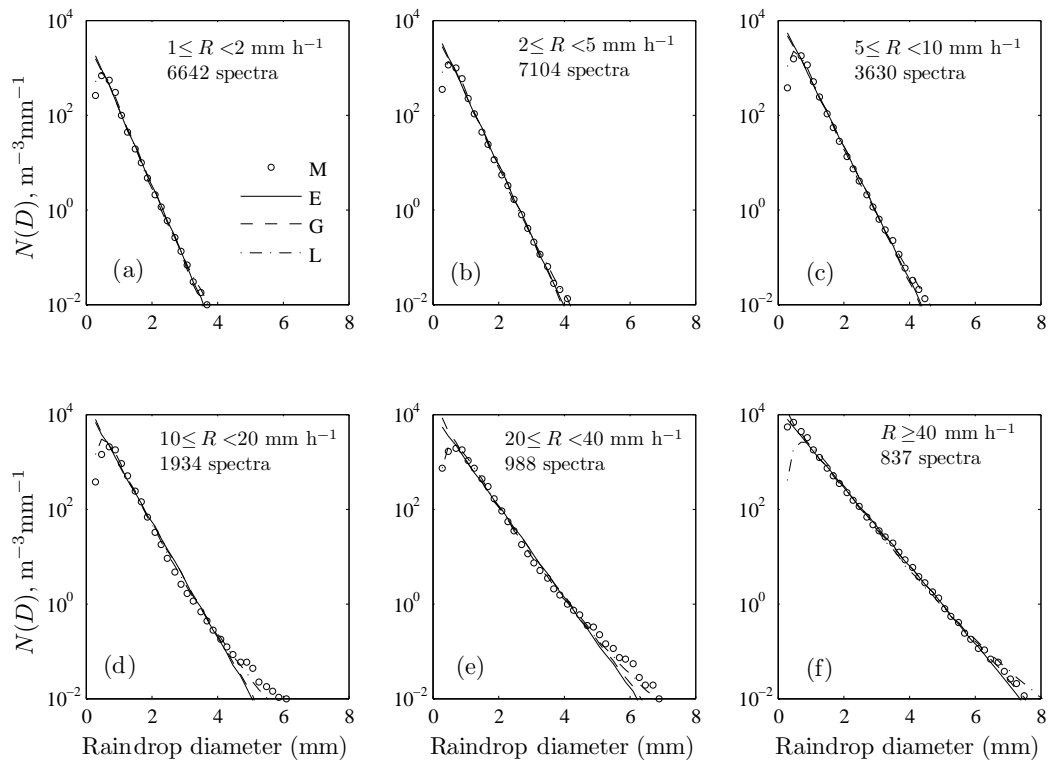
Figure 4.13: Three functional fits for several rainfall rate classes of average DSD. M, E, G and L denote measured DSD, exponential, gamma and lognormal distribution, respectively. The parameters are calculated by the MM.
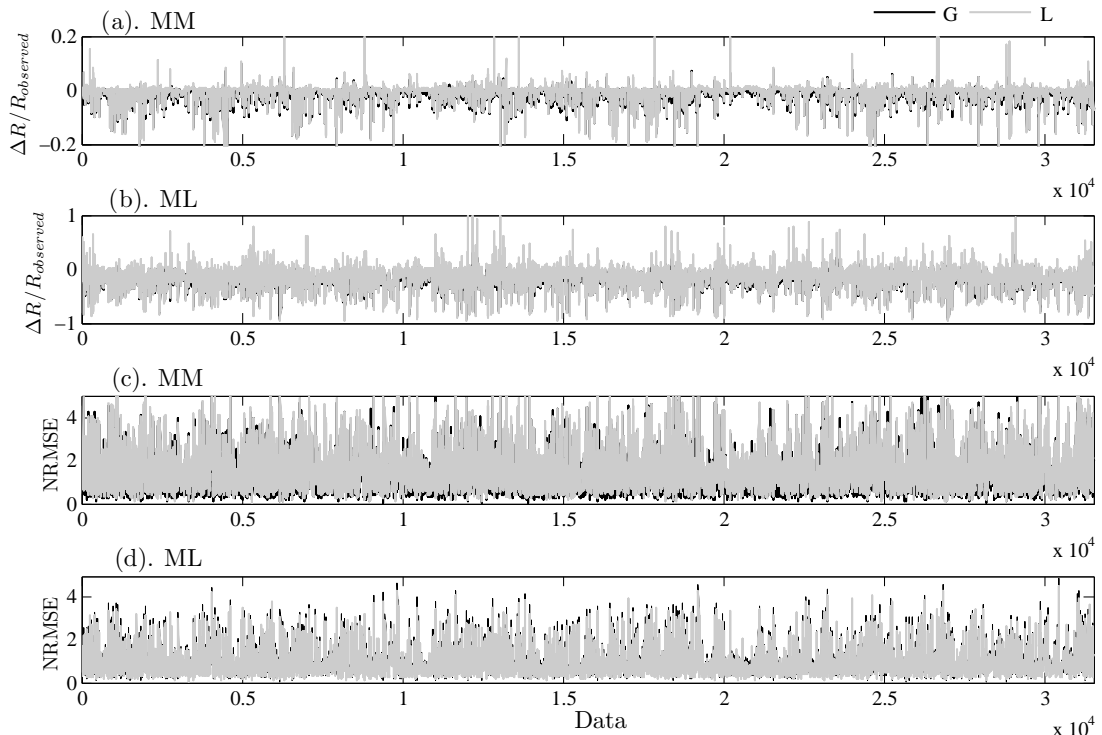
Figure 4.14: Time series of $\Delta R / R_{observed}$ and NRMSE for two model distributions. MM, ML, G and L denote moment method, maximum likelihood, gamma and lognormal distribution, respectively. Data on horizontal axis denotes time (1-min. resolution).

Various methods can be adopted to measure the accuracy of fit of a theoretical distribution function to an observed DSD. We used NRMSE (4.56) and the ability of the model distribution to conserve the rainfall rate of observed DSD, as the test of accuracy of fit for some theoretical distribution functions. Figure 4.14 shows the time series of the NRMSE and $\Delta R / R_{observed}$ for gamma and lognormal distribution, for all analyzed data. The ΔR is defined as the difference between R calculated from models and that from the observed DSD. The exponential function provides large value of NRMSE and $\Delta R / R_{observed}$ (not shown in the figure). Table 4.8 shows the average NRMSE of three model distributions for rain classes as in Fig. 4.13. The gamma and lognormal functions, unlike the exponential function, succeed in reproducing the general shape of the instantaneous

Table 4.8: Average values of NRMSE for various categories of rainfall rate

Rainfall rate (mm h^{-1})	Exponential	Gamma	Lognormal
$0.1 \leq R < 1$	16.54	1.42	1.50
$1 \leq R < 2$	14.63	1.32	1.43
$2 \leq R < 5$	13.76	1.34	1.36
$5 \leq R < 10$	13.24	1.25	1.29
$10 \leq R < 20$	13.13	1.23	1.31
$20 \leq R < 40$	9.55	1.27	1.64
$R \geq 40$	4.25	1.58	2.22
All	14.98	1.37	1.46

DSD spectra. The performance of gamma distribution does not differ from the lognormal much. However, the average NRMSE of gamma is better than that of the lognormal function.

For some practical applications, it is important to keep the conservation of the rainfall rate (R) of the observed DSD. Figure 4.15 shows the histogram of $\Delta R/R_{observed}$ for several rain classes as in Fig. 4.13. It is seen that the exponential distribution underestimates the rainfall rate for all categories (Figs. 4.15a-f). R calculated from the gamma and lognormal distribution are in good agreement with the observed values. However, at very heavy rain (Figs. 4.15e-f) the $\Delta R/R_{observed}$ of gamma is better than that of the lognormal function. In the present discussion, the fitted distributions are based on high moments of the drop spectra (M_3, M_4 and M_6), the population of medium and large-sized drops would mainly determine the parameters of distribution as previously discussed in other sections. Feingold and Levin (1986) developed a method to estimate the parameters of lognormal distribution. The population of small-sized drops would mainly determine the parameters of distribution in their method. If we use the method in Feingold and Levin (1986), the NRMSE of lognormal is better than that of the gamma function. However, lognormal distribution underestimates the rainfall rate. Hence, from this comparative analysis, it is summarized for
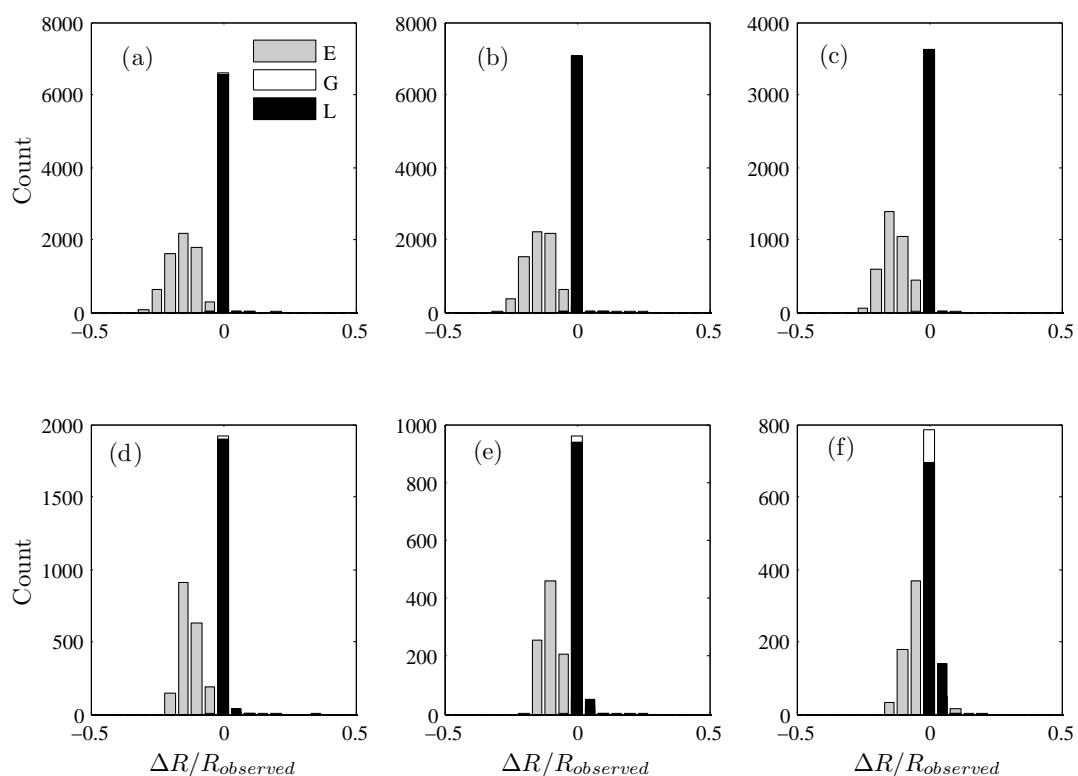
Figure 4.15: Frequency distribution of $\Delta R/R_{observed}$ for three model distribution for rainfall rate classes of $1 \leq R <2$ mm h^{-1} (a), $2 \leq R <5$ mm h^{-1} (b), $5 \leq R <10$ mm h^{-1} (c), $10 \leq R <20$ mm h^{-1} (d), $20 \leq R <40$ mm h^{-1} (e) and $R \geq 40$ mm h^{-1} (f). ΔR is defined as the difference between R calculated from models and that from the observed DSD. E, G and L denote exponential, gamma and lognormal distribution, respectively.

Kototabang that gamma DSD exhibits better agreement between calculated and observed DSD and R than the other two DSD models.

Chapter 5

Bias Due to Bin Width Selection of Distrometer Data in Estimating Parameters of Raindrop Size Distribution

5.1 Introduction

In order to reduce the amount of data, the instruments used to measure raindrop size distribution (DSD) provide DSD at nominal drop diameters that correspond to the mean of the bin sizes (or quantization interval). The users can adjust the width of drop size classes in the software provided by the manufacturer. In case of the 2D - Video Distrometer (2DVD), it provides the DSD with uniform bin size. As was introduced in Chapter 1, some previous investigators have analyzed the raindrop spectra of 2DVD binned at different sizes (e.g., Kozu *et al.*, 2005; Tokay *et al.*, 2001). A mechanical impact device known as Joss and Waldvogel Disdrometer, hereinafter JWD (Joss and Waldvogel, 1969), provides the DSD with nonuniform bin sizes. Raindrop diameters collected by a JWD are sorted into 20 diameter intervals ranging from 0.3 to about 5.0-5.5 mm for 30-s averaging periods (interval sizes and averaging periods may vary depending on the user). The widths of the 20 intervals are not uniform and increase as drop size increases

(0.1 - 0.5 mm). Like a JWD, a rather new optical instrument (Parsivel) also provides non-uniform bin sizes (Löffler-Mang and Joss, 2000).

Besides the bias of the fitting method (see Chapter 4), the bias due to bin width selection could be another factor to be considered in fitting DSDs. The selection of bin width may influence the shape of raindrop spectra. If we choose a too large bin size, data would not represent the shape of the underlying distribution (Shimazaki and Shinomoto, 2007). Binning procedure may not significantly influence the conclusions of ice and raindrop physics studies in Tokay *et al.* (2001) and Kozu *et al.* (2005), but it may be crucial when we are dealing with ground validation of radar and other remote sensing techniques (e.g., Gage and Williams, 2005).

In the following sections we investigated the effect of binning on DSDs especially for uniform bin size as in the 2DVD data. Two types of data were used. First, we studied the effect of binning by examining their ability to recover known parameters of simulated DSDs. Second, real DSDs collected by the 2DVD in 2007 at Kototabang were analyzed. The 2DVD also provides data on drop-by-drop basis. Hence, we compared the DSD parameters calculated from binned data with those calculated from drop-by-drop data basis. A 2DVD can measure the size of the drops with a nominal accuracy of $\pm$ 0.2 mm. Therefore, both simulated and real DSDs were binned at 0.20, 0.25, 0.30, 0.35, 0.40, 0.45 and 0.50 mm.

5.2 Equations Governing Retrieval of DSD Parameters from Drop-by-Drop Data

We have presented equations to calculate the DSD parameters of binned data through moment method (MM), maximum likelihood (ML) and L-moment (LM) in Chapter 4. In this section, we present the equations for drop-by-drop data (unbinned data). As was summarized in Chapter 4, for Kototabang the performance of the gamma distribution is better than the exponential and lognormal distribution. Therefore, in this chapter we will only present the equations for the gamma distribution.

5.2.1 Moment Method

As was explained in the previous chapter , a moment of the DSD in term of the gamma distribution is given by

$$M_n = \int_0^\infty D^n N(D)\, dD = N_0 \Gamma(n + \mu + 1)/\Lambda^{n+\mu+1}, \tag{5.1}$$

where $\Gamma(y)$ is the complete gamma function. The DSD in (5.1) are grouped into several classes with a given bin width (ΔD). Thus, $N(D)$ in (5.1) is the number of drops in the ith bin, D is the midsize of the ith bin and ΔD is the width of the ith bin. Drops distributed in $N(D)$, of course, are not exactly the same as the mean of the bin sizes (D) in (5.1) because drops in $N(D)$ are laying within size interval $D \pm \Delta D/2$. Selection of bin width (ΔD) may influence the shape of raindrop spectra. If we choose a too large bin size, the difference of actual D and binned D (midsize of bin) in (5.1) will be large. On the other hand, if we choose a too small bin size, more spikes and nulls occur in the spectra. Figure 5.1 presents, as example, the stair-step plot of the DSD binned at several bin sizes. Some differences in DSD are visible.

Two moment estimators were used to calculate the parameters of simulated and measured DSD in this chapter. The M_{234} estimator is based on the 2nd, 3rd, and 4th order moments. Similarly, another estimator is referred to as M_{346}. We modified (5.1) by using the DSD definition in (3.1) to yield

$$M_x = \frac{1}{\Delta t} \sum_{j=1}^n \frac{D_j^x}{A_j v_j}. \tag{5.2}$$

Using (5.2), the DSD parameters (N_0, μ, Λ) of drop-by-drop data basis can be then calculated. D_m is calculated by the following equation

$$D_m = \frac{\sum_{j=1}^{j_{max}} \frac{D_j^4}{A_j v_j}}{\sum_{j=1}^{j_{max}} \frac{D_j^3}{A_j v_j}}. \tag{5.3}$$

Physical definition of D_0 is median volume diameter. Therefore, from the drop-by-drop data basis D_0 is retrieved by accumulating the drop volume recorded by 2DVD and taking the drop diameter sharing the total accumulated volume in two equal parts. If half of total accumulative volume does not lie precisely at
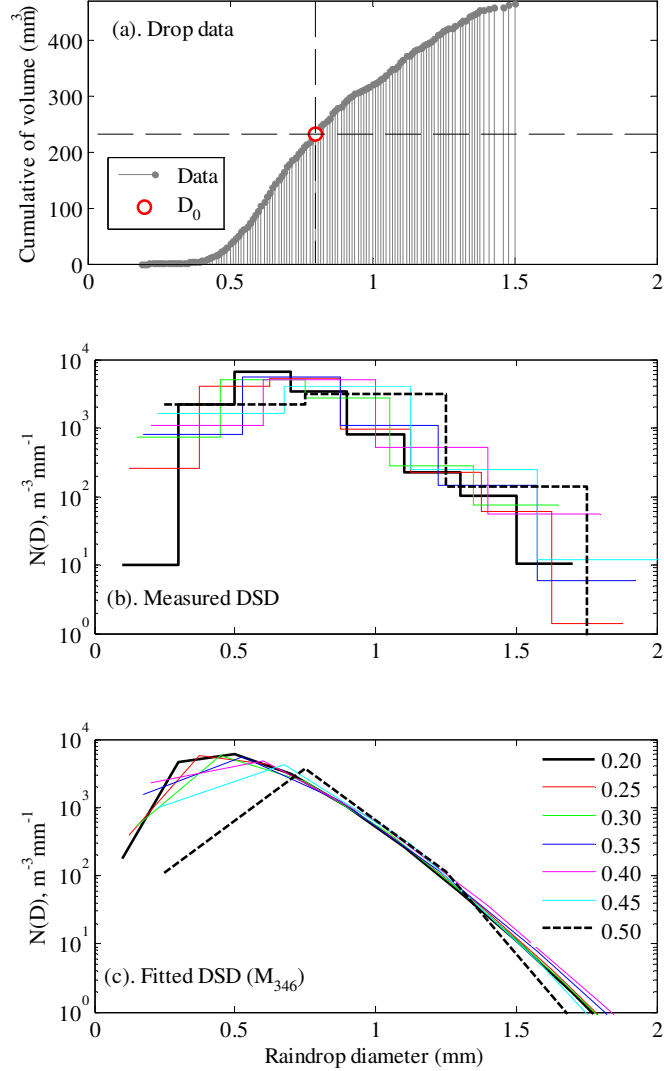
Figure 5.1: Raindrop data observed by 2DVD for the rain event on 23 July 2007 at 03:00 local time (LT) in which (a) is the cumulative distribution of drop volume to calculate D_0 from drop-by-drop data basis, (b) stair-step plot of the DSD binned at several bin sizes and (c) fitted DSD by M_{346} estimator. The value of N_T and R for this event are 2745 and 3.81 mm/h, respectively.

a known diameter, D_0 is then calculated by cubic spline interpolation. The D_0 from binned data is calculated by the equation of $D_0 = (3.67 + \mu)/\Lambda$. Figure 5.1 presents, as example, the computation of D_0 from its physical definition.

5.2.2 Maximum Likelihood Estimation

To calculate the DSD parameters of drop-by-drop data using the ML method, we modify the equations of Λ as

$$\Lambda = \frac{(\mu + 1)N}{\sum_{i=1}^{N} D_i} = \frac{(\mu + 1)}{\bar{D}}, \tag{5.4}$$

where N is the total number of raindrops. Moreover, to estimate μ we modify (4.25) as

$$\ln(\mu + 1) - \Psi(\mu + 1) = \ln\left(\frac{\bar{D}}{\prod_{i=1}^{N} D_i^{1/N}}\right), \tag{5.5}$$

where Ψ is the "psi" or "digamma" function as in (4.26). Let α be as $\alpha = \mu + 1$, (5.5) can be solved by iteration using recursion as

$$\alpha_{j+1} = \alpha_j \frac{\ln(\alpha_j) - \Psi(\alpha_j)}{Y}, \tag{5.6}$$

where

$$Y = \ln\left(\frac{\bar{D}}{\prod_{i=1}^{N} D_i^{1/N}}\right), \tag{5.7}$$

$$\alpha_1 = \frac{1 + \sqrt{1 + 4\exp(Y)/3}}{4\exp(Y)}. \tag{5.8}$$

After getting α, the shape parameter is calculated by $\mu = \alpha - 1$.

5.2.3 L-Moment Estimation

The first two L-moments to calculate two parameters of the gamma distribution are given by (4.46) and (4.47). To use these equations for drop-by-drop data, the equations of b_0 and b_1 are

$$b_0 = \frac{1}{N} \sum_{i=1}^{N} D_{i:N}, \tag{5.9}$$

$$b_1 = \frac{1}{N(N-1)} \sum_{i=1}^{N} (i-1) D_{i:N}. \tag{5.10}$$

In case of binned data (DSD), the mean total number concentration parameter (N_T or N in the above equations) is calculated as the 0th moment of DSD. On the other hand, we can directly calculate N_T for drop-by-drop data.

5.3 Data Description

All the data both simulated and measured data used in this chapter are the same as that in Chapter 4. Both simulated and real DSDs were binned at 0.20, 0.25, 0.30, 0.35, 0.40, 0.45 and 0.50 mm.

5.4 Results

5.4.1 Moment method

5.4.1.1 Simulation data

The moment method is biased and the bias increases with the order of the moments used (see Chapter 4). Table 5.1 shows the average of estimated parameters ($\hat{\mu}$, $\hat{\Lambda}$) for initial values of $\Lambda = 4$, $\mu = 2$ and $N_T = 10^3$. The N_0 value was estimated from (2.10), yielding the value 3.2 x 10^4. Total number of samples is 10^3. In general, the parameters of DSD tend to be much larger than those of the underlying DSD from which the samples are taken, consistent with the aforementioned discussion (Chapter 4)

Two different estimators (M_{234}, M_{346}) are taken worthwhile to study the bin width error because the population of medium and large-sized drops would mainly determine the DSD parameters if we use high order moments. On the other hand, the population of medium and small-sized drops would mainly determine the parameters of distribution if we use low order moments. From Table 5.1, we can observe that the effect of bin width selection is more significant for M_{234} than for M_{346}. The difference between the DSD parameters obtained from DSD binned at 0.20 mm and those from DSD binned at 0.50 mm is more significant for M_{234}

Table 5.1: Average of estimated parameters and AFE for initial values of $\Lambda = 4$, $\mu = 2$ and $N_T = 10^3$.

Bin sizes	Λ		μ		Λ		μ	
(mm)	M_{234}	M_{346}	M_{234}	M_{346}	M_{234}	M_{346}	M_{234}	M_{346}
Parameters					AFE			
0.20	4.18	4.46	2.22	2.61	12.75	25.99	27.43	69.50
0.25	4.20	4.46	2.25	2.62	12.99	26.24	28.21	70.61
0.30	4.22	4.47	2.29	2.65	13.03	25.92	29.11	70.10
0.35	4.26	4.48	2.37	2.67	13.58	26.08	31.16	71.03
0.40	4.30	4.48	2.45	2.69	14.35	26.33	34.14	72.53
0.45	4.38	4.49	2.60	2.74	15.39	27.41	38.88	76.74
0.50	4.49	4.57	2.79	2.88	17.15	27.55	45.85	78.39

than for M_{346}. This result may imply that the binning procedure significantly influences the population of medium and small-sized drops.

The average fractional error (AFE) of Table 5.1 are obtained by (4.55). It can be observed that the degree of scatter increases with increasing bin width. The value of AFE for M_{346} is larger than for M_{234}, indicating larger bias of M_{346} than for M_{234} estimator. However, the difference in AFE for each bin size is more obvious at M_{234} than at M_{346} estimator. This is reasonable because the bin width selection may significantly influence the population of medium and small-sized drops as also observed from average parameters.

Figure 5.2 shows the variation of average estimated parameters ($\hat{\mu}$, $\hat{\Lambda}$) for initial values of $\Lambda = 4$ and $\mu = 2$, with the number of raindrop (N_T). Total sample of each initial value is 10^3. It is seen that the smaller the number of drops (N_T), the larger the bin width errors especially for M_{234}.

5.4.1.2 Measurement data

We collected the DSD for 1-min periods and disregarded drops that are bigger in diameter than 10.25 mm, because drops larger than this size are presumably not real drops. As the accuracy test of fit, we used the normalized root mean

(a) M234 (b) M346
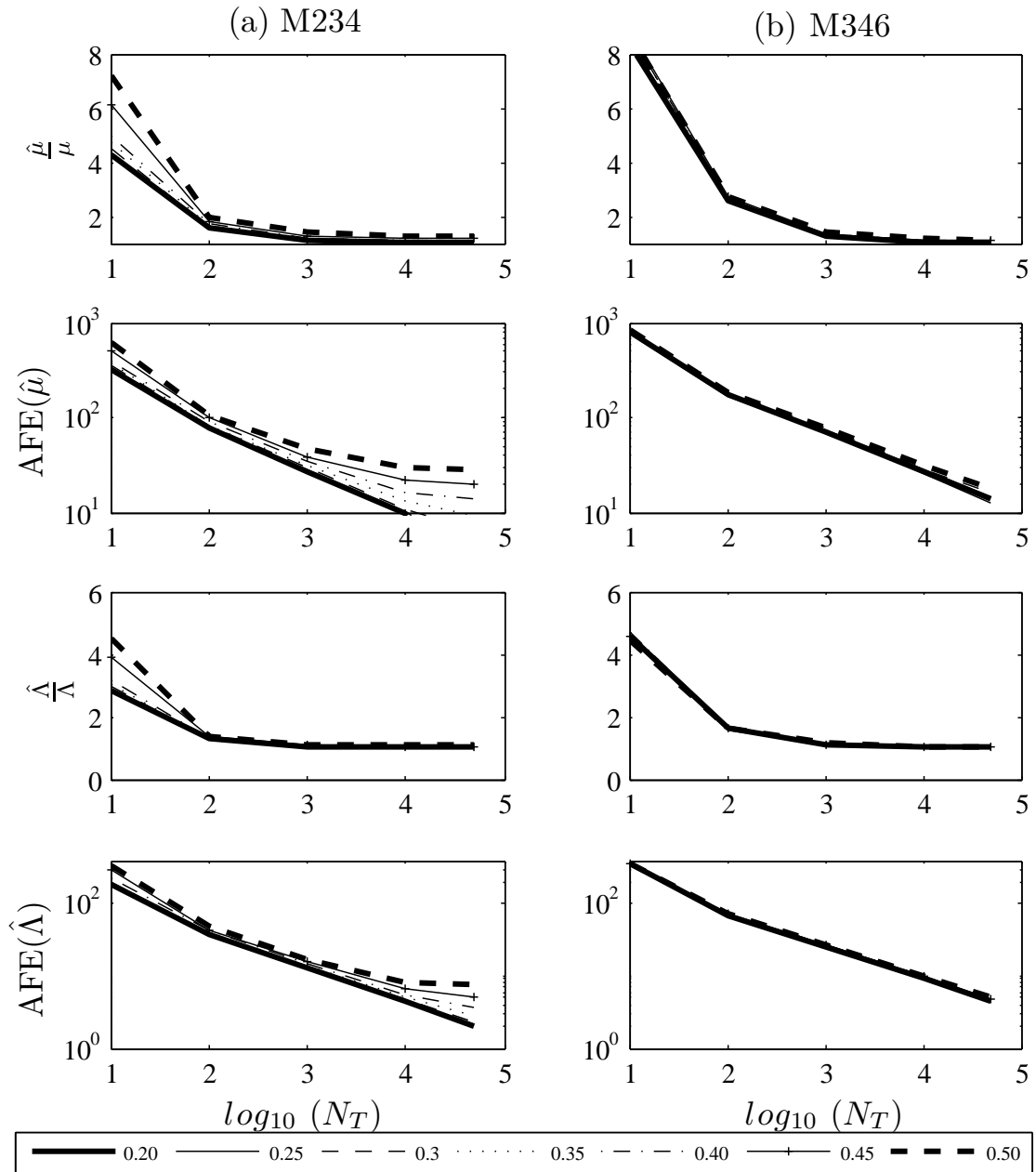
Figure 5.2: Variation of average of ratio of estimated parameters ($\hat{\mu}$, $\hat{\Lambda}$) with the truth (initial) parameters ($\Lambda = 4$, $\mu = 2$) and AFE, with the number of raindrop (N_T). Total sample for each initial parameter is 10^3.

squared error ($NRMSE$) as in (4.56). The ability of the model distribution to conserve the rainfall rate of observed DSD ($|\Delta R|/R_{observed}$) was also used. By
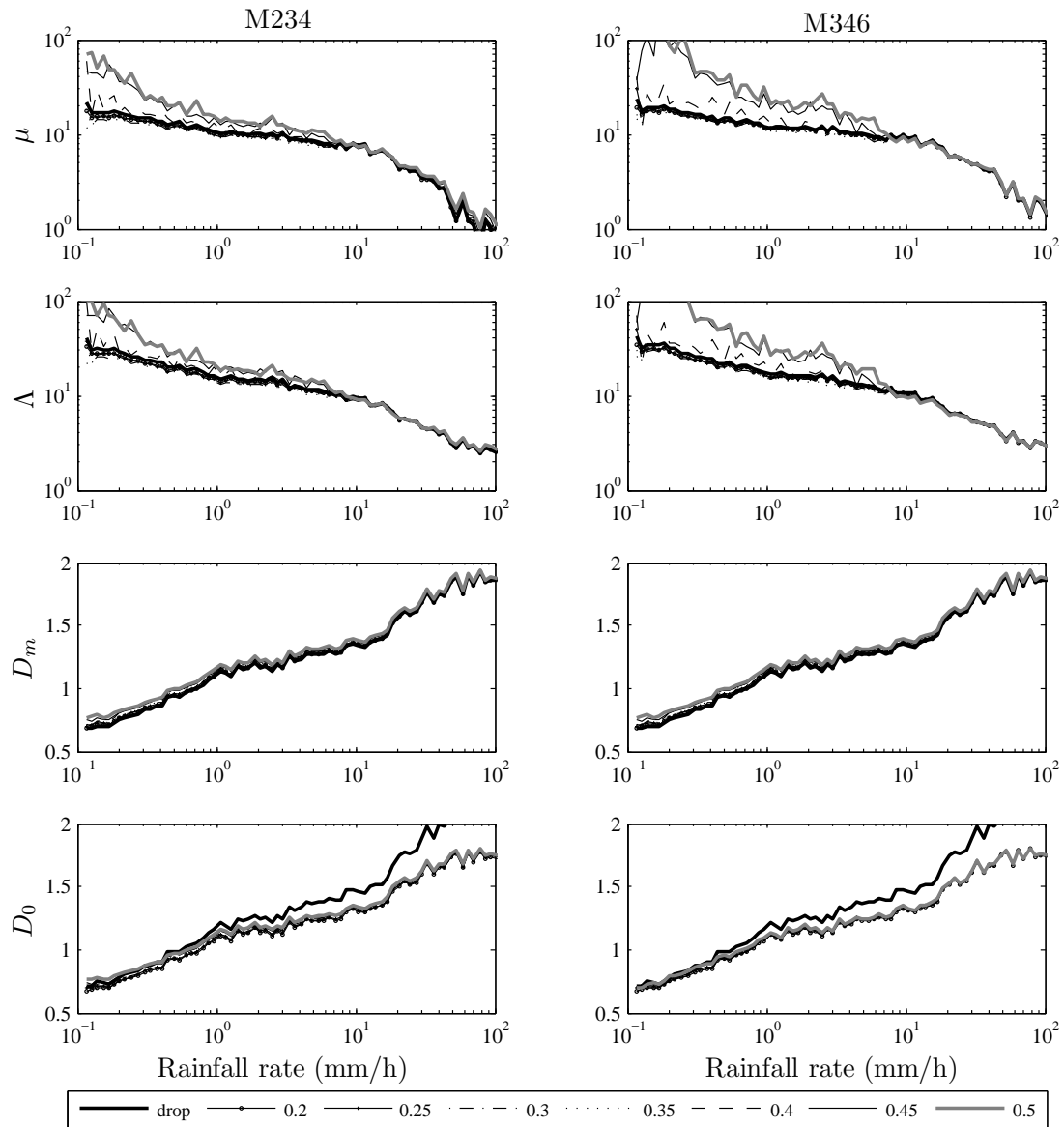
Figure 5.3: Variation of average of DSD parameters (μ, Λ), D_m and D_0 calculated from the DSD (binned data) and those calculated from drop-by-drop data, with rainfall rate.

these statistical tests, we hope to be able to consider only gamma distributions. We considered only the DSD spectra with $NRMSE < 3$, $(|\Delta R|/R_{observed}) < 0.01$ and $N_T > 100$. We excluded also the data for which the estimate of μ by the bin size of 0.2 mm obtained by M_{346} lies outside the interval (-5, 30). Our dataset

Table 5.2: Average fractional errors (%), between parameters calculated from drop-by-drop data basis and binned DSD.

Bin sizes	Λ		μ		D_m		D_0	
(mm)	M_{234}	M_{346}	M_{234}	M_{346}	M_{234}	M_{346}	M_{234}	M_{346}
$0.1 \leq R < 10$								
0.20	4.95	17.29	4.32	11.30	1.14	1.14	7.39	7.20
0.25	7.17	17.72	6.47	11.38	2.06	2.06	6.74	6.54
0.30	10.04	19.33	8.65	12.85	2.44	2.44	6.72	6.52
0.35	15.51	23.36	12.67	15.97	2.90	2.90	6.43	6.25
0.40	26.32	37.65	19.74	25.80	4.14	4.14	6.17	6.03
0.45	44.15	90.51	31.97	65.13	5.30	5.30	6.52	6.46
0.50	52.91	112.79	36.65	79.31	6.59	6.59	7.11	7.14
$R > 10$								
0.20	2.03	28.73	0.83	14.15	0.28	0.28	13.62	13.12
0.25	4.28	29.74	1.24	14.17	0.77	0.77	13.10	12.62
0.30	7.52	30.09	1.69	14.34	0.69	0.69	13.17	12.70
0.35	7.97	29.21	2.53	13.43	1.24	1.24	12.70	12.21
0.40	12.62	29.23	3.07	13.81	1.30	1.30	12.65	12.21
0.45	19.02	29.79	4.14	13.55	1.87	1.87	12.07	11.66
0.50	27.22	30.27	5.78	13.12	2.38	2.38	11.59	11.21

comprises a total of 9181 1-min samples.

Figure 5.3 shows the variation of the average DSD parameters (μ, Λ), D_m and D_0 calculated from the DSD (binned data) and those calculated from drop-by-drop data, with rainfall rate. The difference in DSD parameters (μ, Λ) for each bin size is significant at low rainfall rates $(R < 10 \text{ mm/h})$. This result is consistent with the simulation analysis because the total number of drops is higher for more intense rainfall. Another possible explanation is the stronger impact that binning has on the representation of small and medium-sized drops which will be more pronounced at lower rainfall rates.

Unlike μ, Λ, average D_m and D_0 increase with increasing rainfall rate. The difference between D_m obtained from DSD and drop-by-drop data basis is small.

The degree of scatter is about 6% (at 0.5 mm bin size) for $R < 10$ mm/h and only 2% for $R > 10$ mm/h (Table 5.2). A rather high bias is observed in D_0. Although it is not linear, we can observe in Fig. 5.4 a relationship between $|\Delta D_0|$ and the statistical measures ($NRMSE$, $|\Delta R|/R_{observed}$). Therefore, biases in moment method and shape of the DSD may contribute to the bias of D_0 especially when the data are sparse. In addition, D_0 from the drop-by-drop data basis is retrieved by its physical definition with the help of interpolation procedure, while D_0 from the DSD is calculated by moment method. The difference in the method may also be a reason for the high error of D_0. If both D_0 (DSD and for drop-by-drop data basis) is calculated by the moment method ($D_0 = (3.67 + \mu)/\Lambda$), the difference between D_0 derived from DSD and drop-by-drop data is also small, as for D_m.

It is well known that DSD moments contain important physical information. For example, the 0th moment is equal to the number of drops per unit volume (N_T), the 3rd moment is equal to liquid water content (LWC) and R (with power law of terminal fall velocity as in (2.23)), and 6th moments is equal to radar reflectivity factor (Z). Moreover, the moment error is a key factor in accurately estimating the DSD parameters. Table 5.3 lists the average fractional errors for several moments of DSD. It is seen that the higher R, the smaller the moment errors and the higher the moment order and the bin size, the larger the moment errors. This implies that small bin sizes (0.20-0.30 mm) have the potential to retrieve physical information from the DSD (binned data).

5.4.2 Maximum likelihood and L-moment Estimation

The ML and LM methods are less biased than the MM (see Chapter 4). Thus, these two methods can clarify the bias due to bin width selection found in the MM. Figure 5.5 shows the bias due to bin width selection obtained from the ML and LM methods for the initial values of $\Lambda = 4$, $\mu = 2$ and $N_T = 10^3$. Again it is observed the effect of bin width selection on the DSD parameters. The smaller the bin size is, the closer the parameters to the initial values. The MM overestimates the DSD parameters and the binning procedure increases the overestimation of the parameters. On the other hand, the ML and LM methods underestimate the parameters and the binning procedure increases the underestimation of the
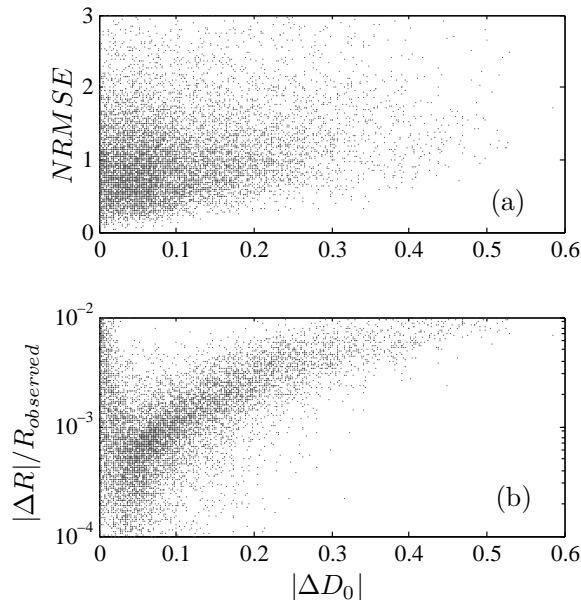
Figure 5.4: $|\Delta D_0|$ (the difference between the M_{346} at 0.20 bin size and the interpolation estimation) versus the statistical measures of DSD ($NRMSE$, $|\Delta R|/R_{observed}$).

parameters. The average of the DSD parameters and their fractional error for Fig. 5.5 are shown in Table 5.4. We can observed that the effect of bin width selection is more significant for the ML than for the LM method. The difference between the DSD parameters obtained from drop-by-drop basis and those from DSD binned at 0.50 mm is more significant for ML than for LM method.

Figure 5.3 shows the scatter plot of the parameters of binned data (y-axis) versus those of drop-by-drop data basis (x-axis) retrieved from several days of 2DVD data. The difference in the DSD parameters for each bin size is significant at ML method. The smaller the bin size is, the closer the parameters to those of drop-by-drop data basis, which is consistent with the simulation analysis.

As was discussed in section 5.2 that the drops distributed in binned DSD, $N(D)$, of course, are not exactly the same as D (midsize of bin). Consequently, If we choose a too large bin size, the difference between actual D and binned D (midsize of bin) will be large. Moreover, because drops also follow gamma distribution in each class, the mean value of drops in that class is not the midsize of bin. Figure 5.7 presents the scatter plot of the DSD parameters of binned

Table 5.3: Average fractional errors (%), between moments calculated from drop-by-drop data basis and binned DSD.

Bin sizes	M_0	M_2	M_3	M_4	M_5	M_6
$0.1 \leq R < 10$						
0.20	0.06	1.76	2.75	3.87	5.15	6.61
0.25	0.43	2.45	4.33	6.47	8.83	11.40
0.30	1.55	1.84	3.51	5.87	8.67	11.86
0.35	2.40	2.19	4.32	7.12	10.52	14.51
0.40	3.23	5.12	9.37	14.00	19.10	24.75
0.45	5.17	6.63	12.55	18.92	25.89	33.55
0.50	8.56	6.12	12.81	20.75	29.62	39.62
$R > 10$						
0.20	0.25	0.77	0.95	1.17	1.43	1.75
0.25	1.13	1.47	2.34	3.12	3.88	4.64
0.30	2.52	0.58	1.33	2.01	2.66	3.35
0.35	3.37	1.05	2.32	3.58	4.88	6.22
0.40	4.41	2.40	3.92	5.21	6.52	7.91
0.45	6.20	2.97	5.27	7.24	9.24	11.37
0.50	8.75	2.44	5.48	8.01	10.55	13.26

DSD versus drop-by-drop data basis. "Midsize", "mean", "mode" and "median" denote that the representative value for the class (bin) of grouped data are the midsize of bin, mean, mode and median of drops in each class. We found in the aforementioned discussion that the bin size of 0.2 mm provides the results which are very close to drop-by-drop data basis. In general, using mean, mode and median of drops instead of midsize of bin give the results larger than those of drop-by-drop data basis. This implies that using midsize of bin as the representative value for the class (bin) of grouped data particularly for small bin sizes (0.20-0.30 mm) are better than using mean, mode and median of drops in each class.
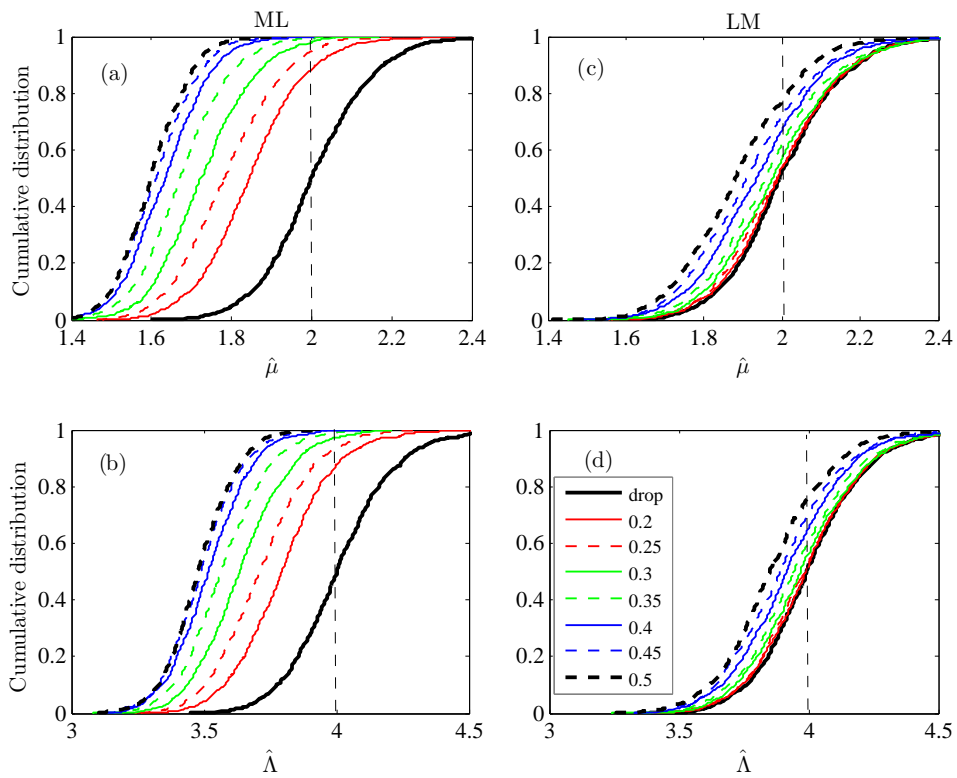
Figure 5.5: Cumulative distribution of estimated parameters for initial values of $\Lambda = 4$, $\mu = 2$ and $N_T = 10^3$. Total sample for each initial parameter is 10^3. Vertical lines denote the population values.

Table 5.4: Average of estimated parameters and AFE for the initial values of $\Lambda = 4$, $\mu = 2$ and $N_T = 10^3$.

Bin sizes	Λ		μ		Λ		μ	
(mm)	ML	LM	ML	LM	ML	LM	ML	LM
Parameters					AFE			
drop	4.01	4.00	2.01	2.00	3.68	3.94	5.09	5.52
0.20	3.80	3.99	1.85	1.99	6.21	4.05	9.48	5.73
0.25	3.72	3.99	1.79	1.99	8.07	4.14	12.63	6.00
0.30	3.64	3.98	1.73	1.98	10.10	4.30	16.11	6.18
0.35	3.57	3.96	1.68	1.96	12.12	4.47	19.74	6.48
0.40	3.52	3.92	1.64	1.94	13.77	4.67	22.68	7.03
0.45	3.49	3.90	1.61	1.92	14.63	5.00	24.35	7.73
0.50	3.48	3.86	1.60	1.89	14.95	5.34	25.16	8.49
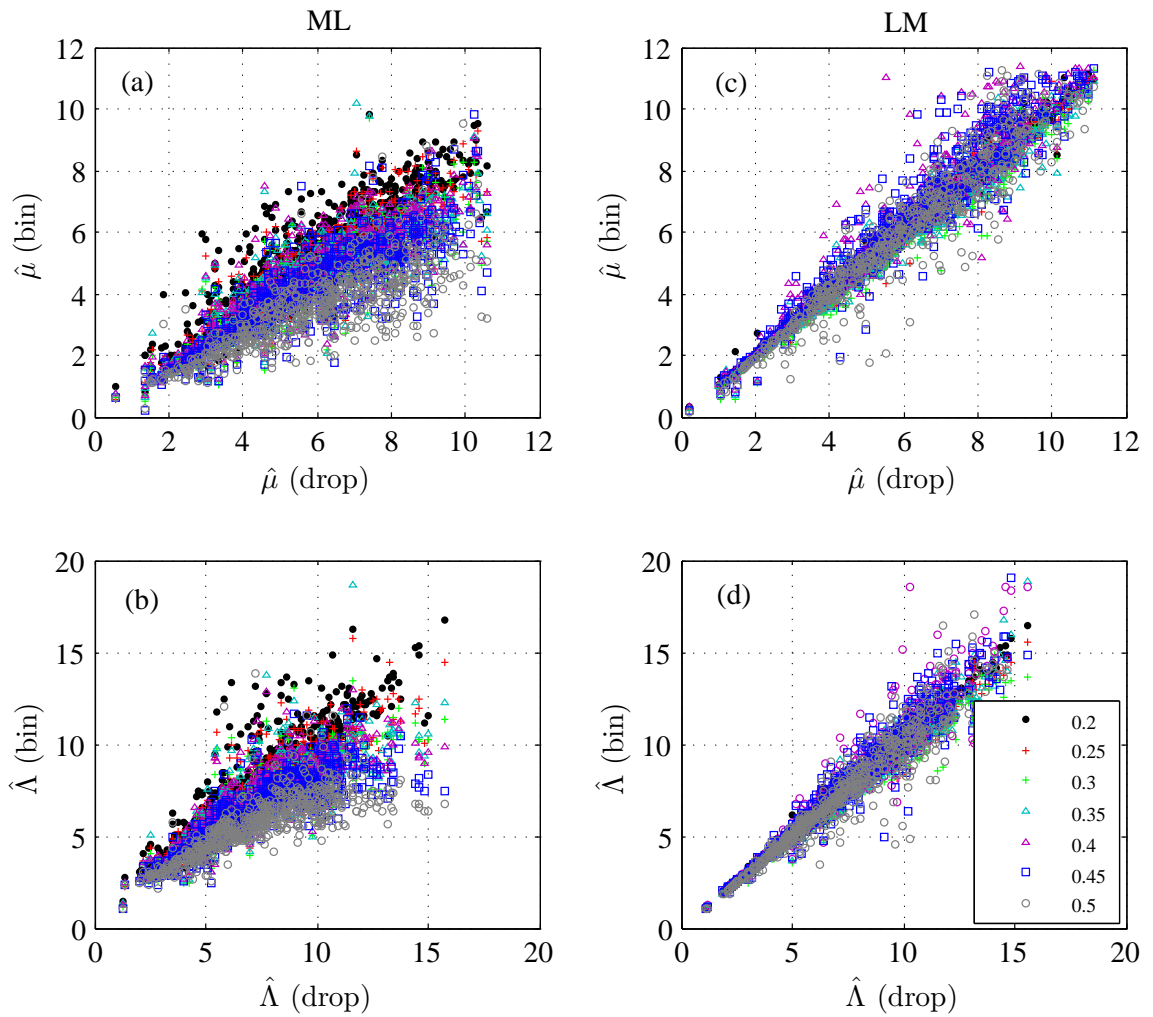
Figure 5.6: Scatter plot of the parameters of binned data (y-axis) versus those of drop-by-drop data basis (x-axis) from 2DVD data. Solid lines denote the line of $y = x$.
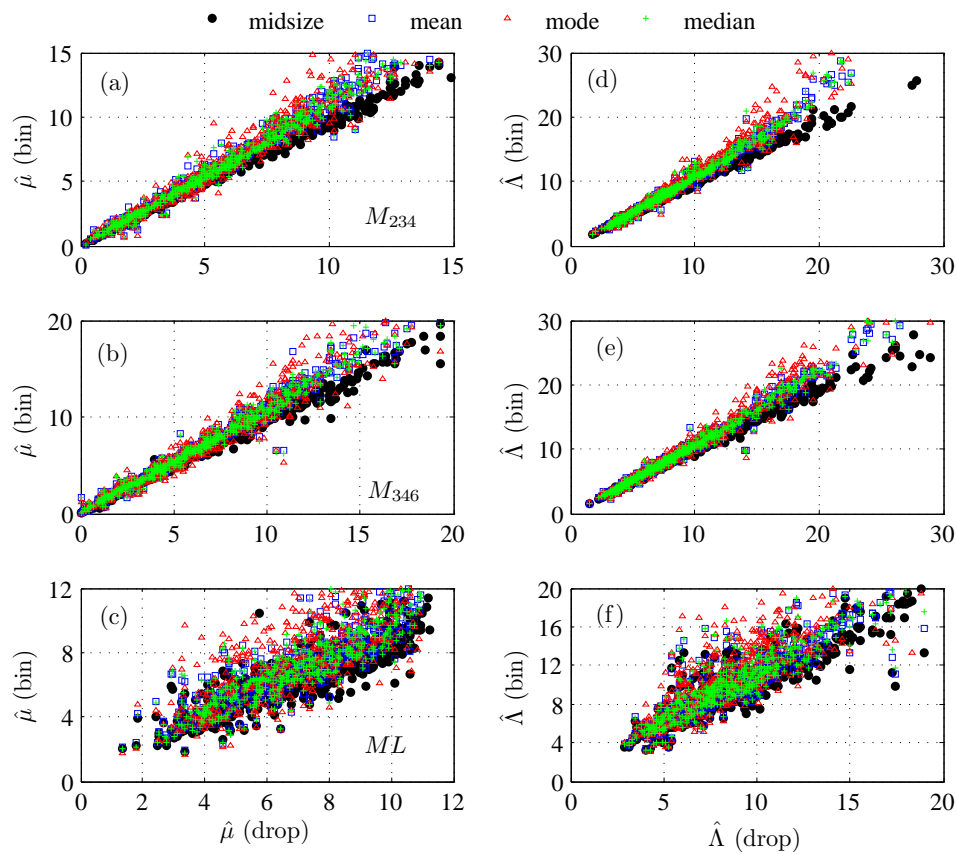
Figure 5.7: Scatter plot of the DSD parameters of binned DSD versus drop-by-drop data basis. "Midsize", "mean", "mode" and "median" denote that the representative value for the class (bin) of grouped data are midsize of bin, mean, mode and median of drops in each class.

Chapter 6

Distributions of Size, Shape, Falling Velocity of Raindrop of Tropical Precipitation over West Sumatra

6.1 Introduction

Raindrop size distribution (DSD) varies not only within a specific storm type but also across differing storms types and climatic regimes (Ulbrich, 1983). Natural variations in DSDs substantially limit the accuracy of radar-derived rainfall estimates. Although some in situ measurements of the DSD have been conducted by using various techniques in many locations all over the world (e.g., Donnadieu, 1980; Hauser *et al.*, 1984; Joss and Waldvogel, 1969; Kruger and Krajewski, 2001; Löffler-Mang and Joss, 2000; Schönhuber, 1998), the DSD is not frequently measured in the tropical latitude especially in the equatorial region. In this chapter, we elucidated the DSD variability based on 2D-Video Distrometer (2DVD) data which have been collected in the equatorial Indonesia, particularly at Kototabang (hereafter called KT), west Sumatra, Indonesia.

Some investigators have reported the characteristics of DSD at KT. Kozu *et al.* (2005) noticed the differences in the DSD during two phases of Madden-Julian

oscillation (MJO). The MJO is large scale propagating mode of tropical atmospheric intraseasonal variability which is associated with a large scale variation in upper and lower level wind, atmospheric moisture content, vertical surface and sea surface temperature (Madden and Julian, 1972). Kozu *et al.* (2005) analyzed the data during the first campaign of Coupling Processes in the Equatorial Atmosphere (CPEA-I) project from April 10 to May 9, 2004. During the campaign, a clear transition of intraseasonal variation (ISV), in response to MJO, from convectively inactive (April 10-22) to convectively active one (April 23-May 6) was observed (Fukao, 2006). They found that during the inactive phase of MJO the DSDs were broader than Marshall and Palmer's model (MP model). This variation is then named as intraseasonal variation (ISV) of the DSD. Recently, Kozu *et al.* (2006) studied the diurnal and seasonal variation of the DSD at KT by classifying rainfall rate into light (3 mm/h) and heavy rain (30 mm/h). They observed the changes in the DSD parameters from early afternoon to midnight, suggesting that local convective rain and organized rain systems have different micro-physical processes. However, the precipitation classification in both studies was not considered seriously. Rainfall rate in excess 10 mm/h are generally convective rain, but lighter rain may be produced by either type (Tokay *et al.*, 1999). Therefore, an analysis on the DSD at KT through a better rain classification is required. Besides the diurnal and seasonal variation, variation of DSD with rainfall type, rainfall rate, event by event even within individual precipitation events was presented.

Knowledge of the raindrop falling velocity, $v(D)$, is important in cloud physics, interpreting the Doppler radar, soil erosion study, and closely related to the measurements of DSDs and various integral rainfall parameters such as rainfall rate. KT is located around 864 m above mean sea level (MSL). Some studies conducted at KT (Kozu *et al.*, 2005, 2006) used the $v(D)$ corrected by multiplying it by a factor $(\rho/\rho_0)^{0.4}$, where ρ_0 and ρ are air densities at sea level and at altitude (864 m at KT), respectively. However, it is possible to find the true $v(D)$ for KT from the 2DVD observation.

The relationship between drop axis ratio and drop size is critical for polarimetric radar rainfall rate algorithm based on reflectivity, differential reflectivity and specific differential phase. The 2DVD is capable of measuring not only the

DSD and fall velocity but also shape of the hydrometeor. Therefore, besides the DSD variability and the raindrop falling velocity, this paper also described the characteristics of raindrop axis ratio at KT.

6.2 Methodology

6.2.1 Description of Data Source

In addition to the 2DVD data, we also operated a 1.3 GHz wind profiler, hereafter called Boundary Layer Radar (BLR). Detailed descriptions of the 2DVD and the BLR are found in Chapter 3. In Chapter 3, we have compared the performance of the standard and re-matching software of the 2DVD. It is found that for light rain, the differences between the two methods are small enough. However, the differences become significant as the rainfall rate increases. Hence, the re-matching software is employed to reduce the small drops mismatch produced by the standard matching software. The continuous measurements of DSDs from 2006 to 2007 are analyzed. Moreover, the data during CPEA-I are also analyzed to re-visit the ISV of the DSD. However, the camera data which are used in the re-matching software are not collected during the campaign. Therefore, the DSD parameters derived from the CPEA-I data may be influenced by the mismatch effect.

The 2DVD and the BLR were simultaneously observing precipitation during 2006-2007 and during the CPEA-I. To determine the precipitating cloud type, 2-min averaged reflectivity, Doppler velocity and spectral width profiles derived from the vertical beam with vertical domain extended from 0.75 km to 9.75 km are used. Hence, 2DVD data are also averaged in two minute intervals. Selection of bin width may influence the shape of raindrop spectra. We have found in Chapter 5 that using 0.20 mm as the representative value for the class (bin) of binned data may be the best choice because the DSD parameters of this bin width were very close to those obtained from drop-by-drop data. As summary, in this chapter we generated the DSD for 2-min periods, adopting a 0.2-mm channel interval from 0.4 to 10.25 mm. The drops in excess 10 mm are presumably not real drops. Moreover, we also disregarded the minutes that had fewer than 100

drops (to reduce the statistical undersampling noise of 2DVD, see Chapter 3) or
rain rates of less than 0.1 mm/h or minute DSD recording less than 4 consecutive
bins with non-zero values.

6.2.2 Convective-Stratiform Separation
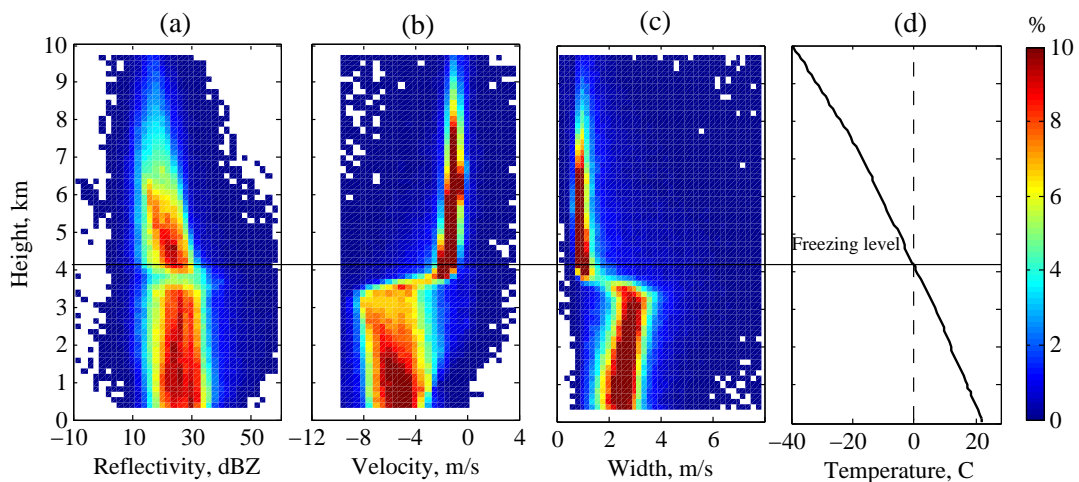
Figure 6.1: Countered Frequency by Altitude Diagrams (CFADs) of reflectivity
(a), vertical velocity (b) and spectral width (c) of simultaneous observation of
BLR and 2DVD during 2006-2007. The bin sizes of CFADs are 2 m/s, 0.5 m/s
and 0.2 m/s, respectively. Figure 6.1d is the average temperature profile obtained
from radiosonde observation during April 10-12, 2004 (four times in a day)

Separation between convective and stratiform is important in precipitation
study because convective and stratiform precipitation are characterized by differ-
ent precipitation growth mechanisms (see Section 2.2). Many investigators have
developed algorithms to classify the precipitation into convective and stratiform
type by using various observational systems such as disdrometer (e.g., Bringi
et al., 2003; Testud *et al.*, 2001), radar echo structures (Biggerstaff *et al.*, 2000),
satellite observations (Hong *et al.*, 1999), and wind profilers (Williams *et al.*,
1995). Lang *et al.* (2003) summarized and examined five algorithms found in
the scientific literature, and introduced a new method based on the ratio of fall
velocity to the vertical velocity of precipitation particles. However, they did not

include an algorithm proposed by Williams *et al.* (1995). In this work, we used a modified version of Williams' method.

Figure 6.1 shows Countered Frequency by Altitude Diagrams (CFADs) of reflectivity (a), vertical velocity (b) and spectral width (c) of simultaneous observation of BLR and 2DVD during 2006-2007. The bin sizes of CFADs are 2 dBZ, 0.5 m/s and 0.2 m/s, respectively. Figure 6.1d is the average temperature profile obtained from radiosonde observation during April 10-12, 2004 (four times in a day). It can be seen that the 0^0 C isotherm (freezing level) at KT is near 4.2 km above the surface. We should be remembered that KT is located about 864 m above sea level. Therefore, in above sea level unit, the freezing level at KT and that of Williams *et al.* (1995) is almost the same, i.e., 5 km. However, in this work, all units are in above ground level (AGL). All data in Fig. 6.1 will be classified into either stratiform, mixed stratiform/convective (sometimes called as transition rain), deep convective, or shallow convective clouds.

Williams' method uses melting layer signature to identify the stratiform and the mixed stratiform/convective (transition) class rain. Doppler velocity gradient (DVG) and maximum spectral width (MSW) are the parameters used to determine these precipitation types. The following thresholds are used in this work to determine stratiform regimes:

DVG > 2.0 m s^{-1} km^{-1} for 3.0 km < height < 4.5 km,
MSW < 2.5 m s^{-1} for 6.5 km < height

On the other hand, if the enhanced turbulence above the melting layer is present, the precipitation is the mixed stratiform/convective (transition) type. The following MSW threshold is used to identify this rain type,

MSW > 2.5 m s^{-1} for 6.5 km < height

If the melting layer signature as determined by the DVG threshold is not observed, the precipitation clouds are classified as deep or shallow convective clouds. Deep convective class has hydrometeors above the melting level, while the shallow convective class does not. In this work, deep convective must meet with the

following Doppler velocity criteria:

Vd < -0.5 m s^{-1} for 4.5 km < height
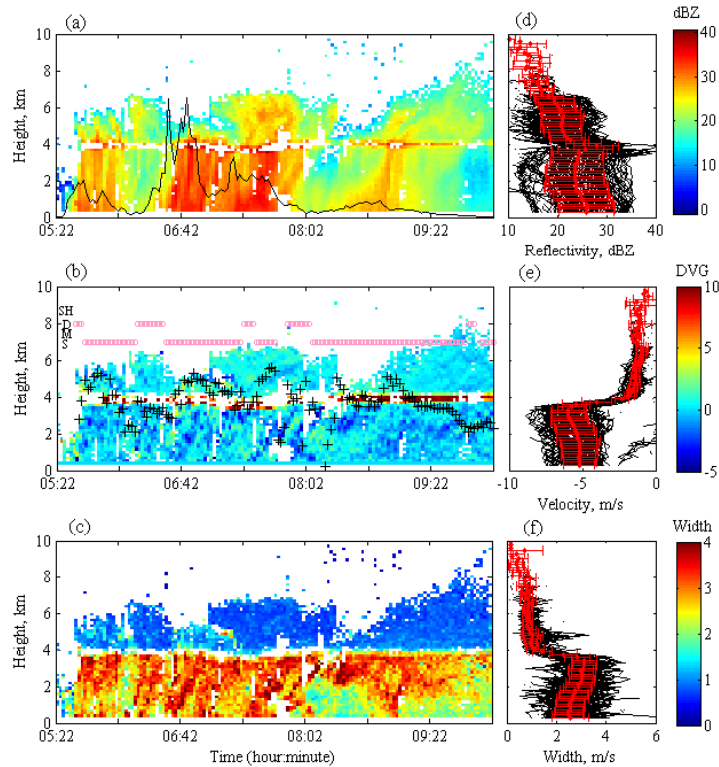
Figure 6.2: Figure a, b and c are the typical height-time–intensity plots for reflectivity factor (dBZ), Doppler velocity gradient (m s^{-1} km^{-1}) and spectral width (s^{-1}), respectively. Furthermore, Fig. d, e, f are the vertical profiles of dBZ, Doppler velocity and spectral width, respectively. Error bars in Figs. 6.3d-f denote standard deviation of the data. Black solid line in Fig.6.3a is rainfall rate ($R/2$), pink circle symbols denote the rain type, black plus symbols denote the DVG calculated by using the linear regression. Rain event was on March 22, 2006.

Williams *et al.* (1995) determined the DVG by calculating the difference in the Doppler velocity between two adjacent range gates or in three adjacent range gates (personal communication). However, we found some limitation of the BLR for the

meteorological applications as previously described by Ralph (1995). When there is no rain (clear-air), the wind profiler receiver has a linear response. However, during rain (when the backscattered signal is very strong) the profiler receiver has a nonlinear response in which an increase in the incident power produces only a small increase in the measured signal power. At some point the receiver even becomes completely saturated and further increase in incident power leads to no measurable increase in signal power. Because of this limitation, it is often found that there are no data in the bright band (BB) region (Fig. 6.2). Hence, calculation of DVG from the difference in the Doppler velocity between two adjacent range gates or in three adjacent range gates is not enough to determine the BB or melting layer especially when the receiver is saturated. To overcome this problem we also used linear regression to calculate the DVG between the heights of 3 km and 4.5 km ("+" symbol in Fig. 6.2b). Some samples in Fig. 6.2b were still misclassified as deep convective. Therefore, a manual quality control procedure was used to improve possible misclassification. Vertical profiles of dBZ, Doppler velocity and spectral width for each rain event are then used (Figs. 6.2d-f). From the vertical profiles (Figs. 6.2d-f) we can see that that all samples in Fig. 6.2 are stratiform with very clear melting layer signature and there is no enhanced turbulence above the melting layer.

The CFAD of each rain type during 2006-2007 are given in Fig. 6.3. The percentage expressed in the figures are relative to the number of profile in each rain type. Simultaneous observation of the wind profiler and the 2DVD provides 15,180 minutes of data (7590 spectra with 2-min interval). Total rainfall is 1,033 mm. Of all spectra, 59% (4463) are classified as stratiform and they contribute 30% of the total rainfall. Furthermore, 4% of the spectra (302) are mixed stratiform/convective (transition) that contribute 5% of the total rainfall, 9% of the spectra (696) are deep convective that contribute 31% of the total rainfall. Finally, 28% of the spectra (2129) are shallow convective that contribute 34% of the total rainfall. It is evident that the occurrence of shallow convective rain is larger than other convective types. Moreover, the occurrence of transition rain (mixed stratiform/convective) is very small in comparison with some previous studies on the tropical precipitation (e.g., Tokay *et al.*, 1999; Williams *et al.*, 1995). There are several possible reasons for the difference in the rain type portion between the
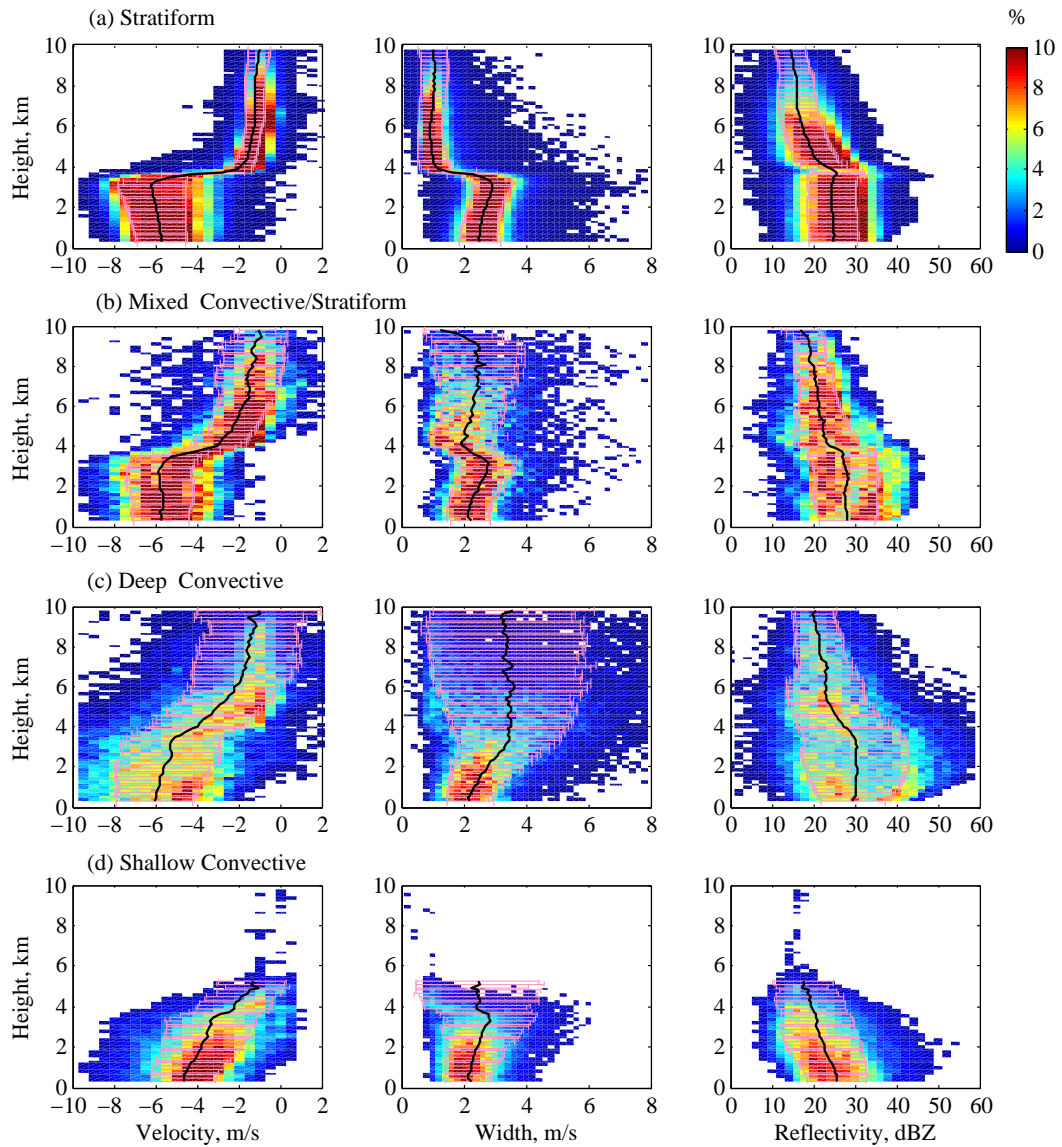
Figure 6.3: Same as Fig. 6.2 but the data have been classified as stratiform (a), mixed stratiform/convective (b), deep convective (c) and shallow convective (d). Average and standard deviation of the data (error bar) are also given.

KT results and other studies. Most of the rainfall in Williams *et al.* (1995) and Tokay *et al.* (1999) may be provided by convective systems, a large number of them being well organized squall lines. In contrast, we never observe any squall line at KT. A large number of rain event at KT was not well organized and do not have stratiform on convective clouds. An often observed situation is a convective event without stratiform region or a stratiform region not being preceded by convective rain. Some rain events had stratiform and convective clouds with very short transition region in between. The transition region between clearly convective events and clearly stratiform ones that occur shortly following the convective stage are more properly classified as convective. These are the reasons why the number of transition rain is small at KT. Precipitation at KT is influenced by the large scale cloud system. Super cloud cluster (SCC) generated over the Indian ocean frequently passed the KT region. The precipitation systems associated with the passage of SCC are characterized by high daily rainfall amount (Kawashima *et al.*, 2006). During the passage of SCC, shallow convective events (with long duration) are dominant in comparison with deep convective (Marzuki *et al.*, 2010). Consequently, the total number of shallow convective data is larger than that of deep convective.

6.2.3   Parameterization of DSD

In Chapter 4 we have discussed several DSD models. For KT, although the performance of gamma distribution does not differ from the lognormal much, gamma distribution exhibits better agreement between calculated and observed DSD and rainfall rate (R) than lognormal as well as exponential distribution. Furthermore, the moment method which is widely used to estimate the DSD parameters is significantly biased. In general, the DSD parameters tend to be much larger than those of the underlying DSD from which the samples are taken. The biases in L-Moment and maximum likelihood method are smaller than those of all moment estimators. In case of truncated samples, the performance of all methods decreases particularly the MM involving low order moments, the LM and ML method. Moreover, in case of gamma distribution, the MM involving M_{3yz}

provides better results than the LM and ML methods as well as lower moment estimators especially when the number of drops is very large.

Some investigators have proposed a normalization procedure to parameterize the DSD (e.g., Sekhon and Srivastava, 1971; Testud *et al.*, 2000; Willis, 1984). For the gamma DSD, this method does not employ a moment of DSD to determine μ. Although other gamma parameters employ a moment based calculation, in general, the bias in normalization procedure will be smaller than that of MM method. Testud *et al.* (2001) developed the procedure to normalize the DSDs without any assumption on its shape as

$$N(D) = N_w f(D/D_m), \tag{6.1}$$

where N_w is the scaling parameter for drop concentration. For gamma distribution, $f(D/D_m)$ and N_w are defined by

$$f(D/D_m) = \frac{6}{4^4} \frac{(4+\mu)^{(\mu+4)}}{\Gamma(\mu+4)} \left(\frac{D}{D_m}\right)^{\mu} e^{-(4+\mu)\left(\frac{D}{D_m}\right)}, \tag{6.2}$$

$$N_w = \frac{4^4}{\pi \rho_w} \frac{LWC}{D_m^4}, \tag{6.3}$$

$$D_m = M_4/M_3, \tag{6.4}$$

with ρ_w being the water density, and M_3 and M_4 the third and the fourth moment of the DSD, respectively. The liquid water content (LWC) is also related to the third moment of the DSD. It is also possible to normalize the intercept parameter of gamma DSD with the number concentration. However, the number of concentration (N_T) is proportional to the zeroth moment of DSD and is significantly underestimated in 2DVD measurement (see Chapter 5). It can be seen from the above equations that N_w and D_m are determined beforehand, without any assumption on the shape of DSD. The μ value can be calculated by minimizing the absolute deviation between the normalized DSD data $(N(D)/N_w)$ and the scaled gamma form (6.2). It is also possible to calculate μ from the normalized standard deviation of the mass spectrum (σ_M) with respect to D_m (Ulbrich and Atlas, 1998), given by

$$\frac{\sigma_M}{D_m} = \frac{1}{(4+\mu)^{0.5}}. \tag{6.5}$$

Bringi *et al.* (2003) have shown that 2DVD measurements agree well with the theoretical relation in (6.5), however the result is still biased relative to (6.5). In order to minimize the possible bias that can be generated by the moment error, we prefer the fitting procedure to the procedure in (6.5). Therefore, the value of μ is not biased. Another important property that can be inferred from (6.5) is that the width of the DSD is more strongly described by the value of D_m or (D_0) than the value of μ.

Figure 6.4 shows the scaled data $[N(D)/N_w]$ versus the normalized drop diameter (D/D_m) of the 7590 simultaneous 2DVD and the BLR observations from 2006 to 2007. The normalized DSDs, are well bounded by the family of scaled Gamma functions as μ varies over the range from -3 to 30. Therefore, we calculate μ in this work ranging between -3 and 30 at step of 0.1.
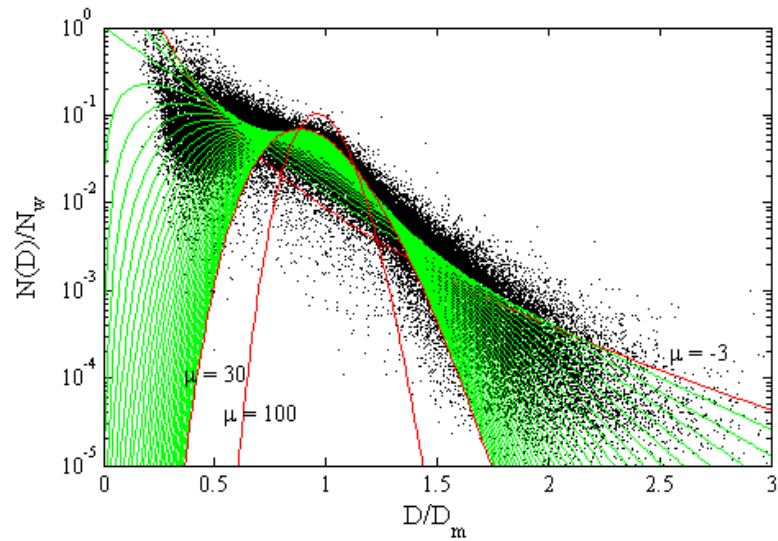
Figure 6.4: Black dots indicate the normalized DSD data $[N(D)/N_w]$ versus normalized diameter (D/D_m) of the 7590 simultaneous 2DVD and BLR observations from 2006 to 2007. Green solid lines indicate the normalized gamma distributions for values of μ ranging between -3 and 30 at step of 1 plus the curve at $\mu = 100$.

6.3 Results

6.3.1 Raindrop Falling Velocity
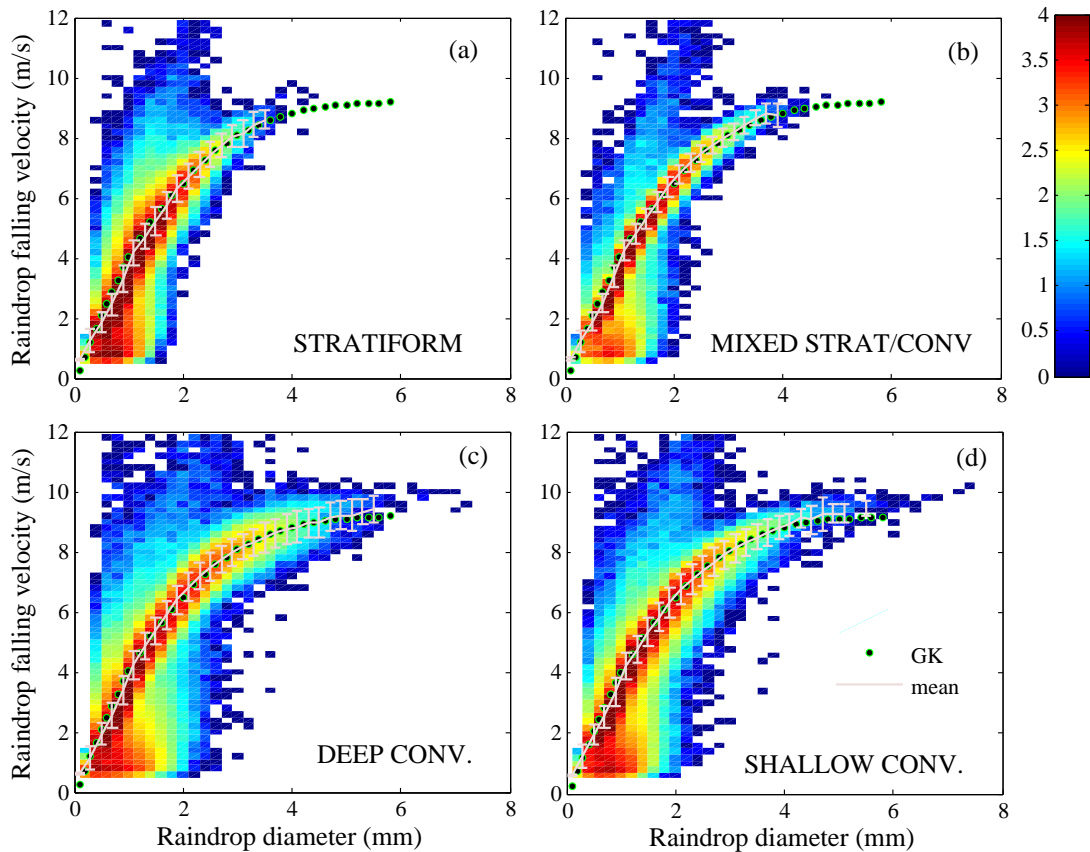
Figure 6.5: Raindrop falling velocity versus raindrop diameter for stratiform, mixed stratiform, deep and shallow convective. The frequency of occurrence is contoured on a log(number) color scale. The mean, $\pm 1\sigma$ (error bars) of the data are also given. Green dots are the laboratory work of Gunn and Kinzer (1949).

Figure 6.5 shows the observed mean number concentration as a function of the drop diameter and the fall velocity for the stratiform, mixed stratiform, deep convective and shallow convective rains, respectively, along with the laboratory measurements by Gunn and Kinzer (1949). Each rain type consists of seven rain events with the amount of the data (minutes) for each type as follows: 499, 292,

236 and 402, respectively. Total number of drops for each rain type is 1,056,158; 349,921; 559,309 and 665,287. It is observed that there is no significant difference in the falling velocity between stratiform and convective rain. Both raindrops in the stratiform and convective rain concentrate in the range of fall velocities of 0.5-9 m/s. Moreover, the average observed drop fall velocities for all rain types tend to be in good agreement with terminal velocities obtained by by Gunn and Kinzer (1949) under the standard sea-level conditions. As was mentioned early that we used a re-matching algorithm to reduce the small drops mismatch produced by the standard matching software. However, some drops still have velocities outside the expected velocities for the corresponding diameters. Hence, we only average the velocity lying inside the range of $|v_{measured} - v_A| < 0.4v_A$ where where v_A represents the formula given in Atlas *et al.* (1973). Besides these similarities, the stratiform and convective rains share some differences too. First, on average, there are large spreads in the raindrop falling velocities at virtually all drop diameters, with convective rain having an even larger spread than stratiform rain. Second, convective rain has larger spread in the drop size than stratiform rain.

Almost all existing drop size-velocity models are based on the experimental work of Gunn and Kinzer (1949) which was conducted under sea-level conditions (1013 millibars and 20ºC). It should be noted that KT is located about 864 m above sea level. Based on a Mobile Automatic Weather Station (MAWS) observation during April-December 2004, average surface temperature, pressure and relative humidity at KT are 21.92 ºC, 917.5 hPa and 87.97 %, respectively. However, there is no air density measurement at this site. Since its location, the raindrop terminal velocity at KT may be larger than the corresponding Gunn-Kinzer terminal velocity (Pruppacher and Klett, 1998). Some studies have been attempted to extrapolate the experimental work at sea level to other atmospheric conditions by multiplying by factor $(\rho/\rho_0)^m$, where ρ_0 and ρ are the air densities at sea level and at altitude, respectively. Foote and Toit (1969) suggested the value of $m = 0.4$, while Atlas *et al.* (1973) suggested $m = 0.5$ for the air density correction. Mitchell (1996) presented a semi-theoretical framework of air density correction by involving the Reynolds and Best number. In this work, m is in

function of diameter dependent as $m = 0.375 + 0.025D$, given by Beard (1985), where D is in millimeter.
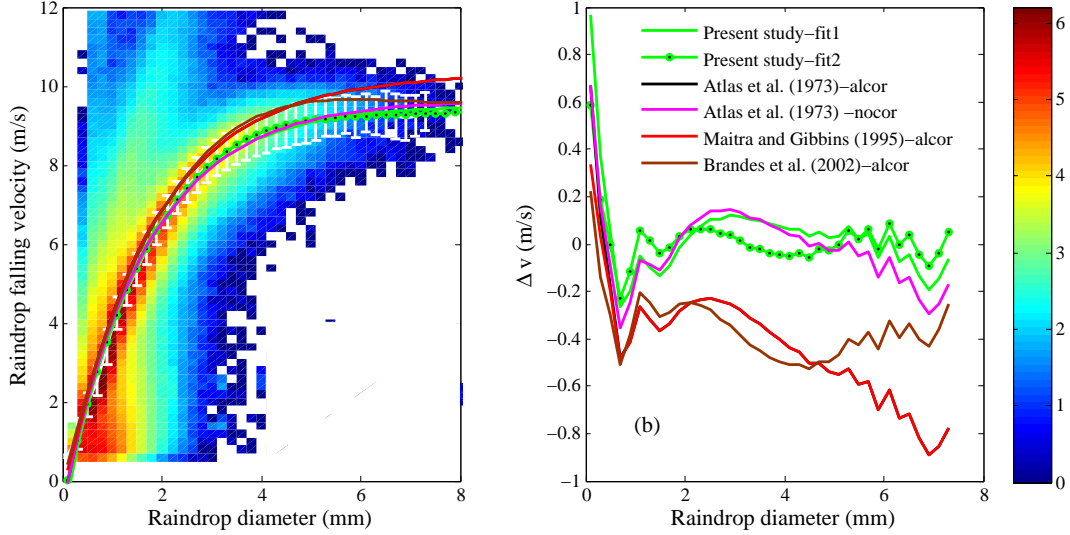
Figure 6.6: Figure (a) is the same as Fig. 6.5 but for all data and all rain type, while (b) the difference in the raindrop falling velocity between the mean of the data and the existing models. The legends with "alcor" denote air density correction, while that with "nocor" denote no correction.

Figure 6.6 shows the observed mean number concentration as a function of the drop diameter and the fall velocity for all data, along with several existing models. Total number of drops in this figure is 34,296,583. The fitting equations between raindrop falling velocity $[v(D)]$ versus drop diameter (D) in m/s unit from average 2DVD measurement at KT are

$$v(D) = 9.51 - 10.51e^{(-0.64D)}, \qquad (\text{fit1}) \qquad (6.6)$$

$$v(D) = -0.4938 + 5.393D - 1.1330D^2 + 0.1067D^3 - 0.00377D^4, \qquad (\text{fit2}) \quad (6.7)$$

where D is in millimeters. The regression coefficient and root mean square error (r^2, RMSE) of the above equations are 0.9974, 0.1223 and 0.9991, 0.07338, respectively. It is evident that the correction for the effect of air density brings the terminal velocities much larger than the observed drop fall velocities. Hence,

the location (864 m above sea level) of KT does not result in a different terminal velocity from Gunn-Kinzer's result.

The large spread in the measurement of the instant drop fall velocity may be due to air turbulence and instrumental errors (e.g., instrument location, container shape and mismatched drop). It is well known that a downdraft will make the drop fall faster than the still-air terminal velocity and on the contrary, an updraft will do just the opposite. However, large spread in the measurement of the instant drop fall velocity for $D < 3$ mm as shown in Figs. 6.5 and 6.6 would be more due to the instrumental errors than the atmospheric turbulence. Turbulent motions should influence the falling velocity for entire drop size range.

6.3.2   Raindrop Axis Ratio

Tokay *et al.* (2001) pointed out that the DSD collected by the 2DVD for $D > 0.2$ mm was reliable. However, raindrop axis ratio are significantly influenced by the calibration of the instrument. The calibration spheres of the 2DVD are in the diameter range 0.5 - 8 mm. Thus, we are not confident about the axis ratio for $D < 0.5$ mm as also evident from Fig. 6.7. Moreover, the data in the interval $0.6 < D < 1.2$ mm may not be sufficiently accurate as inferred from the average value of axis ratios in this range which are larger than one (about 1.01-1.03). This could be due to the residual mismatch problems. Thurai and Bringi (2005) only considered drops larger than 1.5 mm in their analysis.

Figure 6.7 shows our data along with several existing models (e.g., Andsager *et al.*, 1999; Beard and Chuang, 1987; Brandes and Vivekanandan, 2002; Keenan *et al.*, 2001; Pruppacher and Beard, 1970; Thurai *et al.*, 2007).In general, the raindrop size of stratiform rain is narrower than that for convective as also the case for fall velocities. In Fig. 6.7 we only display the average value for the bin containing more than ten drops. The bin size is 0.2 mm. Maximum drop sizes of average axis ratio are 3.5 mm (stratiform), 3.9 mm (mixed stratiform/convective), 5.5 mm (deep convective) and 5.5 mm (shallow convective), respectively. KT results for all rain types show a larger $\langle b/a \rangle$ compared to the Beard and Chuang model as well as other empirical relations. Drop axis ratio for stratiform, mixed stratiform/convective and shallow convective are very close to the result of Keenan
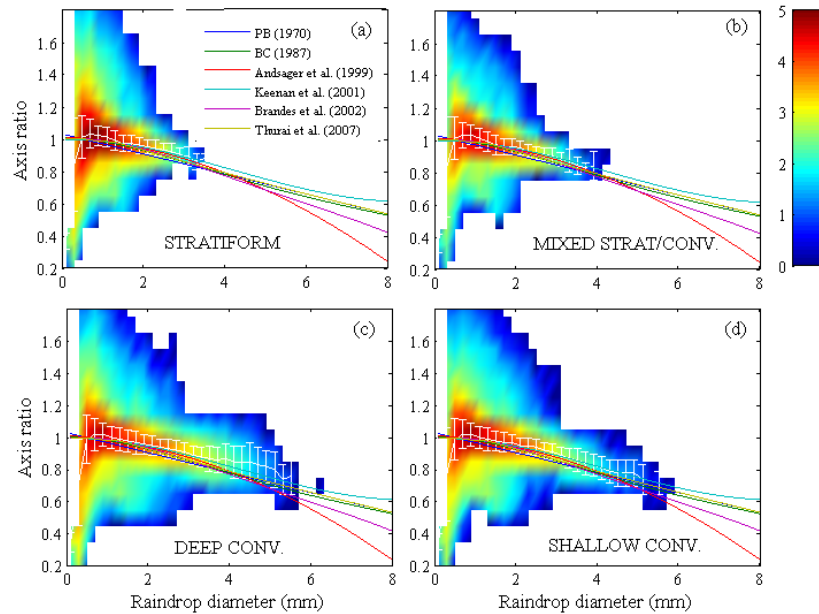
Figure 6.7: Same as Fig. 6.5 but for the axis ratio.White line with error bar denotes the average and standard deviation of the data.

et al. (2001). However, the axis ratios of deep convective rain are bigger than the result of Keenan *et al.* (2001), especially for $D > 3.5$ mm. Figure 6.8 shows the histograms of axis ratio for the 1.6-1.8 mm (a) and 3.4-3.6 mm (b) drop diameter range for all rain types. It is observed that the axis ratio of deep and shallow convective is higher than that for mixed stratiform/convective rain, particularly for Fig. 6.8b. There is no drop observed for stratiform rain in Fig. 6.8b.

For all data sources the results are given in Fig. 6.9 and Table 6.1. The deviation of axis ratio at KT from the equilibrium axis ratio of Beard and Chuang (1987) as well as other empirical relations, is more obvious. As was explained above that we have reasonable confidence for the drop in excess 1.3 mm. We can see from the average axis ratio that there are two regions of axis ratio, i.e, (i) 1.3 $< D < 3.7$ and (ii) $3.7 < D < 6.7$ mm. In region (i), the deviation between axis ratio at KT and previously reported empirical models is relatively small and in agreement with the result of Keenan *et al.* (2001). However, in region (ii) the deviation is larger than that for the region (i). Huang *et al.* (2007) pointed out that raindrop axis ratio at KT (only from three rain events) was very similar to
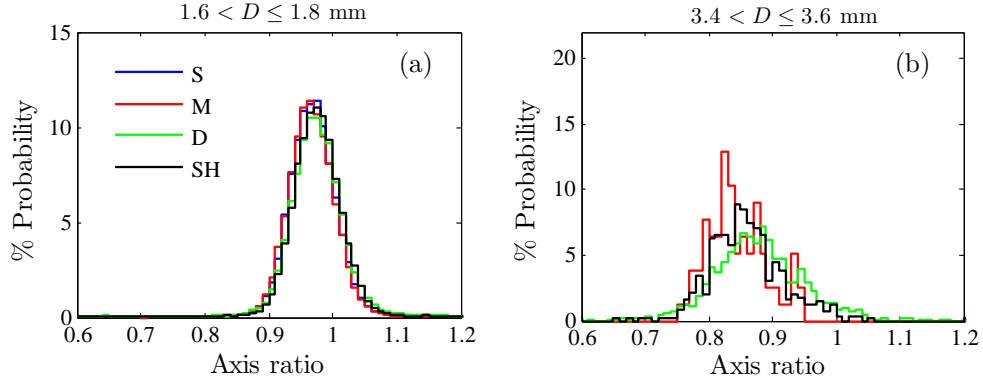
Figure 6.8: Histogram of axis ratio for two drop diameter ranges for stratiform (S), mixed stratiform/convective (M), deep convective (D) and shallow convective (SH) precipitation.

the axis ratio of artificial rain proposed by Thurai *et al.* (2007). In this work, the dataset is much bigger than that of Huang *et al.* (2007) and our results show that raindrops at KT are more spherical than that of artificial rain and equilibrium axis ratio of Beard and Chuang (1987). Our own polynomial fits to the axis ratio at KT for region (i) and (ii), respectively, are:

$$a/b = 1.226 - 0.3999D + 0.2563D^2 - 0.07897D^3 + 0.008516D^4, \qquad \text{(i)} \quad (6.8)$$

$$a/b = 0.4702 + 0.2726D - 0.05779D^2 + 0.003247D^3, \qquad \text{(ii)} \qquad (6.9)$$

The statistical measures (rmse and correlation coefficient) for the two fits are 0.002, 0.999 and 0.006, 0.991, respectively. When inferring R from K_{DP} measured by a dual-polarization radar, it is useful to have a linear equation between the mean axis ratio and drop diameter. The linear fit to our result is:

$$a/b = 1.065 - 0.05601D, \qquad (6.10)$$

where rmse and correlation coefficient are 0.008 and 0.993.

The exact nature of the raindrop axis ratio may be different from the data of the laboratory measurement. In natural rain the raindrops will interact with each other and are influenced by turbulence. Beard *et al.* (1983) and Beard and

Table 6.1: Mean and standard deviation of the axis ratio at KT (all rain types)

Diameter interval	Mean	Std dev	Diameter interval	Mean	Std dev
0.2-0.4	0.80	0.28	3.8-4.0	0.85	0.09
0.4-0.6	1.00	0.13	4.0-4.2	0.84	0.10
0.6-0.8	1.03	0.09	4.2-4.4	0.83	0.11
0.8-1.0	1.03	0.06	4.4-4.6	0.82	0.11
1.0-1.2	1.01	0.06	4.6-4.8	0.81	0.11
1.2-1.4	0.99	0.06	4.8-5.0	0.80	0.11
1.4-1.6	0.98	0.06	5.0-5.2	0.79	0.12
1.6-1.8	0.97	0.06	5.2-5.4	0.78	0.12
1.8-2.0	0.96	0.05	5.4-5.6	0.76	0.12
2.0-2.2	0.95	0.05	5.6-5.8	0.75	0.12
2.2-2.4	0.94	0.05	5.8-6.0	0.74	0.11
2.4-2.6	0.93	0.05	6.0-6.2	0.72	0.10
2.6-2.8	0.91	0.05	6.2-6.4	0.70	0.10
2.8-3.0	0.90	0.05	6.4-6.6	0.68	0.13
3.0-3.2	0.88	0.06	6.6-6.8	0.69	0.12
3.2-3.4	0.87	0.06	6.8-7.0	0.67	0.13
3.4-3.6	0.86	0.07	7.0-7.2	0.69	0.12
3.6-3.8	0.85	0.08	7.2-7.4	0.59	0.08

Jameson (1983) pointed out that collisions, wind shear and turbulence can induce oscillation. These conditions can cause the raindrops be longer in prolate deformation. Hence, larger oscillation amplitudes can be expected at higher rainfall rate due to the increase of raindrop collision (Beard, 1984). Figure 6.10 shows the histograms of the axis ratio for two drop diameter ranges and for several rain classes. It can be seen that the rainfall rate dependence of the axis ratio is visible for large-sized drops. The shift in the axis ratio distribution is toward the less oblate or more spherical as rainfall rate increases. Average values for the composite dataset are given in Fig. 6.11. Tokay and Beard (1996) demonstrated that collisions, wind shear and turbulence are too weak to maintain the oscillations against viscous dissipation. They suggested resonance with vortex shedding and
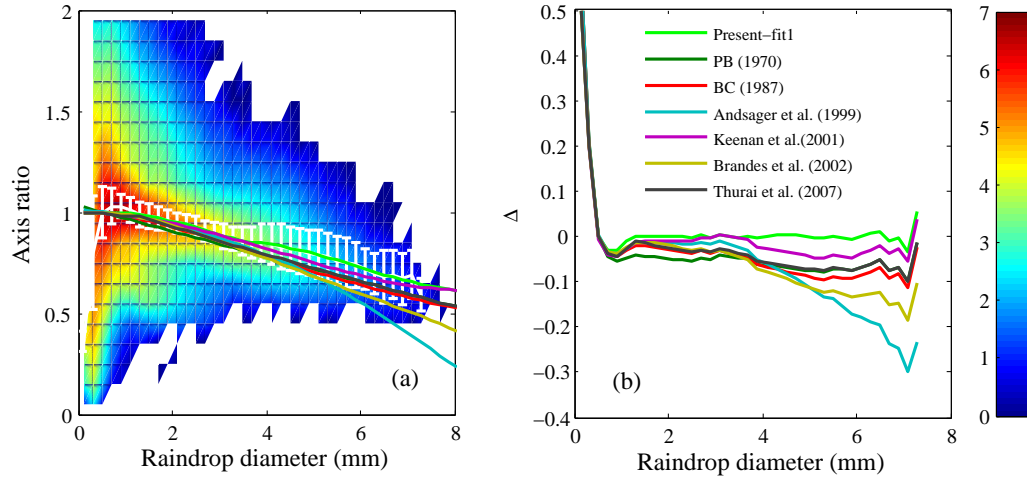
Figure 6.9: Same as Fig. 6.6 but for the axis ratio.While line with error bar denotes the average and standard deviation of the data.

change in drag force as the sources of oscillation. It is very difficult to get the quantitative information on raindrop shape because the drop shape data in the natural rain is very limited. Jones (1959) collected the axis ratio in the turbulent high shear zone of the surface layer. Although his ratio is higher than our result, the pattern of the data is slightly the same as ours.

In their calculation of equilibrium axis ratio, Beard and Chuang (1987) used the parameters which are applicable to the standard laboratory condition. Acceleration of gravity (g) decreases with altitude, since greater altitude means greater distance from the Earth's centre. KT is located about 864 m above sea level. Hence, the atmospheric condition and g at KT may be different from the standard atmosphere. However, Beard (1976) found only very slight changes in raindrop shape with changes in the atmospheric condition. Furthermore, Chandrasekar *et al.* (1988) measured the raindrop axis ratio aloft by aircraft. Their axis ratio is smaller than ours and it is close to the artificial rain data.
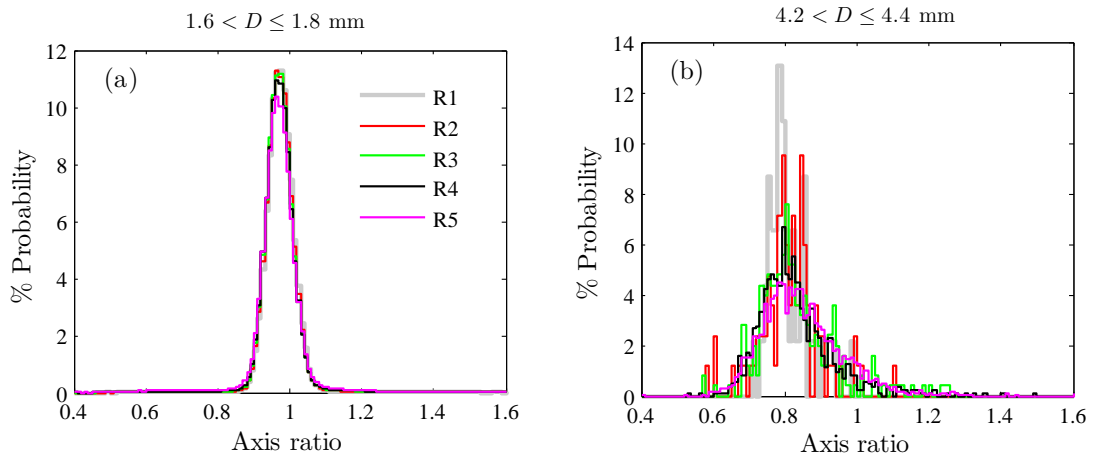
Figure 6.10: Histogram of axis ratio for several classes of rainfall rate: $2 \leq R < 5$ mm/h (R1), $5 \leq R < 10$ mm/h (R2), $10 \leq R < 20$ mm/h (R3), $20 \leq R < 40$ mm/h (R4), $R \geq 40$ mm/h (R5).
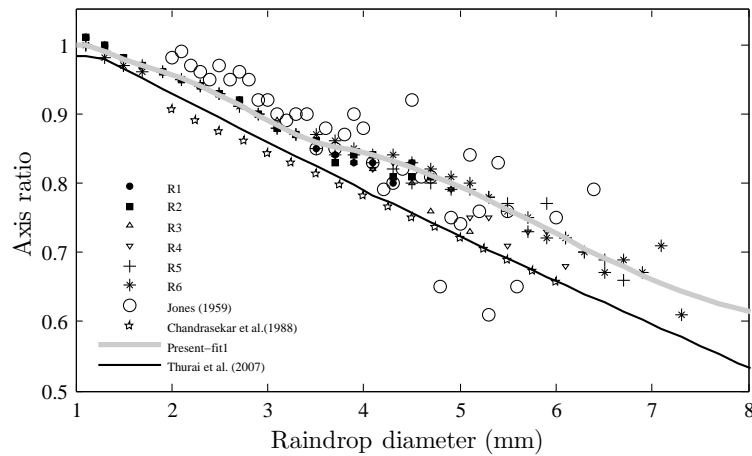
Figure 6.11: Axis ratio of raindrops as a function of drop diameter for several classes of rainfall rate: $1 \leq R < 2$ mm/h (R1), $2 \leq R < 5$ mm/h (R2), $5 \leq R < 10$ mm/h (R3), $10 \leq R < 20$ mm/h (R4), $20 \leq R < 40$ mm/h (R5), $R \geq 40$ mm/h (R6).

127

6.3.3 Natural Variations of DSD and Their Effect on $Z - R$ Relationship

A good knowledge of the DSD variability is important in hydrology, e.g. for radar quantitative precipitation estimation (QPE) and erosive process studies. Adapting the $Z - R$ relationship to different rain types, time scale (diurnal, intraseasonal, seasonal variation) may be a promising way to improve radar QPE.

6.3.3.1 Rainfall Type Variation

Table 6.2 shows mean and standard deviation of $\log_{10}(N_w)$, D_m and μ for each rain type. Convective rain is divided into three rainfall classes: $R < 10$ mm/h, $10 < R < 30$ mm/h, and $R > 30$ mm/h. The physical variability in N_w, D_m and μ are large as indicated by large standard deviation. It should be remembered that the optimal μ for KT was calculated over the range -3 to 30 with the interval of 0.1. The standard deviation of μ will be smaller than the present result if we take a smaller μ range such as from -3 to 15 as in Bringi *et al.* (2003).

Table 6.2: Mean value and standard deviation (std) of $\log_{10}(N_w)$, D_m and μ for each rain type. Each rain type is classified into several rainfall intensities.

Type	$\log_{10}(N_w)$ (std)	D_m (std)	μ (std)
S (0-10 mm/h)	3.46(0.51)	1.20(0.27)	6.48(5.28)
S (>10 mm/h)	4.38(0.33)	1.31(0.21)	5.15(3.49)
M (0-10 mm/h)	3.65(0.41)	1.16(0.25)	9.81(7.34)
M (10-30 mm/h)	4.10(0.23)	1.53(0.20)	5.07(2.34)
M (> 30 mm/h)	4.28(0.14)	1.71(0.14)	2.09(1.41)
D (0-10 mm/h)	3.65(0.57)	1.21(0.47)	9.25(7.88)
D (10-30 mm/h)	3.76(0.60)	1.95(0.72)	2.85(3.07)
D (> 30 mm/h)	4.07(0.37)	2.11(0.44)	0.39(1.42)
SH (0-10 mm/h)	3.88(0.58)	1.02(0.29)	11.93(8.58)
SH (10-30 mm/h)	4.29(0.58)	1.47(0.53)	7.07(4.96)
SH (> 30 mm/h)	4.00(0.52)	2.11(0.65)	2.03(2.92)

Some authors logically associated many small drops in the DSD spectra (large N_w values) with convective clouds and large drops in the spectra (small N_w) with stratiform mode of DSD formation, at the same rainfall rate (e.g., Tokay and Short, 1996; Waldvogel, 1974). In general, they pointed out that the overall mean raindrops are bigger during stratiform regimes than during convective ones, at the same rainfall rate. Our result is consistent with the aforementioned characteristics only at lower rain intensity ($R < 10$ mm/h) in which the stratiform rain has larger (smaller) D_m (N_w) than convective one. On the other hand, at higher rainfall rate the D_m is larger in convective rain than in stratiform one. The characteristics of D_m and N_w at KT is similar to the result reported by Testud *et al.* (2001).
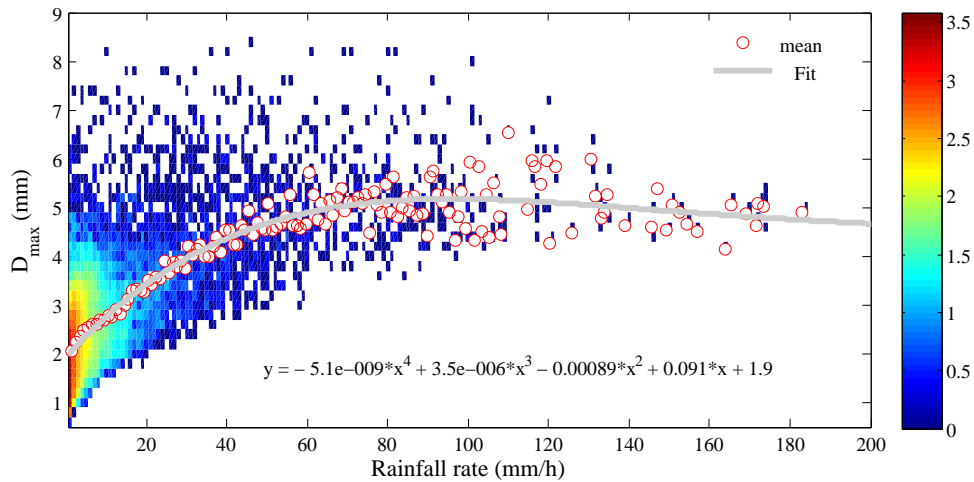
Figure 6.12: Relationship between the rainfall intensity and D_{max}. The color scale represents $\log_{10}[N(R, D_{max})]$, where $N(R, D_{max})$ is the number of data with rainfall rate (R) and maximum drop diameter (D_{max}), both within the interval of 1 mm/h and 0.1 mm, respectively. Circles and gray line denote the mean of D_{max} with increasing R and its polynomial fit, correspondingly.

From Table 6.2, the variation of DSD parameters with rainfall rate is evident. It is observed that D_m and N_w increase with increasing rainfall rate, but, on the other hand, μ decreases with increasing rainfall rate. The increase of N_w with a corresponding rise of D_m as R increases, indicates that the spectrum broadening is mostly due to an increasing number of large-sized drops that substantially

affect the rainfall rate. This result is consistent with the relationship between rainfall rate and maximum drop diameter (D_{max}) given in Fig. 6.12. However, this relationship is not linear. For $R < 30$ mm/h, D_{max} increases rapidly with increasing R. However, for $30 < R < 70$ mm/h the increase in D_{max} with R is considerably smaller. Finally, for $R > 70$ mm/h D_{max} remains remarkably constant (approximately 5 mm). At intense rainfall, the total number of drops continues to increase rather than the drop size as also found by Blanchard and Spencer (1970). This phenomenon is due to the breakup limiting the maximum drop size (e.g., List *et al.*, 1987; Willis and Tattelman, 1989). For intense rainfall rate, collision role is more dominant than that of hydrodynamic instability to cause breakup process since the drop interactions increase approximately with the square of the rainfall rate (e.g., McFarquhar and List, 1991; Srivastava, 1988).
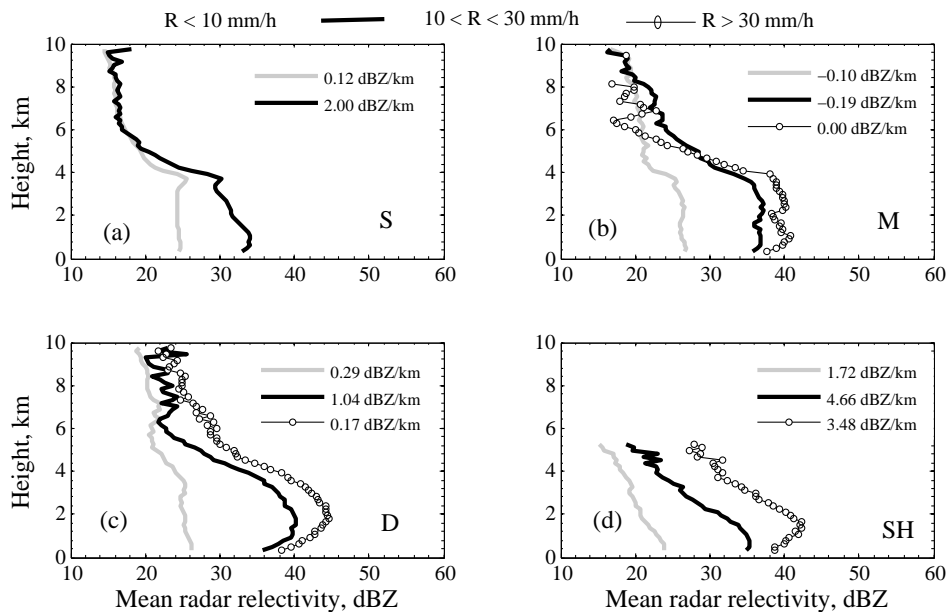
Figure 6.13: Mean vertical profile of Z for all rain type classified into three rain categories. S, M, D and SH indicate stratiform, mixed stratiform/convective, deep convective and shallow convective, respectively. The vertical profile of radar reflectivity gradient (VPRG) on the legends are the gradient calculated by using linear least square fitting of dBZ as function of height for rain column of 1.0 - 3.0 km AGL.

Large-sized drops have a disproportionate effect on reflectivity ($Z \simeq D^6$, where D is drop diameter), therefore, their evolution in rain column causes downward increasing or decreasing of radar reflectivity. Figure 6.13 shows mean vertical profiles of Z for all rain types classified into three rain categories. The vertical profile of radar reflectivity gradient (VPRG) for all profiles in the range of 1.0 - 3.0 km AGL are also given in the legend of the figures. The VPRG was calculated by using linear least square fitting of dBZ as function of height. Positive (negative) gradient indicates downward increasing (decreasing) of reflectivity. Although it is not uniform, the VPRG values during the light rain are generally smaller than for the intense rain indicating that raindrop growth in intense rainfall is heavier than that in light rain. However, at intense rainfall rate (convective rain) downward decreasing of the reflectivity starting from 2.0 km is observed, implying that no further growth of raindrop (drop breakup). Consequently, the maximum drop size of intense rainfall at the surface is relatively small as observed in Fig. 6.12.

Bringi *et al.* (2003) found that, on average, the two parameters (N_w and D_m) for stratiform rain distributions lie on a straight line with negative slope resulting from composite distrometer/radar retrievals that encompass a variety of climatic regimes from near the equator (Papua New Guinea) to the High Plains (Colorado). The two parameters vary from about 2,8 and 1.8 at Colorado to 3.95 and 1.2 at Papua New Guinea. In the present study, the average value of N_w for stratiform rain is close to those found for Papua New Guinea (the closest region to KT). For convective events, Bringi *et al.* (2003) divided their data into two distinct clusters corresponding to maritime-like and continental-like clusters. Maritime-like clusters are located around $< D_m > \propto 1.5 - 1.75$ mm and $\log_{10}(< N_w >) \propto 4 - 4.5$, varying from near the equator (Papua New Guinea) over subtropics (Florida, Brazil) to oceanic (TOGA COARE data). The continental like cluster is characterized by $< D_m > \propto 2.0 - 2.75$ mm and $\log_{10}(< N_w >) \propto 3 - 3.5$, varying from near the U. S. High plains (Colorado) over continental (Graz, Austria) to subtropics (Sydney, Australia). Bringi *et al.* (2003) used a simple scheme to separate stratiform and convective rain types based on the standard deviation of rainfall rate over 5 consecutive DSD samples. If this standard deviation is ≤ 1.5 mm/h then it is classified as stratiform, otherwise it is assumed to be convective. Another point that should be noted in their result is that they only plotted

the convective rain with $R > 5$ mm/h. Therefore, their values for convective may cover what we have classified as deep convective, shallow convective, mixed statiform/convective (transition) and stratiform. For $R > 10$ mm/h, N_w of our result is close to those found for Papua New Guinea, but our D_m is larger. Besides due to the difference in the data filtering, the difference in the DSD parameter of the convective rain found in this work from those of Bringi *et al.* (2003) may suggest the difference in the convective system at KT.
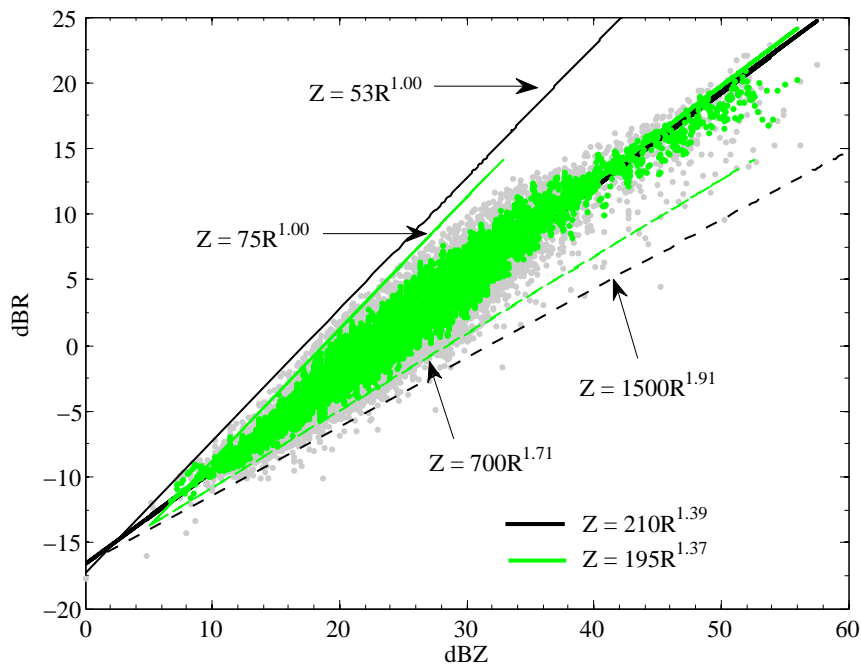
Figure 6.14: Plot of dBR vs. dBZ value for all data points and for all precipitation types at KT. Black points and lines denote the values before using the sequential intensity filtering technique (SIFT), where the green ones are those after using the SIFT method.

The DSD is often analyzed in the context of weather radar application such as the $Z - R$ relations ($Z = AR^b$). Figure 6.14 shows the plot of dBR vs. dBZ value for all data points and for all precipitation types at KT. All points are enclosed between the two relationships $Z = 53R^{1.00}$ and $Z = 1500R^{1.91}$. To minimize the effect of spurious variability of disdrometric data we applied the sequential

Table 6.3: $Z - R$ relations ($Z = AR^b$) obtained for 2006-2007 DSD dataset by considering various estimation methods for each rain type.

Types	LREG1	LREG2	NREG	PMM	RMSD
S	$Z = 229R^{1.33}$	$Z = 230R^{1.29}$	$Z = 237R^{1.24}$	$Z = 229R^{1.30}$	$Z = 233R^{1.27}$
M	$Z = 188R^{1.35}$	$Z = 189R^{1.34}$	$Z = 196R^{1.35}$	$Z = 189R^{1.34}$	$Z = 192R^{1.35}$
D	$Z = 176R^{1.48}$	$Z = 181R^{1.46}$	$Z = 268R^{1.40}$	$Z = 174R^{1.48}$	$Z = 195R^{1.47}$
SH	$Z = 137R^{1.39}$	$Z = 141R^{1.35}$	$Z = 74R^{1.77}$	$Z = 138R^{1.37}$	$Z = 157R^{1.46}$
All	$Z = 195R^{1.37}$	$Z = 199R^{1.32}$	$Z = 178R^{1.51}$	$Z = 195R^{1.35}$	$Z = 221R^{1.38}$

intensity filtering technique (SIFT) as in Lee and Zawadzki (2005)(see Chapter 3). We average groups of 5 DSDs samples of sequential intensity taken within the same rain type. The method of sorting and averaging based on two parameters (SATP) proposed by Cao *et al.* (2008) is not possible for this work because the number of dataset is small. It is clear that the uncertainty is greatly reduced by SIFT and all points are enclosed between the two relationship $Z = 75R^{1.00}$ and $Z = 700R^{1.71}$ after the filtering process. Scatterplots of $Z - R$, for any given storm, may exhibit significant variability that is caused by the variability of the raindrop size distribution during the storm. Moreover, event by event variability of $Z - R$ relation may be also significant and it will be discussed in the next sections.

Variations in A and b of the $Z - R$ relation reflect the real physical difference between the types of rainfall to which the $Z - R$ relations apply. However, the $Z - R$ relations are also dependent on the regression line and on the choice of independent variable. We examined several methodologies to generate the $Z - R$ relations from the KT DSD. First and second, the linear regression on log-transformed values, for a regression R over Z (LREG1) and for a regression of Z over R (LREG2) are used. Since R is the estimated variable from the measured value (Z), the relation is actually derived in reverse order ($R - Z$). The values displayed in Fig. 6.14 are obtained by LREG1. As the third method, we utilized a non-linear regression of Z over R, termed as NREG. In the fourth method, the parameters of $Z - R$ are varied until the root mean square difference (RMSD)

between instantaneous pairs of Z and R become minimum (Steiner and Smith, 2004). In addition to the aforementioned methods, we utilized the probability matching method (PMM) where the $Z - R$ relation is derived by matching the probability density functions of Z and R (Rosenfeld *et al.*, 1993). Since the PMM does not yield the coefficients of $Z - R$ (A, b), we used the linear least squares fit on the matched pairs to retrieve A and b.
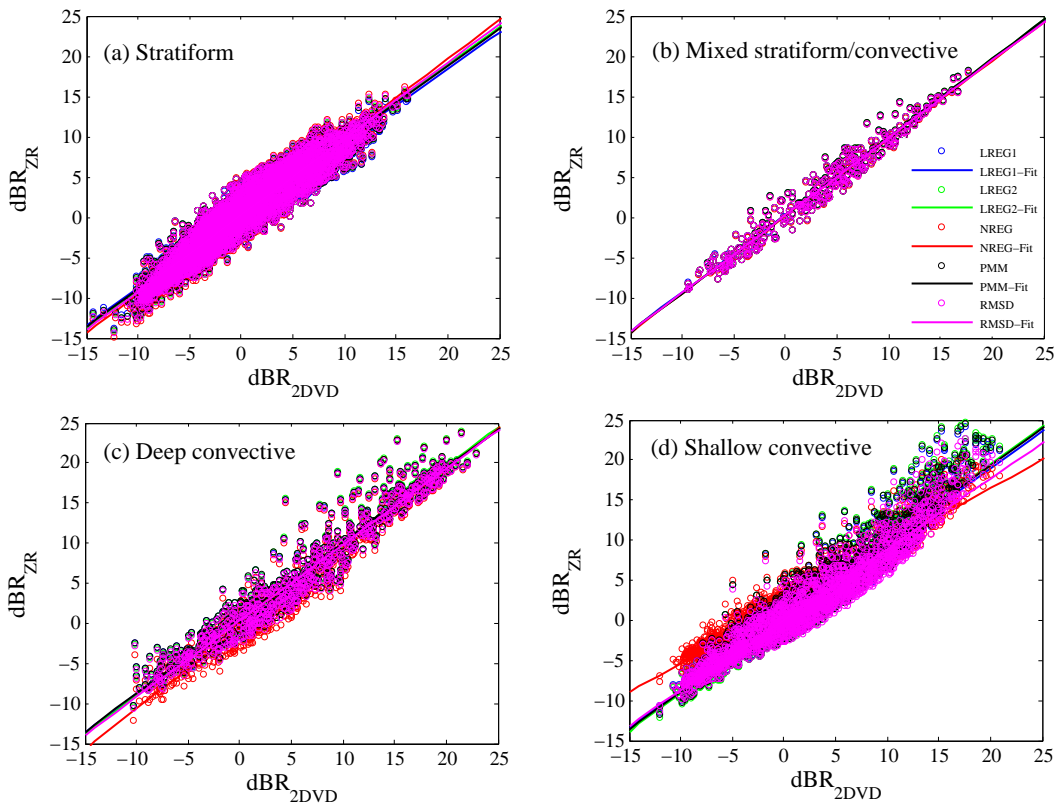
Figure 6.15: Influence of the $Z - R$ relations estimation on the estimation of the rainfall rate (R). The dBR$_{2DVD}$ and dBR$_{ZR}$ are R calculated directly from the DSD spectra and that converted from Z defined by the DSD spectra using the $Z - R$ relations, respectively.

Table 6.3 shows the $Z - R$ relations from the various method for all rain types at KT. Tokay and Short (1996) show higher reflectivities in stratiform rain ($Z = 367R^{1.30}$) as compared with that in convective rain ($Z = 139R^{1.43}$), for a given rain rate. Our results also show the same characteristics of the $Z - R$ relations as

in Tokay and Short (1996). These variations indicate that different microphysical processes are involved from one type to another rain type. Thus, usage of a single $Z - R$ relation such as the MP model ($Z = 200R^{1.6}$) to convert Z into R will underestimate in one type and over estimate in the other types. This rain type dependence of $Z - R$ may be influenced by other variabilities of DSD such as diurnal, seasonal, intraseasonal, event by event variability that will be discussed in the next sections.

All methods result in biased rain estimates. It is important to examine the consistency of the $Z - R$ relations in terms of rainfall estimation. We define the reflectivity from each DSD spectrum and then we convert the reflectivity into the rainfall rate using the $Z - R$ relations in Table 6.3. Figure 6.15 shows the results of the sensitivity test concerning the influence of the $Z - R$ relations estimation on the estimation of the rainfall rate. It can be seen that the performance of LREG1, LREG2, PMM and RMSD are not significantly different for all rain types (after SIFT correction). However, the PMM should be used only for sufficiently large data volume to assure that the probability density functions are appropriate (Ulbrich and Atlas, 2002). In the next sections we will only apply LREG1 to calculate the $Z - R$ relations.

6.3.3.2 Diurnal Variation

In this section, we re–visit the diurnal variation of DSD at KT with a better rain classification. Regional variation of the diurnal rainfall cycle over Sumatra Island observed by the Tropical Rainfall Measuring Mission (TRMM)-Precipitation Radar (PR) showed a rainfall peak which migrates from the coastline toward the inland region of Sumatra Island (KT) during 12:00-24:00 local time (LT). On the other hand, during 00:00-12:00 LT the rainfall peak migrates from the southwestern coastline toward an offshore region of the Indian Ocean (Mori *et al.*, 2004). Kozu *et al.* (2006) stratified the data into four categories with 6-hour interval: 00-06, 06-12, 12-18, and 18-24. Based on the above finding, the data during 06-12 may be leakage of 00-06. Therefore, we only divided the data over 12-hour interval; 00:00-11:58 (hereafter morning) and 12:00-23:58 (hereafter evening).
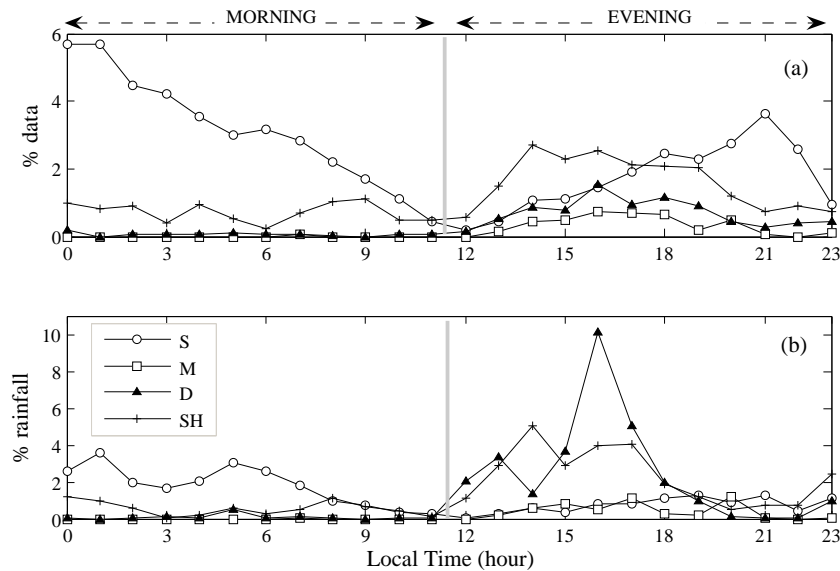
Figure 6.16: Diurnal variation of the rainfall at KT. The percentage expressed in the figures are relative to the total number of profiles (7590) and the rainfall (1,033 mm).

Figure 6.16 shows the diurnal variation of the rainfall at KT. The percentages expressed in the figures are relative to the total number of profiles (7590) and the rainfall (1,033 mm). From the whole dataset, 71% of the total rainfall are in the evening hours that comes from 52% of the profiles. The distribution of each rain type in the evening hours as calculated in % rainfall (% profile) are 28% (35%) for stratiform, 99.6% (98%) for mixed stratiform/convective, 97% (92%) for deep convective and 80% (69%) for shallow convective, respectively. The percentages of rainfall and profiles shown above are relative to the total number of profiles and the rainfall for each rain type. More than 80% of the total rainfall or 60% of the total profiles in evening hours are composed of convective rain, whereas about 73% of the total rainfall or 80% of the total profile in the morning hours are composed of stratiform rain. The main peak of convective data appears around 14:00-17:00 LT with the main peak of deep convective rainfall observed at 16:00 LT. Stratiform rain shows bimodal variation with the main peak around 00:00-01:00 LT and a subpeak at 21:00 LT. In general our result is consistent with the

Table 6.4: Mean value of $\log_{10}(N_w)$, D_m and μ and $Z - R$ relations for each rain type on a diurnal basis. M and E denote morning and evening, respectively and xxxx denotes that the number of the data is small. I and II are representative for $R < 10$ mm/h and $R > 10$ mm/h, respectively.

Types	N_w		D_m		μ		$Z - R$	
	M	E	M	E	M	E	M	E
S-I	3.52	3.33	1.17	1.23	6.30	6.80	$Z = 216R^{1.32}$	$Z = 257R^{1.36}$
S-II	4.39	4.34	1.30	1.34	4.67	6.65		
M-I	3.76	3.65	0.99	1.16	12.86	9.74	xxx	$Z = 189R^{1.35}$
M-II	xxxx	4.13	xxxx	1.57	xxxx	4.52		
D-I	4.02	3.61	1.01	1.23	11.89	8.92	$Z = 140R^{1.30}$	$Z = 183R^{1.48}$
D-II	4.22	3.93	1.59	2.06	5.50	1.27		
SH-I	3.90	3.87	0.98	1.05	10.98	12.41	$Z = 137R^{1.29}$	$Z = 137R^{1.42}$
SH-II	4.40	4.18	1.42	1.67	7.81	5.40		

diurnal rainfall variation in Renggono *et al.* (2001) and Mori *et al.* (2004), but the percentage of occurrence of stratiform rain for the morning hours in our result is larger than theirs.

Table 6.4 shows the average DSD parameters and $Z - R$ relations on a diurnal basis. It is clearly observed that there is a difference in the DSD parameters between morning (M) and the evening (E). The mean D_m values in the evening are larger than their counterparts in the morning hours, whereas the mean N_w values in the evening are smaller than those in the morning hours. Moreover, mean μ values in the evening hours are also smaller than those in the morning hours, especially for convective rain. Therefore, the DSDs in the morning hours are narrower than those in the evening hours. Furthermore, the DSDs in the morning hours may be composed of more small drops and drop concentration, fewer large drops than the evening ones. Our result is consistent with the results of Kozu *et al.* (2006).

The differences in the DSD between convective and stratiform are probably the best recognized and documented today, particularly in the context of tropical

rainfall. However, the diurnal variation of DSD has also important implications on rainfall estimation with radar. Diurnal variation of DSD will lead to diurnal variation of $Z - R$ relations. The DSD-based Z-Rs calculated so far (Tables 6.4 and 6.3) were compiled in Fig. 6.17. According to the figure, the same Z translates to R greater in morning compared to evening rainfall. Thus, usage of a single $Z - R$ relations to convert Z into R will underestimate in one time and overestimate in the other times.
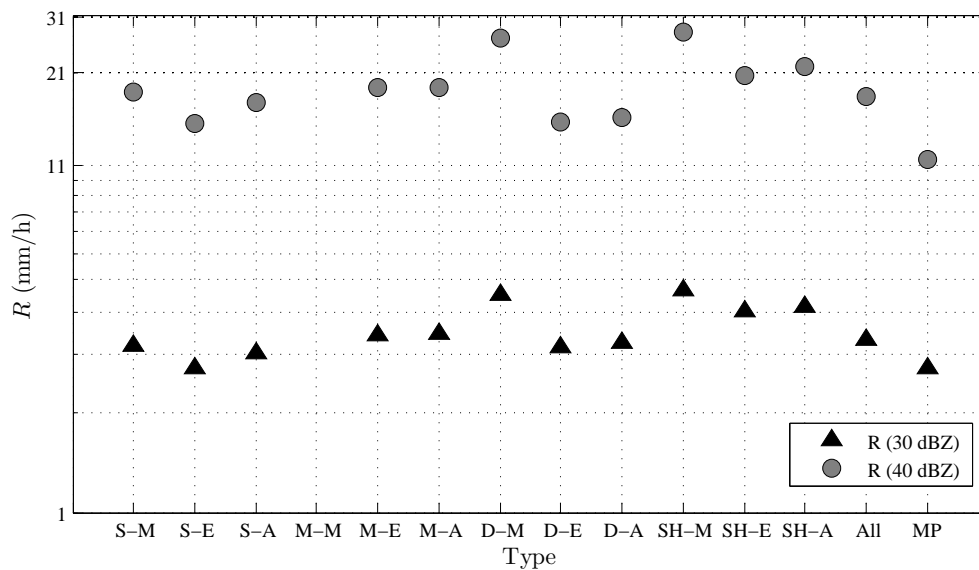
Figure 6.17: Rain intensities for 30 and 40 dBZ. The $Z - R$ relations used in this figure, labeled in Type-time (morning "M" or evening "E") and labeled in Type-A (A indicates all, without diurnal scheme) are from Tables 6.4 and 6.3, respectively. MP denotes MP model ($Z = 200R^{1.6}$).

The difference in the DSD from morning to evening may reflect the difference in the DSD formation and evolution during these periods. For stratiform rain, the variation of the strength of bright band (ΔZ) and the height of melting level may cause some difference in the DSD at the surface. The value of ΔZ is defined as ratio between the maximum reflectivity in the BB and its minimum in a layer just below the melting layer (Huggel *et al.*, 1996). Raindrop spectra with many small drops are associated with small ΔZ, whereas raindrop spectra

with few small drops and many large drops are associated with large ΔZ (well defined bright band). Furthermore, the possibility of the raindrop spectra to be modified through coalescence, breakup and evaporation increase as the height of melting layer increases. However, we found that the height of melting layer of morning event is the same as that of evening event, but the strength of bright band during evening event is larger than during morning one (Fig. 6.18a). Diurnal variation of the surface meteorological parameters such as temperature and relative humidity may also influence the DSD. High temperatures in the evening hours (12:00-23:00 LT) particularly in the daytime (12:00-18:00 LT) may cause evaporation of raindrops particularly for small-sized drops. Mean vertical profile of Z of convective rain is larger in evening than in morning event, indicating more large-sized drops and more intense convective. Intense convective activity during the evening may be associated with strong updrafts. Strong updrafts modify the drops through the drop sorting and enhancing the collision-coalescence process. Both of these processes will increase D_m, the former by not allowing the smaller drops to fall and the another by consuming the smaller drops for the growth of medium drops. Mori *et al.* (2004) found that the precipitating cloud over the inland region of Sumatra Island (KT) in the afternoon are composed of isolated convective clouds which are accompanied by a smaller component of stratiform. Their result is consistent with our convective/stratiform ratio previously mentioned. However, more research needs to be done in the future, particularly on the anatomy of isolated convective system over KT.

6.3.3.3 Seasonal Variation

KT is located in the Asian monsoon climate region. Moreover, Sumatra Island faces the Indian Ocean so that this region will receive more rainfall during the southwesterly monsoon (Mori *et al.*, 2004). The difference in the vector winds between southwest (SW) monsoon and northeast (NE) monsoon at KT is not as clear as in Gadanki, India (Okamoto *et al.*, 2003). Figure 6.19 shows the time series of wind velocity for the two years observation. Positive (negative) of meridional wind indicates the wind blowing from south (north) whereas positive (negative) of zonal wind indicates the wind blowing from west (east), hereafter
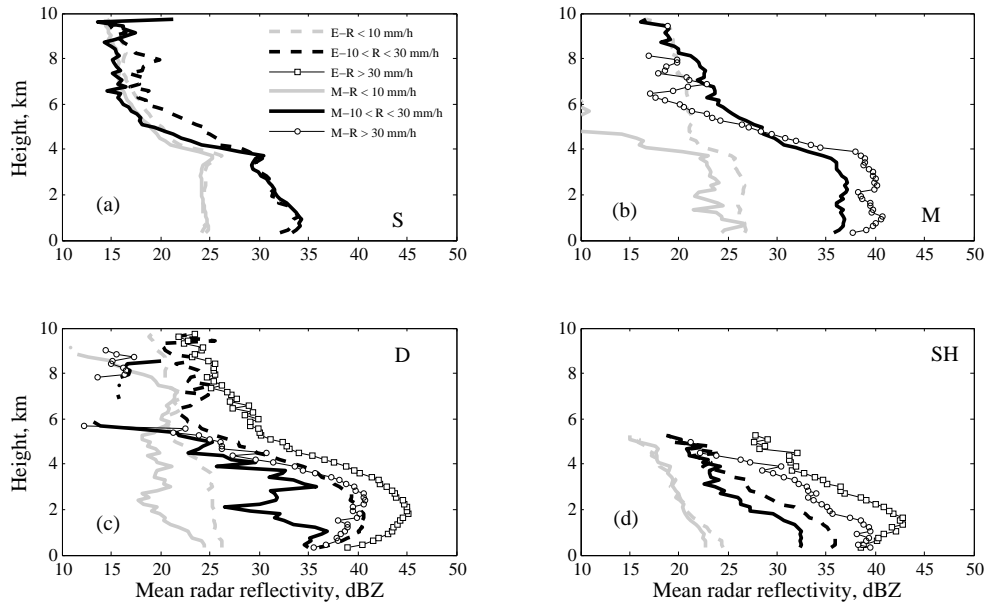
Figure 6.18: Same as in Fig. 6.13 but on a diurnal basis. Capital M and E of the legends indicate morning and evening, respectively.

called westerly (easterly). We can see a shift in direction of zonal wind from westerly to easterly in September. However, we can not see significant change of direction of the meridional wind. Therefore, the shift in wind direction from northeasterly to southwesterly as indication of NE and SW monsoon is not significantly observed at KT as previously found by Okamoto *et al.* (2003).

To describe the seasonal variability of DSD, we used the same season classification as in Kozu *et al.* (2006) in which a year divided into pre-SW (April-May), SW (June-September), pre-NE (October-November) and NE (December-March) monsoon, respectively. However, in this work the data amount of simultaneous observation by 2DVD and wind profiler during pre-NE is very small. Therefore, we will only show the result for 3 other seasons. Figure 6.20 shows the diurnal variation of the precipitation occurrence for the three seasons. In general, there is no significant difference in the diurnal variation pattern for each season in which convective is dominant during the evening and stratiform rain is dominant during the morning hours.

Figure 6.21 shows the plot of N_w vs. D_m for all rain types in diurnal and
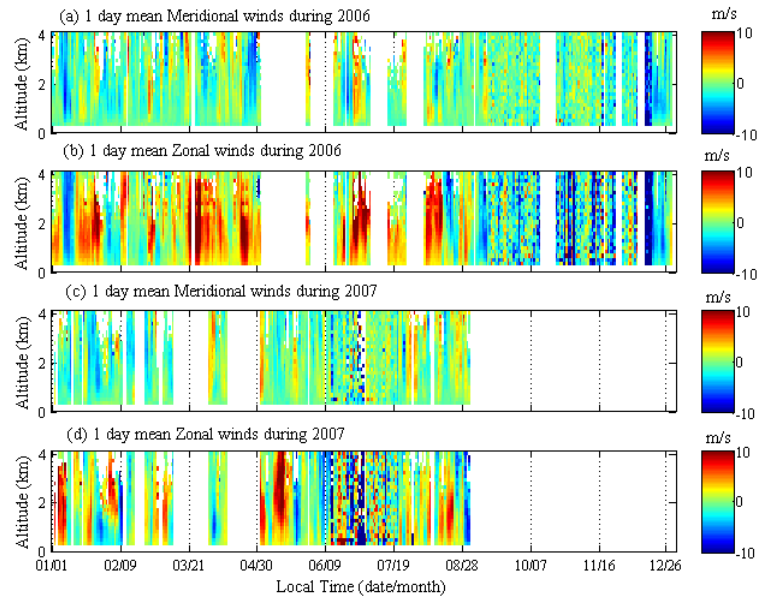
Figure 6.19: 1 day mean horizontal winds observed by 1.3 GHz wind profiler from 2006 to 2007.
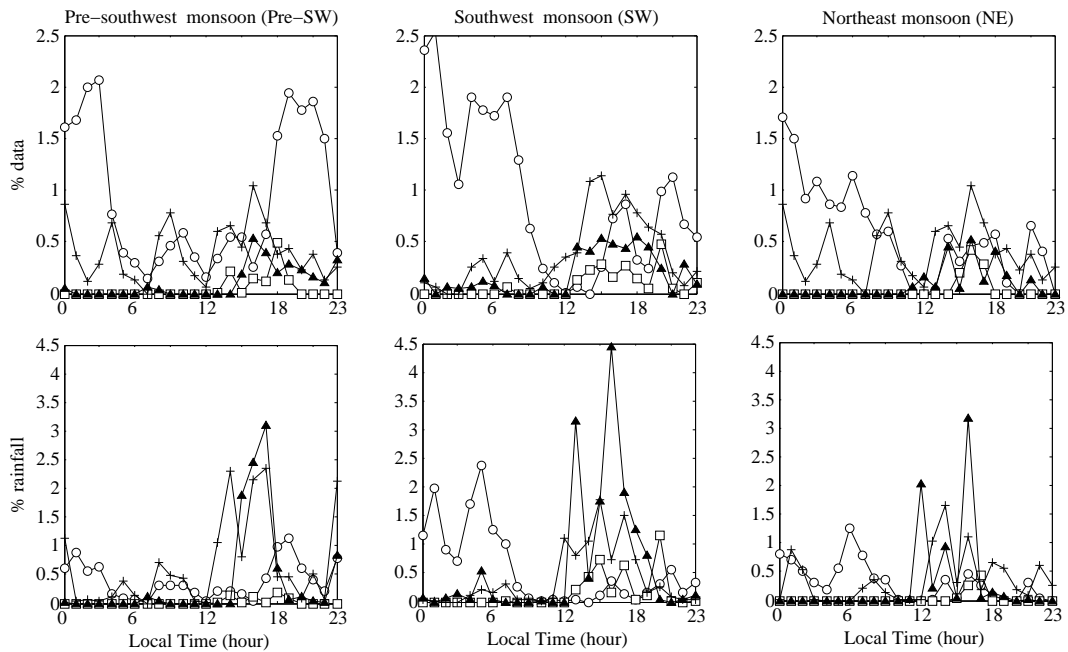
Figure 6.20: Same as Fig. 6.16 but divided into seasonal basis.

seasonal basis. Furthermore, the $Z - R$ relations are given in Table 6.5. We can see some difference in D_m between SW and NE monsoon. However, it is not significant and not uniform. It is slightly apparent from the figure that D_m (N_w) is larger (smaller) in the NE monsoon than in the SW monsoon. The same features are also found by Kozu *et al.* (2006). On the other hand, Rao *et al.* (2009) found that D_m values is larger in the SW monsoon than in the NE monsoon. They pointed out that the DSDs in the SW and NE monsoons are continental and oceanic in nature, respectively. However, there is no clearly separated segment between the SW and NE monsoons that indicate maritime-like and continental-like clusters in Fig. 6.21. On the other hand, relatively large values of D_m ($>$ 2 mm) which is categorized as continental like cluster in Bringi *et al.* (2003) are found in the NE monsoon.
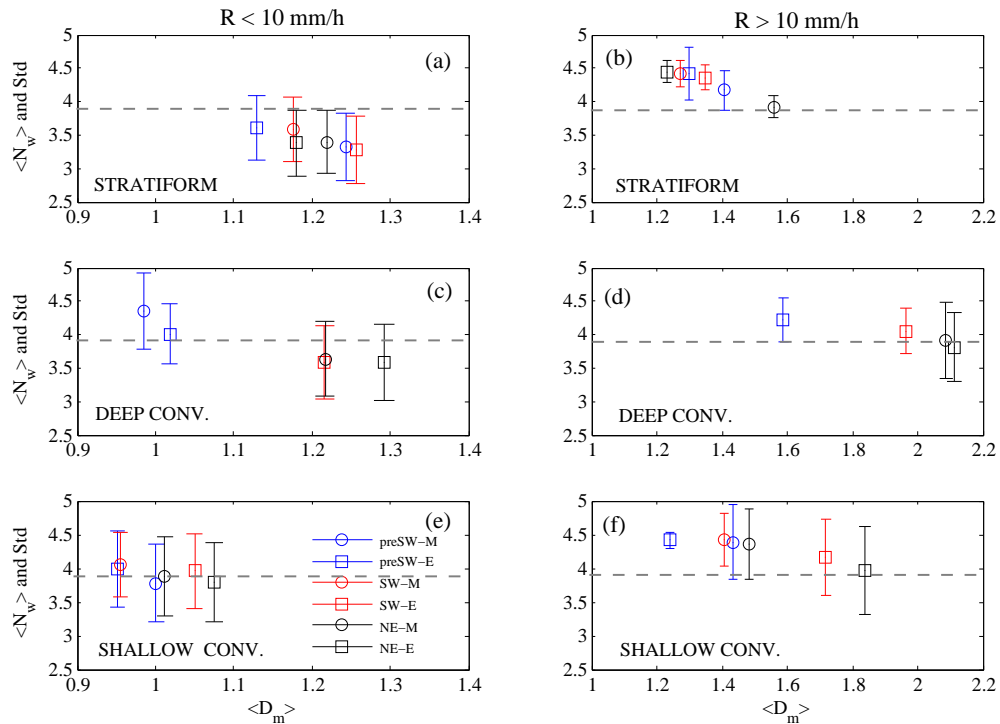
Figure 6.21: Average value of $\log_{10} N_w$ (with $\pm 1\sigma$ standard deviation) vs average D_m on diurnal and seasonal basis. Dashed line is the Marshall-Palmer value ($\log_{10} N_w = 3.9$).

Kozu *et al.* (2006) argued that the lack of seasonal variation of DSD at KT in comparison with Gadanki, India was probably due to the local convective and the effect of complex topography of Sumatra Island. The significant mountain range along Sumatra with an average height of 2 km plays an important role on the convective cycle over this region (Mori *et al.*, 2004). Rosenfeld and Ulbrich (2003) pointed out that the orographic convection is characterized by small D_0 or D_m (<1 mm) even in heavy rain. Of all convective data, 206 spectra have rainfall rates more than 10 mm/h. However, of these 206 spectra there is no spectrum with $D_m < 1$ mm. Moreover, 314 spectra of shallow convective have rainfall rates more than 10 mm/h and only 40 spectra of the total number have $D_m < 1$ mm. Although the value of D_m does not follow the characteristics of warm orographic precipitation summarized by Rosenfeld and Ulbrich (2003), it is still difficult to conclude the effect of orographic on the KT DSD. Some results cited in Rosenfeld and Ulbrich (2003) such as those of Fujiwara and Yanase (1971) for Mount Fuji, at height of 1300 m and that of Stout and Mueller (1968) have D_m $\propto 1.0 - 2.0$ mm which is commonly found in our result. In very special cases, i.e, during the passage of SCC over Sumatra Island, the effect of orographic may be more obvious (see Section 6.3.3.5). Another feature to be considered is that the

Table 6.5: As in Table 6.4, except on a seasonal basis.

Season	Type	Morning (M)		Evening (E)	
		Profile	$Z - R$	Profile	$Z - R$
Pre-SW	S	811	$Z = 260R^{1.42}$	865	$Z = 268R^{1.32}$
	D	12	xxxx	182	$Z = 186R^{1.44}$
	SH	338	$Z = 150R^{1.28}$	403	$Z = 125R^{1.46}$
SW	S	1295	$Z = 200R^{1.29}$	440	$Z = 249R^{1.48}$
	D	45	$Z = 133R^{1.39}$	295	$Z = 175R^{1.48}$
	SH	139	$Z = 127R^{1.24}$	546	$Z = 134R^{1.36}$
NE	S	780	$Z = 211R^{1.31}$	272	$Z = 241R^{1.27}$
	D	5	xxxx	157	$Z = 195R^{1.50}$
	SH	180	$Z = 123R^{1.33}$	523	$Z = 148R^{1.45}$

value of D_m at KT is located in the intermediate region (between maritime and continental -like cluster). Therefore, it is worthwhile in the future to classify the microstructure of rain clouds over distrometer sites into continental, intermediate and maritime as well as orographic type. This study can be done by using the VIRS (Visible and Infrared Sensor) onboard the TRMM satellite. The DSDs from the continental and maritime classes will be able to clarify some result of our present achievement.
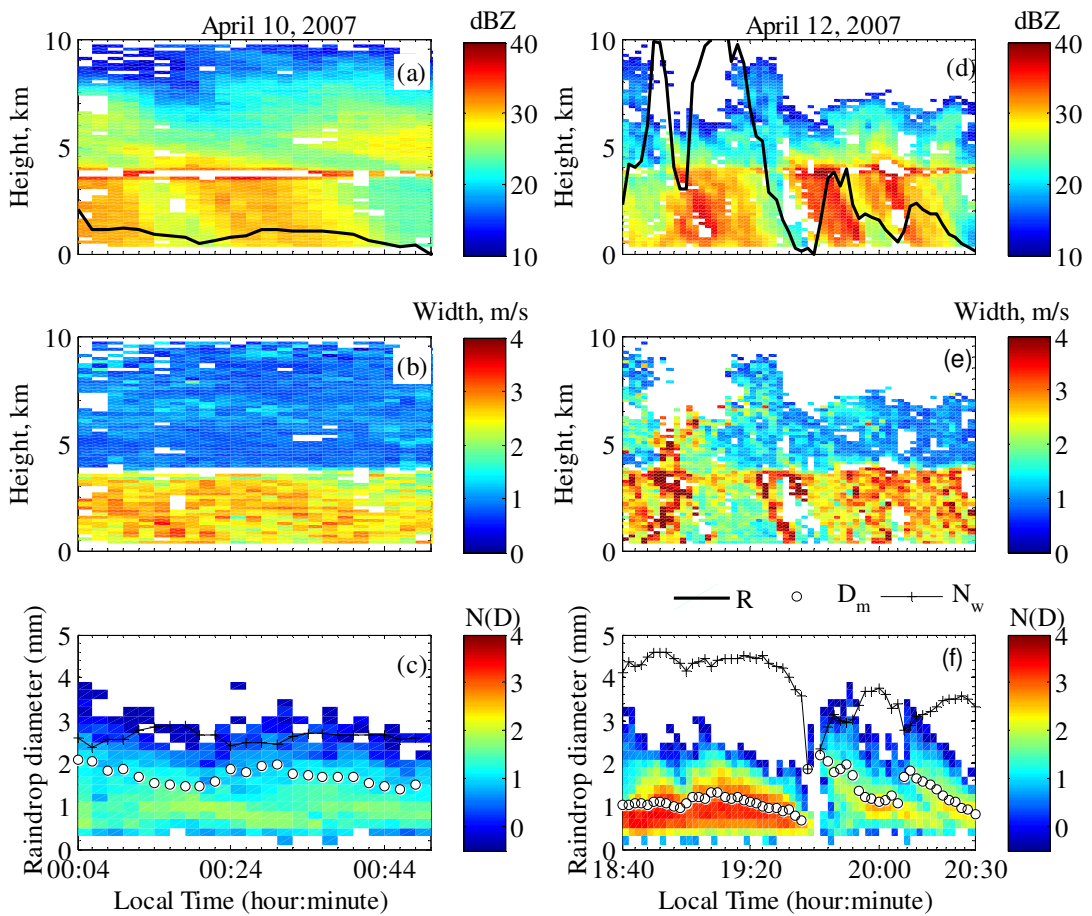
Figure 6.22: Contour plots for temporal variation of dBZ, spectral width and drop size distribution [N(D)] during stratiform rain on April 10 (left) and 12, 2007 (right). N_w is in $\log_{10}$ scale.

6.3.3.4 Event by Event Variation

We have discussed large temporal scale variation of DSD at KT. However, it is also possible for the DSD to be varied from event to event or intra-event. In this section, we explore the variation of DSD parameters for several case studies of stratiform, deep convective and shallow convective. The rain events with large value of D_m are selected.

a) Stratiform

Of 4412 spectra of stratiform, we found the maximum D_m value about 2.0 mm. Stratiform rain events on April 10 and 12, 2007 are selected where the value of D_m of these events are larger than 2.0 mm. The temporal variation of dBZ, spectral width and drop size distribution [N(D)] for these rain events are shown in Fig. 6.22. On April 10, the bright band (BB) are clearly visible. Although it is difficult to calculate the DVG accurately because of missing data at BB level, we found some DVG values of 13 m/s/km at the core of the BB. Hence, the BB of this event is very well developed as also observed from the turbulence activity above the melting layer (Fig. 6.22b). The maximum rainfall rate on April 10 is 2 mm/h. The maximum D_m during this event is 2.08 mm with average (standard deviation) being 1.68 mm (0.21 mm). The maximum value of N_w is 2.90 which is observed at $D_m = 1.45$ mm and the minimum value of N_w is 2.36 which observed at $D_m = 2.05$ mm. The average and standard deviation of μ during this event is 3.61 and 1.82, respectively. The $Z - R$ relation for this event is $Z = 656R^{1.69}$.

On April 12, the BB is not clearly visible during the leading edge of the events. At around 18:48 LT relatively high MSW are observed above the melting layer. This relatively strong MSW is observed until 19:04 LT. Thereafter, clear weak BB are observed until 19:36 LT. Rain event of the aforementioned duration is still categorized as stratiform because strong MSW occurs between stratiform events not between convective and stratiform events. Transition (mixed stratiform/convective) rain should have occurred between convective and stratiform rain. After a weak BB phase, two strong BBs are observed at 19:42-19:48 LT and 20:08-20:16 LT. We found the DVG value of 14 m/s/km at the core of the BB for

these two periods. The maximum rainfall rate on April 12 is 12.8 mm/h observed during weak BB. The maximum D_m during weak BB is 1.31 mm with average (standard deviation) being 1.06 mm (0.14 mm). The maximum value of N_w is 4.59 which is observed at $D_m = 1.11$ mm (18:52 LT). The average and standard deviation of μ during weak BB is 6.32 and 4.81, respectively. During 19:38-20:30 LT we observed two strong BBs as mentioned above. The maximum D_m during the first strong BB (19:42-19:48 LT) is 2.18 mm with average (standard deviation) being 1.97 mm (0.18 mm). The maximum value of N_w is 3.14 which is observed at $D_m = 1.80$ mm (19:46 LT). The average and standard deviation of μ during weak BB is 7.10 and 3.42, respectively. Furthermore, the maximum D_m during the second strong BB (20:08-20:16 LT) is 1.83 mm with average (standard deviation) being 1.65 mm (0.12 mm). The maximum value of N_w is 3.2 which is observed at $D_m = 1.50$ mm (20:16 LT). For the entire event from 19:38 to 20:30 LT, the maximum value of N_w is 3.75 which is observed at $D_m = 1.11$ mm (20:00 LT). The $Z - R$ relation for whole data during 18:40-20:30 LT is $Z = 205R^{1.21}$. While the $Z - R$ relation for the data from 18:40-19:36 LT is $Z = 136R^{1.26}$ and that for the data during 19:38-20:30 LT is $Z = 290R^{1.80}$.

Hence, the larger D_m on these two events are found to be associated with strong BB, whereas smaller D_m is associated with weak BB. This features is the same as in Huggel *et al.* (1996). Strong BB reflects melting of larger, low-density and dry snowflakes into rain, which leads to larger D_m and smaller N_w. On the other hand, weak BB reflects melting of tiny, compact graupel or rimed snow particles that leads to smaller D_m and larger N_w.

b) Deep and Shallow convective

Deep convective rain events on February 13 and May 27, 2007 are selected because their D_m values are larger than 5.0 mm. Figure 6.23 is the same as in Fig. 6.22, but for deep convective. On February 13, the convective system is a little bit shallow, however, it is still deep convective based on our rain classification scheme. Very intense convective is observed at the leading edge of the convective system. The maximum rainfall rate on February 13 is 23.7 mm/h. The maximum D_m value during this event is 5.16 mm and its N_w is 1.52. Very large and small

value of D_m and N_w, respectively, occurred at the very start of the convective system. Relatively large D_m (> 3 mm) is still observed until few minutes after the maximum value (14:00-14:08 LT). During this period, the value of $N_w < 2.74$ and the value of $\mu \propto$ -0.2-(-1.1). Thereafter, N_W and D_m remain constant or decrease as rainfall rate decreases. The $Z - R$ relation for this event is $Z = 144R^{2.03}$.
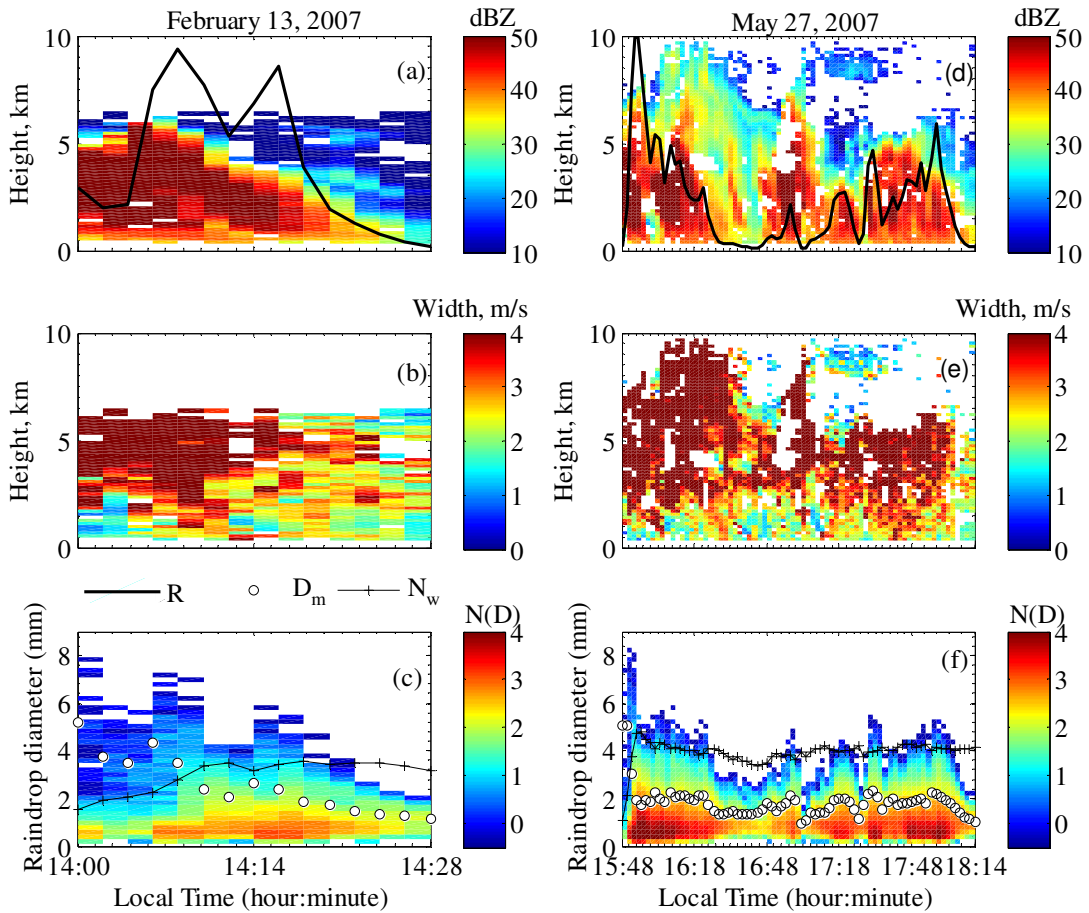
Figure 6.23: Same as in Fig. 6.22, but for deep convective rain. R (black line) in (a) and (d) is divided by 3 and 15, respectively.

On May 27, the duration of convective rain is longer. The turbulence is observed for the entire event. The maximum rainfall rate is 193.96 mm/h at 15:54 LT. The maximum D_m during this event is 5.06 mm and its N_w is 2.15. The second largest value of D_m and its N_w is 5.05 mm and 1.08 which is observed

at 15:48 LT. Hence, very large and small values of D_m and N_w, respectively, again occurred at the very start of the convective system. Relatively large D_m (> 3 mm) is still observed for few minutes (15:48-15:52 LT). During this period, the value of $\mu \propto$ -1.2-(-1.8). After this period, N_w and D_m remain constant or decrease as rainfall rate decreases. The DSD parameters of the largest rainfall rate (193.96 mm/h) are 4.71 for N_w, 1.95 mm for D_m and -0.9 for μ. The $Z - R$ relation for this event is $Z = 161R^{1.49}$.
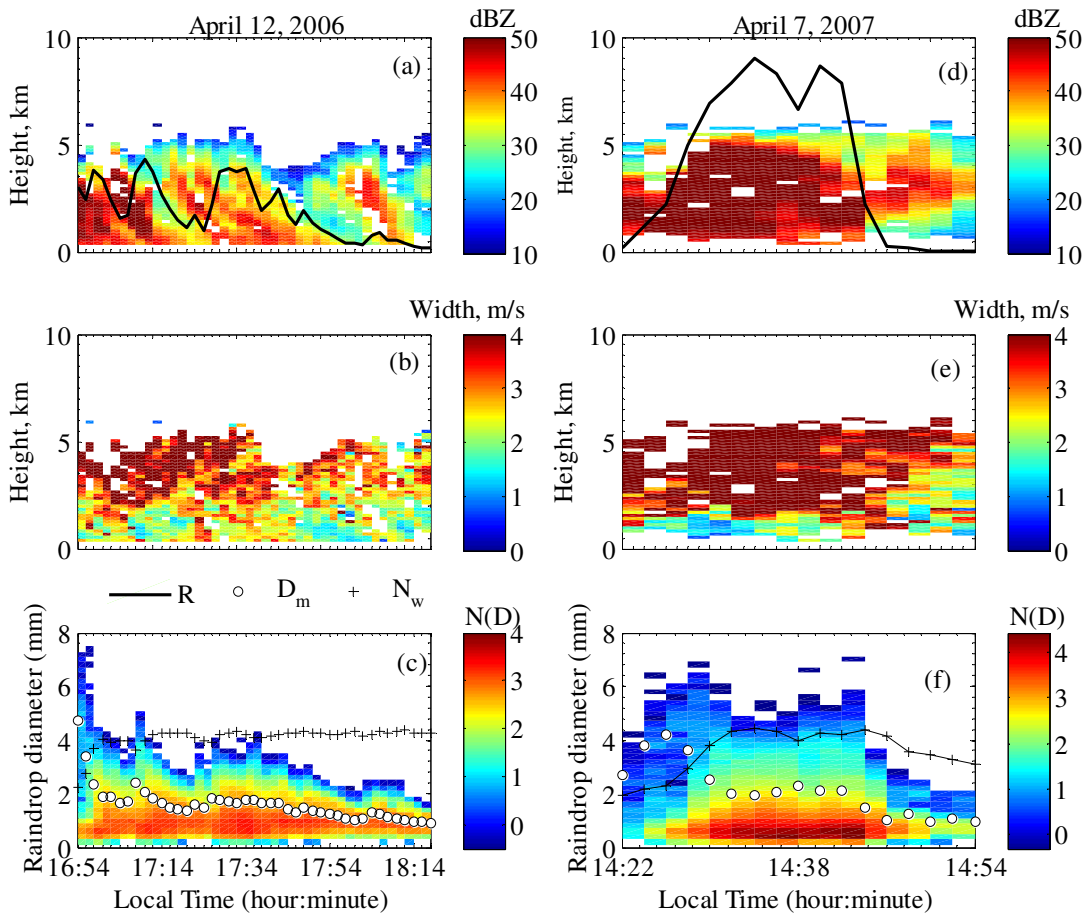
Figure 6.24: Same as in Fig. 6.22, but for shallow convective rain. R in (a) and (d) are divided by 11.

Of all spectra of shallow convective rain, we also found some spectra containing very large-sized drop ($D_m > 4$ mm) such as on April 12, 2006 and April 7, 2007.

Figure 6.24 is the same as in Fig. 6.22, but for shallow convective. On April 12, the maximum rainfall rate is 48.4 mm/h at 17:10 LT. The maximum D_m during this event is 4.72 mm and its N_w is 2.24. The very large and small value of D_m and N_w, respectively, again occurred at the very start of the convective system. Relatively large D_m (= 3.4 mm) and small N_w (2.73) is still observed at 16:56 LT. The values μ for these two spectra are -0.2 and -1, respectively. After a large value of D_m, N_w and D_m remain constant or decrease as rainfall rate decreases. The average (standard deviation) value of N_w and D_m during 16:58-18:18 LT are 4.16 (0.17) and 1.50 mm (0.36 mm). The $Z - R$ relation for this event is $Z = 54R^{1.77}$.
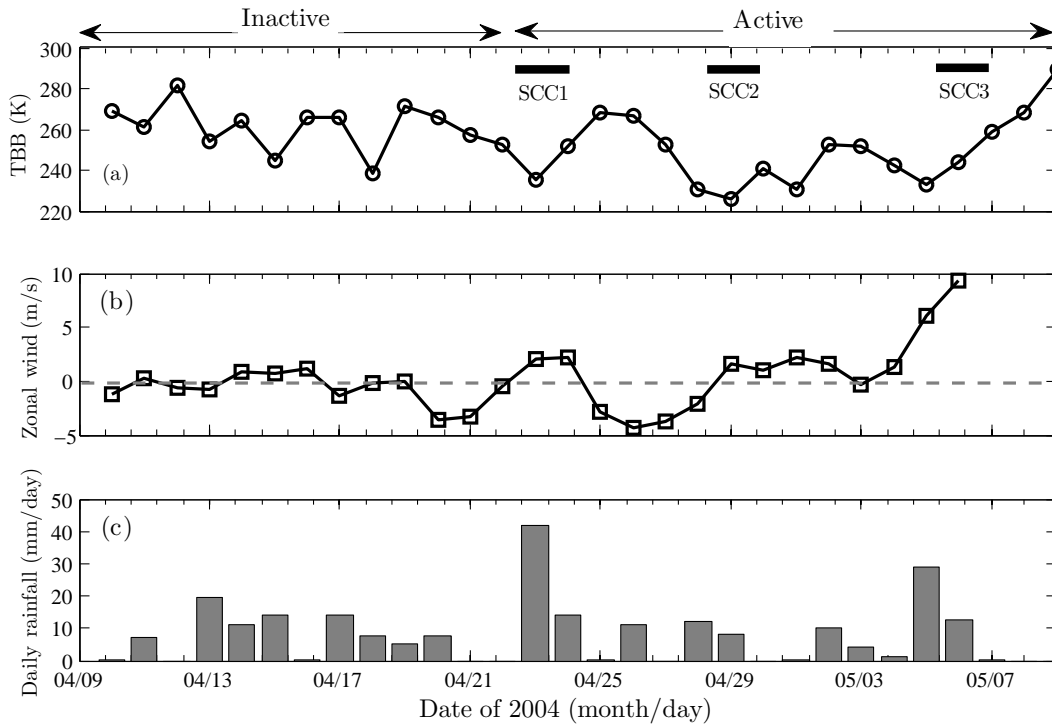
Figure 6.25: Time plot of the TBB along 0.20ºS latitude of radar site with spatial and time resolutions of 1º longitude x 1º latitude and one day, respectively (a), mean low level zonal wind (1-2 km)(b) and surface instrument (MAWS)-based daily rainfall information (c), during April 10 to May 9, 2004 (CPEA-I) at KT.

On April 7, the convective system is more intense than that of April 12. The

maximum rainfall rate is 101.4 mm/h at 14:34 LT. The maximum D_m during this event is 4.20 mm and its N_w is 2.28. The second largest value of D_m and its N_w is 3.80 mm and 2.18, respectively, which is observed at 14:24 LT. Hence, very large and small values of D_m and N_w, respectively, again occurred at the very start of the convective system. The DSD parameters of the largest rainfall rate (101.4 mm/h) are 4.41 for N_w, 2.0 mm for D_m and -0.3 for μ. The $Z - R$ relation for this event is $Z = 382R^{1.38}$.

From the above convective case studies, it can be seen that very low N_w and very large D_m for KT occurred mainly at the very start, as expected from long experience, as a result of a relatively large sample of big drops. Therefore, at the start of a storm a given rain rate is matched to a much higher reflectivity. Therefore, besides long time scale variation of DSD (e.g., diurnal variation), a distinct difference in the $Z - R$ relations between the start of convective and the trailing regions also needs to be considered.

6.3.3.5 Intraseasonal Variation

Marzuki (2005) has studied the intraseasonal variation (ISV) of the vertical structure of the precipitation at KT and some of his results are published in Kozu *et al.* (2005). We have published a comprehensive follow-up of Kozu *et al.* (2005), the characteristics of DSD aloft as well as at the ground level in Marzuki *et al.* (2010). The following sentences are our summary in Marzuki *et al.* (2010). Intraseasonal variation of ΔZ_{MP} was only found at heavy rain (ΔZ_{MP} defined as the difference between a measured radar reflectivity and that from Marshall and Palmer's model). Consistent with the previous study, during the inactive phase (April 10–22, 2004), ΔZ_{MP}s were generally positive (broad DSD) and decrease toward negative values (narrow DSD) as the phase of ISV shifts to active ones (April 23–May 6, 2004). We found that a broad DSD and skewness towards higher drop diameters during the inactive ISV phase came mainly from deep convective, while a narrow DSD during the active phase came mainly from shallow convective events. Like surface DSD, mass-weighted mean diameter (D_m) revealed from the EAR measurement was also larger during the inactive phase (deep convective) than that for the active phase (shallow convective). In general, we found that

vertical profile of reflectivity gradient (VPRG) from 1.3-GHz wind profiler observations during the inactive phase was larger than for the active phase. This phenomenon may be due to significant coalescence process during the inactive phase.

In this section, we provide the follow-up of Marzuki *et al.* (2010). The summary of DSD parameters for all rain events during CPEA-I are given. Time plot of the equivalent black body temperature (TBB) along 0.20°S latitude of radar site with spatial and time resolutions of 1° longitude x 1° latitude and one day, respectively, low level wind (1-2 km) and the surface daily rainfall observed by a Mobile Automatic Weather Station (MAWS) during CPEA-I are given again in Fig. 6.25. The data of TBB and MAWS are from the result of Marzuki (2005). On April 21-22, the MAWS data were not available. The TBB data are from GOES-9 satellite observation. Rainfall events were observed almost every day. The largest amount of rainfall ($\simeq$ 43 mm/day) was observed on April 23. Relatively large amount of rainfall ($\simeq$ 30 mm/day) was also observed on May 5. Therefore, it can be concluded that rainfall events at KT are strongly modulated by ISV in which high rainfall totals occurred when super cloud clusters (SCCs) passed over the observation site.

Tables 6.6 and 6.7 show the DSD parameters for all rain events in the inactive and active phase during CPEA-I, respectively. The summary of Tables 6.6 and 6.7 is given in Table 6.8. It can be seen that the majority of the rain event occurs in the evening hours (12:00-24:00 LT), consistent with the diurnal features of KT precipitation described before. Moreover, rain top height during the active phase is lower than during the inactive phase and majority of shallow convective rains occurs during the active phase. We have found in Marzuki *et al.* (2010) that a broad DSD and skewness towards higher drop diameters during the inactive ISV phase came mainly from deep convective, while a narrow DSD during the active phase came mainly from shallow convective events. However, we can also see some D_m values in excess 3 mm during the active phase such as 16:04-17:10 LT (April 23, SH), 12:58-13:20 LT (April 28, D/DH) and 15:02-15:34 LT (April 28, SH). These large D_m values are observed at the very start of rain event as described above. The largest (smallest) value of N_w (D_m) is observed during SCC3. During the passage of SCC3 (5-6 May), strong updrafts were present, indicating the

orographic lifting due to the lowest-level westerly wind (Shibagaki *et al.*, 2006). Orographic lifting can supply a large amount of condensates, which create a large number of small-sized drops that fall to the mountain slope (Rosenfeld and Ulbrich, 2003). The value of D_m during SCC3 is consistent with that of Rosenfeld and Ulbrich (2003) in which the orographic convection is characterized by small D_m (<1 mm) even in heavy rain. Westerly wind intensified at the passages of SCC3 and regarded as a westerly wind burst (e.g., Kawashima *et al.*, 2006; Shibagaki *et al.*, 2006). Some wind tunnel studies have shown that horizontal wind influenced the DSD and its kinetic energy (e.g., Erpul *et al.*, 1998, 2000). Erpul *et al.* (1998) obtained a narrower raindrop distribution under wind-driven rain compared to vertical rainfall (without wind). Hence, these two processes may be related to the characteristics of DSD during SCC3. However, more study needs to be done particulary to examine the effect of wind on the drop in nature because wind also influences the performance of 2DVD.

Table 6.6: Value of rainfall rate (R), $\log_{10}(N_w)$, D_m, μ and $Z - R$ relations for all events during the inactive ISV phase (April 10–22, 2004). Max, avg, std denote maximum, mean and standard deviation. R_{top} is rain top height in km above ground level which is observed from the vertical profile of BLR data.

Date	Time	Type	R_{top}	R			D_m			N_w			μ		$Z - R$
				max	avg	std	max	avg	std	max	avg	std	avg	std	
11/4	12:40-13:20	D	7.05	38.29	15.08	11.89	2.28	1.46	0.34	4.57	4.09	0.43	2.68	4.34	$Z = 200R^{1.37}$
15/4	15:56-16:06	D	7.35	16.72	5.96	7.49	1.92	1.21	0.40	4.67	3.88	0.87	6.10	5.56	$Z = 248R^{1.17}$
	18:08-18:52	D	9.60	52.77	16.58	16.27	2.51	1.49	0.53	4.63	4.09	0.60	1.97	5.59	$Z = 204R^{1.42}$
	19:20-19:52	S	9.75	6.72	2.94	2.26	1.90	1.45	0.32	3.70	3.36	0.25	3.21	6.87	$Z = 301R^{1.56}$
17/4	16:48-17:16	D	6.00	14.11	2.35	4.74	2.61	1.16	0.60	4.45	3.83	0.60	4.45	8.40	$Z = 207R^{1.85}$
	18:52-19:32	D	9.75	18.21	4.28	4.85	2.43	1.30	0.50	4.50	3.79	0.45	3.90	5.86	$Z = 97R^{2.06}$
18/4	06:54-07:20	SH	3.30	20.33	5.65	7.48	1.08	0.89	0.14	5.31	4.64	0.51	8.66	9.67	$Z = 100R^{1.28}$
	07:22-08:00	D	6.75	18.61	7.41	5.05	1.17	0.96	0.08	5.37	4.80	0.45	2.81	2.73	$Z = 247R^{0.88}$
	08:02-08:50	SH	4.20	8.85	1.62	2.09	1.08	0.89	0.10	5.10	4.13	0.46	8.41	10.02	$Z = 127R^{1.19}$
19/4	16:28-16:48	D	6.30	38.13	11.49	14.49	2.69	1.38	0.53	4.57	3.91	0.44	3.12	5.74	$Z = 138R^{1.63}$
	16:50-17:34	M	8.40	3.49	1.11	1.06	1.18	0.97	0.09	4.50	3.75	0.48	6.70	5.73	$Z = 161R^{1.17}$
20/4	12:38-13:12	D	6.75	61.38	12.24	18.55	1.69	1.26	0.26	5.33	4.00	0.67	2.68	5.69	$Z = 247R^{1.27}$
22/4	20:44-21:28	S	9.30	24.22	6.84	7.37	2.37	1.38	0.50	4.73	3.91	0.75	4.77	6.80	$Z = 103R^{1.71}$
	23:34-23:54	S	7.65	0.66	0.36	0.23	1.25	1.04	0.19	3.34	3.16	0.13	5.05	3.88	$Z = 363R^{1.47}$

Table 6.7: Same as in Table 6.6, but for the active phase (April 23–May 6, 2004).

Date	Time	Type	R_{top}	R			D_m			N_w			μ		$Z - R$
				max	avg	std	max	avg	std	max	avg	std	avg	std	
23/4	00:04-00:50	S	7.80	2.44	1.03	0.47	1.73	1.45	0.20	3.22	2.97	0.15	3.10	2.30	$Z = 470R^{1.65}$
	13:00-13:34	D	9.75	4.16	0.75	0.99	1.34	1.04	0.14	4.19	3.39	0.43	6.11	3.43	$Z = 213R^{1.23}$
	13:36-14:56	S	9.00	16.10	3.89	4.35	1.88	1.20	0.27	4.50	3.80	0.45	1.48	4.20	$Z = 212R^{1.42}$
	16:04-17:10	SH	4.65	78.92	7.65	15.90	3.27	1.27	0.52	5.08	3.81	0.52	6.31	5.39	$Z = 170R^{1.44}$
	20:14-21:32	D	6.15	36.52	12.28	10.31	1.62	1.15	0.19	5.15	4.54	0.64	2.66	3.49	$Z = 161R^{1.22}$
	21:42-22:32	D	6.15	17.57	7.97	4.66	1.39	1.14	0.13	5.15	4.48	0.48	2.57	3.47	$Z = 146R^{1.27}$
	22:34-23:58	S	8.25	6.39	2.97	1.46	1.95	1.44	0.26	4.37	3.48	0.35	0.32	1.11	$Z = 266R^{1.58}$
24/4	00:04-03:50	S	7.20	9.95	1.26	1.31	1.69	1.02	0.18	4.23	3.73	0.33	6.23	5.11	$Z = 185R^{1.47}$
	18:28-20:26	M	8.70	26.64	4.41	5.10	1.65	1.22	0.17	4.64	3.87	0.51	2.13	3.57	$Z = 244R^{1.20}$
	20:28-21:40	S	8.40	4.14	0.85	0.99	1.70	1.22	0.28	4.19	3.21	0.50	5.01	5.49	$Z = 350R^{1.51}$
26/4	01:18-01:58	D	9.15	53.18	13.29	17.87	1.52	1.02	0.27	5.04	4.50	0.46	5.53	5.97	$Z = 98R^{1.43}$
28/4	12:58-13:20	D	5.70	6.92	1.55	2.22	3.17	1.70	0.95	4.03	2.84	0.64	0.74	3.99	$Z = 998R^{2.13}$
	14:20-14:34	SH	3.30	4.74	1.45	1.37	1.64	1.26	0.22	3.81	3.40	0.28	3.15	3.65	$Z = 274R^{1.58}$
	15:02-15:34	SH	5.25	24.71	8.71	11.01	3.16	1.18	0.62	4.71	4.07	0.43	7.99	7.28	$Z = 128R^{1.51}$
	15:42-16:16	D	6.30	22.87	9.08	6.95	1.30	1.13	0.13	4.90	4.52	0.28	4.08	6.24	$Z = 138R^{1.32}$
29/4	02:52-05:04	S	8.25	1.60	0.71	0.37	1.71	1.29	0.20	3.51	3.05	0.29	4.06	2.40	$Z = 430R^{1.66}$
	10:12-10:34	SH	3.60	41.13	9.38	12.33	1.80	1.05	0.30	4.95	4.38	0.56	5.41	8.68	$Z = 125R^{1.39}$
	13:30-13:56	S	7.05	2.60	1.16	0.77	1.71	1.37	0.23	3.41	3.10	0.24	3.24	2.77	$Z = 394R^{1.36}$
	14:58-16:24	S	6.15	3.08	1.04	0.69	1.67	1.21	0.21	3.68	3.34	0.26	3.83	3.32	$Z = 294R^{1.56}$
2/5	18:18-19:28	D	5.85	28.75	8.07	9.52	1.71	1.11	0.26	4.88	4.21	0.40	6.09	7.67	$Z = 139R^{1.36}$
5/5	12:56-20:08	SH	4.80	24.68	2.79	3.18	1.20	0.80	0.12	5.64	4.77	0.35	9.25	8.46	$Z = 81R^{1.26}$
6/5	00:36-01:46	SH	4.80	1.38	0.53	0.31	1.58	1.12	0.23	3.93	3.24	0.27	5.55	6.06	$Z = 508R^{2.10}$
	02:20-02:48	SH	2.55	6.33	2.23	2.35	0.71	0.67	0.02	5.58	5.04	0.62	11.40	5.08	$Z = 71R^{1.01}$
	15:38-17:04	S	6.00	3.14	0.99	0.60	0.71	0.64	0.03	5.28	4.76	0.36	16.37	10.21	$Z = 65R^{1.10}$
	22:56-23:58	S	7.05	1.12	0.61	0.35	1.27	1.06	0.13	3.71	3.37	0.25	5.17	3.76	$Z = 251R^{1.39}$

Table 6.8: Summary of Table 6.6 and Table 6.7.

Type	ISV	Profile	R			D_m			N_w			μ		$Z - R$
			max	avg	std	max	avg	std	max	avg	std	avg	std	
S	Inactive	68	24.22	3.84	5.08	2.37	1.36	0.40	4.73	3.51	0.55	4.03	6.43	$Z = 228R^{1.52}$
	Active	460	16.10	1.43	1.86	1.95	1.18	0.28	5.28	3.48	0.51	4.58	5.31	$Z = 222R^{1.68}$
M	Inactive	23	3.49	1.11	1.06	1.18	0.97	0.09	4.50	3.75	0.48	6.70	5.73	$Z = 161R^{1.17}$
	Active	60	26.64	4.41	5.10	1.65	1.22	0.17	4.64	3.87	0.51	2.13	3.57	$Z = 244R^{1.20}$
D	Inactive	136	61.38	10.04	12.71	2.69	1.29	0.44	5.37	4.09	0.62	3.13	5.34	$Z = 155R^{1.42}$
	Active	171	53.18	8.56	10.25	3.17	1.14	0.34	5.15	4.22	0.70	4.11	5.47	$Z = 158R^{1.27}$
SH	Inactive	39	20.33	3.06	5.08	1.08	0.89	0.11	5.31	4.30	0.53	8.50	9.76	$Z = 116R^{1.22}$
	Active	339	78.92	3.51	6.92	3.27	0.94	0.34	5.64	4.37	0.70	8.08	7.76	$Z = 98R^{1.34}$

Chapter 7

Complex Dielectric Constant of Rainwater

7.1 Introduction

As mentioned in Chapters 1 and 2, this work includes the study on the interaction of electromagnetic waves and hydrometeors. A fundamental step in hydrometeorological applications has been to introduce the use of weather radar. Radars emit radiation to the atmosphere and this radiation is partially backscattered by hydrometeors located at certain distance and height over the ground. Radars are able to establish the position of detected targets and measure the returned power, which can then be transformed into radar reflectivity factor (Z). Chapter 6 have showed an analytical formulation of raindrop size distribution (DSD) that can provide relations between different rainfall variables such as $Z - R$ to convert Z from radar to the rainfall rate (R). In addition to providing the advantages, interaction of electromagnetic waves and hydrometeors also generates some problems in weather radar and radio communication systems. Besides errors in the radar calibration, the signal attenuation due to precipitation is also a problem which requires careful corrections in weather radar. Moreover, the attenuation due to rain restricts the path length of radio communication systems and limits the usage of higher frequencies for terrestrial point-to-point microwave links and satellite communications (e.g., Oguchi, 1983).

Studying the interaction of electromagnetic waves and raindrop needs the knowledge of the complex dielectric constant of rainwater. Most of the empirical models which are widely used for modeling wave propagation in rain (e.g., Liebe *et al.*, 1991; Ray, 1972), used the data of pure water (e.g., Cook, 1952; Grant and Shack, 1967) or an unspecified type of water (e.g., Collie *et al.*, 1948; Grant *et al.*, 1957; Sandus and Lubitz, 1961). The composition of rainwater may not be the same as pure water or distilled water because of multiple inputs from the atmosphere, sea-spray and continental dust (e.g., Mphepya *et al.*, 2006; Puxbaum *et al.*, 1998). The contribution of this work is the measurement of the complex dielectric constant of real rainwater, as collected in nature.

7.2 Theoretical Background

7.2.1 Models of Water Dielectric Property

The Maxwell's equations which are based on the Faraday's law and Ampere's law are the key point to determine how the electromagnetic wave propagates through a material. These equations are given in Chapter 2 (see Eqs. 2.30-2.36. The permittivity (ϵ), permeability (μ), and conductivity (σ) in the aforementioned equations are known as the electromagnetic properties of material.

The complex dielectric constant (permittivity) describes the interaction of dielectric materials and electrical fields. Dielectric materials become polarized in the presence of a field that displaces the electrons within a molecule away from their average position. The separation of the charge is equivalent to a dipole moment where polarization is used as a measure between the electric field and the dipole moment.

The water molecule is the most well-known material that exhibits a permanent dipole moment, and in the presence of an electric field, experiences a torque that attempts to align the dipole in the direction of the field. The complex dielectric constant is usually expressed by $\epsilon* = \epsilon' - i\epsilon''$. As polar liquid, the dielectric property of water can be described by the classical theory of Debye where orientation due to external fields can be modeled as a relaxation process

with a characteristic time constant, given by Debye (1929)

$$\epsilon^* - \epsilon_\propto = \frac{\epsilon_s - \epsilon_\propto}{1 + j\omega\tau}, \tag{7.1}$$

which can be rearranged to real and imaginary part as:

$$\epsilon' - \epsilon_\propto = \frac{\epsilon_s - \epsilon_\propto}{1 + (\omega\tau)^2}, \tag{7.2}$$

$$\epsilon'' = \frac{(\epsilon_s - \epsilon_\propto)\omega\tau_0}{1 + (\omega\tau)^2}, \tag{7.3}$$

where ω represents the angular frequency and τ_0 is the characteristic relaxation time, ϵ_s and $\epsilon_\propto$ are the static and infinite frequency dielectric constants, respectively. It is known, however, from a considerable amount of experimental data that the dispersion processes of many liquids and solids can not be accurately described by the Debye Equation (7.1). The dispersive behavior displays a broadening throughout the frequency band of interest and can be more accurately described using a modified form of the Debye Equation, known as the Cole-Cole Equation Cole and Cole (1941), given by

$$\epsilon^* - \epsilon_\propto = \frac{\epsilon_s - \epsilon_\propto}{(1 + j\omega\tau)^{1-\alpha}}, \tag{7.4}$$

which can be rearranged to real and imaginary part as:

$$\epsilon' - \epsilon_\propto = \frac{(\epsilon_s - \epsilon_\propto)[1 + (\omega\tau)^{1-\alpha}\sin(\alpha\pi/2)]}{1 + 2(\omega\tau)^{1-\alpha}\sin(\alpha\pi/2) + (\omega\tau)^{2(1-\alpha)}}, \tag{7.5}$$

$$\epsilon'' = \frac{(\epsilon_s - \epsilon_\propto)(\omega\tau)^{1-\alpha}\cos(\alpha\pi/2)}{1 + 2(\omega\tau)^{1-\alpha}\sin(\alpha\pi/2) + (\omega\tau)^{2(1-\alpha)}}, \tag{7.6}$$

The Cole-Cole equation reduces to the Debye equation when $\alpha = 0$. Yet when α has values greater than 0, the dispersion region is broader and the maximum value of ϵ'' decreases.

It is often necessary for conductive materials to include a conductivity term in the Cole-Cole expression, leading to

$$\epsilon^* - \epsilon_\propto = \frac{\epsilon_s - \epsilon_\propto}{(1 + j\omega\tau)^{1-\alpha}} + \frac{\sigma}{j\omega\epsilon_0}. \tag{7.7}$$

This term accounts for ionic conduction, or any type of charge carrying conduction that dominates the dielectric loss in the lower frequency spectrum. When obtaining dielectric permittivity measurements in the frequency domain, this allows the loss to be decomposed relatively easily into the conduction and polarization mechanisms. Other modified versions of (7.7) could be found in several studies (e.g., Davidson and Cole, 1950).

Ray (1972) developed a regression model that covers the Debye and Cole-Cole equation. However, this model needs more than 30 coefficients. Then Liebe *et al.* (1991) carefully examined the existing data and obtained a new empirical model of the complex dielectric constant of pure liquid water as

$$\epsilon^* = \epsilon_2 + \frac{\epsilon_1 - \epsilon_2}{1 - i(f/\gamma_2)} + \frac{\epsilon_0 - \epsilon_1}{1 - i(f/\gamma_1)}, \tag{7.8}$$

which can be rearranged to real and imaginary part as:

$$\epsilon' = \epsilon_2 + \frac{\epsilon_1 - \epsilon_2}{1 + (f/\gamma_2)^2} + \frac{\epsilon_0 - \epsilon_1}{1 + (f/\gamma_1)^2}, \tag{7.9}$$

$$\epsilon'' = \epsilon_2 + \frac{(\epsilon_1 - \epsilon_2)(f/\gamma_2)}{1 + (f/\gamma_2)^2} + \frac{(\epsilon_0 - \epsilon_1)(f/\gamma_1)}{1 + (f/\gamma_1)^2}, \tag{7.10}$$

where

$$\theta = 1 - 300/T(K),$$

$$\epsilon_0 = 77.66 - 103.3 \cdot \theta,$$

$$\epsilon_1 = 0.0671 \cdot \epsilon_0,$$

$$\gamma_1 = 20.2 + 146.4\theta + 316\theta^2,$$

$$\epsilon_2 = 3.52 + 7.52\theta,$$

$$\gamma_2 = 39.8\gamma_1.$$

In Liebe *et al.* (1993), they used $\epsilon_2 = 3.52$. Liebe's model is actually an update of Ray's model by using some new experimental data that fits the data at frequencies < 1000 GHz for both ice and water. Besides covering the Debye and Cole-Cole equations, this model also covers the mixed equation (Debye+Lorentzian).

Table 7.1: Summary of some previous studies on rainwater property

Authors	Sampling sites [Periode]	pH min - max (mean)	σ ($\mu S/cm$) (mean)
Zeng and Hopke (1989)	Ontario (Canada) [1980-1984]	(5.3)	-
Lacaux *et al.* (1992)	Congo [1986-1987]	(5)	-
Al-Momani *et al.* (1995)	Izmir (Turkey) -	(5.6)	-
Puxbaum *et al.* (1998)	Central Austria [1984-1993]	(4.78)	-
Kulshrestha *et al.* (2003)	Hyderabad (India) [1999-2001]	5.5-7.2(6.4)	-
Polkowska *et al.* (2005)	Poland [1996-1999]	(4.72)	(47.25)
Beiderwieden *et al.* (2005)	Ecuador [2003-2004]	4.5-5.61(5.11)	(6)
Han and Liu (2006)	Guiyang (China) [1999-2001]	3.55-6.83(4.53)	-
Beysens *et al.* (2006)	Bordeaux(France) [2002-2003]	(5.4)	(45.1)
Al-Khashman (2009)	western Jordan [2006-2007]	4.8-8.2(6.9)	-

7.2.2 Compositions of Rainwater

The composition of rainwater may not be the same as pure water or distilled water because of multiple inputs from the atmosphere, sea-spray and continental dust. The composition of rainwater could be affected by a number of factors, including human and industrial activities, forest type, canopy density, tree age, amount of precipitation and/or wind direction. Therefore, the composition of rainwater shows significant temporal and spatial variation. The determination of the composition of rain is crucial to evaluate the relative importance of the

different sources of gases and particular matter. Thus research on rainwater properties has been mainly focused on the field of acid deposition (e.g., Jiries, 2001; Mphepya *et al.*, 2006; Polkowska *et al.*, 2005; Puxbaum *et al.*, 1998). The acidity of water is one of property commonly used to distinguish the type of water. In general, pure water has a pH value of 7.0. The natural acidity of rainwater is often taken to be pH = 5.6. In the absence of common basic compounds such as NH_3 and $CaCO_3$, pH value of rainwater may be expected to range from 4.5 to 5.6 due to natural sulfur compounds alone. The pH of rainwater is expected to be lower than 5.6 for the areas which are exposed to strong influence of SO_2 and NO_x gases, and free from any natural cleansing mechanism of the atmosphere (e.g., Demirak *et al.*, 2006).

This work will not review the studies on the chemical properties of rainwater. Some previous studies on pH value and conductivity (σ) of rainwater published by several authors are given in Table 7.1. Although there have been published various studies on the chemical properties, it is still difficult to find studies on the physical properties of rainwater. Kool *et al.* (1992) reported their study on microwave complex permittivity of rain water for frequencies 26.5, 30 and 40 GHz. They found that the complex permittivity of rain water differs slightly from distilled water.

7.3 Measurements of Rainwater Complex Dielectric Constant

7.3.1 Sampling Location and Collection

Rainwater samples were collected at Graz, Austria (47.04^{o}N, 15.26^{o}E, 353 m above mean sea level), and Kototabang, West Sumatra, Indonesia (0.20^{o}S, 100.32^{o}E, 865 m above mean sea level). Fresh rainwater was simply collected and stored in glass or polyethylene bottles with sealed top to minimize any possibility of it reacting with the ambient atmosphere. At Graz, the rainwater sampler was installed on the flat roof of the Institute of Broadband Communication building, Graz University of Technology (Inffeldgasse). Rainwater on 7, 11 November 2008,

19, 22, 27, 30 May and 11 June 2009 was collected and analyzed. At Kototabang, the rainfall sampler was placed on the ground surface, side by side with a 2D-Video Disdtrometer. Rainwater which fell on 13 and 15 March 2009 was collected and analyzed.

7.3.2   Complex Dielectric Constant Measurement

The complex dielectric constant measurements were made using an Agilent Technologies 85070E dielectric probe kit and the Agilent N5242A-400 Vector Network Analyzer (VNA) from 500 MHz to 26.5 GHz. The accuracy (typical) of the dielectric constant, ϵ' measurements are $\pm 5\%$ and the loss tangent, ϵ''/ϵ' measurements are ± 0.05 Agilent (2008). All measurements were made using a single VNA calibration in order to minimize calibration variation errors during data acquisition. The apparatus was calibrated using distilled water (type in accordance with DIN 57510-manufacturer Alpin) in an air conditioned room at 23°C. A Fluke 51 thermometer with J-type thermocouple covering the temperature range between -200 and 750°C with 0.1^{o}C resolution accuracy was used to monitor the temperature of the test rainwater. Each value is the average of the values obtained from five measurement sequences at each temperature.

7.3.3   Results

7.3.3.1   Complex Dielectric Constant of Rainwater

Figure 7.1 shows the measured and modeled (i.e., Kaatze, 1989; Liebe *et al.*, 1991) complex dielectric constant for distilled water at 23°C. The model in Kaatze (1989) is a nonlinear regression analysis of the measured dielectric spectra of pure water. It is observed that the accuracy of our measurement is good in comparison with the models.

All rainwater samples were first cooled in the refrigerator. Once refrigerated, the samples were removed and slowly heated in a water bath to reach a given temperature. Figure 7.2 shows the average of the measured complex dielectric constant for various observation days at 23°C along with the value for distilled

water. The daily variation is not significant and can be excluded in this analysis. Hence, all measurements in Graz and Kototabang are then averaged, respectively.
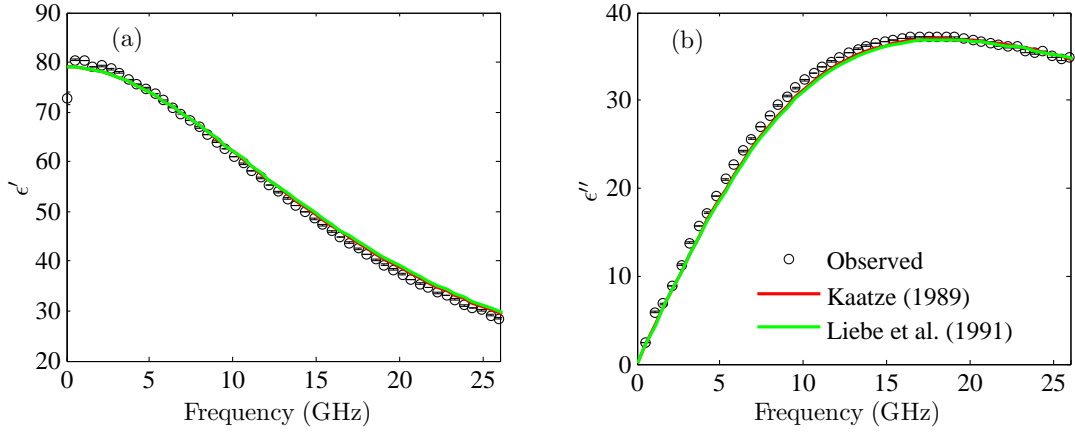
Figure 7.1: Average of the distilled water complex dielectric constant at 23°C along with the value obtained by Liebe's (Liebe *et al.*, 1991) and Kaatze's model (Kaatze, 1989).

Figure 7.3 plots the value of $\Delta\epsilon/\epsilon_{observed}$ for several selected temperatures. $\Delta\epsilon$ is defined as the difference between ϵ calculated from Liebe's model and that from the measurement. In general, the complex dielectric constants derived from the model are lower than the measured values. The statistical measure which is used to study the bias, between dielectric properties from model (x_{mod}) and those from measurement (x_{obs}), is the percentage of relative root mean square error (RRMSE), given by

$$\text{RRMSE} = \frac{\sqrt{\frac{1}{n}\sum_{j=1}^{n}(x_{mod}-x_{obs})^2}}{\overline{x_{obs}}}.100 \tag{7.11}$$

where n is the number of frequency intervals. The percent RRMSE of ϵ' (ϵ'') for temperatures 11, 16, and 23°C are 2.16 (4.14), 0.71 (1.01) and 0.61 (0.65), respectively. From RRMSE, it can be observed that rainwater dielectric properties do not differ greatly from the model. The values of $\epsilon'(f)$ and $\epsilon''(f)$ in Fig. 5.3 were fitted to empirical polynomials with the frequency (GHz) as the independent variable, and given by (with r^2 is the correlation coefficient)
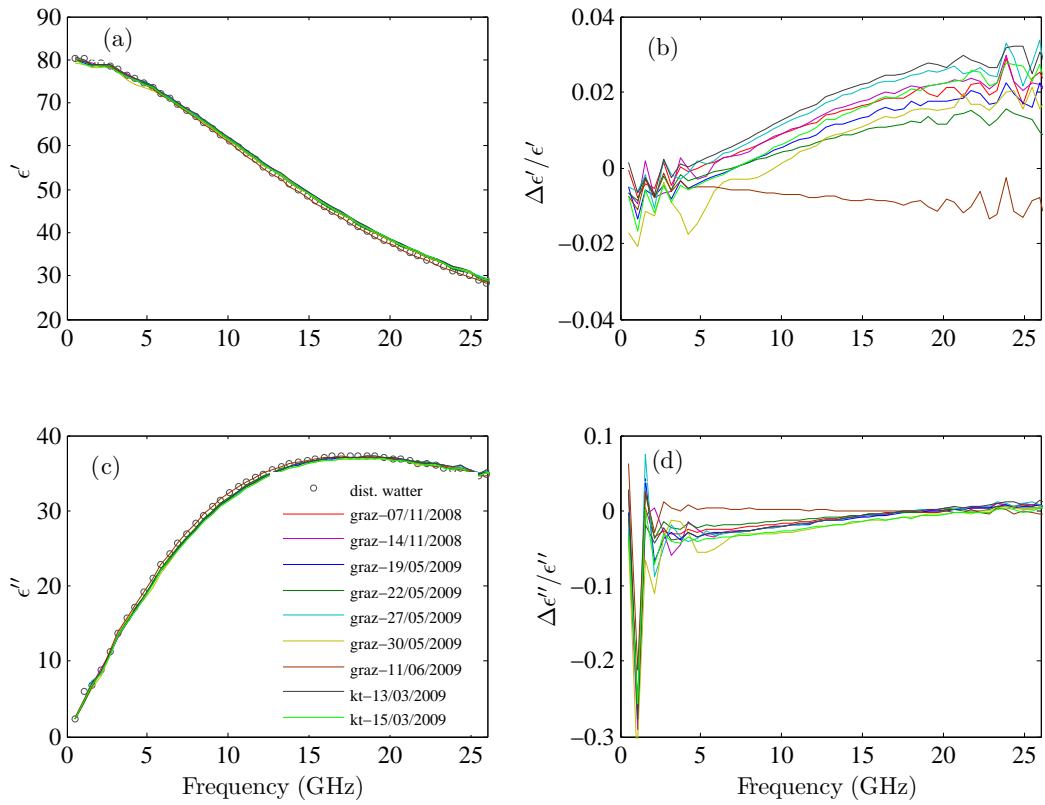
Figure 7.2: Average of the measured rainwater complex dielectric constant for various observation days at 23°C along with the value for distilled water. Graz and KT denote rainwater collected in Graz and Kototabang, respectively.

$$T = 11^{o}C$$

$$\epsilon'(f) = 84.62 + 0.5538f - 0.7637f^2 + 0.05664f^3$$
$$-0.00173f^4 + 1.973\text{x}10^{-5}f^5, (r^2 = 0.9999),$$

$$\epsilon''(f) = -0.8468 + 7.303f - 0.3333f^2 - 0.005902f^3$$
$$+0.0006909f^4 - 1.2\text{x}10^{-5}f^5, (r^2 = 0.9996),$$

$$T = 16^{o}C$$

$$\epsilon'(f) = 82.81 + 0.4103f - 0.5744f^2 + 0.03838f^3$$
$$-0.001069f^4 + 1.128\text{x}10^{-5}f^5, (r^2 = 0.9999),$$

$$\epsilon''(f) = -0.4529 + 5.941f - 0.1817f^2 - 0.01105f^3$$
$$+0.000716f^4 - 1.1\text{x}10^{-5}f^5, (r^2 = 0.9997),$$

$$T = 23^{o}C$$

$$\epsilon'(f) = 79.65 + 0.2178f - 0.3576f^2 + 0.01979f^3$$
$$-0.0004728f^4 + 4.528\text{x}10^{-6}f^5, (r^2 = 0.9999),$$

$$\epsilon''(f) = -0.1074 + 4.47f - 0.07113f^2 - 0.00999f^3$$
$$+0.0004767f^4 - 6.353\text{x}10^{-6}f^5, (r^2 = 0.9999).$$

As mentioned above, we have collected rainwater at Kototabang radar station on 13 and 15 March 2009. Figure 7.4 shows the frequency dependence of the real part (ϵ') and the imaginary part (ϵ'') of rainwater complex dielectric constant for several selected temperatures along with the values calculated using the fitted equations. The agreement is good, indicating that the difference in rainwater complex dielectric constant at Kototabang and Graz would not be significant.

7.3.3.2 Sensitivity in Wave Propagation Modeling Applications

In this part, we describe the impact of real rainwater permittivity on scattering and propagation characteristics of electromagnetic waves in tropospheric precipitation. Figure 7.5 shows the Mie extinction (Q_{ext}) of water spheres which is a function of the drop diameter D, the wavelength and the complex refractive index of the water drop. The detailed explanation of Q_{ext} is given in Chapter 2. The
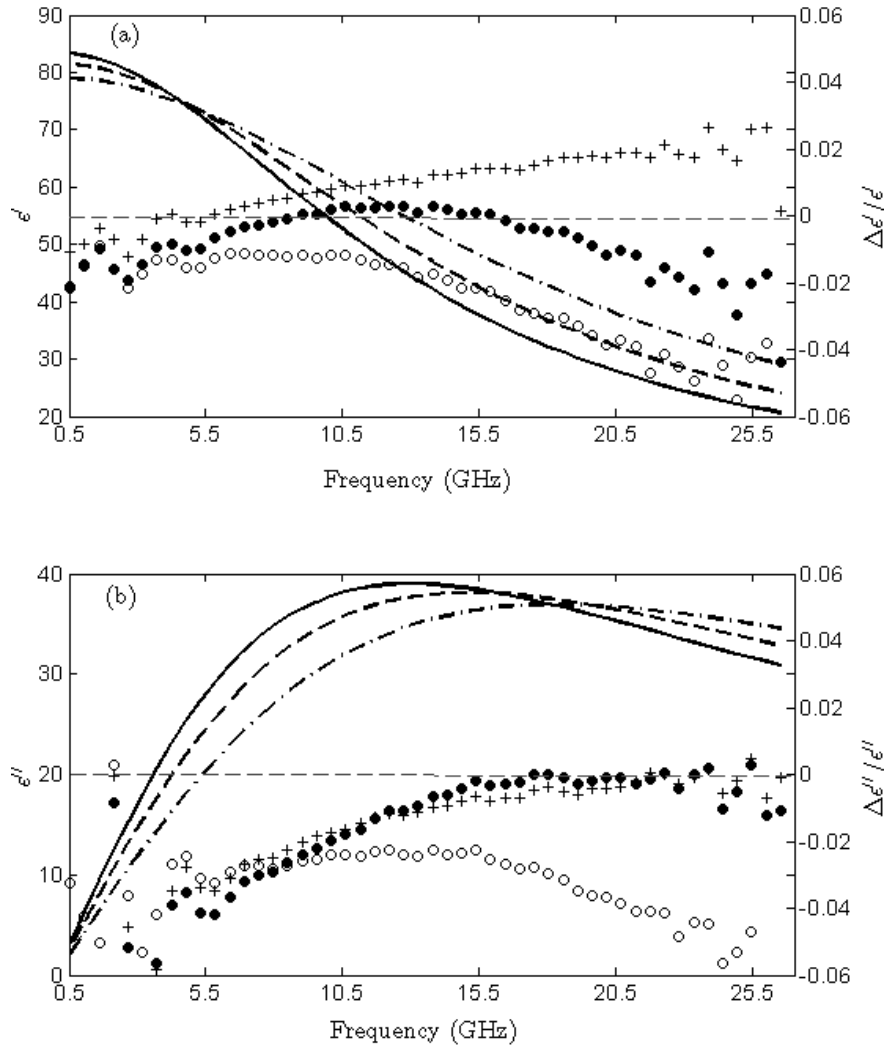
Figure 7.3: Rainwater complex dielectric constants and $\Delta\epsilon/\epsilon_{observed}$ for several selected temperatures from the measurement in Graz environment. $\Delta\epsilon$ is defined as the difference between ϵ calculated from Liebe's model and that from the measurement. Bold solid, dashed and dashdot lines denote the value from the model at 11, 16, and 23^oC, respectively, while circle, bullet and plus denote the value of $\Delta\epsilon/\epsilon_{observed}$. Horizontal dashed line denotes the value of $\Delta\epsilon/\epsilon_{observed} = 0$.
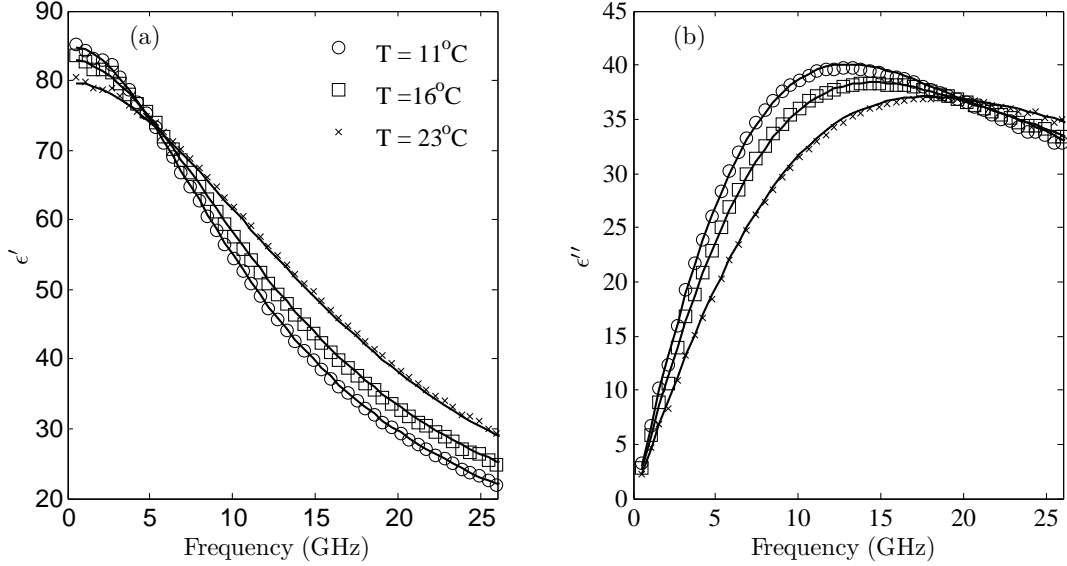
Figure 7.4: Average of the measured rainwater complex dielectric constant in Kototabang environment for several temperatures along with the fitted equation.

solid line denotes Q_{ext} calculated using the complex refractive index estimated from Liebe's model while plus ($+$) denotes the values of $\Delta Q_{ext}/Q_{ext}(observed)$. ΔQ_{ext} is defined as the difference between Q_{ext} calculated using the complex refractive index based on Liebe's model and that from the measurement. We used (7.11) to calculate the percentage of relative root mean square error between Q_{ext} derived using the complex refractive index from Liebe's model and measurement. A 4.14% bias in the imaginary part of the complex dielectric constant at $T = 11^oC$ results in 0.0033, 0.0050 and 0.0086% bias in the Mie extinction coefficients for 10.08, 20.14 and 25.97 GHz, respectively. For $T = 16$ and 23 ^oC, the percent RRMSE of Q_{ext} over all frequencies and temperatures are less than 10^{-3}.

The acidity of rainwater is beyond the scope of this work. Therefore, during collecting rainwater samples for complex dielectric constant measurement, pH and conductivity of samples were not measured. However, we investigated the acidity of rainwater during July-September 2009. During this period, 5 rain events were measured. The values of pH for each sampled day are 6.39 (10 July 2009), 6.52 (03 August 2009), 6.33 (4 August 2009), 6.53 (4 Sept 2009) and 6.60

(11 Sept 2009). It can be observed that pH of rainwater at Graz is very close to pure water or distilled water. This may be one of the reason why the complex dielectric constant in this study do not differ much from distilled water. It would be worthwhile to study the complex dielectric constant of acid rain in the future since it is quite possible that sometimes the electromagnetic waves of remote sensing or communication systems have to penetrate acid rain.
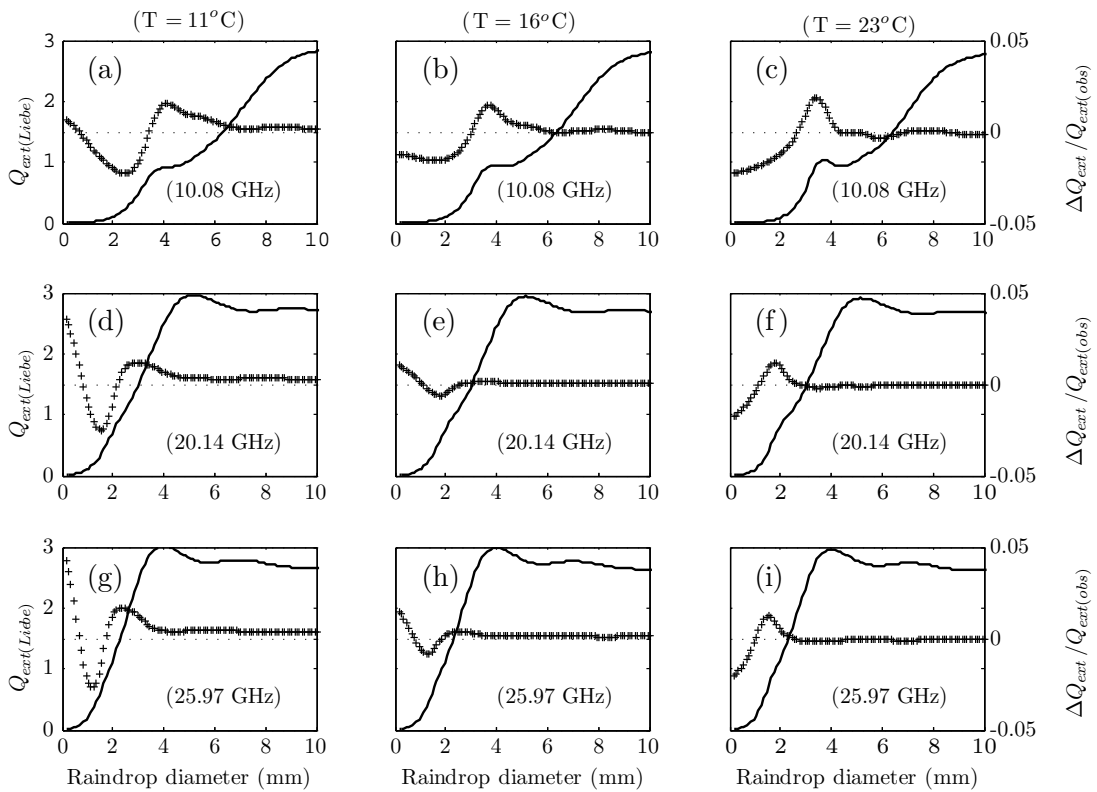
Figure 7.5: Mie extinction efficiencies (Q_{ext}) for spherical raindrops at several selected frequencies and temperatures. Solid line denotes the value estimated using Liebe's model (ordinate labeling on the left) while plus denotes the value of $\Delta Q_{ext}/Q_{ext}(observed)$ (ordinate labeling on the right). ΔQ_{ext} is defined as the difference between Q_{ext} calculated using the complex refractive index based on Liebe's model and that from the measurement. Horizontal dashed line denotes the value of $\Delta Q_{ext}/Q_{ext}(observed) = 0$.

Chapter 8

Rain Attenuation Modeling for Sumatra

8.1 Introduction

In Chapter 6 we have analyzed the natural variation of raindrop size distribution (DSD) at Kototabang (KT), Sumatra. It is well known that attenuation and scattering of electromagnetic waves depend on the DSD. Radio frequencies above 10 GHz particularly tend to be significantly attenuated by rain. For the attenuation range of higher than 10 dB, Maekawa *et al.* (2006) presented statistically a slightly larger attenuation ratio between uplink (14 GHz) and downlink (12 GHz) of Ku-band satellite communication links at KT, then they predicted that this phenomenon was due to the effect of small-sized drops. However, there has no detailed analysis been carried out concerning the role of natural variations of the DSD on the specific attenuation in this region.

In this chapter, we studied the effect of natural variations of rain and DSD at KT on the rain attenuation modeling for Sumatra, particularly for KT. The specific rain attenuation obtained from the measured DSD was calculated by the Mie scattering theory. Predicted rain attenuation was then compared with the attenuation data of Ku-band satellite communication links that connect Research Institute for Sustainable Humanosphere (RISH), Kyoto University in Japan to KT, using the satellite Super bird C (144^0E in orbit). As it was discussed in Chapter 6, significant diurnal variation and rain type dependence of DSD were

observed at KT. Using long-term attenuation statistics analysis, Fiebig and Riva (2004) revealed that diurnal variations have to be considered for the fade margin design. Hence, we investigate the effect of diurnal variation and rain type dependence of DSD on the specific rain attenuation. Shortly before rain attenuation study, a statistical analysis of rainfall rate cumulative distribution for KT was discussed. Some points of this chapter were partially published on Marzuki *et al.* (2009).

8.2 Rainfall Rate Cumulative Distribution

8.2.1 Diurnal Statistics of Rainfall

Rain rate cumulative distribution is crucial in the assessment of the attenuation due to rainfall in the region in both satellite and terrestrial line-of-sight communication. In this study, precipitation data collected by Optical Rain Gauge (ORG) to observe the distribution of rain rate was used. The instrument is ORG-815 (Optical Scintec) sampling rain rate every 1 minute. Detailed specification of this instrument can be found in http://www.opticalscientific.com/. The data analyzed in this paper are those collected from January 12, 2005 to December 31, 2005 (356 days; 97 % of the year); and January 1, 2006 to December 3, 2006 (332 days; 91 % of the year), respectively. Fig. 8.1 shows the ratio of hourly recorded samples to the total number of samples that would have been recorded had no measurement failures occurred. At all times, the recorded-to-total time ratio is very high with values around 97%.

The cumulative distribution of measured rain rates is depicted in Fig. 8.2. This cumulative distribution is derived from the recorded data averaged in the period mentioned above. The solid line is the cumulative rain rate distribution at KT (0.20^0S, 100.32^0E) obtained from the International Telecommunication Union-Radiocommunication Sector (ITU-R) prediction (ITU-Recommendations, 2001, P.837-3). It is clearly seen that rain at KT primarily occurs in the afternoon as in Chapter 6. At large time percentages, the cumulative distribution of measured rain rates is in fairly good agreement with that obtained from the ITU-R model. Of all data, the 0.3% and 1% percentage time rainfall rates from
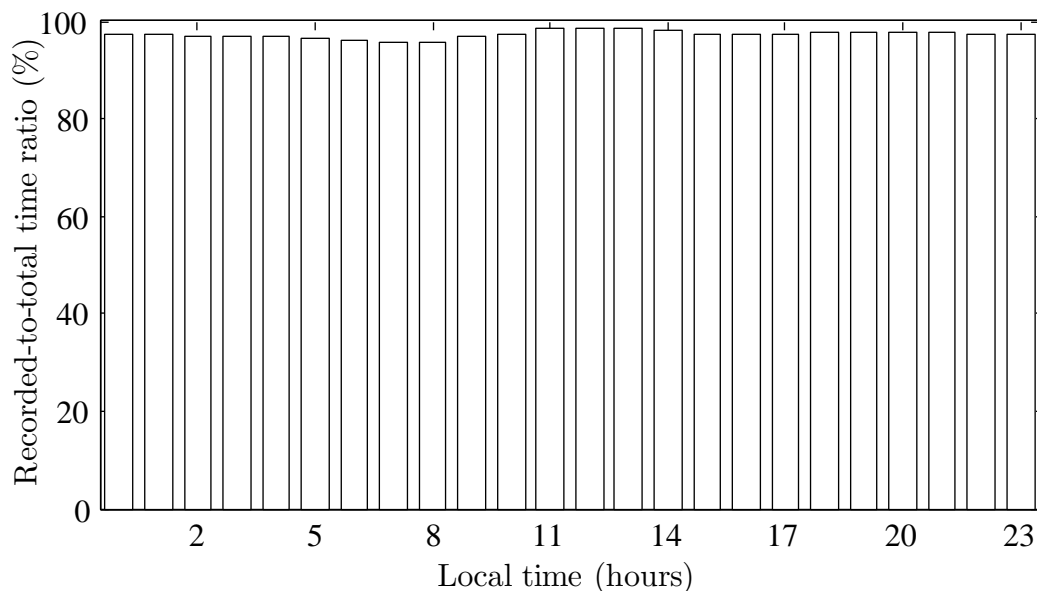
Figure 8.1: Recorded-to-total time ratio for every hour of the day during period of 2005 to 2006.

our experiment are 19.97 and 7.87 mm/h, correspondingly. These are in good comparison with 22.11 and 8.01 mm/h, respectively, from the ITU-R model. The differences between the recorded data and the ITU-R model become large at small time percentage. The 0.1%, 0.01% and 0.001% percentage time rainfall rates from our data are 39.33, 83.34 and 132.06 mm/h, each, slightly lower than 42.97, 94.47 and 148.33 mm/h in the ITU-R model.

The rainy season of the equatorial region of Sumatera is boreal spring (from March to May) and fall (from September to November) seasons. The precipitating clouds have their peak of occurrence from September to October (Renggono et al., 2001). It means that our data cover all rainy seasons during years of 2005 and 2006. It is obvious that considerable differences between the recorded data and ITU-R model at small time percentage may not be due to our data having missed short-term events containing very high rainfall rates. In addition, the percentage rainfall rate exceeded is derived from the recorded data averaged in the period mentioned above not in complete year. This phenomenon seems to be a
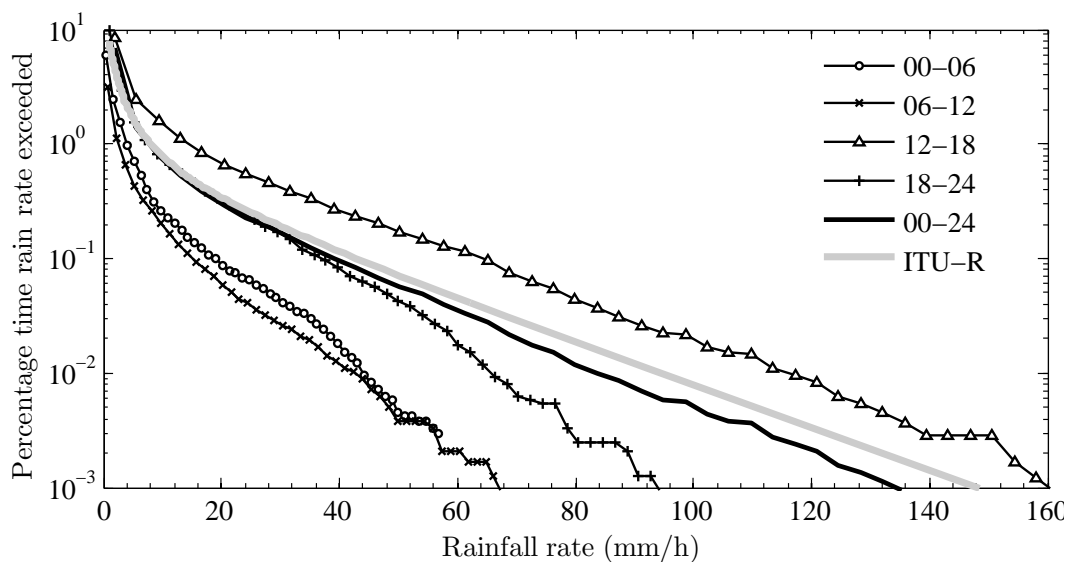
Figure 8.2: Cumulative distribution of rainfall rate at Kototabang on a diurnal basis for the period from 2005 to 2006, compared with the ITU-R prediction (ITU-Recommendations, 2001, P.837-3).

characteristic of the KT rainfall which is not well described by the ITU-R model at small time percentages. However, reliable statistics regarding rainfall rate distribution require an observation period of many years. Hence, in the future, it will be worthwhile to analyze long period data.

8.2.2 Worst-Month Statistics

The concept of the worst month is important for the design of radio telecommunication systems, in particular if the system has to fulfill quality criteria in any month of the year. The concept of worst month statistics which can be applied to quantities such as rainfall rate, rain attenuation and cross polarization discrimination (XPD) can be found in the ITU-Recommendation (ITU-Recommendations, 1990, P.581-2). For a period of 12 consecutive calender months, the annual worst month is calculated by selecting the worst performance (highest probability of occurrence) among all months of data at each annual occurrence level. Let X_{ij} be the probability of exceeding a threshold level j in the ith month. Then the worst

month at level j is determined by the highest X_{ij}, X_{hj}, among all 12 months. The resulting worst month probability distribution for particular year consists of all the X_{hj}, values for the various j levels. The calendar month to which each X_{hj} belongs may vary from one level j to the next. For multiple year data, the average annual worst-month probability is formed by taking averages of the individual annual worst-month probabilities for each level j (Chebil and Rahman, 1999).
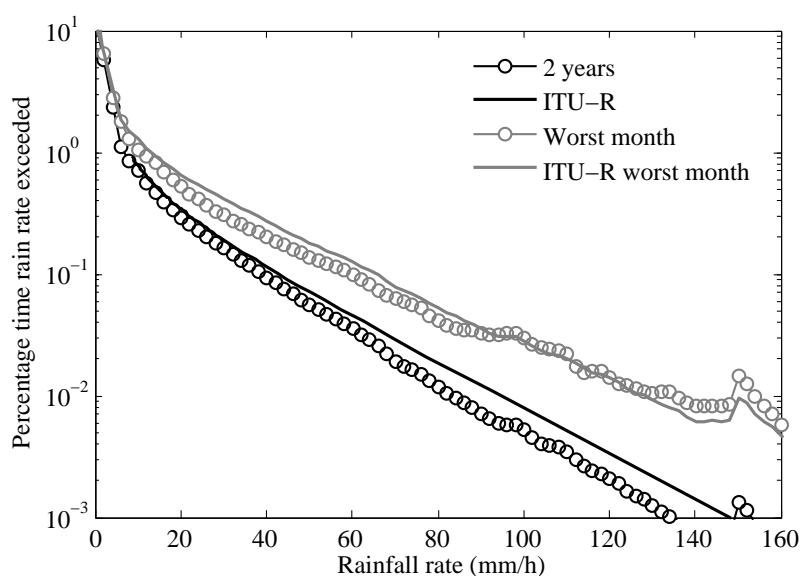
Figure 8.3: Annual and worst month cumulative distribution of rainfall rate at KT for the period from 2005 to 2006, compared with the ITU-R (ITU-Recommendations, 2001, P.837-3) and the ITU-R of worst month (ITU-Recommendations, 2005, P.841-4).

It is possible to relate the average worst month statistic probability (X) and the average annual statistics (Y) as given by

$$Q = X/Y. \tag{8.1}$$

where Q is a function of the occurrence level and the climatic region. Q may be expressed by the power law of the form (ITU-Recommendations, 2005, P.841-4)

$$Q = AY^{-\beta}. \tag{8.2}$$

173

To relate X and Y, (8.2) can be written as

$$X = AY^{1-\beta}. \tag{8.3}$$

The ITU-R suggested that the values of $A = 2.85$ and $\beta = 0.13$ can be used for global planning purposes. In case, the worst month and annual statistics are expressed as percentages rather than probabilities, then $A = 3.0$ and $\beta = 0.13$.
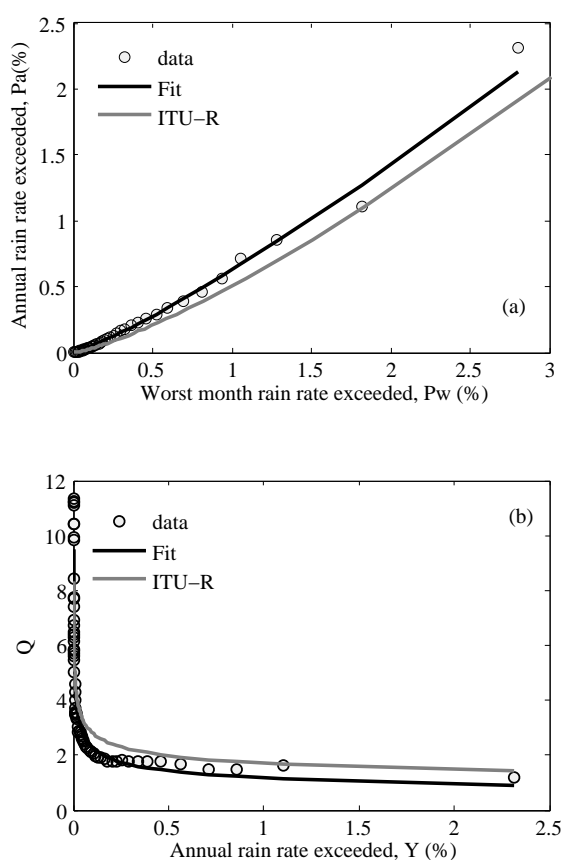
Figure 8.4: Two years averaged annual rainfall exceedance against worst month attenuation exceedance (a) and Q factor as a function of annual percentage of rainfall exceedance (b) along with the ITU-R model (ITU-Recommendations, 2005, P.841-4).

Figure 8.3 shows a composite curve of rain rate exceedance for worst month. The relationship between the annual rain rate exceedance to the worst month

rain rate exceedance is shown in Fig. 8.4a. The relationship is described as:

$$P_a = 0.63P_w^{1.18}, \qquad r^2 = 0.998 \qquad (8.4)$$

where P_a is the annual rainfall rate exceedance and P_w is the worst month rainfall rate exceedance. Figure 8.4b shows the Q factor as a function of annual percentage of rain rate exceedance. Q was found to follow the power law of the form:

$$Q = 1.17Y^{-0.29}, \qquad r^2 = 0.962 \qquad (8.5)$$

It can be seen that the Q factor for the rainfall rate at KT is different from the proposed value by ITU-R for global planning purpose. Moreover, it is also different from the recommended value for Indonesia, i.e., $A = 1.7$ and $\beta = 0.22$ (ITU-Recommendations, 2005, P.841-4). However, to improve the ITU-R values with a better estimate for the worst month statistics in Indonesia, more data are needed.

8.3 Rain Attenuation

8.3.1 Rain Attenuation Obtained from DSD

The specific attenuation coefficient due to rain using the DSD in decibels per kilometer (γ[dB/km]) was obtained from the relation in (2.64). As it was discussed in Chapter 6 and Section 8.2.1, minimum total rain at KT has been observed in the morning hours. Partitioning off the measured DSD on a diurnal and rain type basis for several different rain intensities will result in a very small number of samples especially in heavy rain. Therefore, instead of partitioning off the measured DSD, the DSD parameters of normalized gamma distribution analyzed in Chapter 6 are considered to be dependent on rainfall rate (R). Table 8.1 presents the results of fitting functional relations between the scaling parameter for drop concentration (N_w), mass-weighted mean diameter (D_m), and shape parameter (μ) versus R for two non-overlapping time intervals of 12 hours. The data set comprises a total of 15,180 minutes (7590 spectra with 2-min interval) as in Chapter 6 which has been collected during 2006-2007. To minimize the effect of the spurious variability on disdrometric data we applied the sequential

Table 8.1: Rainfall rate dependence of DSD parameters for specific daytime and rain type. S, M, D and SH denote stratiform, mixed stratiform/convective, deep and shallow convective, respectively.

Rain type	Day time	$N_w - R$	$D_m - R$	$\mu + 4 - R$
	00-12	$N_w = 4365R^{0.509}$	$D_m = 1.068R^{0.103}$	$\mu + 4 = 8.264R^{-0.209}$
S	12-24	$N_w = 3491R^{0.439}$	$D_m = 1.147R^{0.117}$	$\mu + 4 = 7.887R^{-0.172}$
	00-24	$N_w = 3908R^{0.496}$	$D_m = 1.093R^{0.105}$	$\mu + 4 = 8.039R^{-0.198}$
	00-12	-	-	-
M	12-24	$N_w = 4819R^{0.349}$	$D_m = 1.045R^{0.136}$	$\mu + 4 = 11.614R^{-0.151}$
	00-24	$N_w = 4852R^{0.349}$	$D_m = 1.044R^{0.136}$	$\mu + 4 = 11.722R^{-0.156}$
	00-12	$N_w = 8629R^{0.518}$	$D_m = 0.926R^{0.101}$	$\mu + 4 = 11.142R^{-0.105}$
D	12-24	$N_w = 5395R^{0.188}$	$D_m = 1.021R^{0.173}$	$\mu + 4 = 8.919R^{-0.154}$
	00-24	$N_w = 5794R^{0.192}$	$D_m = 1.006R^{0.172}$	$\mu + 4 = 9.164R^{-0.160}$
	00-12	$N_w = 10423R^{0.492}$	$D_m = 0.890R^{0.105}$	$\mu + 4 = 9.629R^{-0.099}$
SH	12-24	$N_w = 9462R^{0.293}$	$D_m = 0.910R^{0.148}$	$\mu + 4 = 10.839R^{-0.165}$
	00-24	$N_w = 9705R^{0.330}$	$D_m = 0.905R^{0.140}$	$\mu + 4 = 10.320R^{-0.145}$

intensity filtering technique (SIFT) as in Lee and Zawadzki (2005)(see Chapter 3). We average groups of 5 DSDs samples of sequential intensity taken within the same rain type.

We found in Chapter 7 that the measured complex permittivity of real rainwater did not differ significantly from the results of Ray (1972) and Liebe *et al.* (1991). In this section, the complex refractive indices are taken from Ray (1972). The extinction cross-section of water spheres is found by applying the theory of Mie and is deduced from Bohren and Huffman (1983).

Figure 8.5 shows the specific attenuation values over the frequency range 1-100 GHz at two rain rates of 20 and 60 mm/h obtained from the DSD models in Table 8.1. For same rainfall rate, it can be seen that rain attenuation of convective rain is higher than that of stratiform type since raindrop concentration in convective is higher than that in stratiform rains. For convective rain (deep and shallow convective), the diurnal variation of rain attenuation is clearly observed in all rain intensities. The diurnal variation is very serious for frequencies higher than
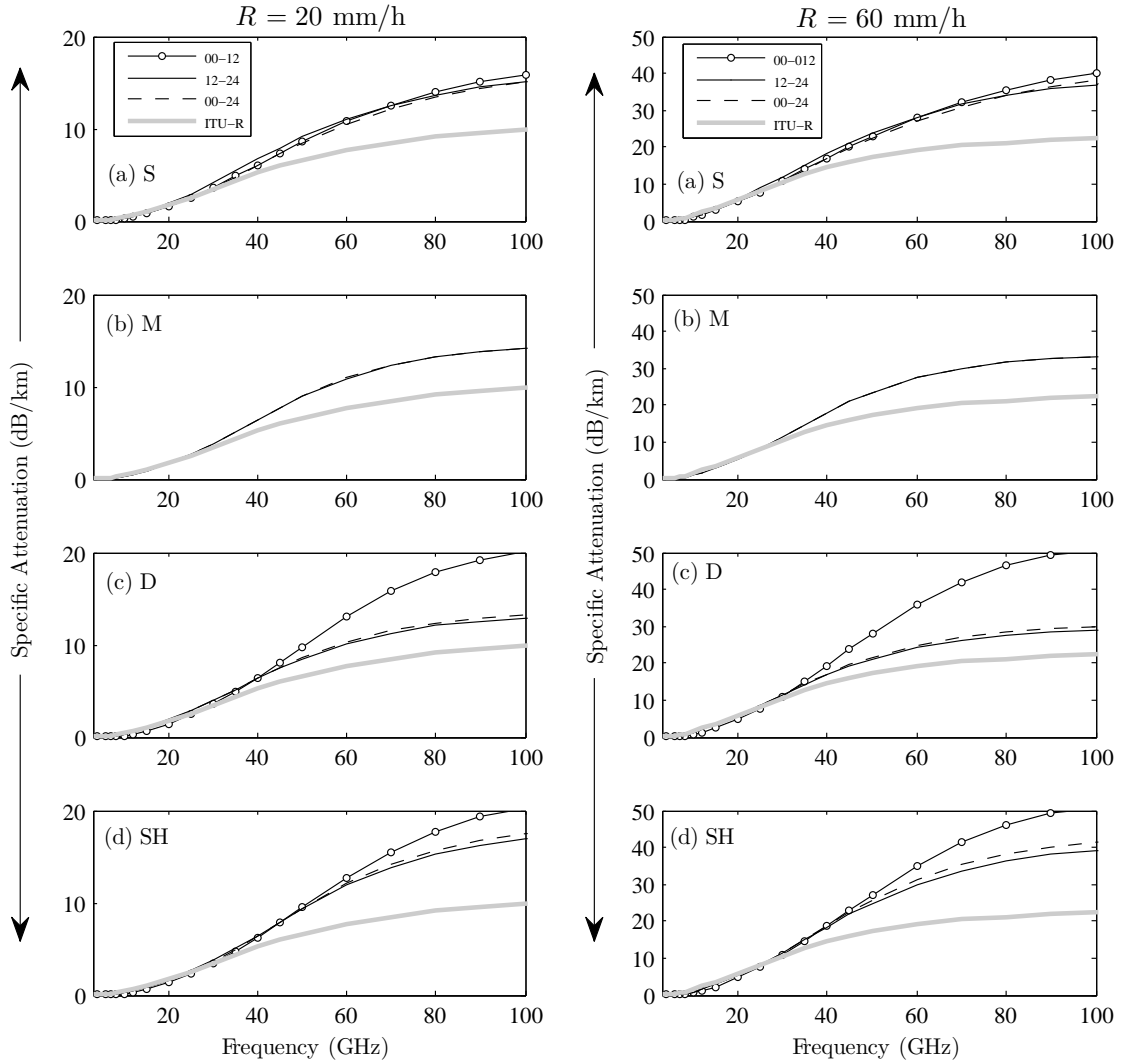
Figure 8.5: Specific attenuation obtained from the DSD models in Table 8.1 over the frequency range 1-100 GHz at two rain rates 20 (a) and 60 mm/h (b), along with the attenuation values obtained from the ITU-R model (ITU-Recommendations, 2002, P.838-3). S, M, D and SH denote stratiform, mixed stratiform/convective, deep and shallow convective, respectively.

Table 8.2: Relationship between specific attenuation coefficient (γ[dB/km]) and rainfall rate (R) on diurnal and rain type basis for frequencies 12 and 14 GHz, where r^2 is the correlation coefficient of regression.

Rain type	Day time	$\gamma - R$(12 GHz)	$[r^2]$	$\gamma - R$ (14 GHz)	$[r^2]$
	00-12	$\gamma = 0.0147R^{1.142}$	[0.97]	$\gamma = 0.0236R^{1.153}$	[0.97]
S	12-24	$\gamma = 0.0159R^{1.163}$	[0.98]	$\gamma = 0.0259R^{1.170}$	[0.98]
	00-24	$\gamma = 0.0151R^{1.146}$	[0.97]	$\gamma = 0.0244R^{1.156}$	[0.98]
	00-12	-		-	
M	12-24	$\gamma = 0.0136R^{1.183}$	[0.99]	$\gamma = 0.0219R^{1.196}$	[0.99]
	00-24	$\gamma = 0.0136R^{1.183}$	[0.99]	$\gamma = 0.0218R^{1.196}$	[0.98]
	00-12	$\gamma = 0.0121R^{1.129}$	[0.96]	$\gamma = 0.0191R^{1.137}$	[0.97]
D	12-24	$\gamma = 0.0138R^{1.248}$	[0.99]	$\gamma = 0.0220R^{1.221}$	[0.99]
	00-24	$\gamma = 0.0135R^{1.246}$	[0.94]	$\gamma = 0.0217R^{1.220}$	[0.99]
	00-12	$\gamma = 0.0125R^{1.091}$	[0.88]	$\gamma = 0.0194R^{1.105}$	[0.92]
SH	12-24	$\gamma = 0.0125R^{1.171}$	[0.96]	$\gamma = 0.0195R^{1.174}$	[0.98]
	00-24	$\gamma = 0.0125R^{1.153}$	[0.96]	$\gamma = 0.0195R^{1.159}$	[0.98]

60 GHz. The DSDs of rain events in the first half of the day (00:00-12:00) give more rain attenuation than those of the second half of the day. Considerable differences in attenuation between the second half and the first half of the day are more obvious as the rain rate increases. As a result, at KT, even though, rainfall rates are the same but falling in different day time and rain type, could provide different rain attenuation because of the DSD variations.

The specific rain attenuation in the ITU-R model (ITU-Recommendations, 2002, P.838-3) is based on the Laws-Parsons size distribution. In all data (00:00-24:00), the deviation from the ITU-R values are less than 10 dB/km at 100 GHz for a rain rate 20 mm/h (for all rain types) and about 15 dB/km and 20 dB/km at 100 GHz for stratiform and shallow convective, respectively, at a rain rate of 60 mm/h. Over the frequency range of 1-40 GHz, the specific attenuation values obtained from the DSD are in fairly good agreement with that obtained from the ITU-R model.

It is common to write a relationship between specific attenuation coefficient
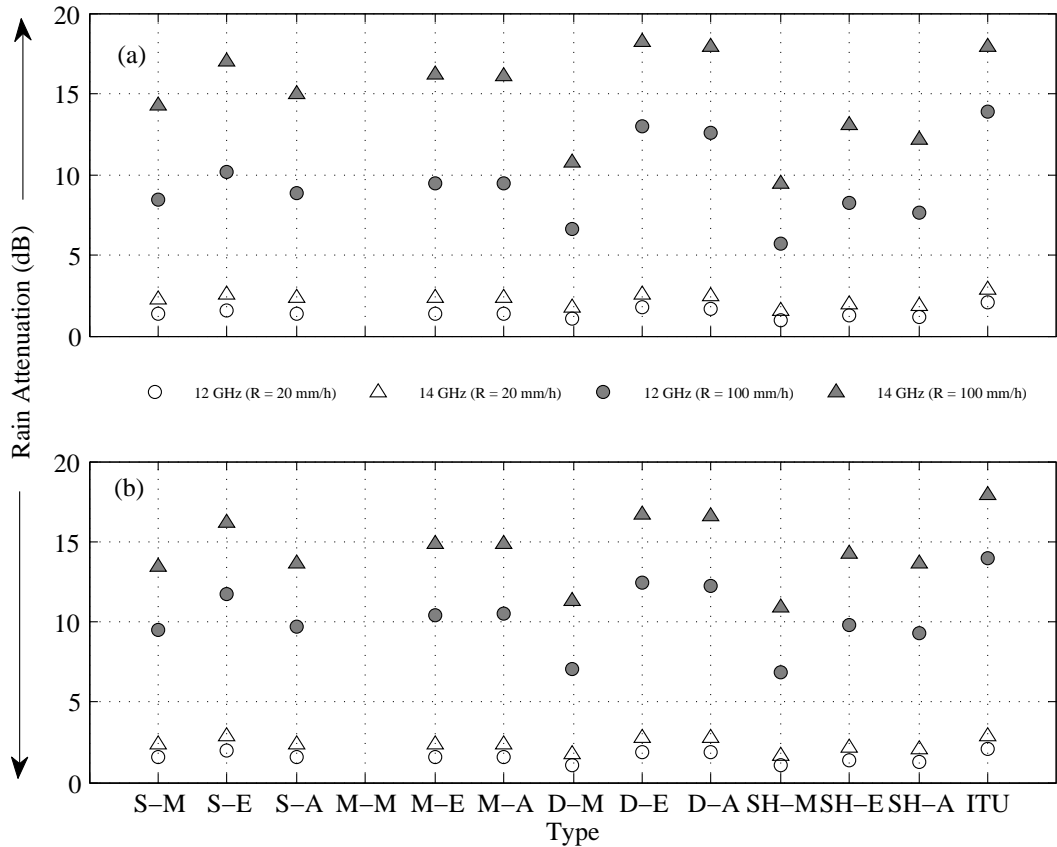
Figure 8.6: Rain attenuation for rainfall rates 20 and 100 mm/h and frequencies 12 and 14 GHz. The DSD (Table 8.1) and $\gamma - R$ relations (Table 8.2) were used in (a) and (b), respectively. S, M, D and SH denote stratiform, mixed stratiform/convective, deep and shallow convective, correspondingly. While M, E and A after rain type indicates morning, evening and all data (without diurnal scheme). The path length was assumed 3 km. ITU is the rain attenuation predicted by the ITU-R (ITU-Recommendations, 2002, P.838-3).

(γ[dB/km]) and R as

$$\gamma[\text{dB/km}] = aR^b, \tag{8.6}$$

where R is rainfall rate in mm/h, a and b are constants. The theoretical explanation of this form has been described by Olsen *et al.* (1978). Table 8.2 shows the $\gamma - R$ relationship for Ku-band frequencies (14/12GHz). The differences in the DSD between convective and stratiform are probably the best recognized and documented today, particularly in the context of tropical rainfall. However, the diurnal variation of DSD has also important implications on rain attenuation modeling. Diurnal variation of DSD will lead to diurnal variation of $\gamma - R$ relations. The specific rain attenuation modeled so far (Tables 8.1 and 8.2) were compiled in Fig. 8.6. Total rain attenuation (A_t[dB]) is calculated by

$$A_t[\text{dB}] = \gamma.L, \tag{8.7}$$

where L is path length and assumed 3 km in Fig. 8.6 as also used by Maekawa *et al.* (2006). According to the figure, the same R translates to A_t greater in evening compared to morning rainfall (for Ku-band). Thus, usage of a single DSD model or $\gamma - R$ relation to convert R into A_t will underestimate in one time and over estimate in other times. The effect of DSD variation on rain attenuation for Ku-band is not significant and the attenuation values are generally close to the ITU-R. However, the variation would be significant for higher frequencies as seen in Fig. 8.5.

For the attenuation range of higher than 10 dB, Maekawa *et al.* (2006) presents statistically a slightly larger attenuation ratio between uplink (14.4651 GHz) and downlink (12.3992 GHz) of Ku-band satellite communication links at KT. They argued that this phenomenon is due to the effect of small-sized drops. Because of its higher frequency, attenuation of 14 GHz is about 10-20% larger than that of 12 GHz (Maekawa *et al.*, 2006). A slightly larger attenuation ratio between 14 GHz and 12 GHz is also observed in Fig. 8.6, especially for very extreme rain. Using average measured DSD for two rain rates (10 and 50 mm/h), Marzuki *et al.* (2009) evaluated the role of particular rain drop size classes on specific attenuation for the frequencies of 12 and 14 GHz. For rain rate of 10 mm/h, it is very interesting that the prevailing contribution to the specific attenuation is

formed by drops of diameter not exceeding 3 mm (87 %). The drop size which is producing the prevailing contribution to the specific attenuation increases with increasing rain rate. In a very extreme rain, the predominant contribution to the specific attenuation is formed by small-sized drops (0.3< D <2 mm; 17%) and medium-sized drops (2< D <4 mm; 62%).

8.3.2 Effect of Rain Type on Equivalent Path Length Estimation

8.3.2.1 Satellite Link System at Kototabang

The satellite link of Superbird C was used to transfer the data from KT to the RISH of Kyoto University in Japan. The description and performance of the link were described in detail by Maekawa *et al.* (2006). The data transmission rate of the link is 128 kbps and the up(down)-link carrier frequency of Very Small Aperture Terminal (VSAT) at KT is 14.4651 (12.3992 GHz). At RISH, on the other hand, the up(down)-link frequency is 14.1292 (12.7351 GHz). At both stations, the up-link radio wave uses the vertical linear polarization, while the down-link radio wave uses the horizontal linear polarization. The receiver antenna at both stations is an off-set 1.8 m Gregorian parabolic dish and the elevation angles at RISH and KT are 49° and 39°, respectively. At both stations, personal computers (PCs) equipped with 16-bit A/D converter boards measure Automatic Gain Control (AGC) voltage of the In Door Unit (IDU) of the VSATs every second.The AGC voltage must be converted into received signal levels (in dBm) to extract the rain attenuation of the signal. The calibration equation between the AGC voltage and the received signal level for the EAR station (Pr_E) is given by

$$Pr_E = 9.984 AGC - 94.731. \qquad \text{[dBm]} \qquad (8.8)$$

The rain attenuation is estimated every minute by the difference between the signal levels received in each rain event and those received in clear sky condition. To estimate the clear sky level we need rain information at RISH and at KT. Due to primarily the fluctuation of the satellite attitude, Maekawa *et al.* (2006) found a distinct diurnal variation of the clear sky level with amplitude of 1-2 dB.

Therefore, they calculated the clear sky level for each local time using hourly values averaged over a few days before and after the respective rainfall events at both stations. When rain is falling at KT (Indonesia), down- and up-link attenuation is measured at KT and RISH, respectively. In this work, we have only rain data at KT. Hence, we are only possible to analyze the rain attenuation of down-link frequency for KT (12.3992 GHz). The zero level during the event was calculated by averaging the signal samples in several minutes before and after the event. A straight line, which connected both average levels, was taken as zero level for the event. Of course we assumed that RISH and KT did not necessarily encounter rain attenuation at the same time because of very large distance between them.

8.3.2.2 Comparison of Rain Attenuation Prediction Models with Measurement

In this section we compared the rain attenuation obtained from the measurement and that calculated from the DSD and power law (Table 8.2) as well as from simple attenuation model (SAM) and the ITU-R model (ITU-Recommendations, 2007, P.618-9). Description about the SAM can be found in Stutzman and Dishman (1982). Computation of specific attenuation has used the following assumption: raindrops are spherical and the DSDs that may occur along the line-of sight paths are identical to those being observed at the surface. As was discussed in Chapter 6, falling raindrops observed in quiet conditions are flattened on the bottom and rounded on the top. The specific attenuation calculated using observed drop shape shows maximum possible deviation from the spherical case of less than 15 percent when all the raindrops are oriented in the same direction (Crane, 1975). However, for Ku-band the effect of drop-shape on the calculation of specific rain attenuation is negligible (Choi *et al.*, 1999).

a). *Stratiform*

Figure 8.7 shows the variation of DSD observed by 2DVD during two stratiform rain events, i.e., on March 27 and April 20, 2006. The contour colourmap in the figure indicates the DSD in logarithmic scale at different sizes. Rainfall rate
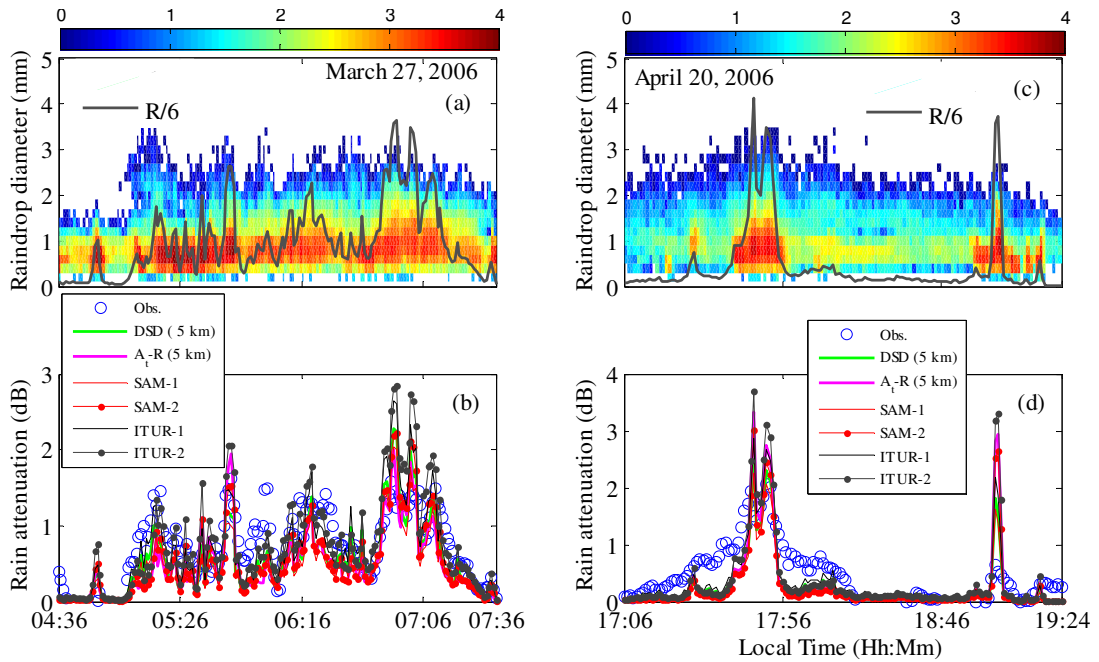
Figure 8.7: (a) and (c) are contour colourmap showing the variation of the DSD at different sizes during two stratiform rain events, i.e., March 27 and April 20, 2006, respectively, along with the variation of rain rate (R). (b) and (d) show the measured rain attenuation ("Obs."), SAM and ITU-R model generated attenuation values during the same event. Rain attenuation of DSD (5 km) and $A_t - R$ (5 km) denote the attenuation obtained from the measured DSD and Table 8.2, correspondingly, with constant equivalent path lengths of 5 km. Number "1" and "2" accompanying SAM and ITU-R legends indicate the specific rain attenuation (γ) calculated from the measured DSD and Table 8.2, respectively.

calculated from the DSD measurement is also provided. The maximum rain rate recorded for Fig. 8.7a and c are around 22 mm/h and 25 mm/h, respectively. Figures 8.7b and d show simultaneous attenuation measurements and they are compared with the attenuation calculated from the DSD and from the power law of Table 8.2. Maekawa *et al.* (2006) assumed, in average, a constant equivalent path length being 3 km at KT. However, they also found that at KT, the equivalent path length estimated based on the Marshall-Palmer DSD rapidly decreases down to 2 km as the rainfall rate reaches 130 mm/h, although it remains more than 3 km below 60 mm/h. Figures 8.7b and d provide a typical comparison between the model-generated attenuation for equivalent path lengths of 5 km and the measured attenuations during the two stratiform events. It can be seen that taking 5 km as a constant equivalent path length for stratiform rain at KT is generally acceptable in which the model-generated attenuation has been found to closely follow the measured attenuation. Sharp changes in rain rates are reflected in the measured attenuation indicating that such changes occur homogeneously and over the entire satellite path.

The SAM model is based on an exponential shape of the rain spatial distribution, includes the distinction between stratiform ($R < 10$ mm/h) and convective rain ($R > 10$ mm/h). Of course, this precipitation classification is not totally acceptable. Rainfall rates in excess 10 mm/h are generally convective rain, but lighter rain may be produced by either type (Tokay *et al.*, 1999). The ITU-R model (ITU-Recommendations, 2007, P.618-9) considers variation of both horizontal and vertical extent of rainfall. The path length of these two models varies with rain intensity. We try to predict instantaneous attenuation from point rain rate measurements instead of using $R_{0.01}$ for these two models. Other input parameters for the SAM and ITU-R models are height above mean sea level of the earth station (h_s) = 0.864 km, the rain height (h_R) = 5 km, elevation angle (θ) = 39°, latitude of the earth station (φ) = 0.2^o, frequency (f) = 12.3992 GHz, and effective radius of the Earth (a_e) = 8500 km. In general, the SAM and ITU-R model generated attenuation do not differ much from those obtained by a constant equivalent path lengths assumption. However, at maximum peak of rainfall rate, the values from the SAM and ITU-R are higher than the measured values and those obtained by a constant equivalent path length assumption.
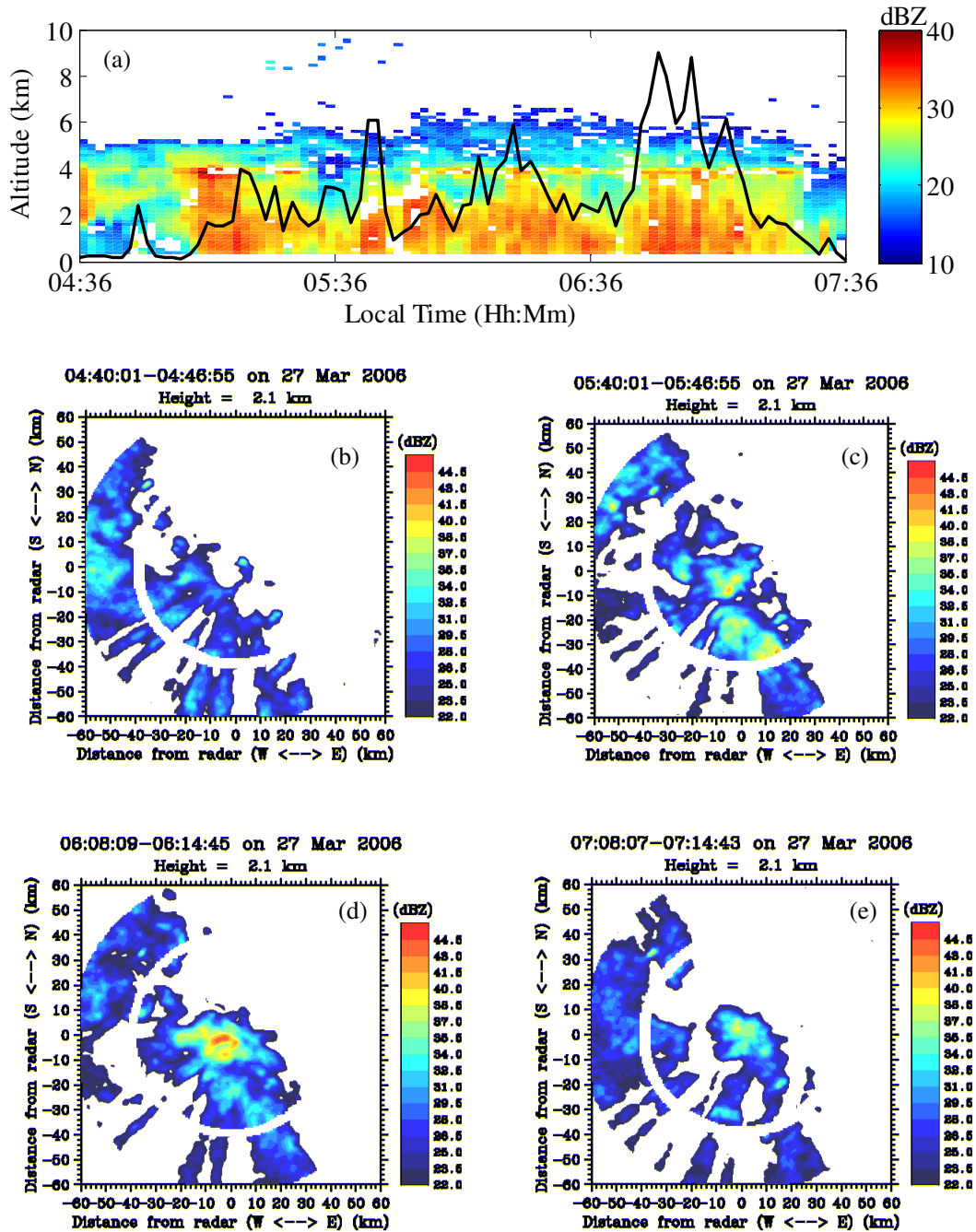
Figure 8.8: Rain height from 1.3 GHz wind profiler observation (a) and horizontal extension of rain cell at height of 2.1 km obtained from X-band radar observation (b-e) for stratiform event on March 27, 2006. Black-solid line in (a) is the rainfall rate from 2DVD observation (R/2). Contour plots of X-band radar are obtained from http://www.rish.kyoto-u.ac.jp/ear/x-radar/index.html.

185
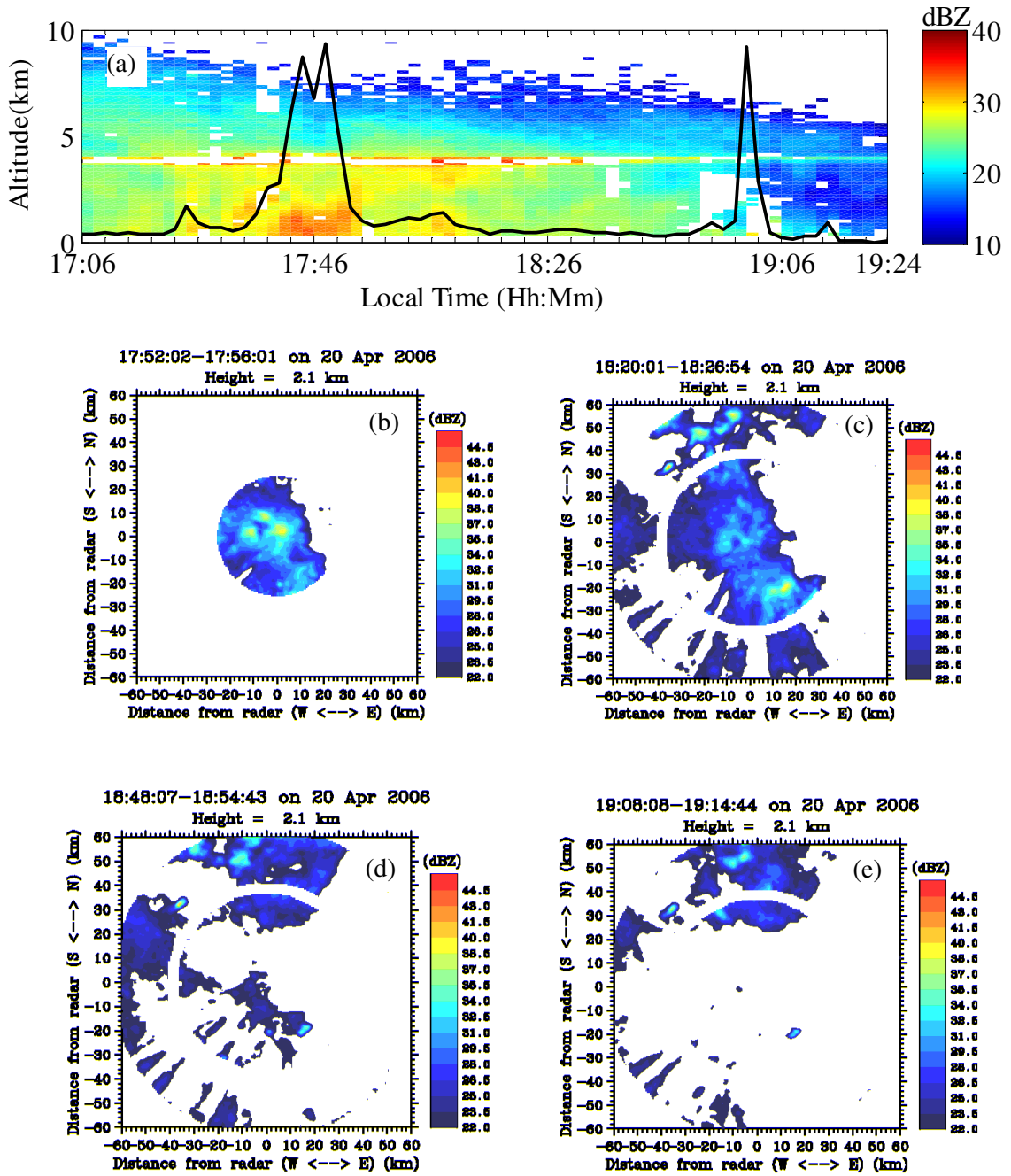
Figure 8.9: Same as Fig. 8.8 but for stratiform event on April 20, 2006. Black-solid line in (a) is the rainfall rate from 2DVD observation (R/2).

Stratiform precipitation areas are characterized by statistically small vertical velocities, low rain rates and widespread, horizontally homogeneous radar echo. Figure 8.8 and 8.9 provide the horizontal extension of rain cell at height of 2.1 km obtained from X-band radar observation and the rain height from 1.3 GHz wind profiler observation. It can be seen that the spatial distribution of rain event on March 27 is almost uniform throughout the event. Therefore, assuming a constant equivalent path length of 5 km for whole minute data for this event seems acceptable. On the other hand, the spatial distribution of rain event on April 20 is uniform in the onset of event, however, it decays into small cells in the end of the event. The characteristics of the horizontal extension of rain cell is consistent with the attenuation characteristics. The DSD and power law-generated values both obtained by a constant equivalent path length assumption and by the SAM and the ITU-R model are in good agreement with the measured values when the precipitation is still homogenously distributed. Equivalent path length decreases when the rain cell decays, for example path length being about 2 km at the second peak of rain on April 20, 2006. Although heavy rain still occurs at KT, sharp changes in rain rates occur locally and not over the entire satellite path as observed from X-Band radar data.

b). *Deep convective*

Figure 8.10 is the same as Fig. 8.7 but for two deep convective events on September 5 and September 7, 2006. The maximum rain rate recorded for Fig. 8.10a and Fig. 8.10c are around 30 mm/h and 106 mm/h, respectively. Figure 8.10b and Fig. 8.10d show simultaneous measurements of attenuation and they are compared with the attenuation calculated from the DSD and from the power law of Table 8.2. The maximum value of observed attenuation is in good agreement with the attenuation obtained by a constant equivalent path length assumption and by the SAM and the ITU-R model. However, the shape of time series of observed attenuation is different from the rainfall rate time series. On September 5, changes in rain rates in the first and the third peak of rainfall rate were not reflected in the measured attenuations indicating that such changes of rainfall rate occur locally. However, at the second peak of rainfall rate the

agreement between the measured attenuation and that obtained by a constant equivalent path length assumption and by the SAM and the ITU-R model is very good. On September 7, on the onset of event the agreement between the measured attenuation and that obtained by a constant equivalent path lengths assumption and by the SAM and the ITU-R model is very good. Thereafter, the shape of time series of observed attenuation is much different from those of rainfall rate.

Deep convective precipitation areas are characterized by statistically large vertical velocities and the horizontal inhomogeneity of radar echo. Figure 8.11 and 8.12 provide the horizontal extension of rain cell at 2.1 km from X-band radar observation and the rain height from 1.3 GHz wind profiler observation. It can be seen that the spatial extension of the two rain events is small. The distribution of deep convective rain along the path of the satellite link may be some time uniform so that the measured attenuation and that obtained by a constant equivalent path lengths assumption and by the SAM and the ITU-R model are in good agreement, for example at the second peak of the event on September 5 and at the onset of September 7. However, this condition remains only for a short time. Roughly speaking, changes in rain rates of deep convective occur locally and not over the entire satellite path. Hence, measured attenuation and model-generated attenuation are different.

c). *Shallow convective*

Figure 8.13 is the same as Fig. 8.7 but for two shallow convective events on March 9 and April 21, 2006. The maximum rain rate recorded for Fig. 8.13a and Fig. 8.13c are around 83 mm/h and 52 mm/h, respectively. Figure 8.13b and Fig. 8.13d show simultaneous measurements of attenuation and they are compared with the attenuation calculated from the DSD and from the power law of Table 8.2. Unlike the deep convective, the maximum value of observed attenuation is not in agreement with the attenuation obtained by a constant equivalent path length assumption and by the SAM and the ITU-R model. Moreover, the pattern of time series of observed attenuation is different from the rainfall rate time series.
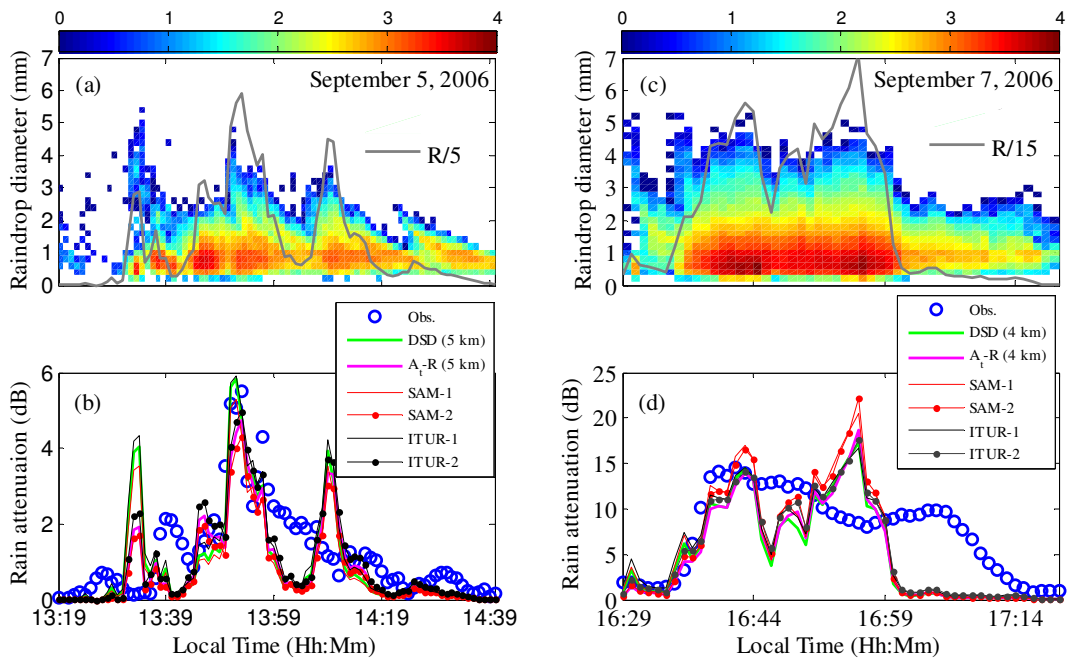
Figure 8.10: Same as Fig. 8.7 but for deep convective events on September 5 and 7, 2006.
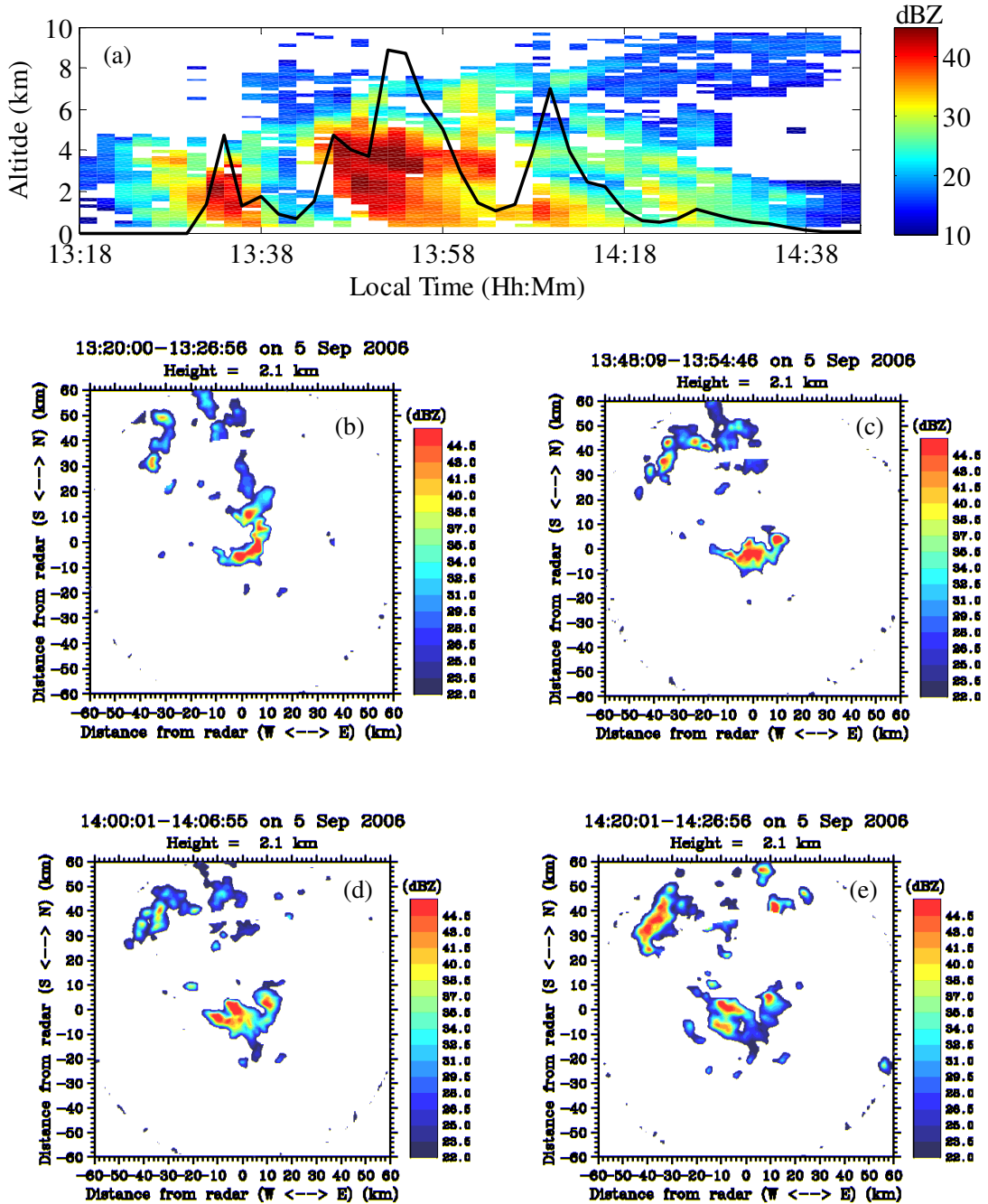
Figure 8.11: Same as Fig. 8.8 but for deep convective events on September 5, 2006. Black-solid line in (a) is the rainfall rate from 2DVD observation (R/3).
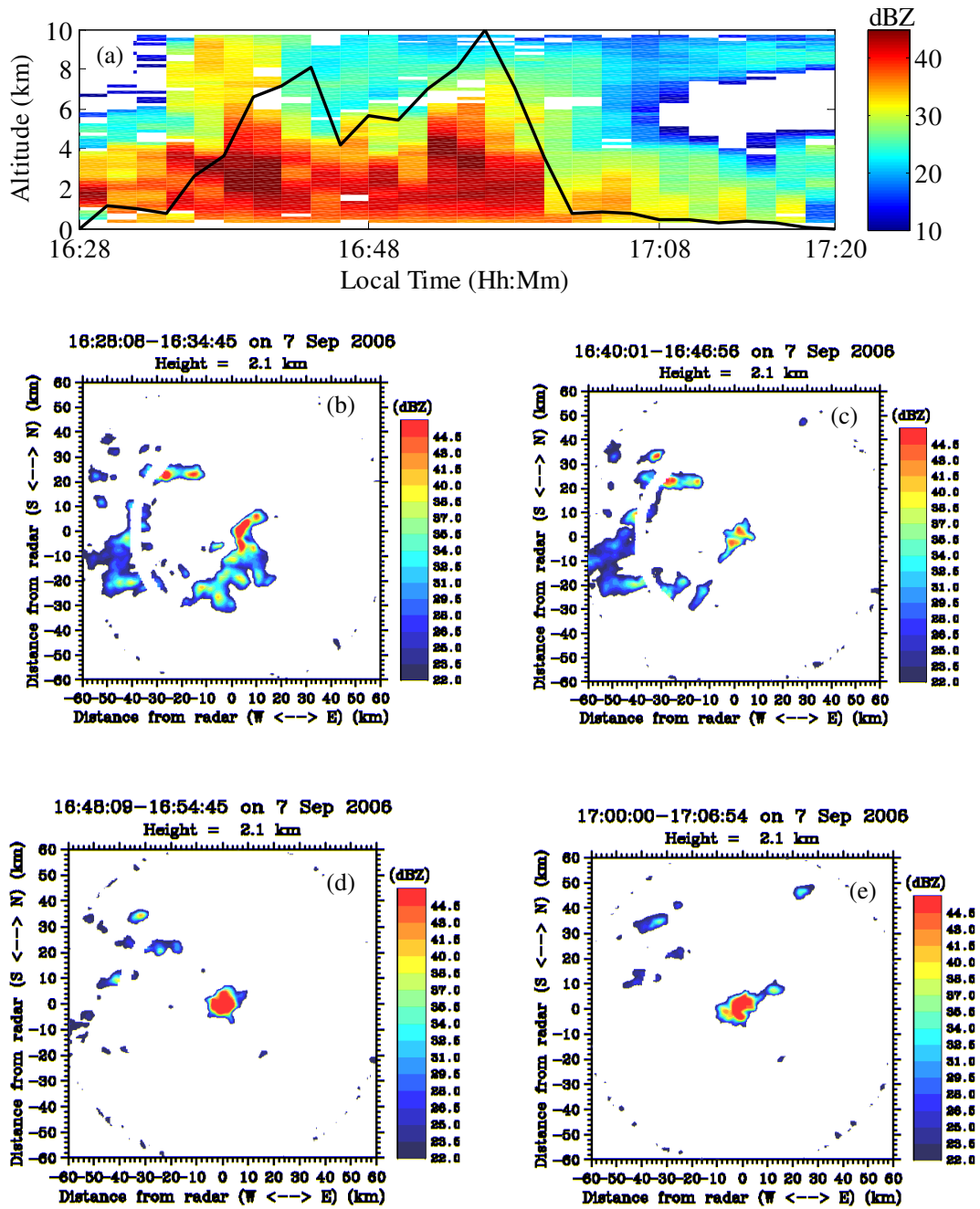
Figure 8.12: Same as Fig. 8.8 but for deep convective events on September 7, 2006. Black-solid line in (a) is the rainfall rate from 2DVD observation (R/9).

On March 9, changes in rain rates did not reflect in the measured attenuations. Maximum measured attenuation occurs at the onset of the event in which the rainfall rate is not maximum at that time. On April 21, although the rain intensity is high, the observed attenuation is smaller than 2 dB throughout the event. The DSD spectra of this event are very narrow (< 2.5 mm).

Besides the difference in the pattern of time series, the maximum value of observed attenuation is also much different from the models. It can be seen that taking 3 km and 2 km for Fig. 8.13b and Fig. 8.13d, respectively, as a constant equivalent path length provides the maximum value of model-generated attenuation being close to the maximum of measured attenuation. We have calculated the SAM and the ITU-R model by assuming the rain height of 5 km. Consequently, the attenuation generated by these models is much larger than the measured values. Figure 8.15 and 8.14 provide the horizontal extension of rain cell at 2.1 km from X-band radar observation and the rain height from 1.3 GHz wind profiler observation. Like in deep convective rain, the spatial distribution of the two shallow events is also small. At the onset of the event on March 9, the rain shows a deep convective type so that the maximum attenuation is visible. Thereafter, the rain height decreases as the time increases. On April 21, the rain height is generally less than 4 km and some time only 2 km. Therefore, besides the narrow DSD and inhomogeneity of rain cell, low rain height of shallow convective also contribute to the small attenuation during this event.

Schumacher and Houze (2003) found that the ratio of the convective rain rate to the stratiform rain rate is 4.1 on average at the horizontal resolution of the Tropical Rainfall Measuring Mission (TRMM) Precipitation Radar (PR) data. They also found that the shallow, isolated rain elements dominate the outer fringes of the tropical rain. In Chapter 6 we have observed stratiform, mixed stratiform/convective, deep convective and shallow convective precipitation accounting for 59%, 4%, 9% and 28% of the data covered by rain over a 2-yr period (2006-2007). Shallow precipitation contributes much to overall rain accumulation. From the above case studies, the agreement between the measured and the model-generated attenuation is not good for convective particularly for shallow convective rain. Using rain height of 4.5-5 km in the attenuation models for equatorial region may be acceptable for general case (mainly for stratiform

and deep convective rain). However, it may be lower (e.g., < 3 km) for shallow convective rain.
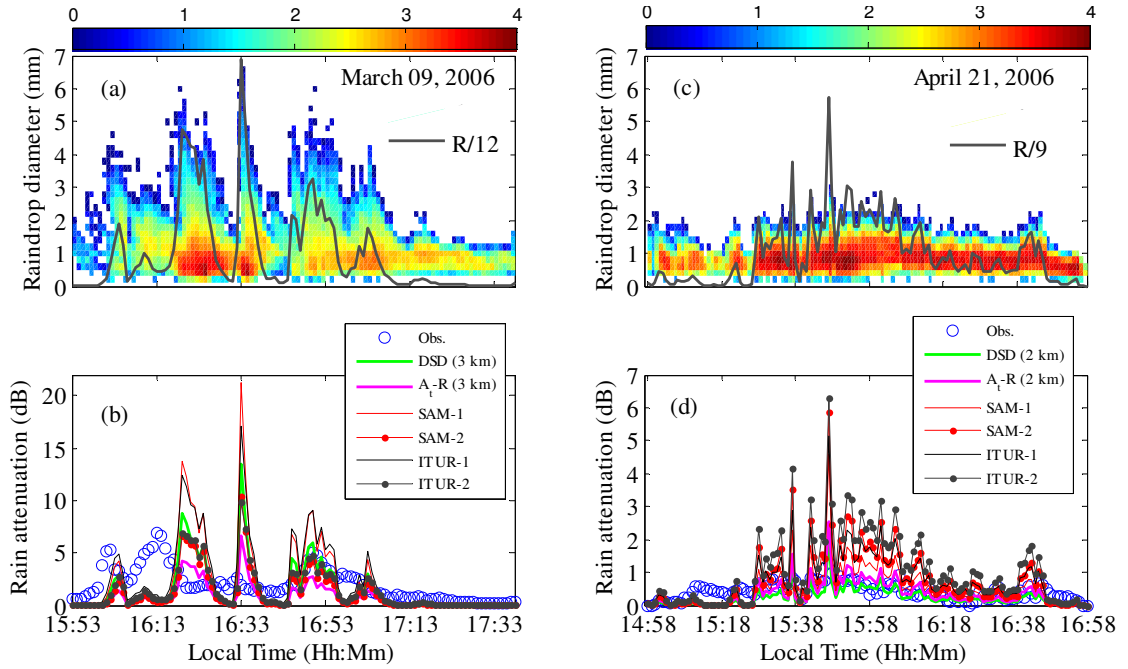
Figure 8.13: Same as Fig. 8.7 but for shallow convective events on March 9 and April 21, 2006.
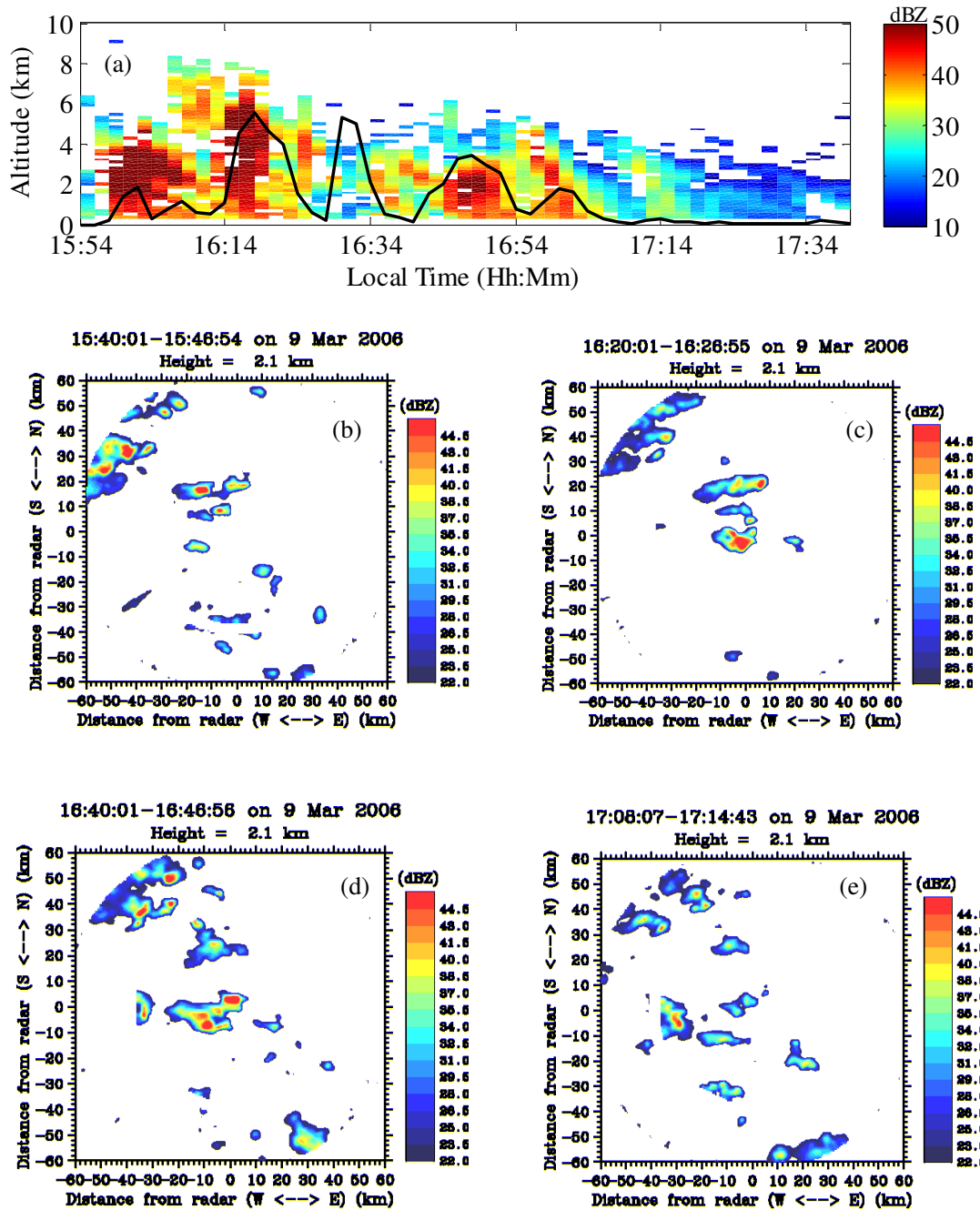
Figure 8.14: Same as Fig. 8.8 but for shallow convective events on March 9, 2006. Black-solid line in (a) is the rainfall rate from 2DVD observation (R/9).

194
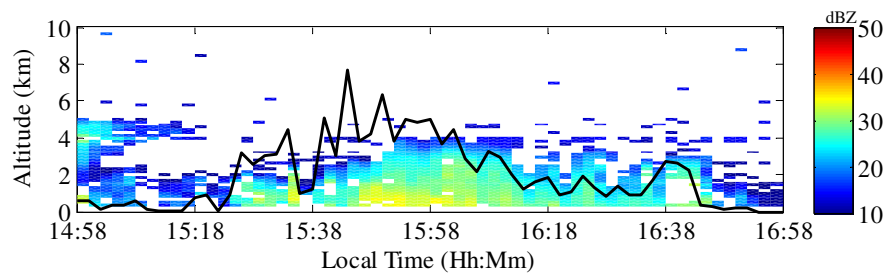
Figure 8.15: Same as Fig. 8.8 but for shallow convective events on April 21, 2006. Black-solid line in (a) is the rainfall rate from 2DVD observation (R/4).

Chapter 9

Summary and Conclusion

The first part of this thesis considered the importance of precipitation microstructure study for several fields. In Chapter 2 the reviews of precipitation formation, microphysical properties of raindrops, observation of precipitation using radar and attenuation due to rain were given. Chapter 3 was devoted to presenting an overview of the instrumentation. 2D-Video Distrometer (2DVD) standard matching algorithm were evaluated and shown to be inadequate, whereas the new matching algorithm (re-matching) proves to be highly accurate. In Chapter 3 we also evaluated the sampling size error of 2DVD. It was found that the uncertainties of rainfall rate and radar reflectivity decrease with increasing number of raindrops. In addition to a 1-min rainfall-rate threshold of 0.1 mm/h, it is important to consider a 1-min number of drops threshold to reduce the sampling size error of 2DVD measurement. We used a 1-min number of drops threshold of 100 in this thesis.

Chapter 4 was devoted to evaluating the bias of moment method (MM), maximum likelihood method (ML) and L-moment method (LM), to calculate the DSD parameters of exponential, gamma and lognormal functions. The biases of all moment estimators were larger than those of the LM and the ML methods. In general, the DSD parameters obtained by the MM were larger than those of the underlying DSD from which the samples are taken. In case of exponential and gamma DSD, the biases were significantly influenced by the total number of drops (N_T) and the moment estimator used. The biases decreased with increasing N_T and vice-versa (moment estimators). The MM might provide the results

of sufficient accuracy even very close to those of the LM and the ML methods if very large samples of drops were available. On the other hand, transforming the moment of DSD to logarithmic scale in lognormal distribution might reduce the sensitivity of MM to the number of drops and the shape of DSD. Unlike the MM, ML and LM methods were not significantly affected by the number of drops. For truncated samples, the performance of all methods decreased, particularly for the MM involving low order moments, the ML and LM methods, even in case of gamma and exponential distribution, the MM involving the third moment M_3 gave better results than the ML and the LM and lower moment estimators if very large samples of drops were available. For the lognormal distribution, the LM and ML methods are always gives superior results in comparison with the MM. It was also found that the truncation procedure has significant impact on the DSD parameters estimation when the spectrum is broad, particulary for low order moments, ML and LM method. Besides selection of the method used, the selection of correct fit or distribution was also an important factor in fitting the DSD. Selection of correct fit or distribution will provide the result that corresponds to the population from which the samples are drawn. For Kototabang (KT) data, although the performance of gamma distribution did not differ from the lognormal much, it exhibited better agreement between calculated and observed DSD and rainfall rate than the lognormal as well as the exponential distribution.

In Chapter 5 the bias study was extended to the bin width selection of 2DVD data. It was shown that the bin width selection influence the shape of DSD. With very large number of raindrop which should be accompanied by heavy rain, the bin width error was relatively small. However, the bias was significant in the opposite case. Thus, this sensitivity to the bin width selection by which DSDs are determined should be kept in mind when comparing the DSD and integral rainfall parameters from various study, all of which may have different bin size for quantization of DSD. For 2DVD, using midsize of bin (bin size of 0.20-0.30 mm) as the representative value for the class (bin) of binned data may be the best choice because the DSD parameters of these bin widths are very close to those obtained from drop-by-drop data. Unlike the 2DVD, the widths of bin used in some other instruments such as Joss and Waldvogel Disdrometer (JWD)

and Parsivel are not uniform and increase as drop size increases. In the future, it is also worthwhile to study the effect of binning procedure for these instruments.

Chapter 6 was devoted to presenting a follow-up study on the diurnal, seasonal and intraseasonal variation of DSD at KT. With simultaneous observations of 2DVD and 1.3-GHz wind profiler, we could study not only rainfall rate and type dependence of the DSD but also the precipitation type dependence of the raindrop falling velocity and axis ratio. Rain type dependence of raindrop falling velocity and axis ratio were not significantly observed. Therefore, usage of single velocity–drop size and axis ratio–drop size for all rain types are acceptable. However, it was evident that correction for the effect of air density brings the terminal velocities much larger than the observed drop fall velocities. Hence, the location (864 m above sea level) of KT did not result in a different terminal velocity from Gunn-Kinzer's data. Furthermore, the raindrop axis ratio at KT was more spherical than that of artificial rain and equilibrium axis ratio. It was close to Jones' result, the axis ratio collected in the turbulent high shear zone of surface layer.

Of some DSD variabilities at KT, rainfall type dependence and diurnal variation of the DSD parameters such as the scaling parameter for drop concentration (N_w), the shape parameter (μ) and the mass-weighted mean diameter (D_m), were significantly observed. For light and moderate rain ($R < 10$ mm/h), stratiform rain had larger (smaller) D_m (N_w) than convective one. On the other hand, at higher rainfall rate the D_m was larger in convective rain than in stratiform one. Bigger mean raindrops during stratiform rains were associated with a strong bright band (BB), while bigger mean raindrops during convective rains were found at the very start of rain. It was also observed that D_m and N_w increase with increasing rainfall rate, but, on the other hand, μ decreases with increasing rainfall rate. The increase of N_w with a corresponding rise of D_m as R increases, indicated that the spectrum broadening is mostly due to increase of large-sized drops that substantially affect the rainfall rate. This result was consistent with the relationship between rainfall rate and maximum drop diameter (D_{max}). For $R < 30$ mm/h, D_{max} increased rapidly with increasing R. However, for $30 < R < 70$ mm/h the increase of D_{max} with R was considerably smaller. Finally, D_{max} remained remarkably constant (approximately at 5 mm) for $R > 70$ mm/h. At intense rainfall, the total number of drops continued to increase rather than the

drop size which is probably due to the increase of breakup induced by collision, limiting the maximum drop size.

From the whole dataset, 71% of the total rainfall were in the evening hours that comes from 52% of the profiles. More than 80% of the total rainfall or 60% of the total profile in the evening hours was composed of convective rain, whereas about 73% of the total rainfall or 80% of the total profiles in the morning hours was composed of stratiform rain. The main peak of convective data appeared around 14:00-17:00 LT with the main peak of deep convective rainfall observed at 16:00 LT. Stratiform rain had a bimodal variation with the main peak around 00:00-01:00 LT and a subpeak at 21:00 LT. In general our result is consistent with previous studies, but the percentage of occurrence of stratiform rain for the morning hours in our result is larger. Clearly observed was the difference in the DSD parameters between morning and the evening. The mean D_m values in the evening were larger than their counterparts in the morning hours, whereas the mean N_w values in the evening were smaller than those in the morning hours. Therefore, the DSDs in the morning hours are narrower than those in the evening hours. Diurnal variation of DSD leads to diurnal variation of $Z - R$ relations. Consequently, usage of a single $Z - R$ relation to convert Z into R will underestimate at one time and overestimate at other times.

The seasonal variation of DSD at KT was not clearly visible. We did not find the continental-like and oceanic-like cluster of the DSD in the SW and NE monsoons, respectively, as found in the Asian monsoon region (e.g., Gadanki, India). Lack of seasonal variation of DSD at KT in comparison with Gadanki, India was probably due to the local convection and the effect of complex topography of Sumatra Island (orographic effect). However, the mean D_m value in our result was larger than that considered as orographic rain, particularly for 2006-2007 data. Orographic effect may be significant during the MJO phase which is associated with the passage of large scale cloud systems over Sumatra. In the end of active MJO phase associated with very strong westerly wind regarded as a westerly wind burst, very small (large) value of D_m (N_w) (in the range of those of orographic precipitation) were observed (case study: during CPEA-I). In the future, more study is needed to fully understand the microstructure of rain clouds

over Sumatra that can be classified into continental, intermediate and maritime as well as orographic type.

In Chapter 7 the complex dielectric constant of real rainwater, as collected in nature, was evaluated. The complex permittivity of a few rainwater samples, which is required for the modeling electromagnetic waves propagation in rain, has been measured in the frequency range 0.5-26.5 GHz using an Agilent Technologies 85070E dielectric probe kit and an Agilent N5242A-400 Vector Network Analyzer (VNA). It was found that the measured values do not differ significantly from the results of Liebe's model. In addition, the difference in the complex permittivity of rainwater between the measurement and model results exhibits very small biases in the Mie extinction coefficients.

Chapter 8 were devoted to modeling the rain attenuation for Sumatra (KT). We found some discrepancies of the International Telecommunication Union-Radiocommunication Sector (ITU-R) models to predict the rain attenuation for Sumatra. At large time percentages, the cumulative distribution of measured rain rates was in fairly good agreement with that obtained from the ITU-R model. Considerable differences between the recorded data and the ITU-R model were observed at small time percentages of annual rainfall rate and at the average worst month and its relationship with the average annual distribution. Thus, this discrepancy should be kept in mind when modeling the rain attenuation for Sumatra, particularly for KT. The natural variations (diurnal and rainfall type) of the DSD at KT influence the rain attenuation modeling for this region. The effect of diurnal variation of the DSD on the specific rain attenuation was obvious for convective rain in which the largest rain attenuation occurs when rain events occur in the first half of the day. The diurnal variation was serious for frequencies higher than 60 GHz especially in very extreme rain. Measured rain attenuation of Ku-band satellite communication links for stratiform rains was in good agreement with the values obtained by the DSD and $\gamma - R$ relationship through Simple Attenuation Model (SAM) and the ITU-R. However, the agreement for convective rain, especially for shallow convective, was not good. Some assumption on the models such as rain height and spatial distribution of shallow convective rain for Sumatra need to be characterized in the future.

Appendix A

List of Acronyms

2DVD	2D-Video Distrometer
AFE	Average Fractional Errors
BB	Bright Band
BLR	Boundary Layer Radar (1.3 GHz Wind Profiler)
BMKG	Meteorology, Climatology and Geophysics Agency of Indonesia
CAPPI	Constant Altitude Plan Position Indicator
CFAD	Countered Frequency by Altitude Diagrams
CPEA	Coupling Processes in the Equatorial Atmosphere
DVG	Doppler Velocity Gradient
EAR	Equatorial Atmosphere Radar
GAW	Global Atmosphere Watch
GMT	Generic Mapping Tools
IRPs	Integrals Rainfall Parameters
ISV	Intraseasonal Variation
JWD	Joss and Waldvogel Disdrometer
KT	Kototabang
LM	L-Moment Method
LWC	Liquid Water Content
LT	Local Time
MAWS	Mobile Automatic Weather Station
MEWS	Meteorological Early Warning System
MJO	Madden-Julian Oscillation
MM	Moment Method
ML	Maximum Likelihood Method
MP	Marshall and Palmer's model
MSW	Maximum Spectral Width

NRMSE	Normalized Root Mean Squared Error
OEU	Outdoor Electronics Unit
PMM	Probability Matching Method
POSS	Precipitation Occurrence Sensor System
ORG	Optical Rain Gauge
QPE	Quantitative Precipitation Estimation
RISH	Research Institute for Sustainable Humanosphere
RHI	Range Height Indicator
RMSE	Root Mean Square Error
RMSD	Root Mean Square Difference
SAM	Simple Attenuation Model
SATP	Sorting and Averaging Based on Two Parameters
SAR	Synthetic Aperture Radar
SCC	Super Cloud Cluster
SIFT	Sequential Intensity Filtering Technique
SRTM	Shuttle Radar Topography Mission
SW	Southwest Monsoon
NE	Northeast Monsoon
TRMM	Tropical Rainfall Measuring Mission
VNA	Vector Network Analyzer
UHF	Ultra High Frequency
VHF	Very High Frequency
VPRG	Vertical Profile of Radar Reflectivity Gradient

References

AGILENT, T. (2008). *Agilent 85070E Dielectric Probe Kit 200 MHz to 50 GHz; Technical Overview*. USA: Agilent Technologies, Inc., (available at http://cp.literature.agilent.com/litweb/pdf/5989–0222EN.pdf). 54, 162

AL-KHASHMAN, O.A. (2009). Chemical characteristics of rainwater collected at a western site of Jordan. *Atmos. Environ.*, **91**, 53 – 61. 160

AL-MOMANI, I.F., ATAMAN, O.Y., ANWARI, M.A., TUNCEL, S., KSE, C. AND TUNCEL, G. (1995). Chemical composition of precipitation near an industrial area at Izmir, Turkey. *Atmos. Environ.*, **29**, 1352–2310. 160

ANDSAGER, K., BEARD, K. AND LAIRD, N. (1999). Laboratory measurements of axis ratios for large raindrops. *J. Atmos. Sci.*, **56**, 2673–2683. 17, 20, 122

ATLAS, D. AND ULBRICH, C. (1977). Path- and area-integrated rainfall measurement by microwave attenuation in the 13 cm band. *J. Appl. Meteorol.*, **16**, 1322–1331. 20

ATLAS, D., SRIVASTAVA, R.C. AND SEKHON, R.S. (1973). Doppler radar characteristics of precipitation at vertical incidence. *Rev. Geophys. Space Phys.*, **11**, 1–35. 20, 47, 120

ATLAS, D., ULBRICH, C.W. AND MENEGHINI, R. (1984). The multiparameter remote measurement of rainfall. *Radio Sci.*, **19**, 3–22. 31

BATTAN, J.L. (1973). *Radar Observation of the Atmosphere*, vol. 2. University of Chicago Press. 22, 23, 28

BEARD, K. AND JAMESON, A. (1983). Raindrop canting. *J. Atmos. Sci.*, **40**, 448–454. 21, 124

BEARD, K., JOHNSON, D.B. AND JAMESON, A.R. (1983). Collisional forcing of raindrop oscillations. *J. Atmos. Sci.*, **40**, 455–462. 124

BEARD, K.V. (1976). Terminal velocity and shape of cloud and precipitation drops aloft. *J. Atmos. Sci.*, **33**, 851–864. 126

BEARD, K.V. (1984). Raindrop oscillations: Evaluation of a potential flow model with gravity. *J. Atmos. Sci.*, **41**, 1765–1774. 125

BEARD, K.V. (1985). Simple altitude adjustments to raindrop velocities for doppler radar analysis. *J. Atmos. Oceanic Tech.*, **2**, 468–471. 121

BEARD, K.V. AND CHUANG, C. (1987). A new model for the equilibrium shape of raindrops. *J. Atmos. Sci.*, **44**, 1509–1524. xvi, 16, 17, 18, 20, 122, 123, 124, 126

BEARD, K.V. AND PRUPPACHER, H. (1969). A determination of the terminal velocity and drag of small water drops by means of a wind tunnel. *J. Atmos. Sci.*, **26**, 1066–1072. 20

BEARD, K.V., FENG, J. AND CHUANG, C. (1989). A simple perturbation model for the electrostatic shape of falling drops. *J. Atmos. Sci.*, **46**, 2404–2418. 16

BEIDERWIEDEN, E., WRZESINSKY, T. AND KLEMM, O. (2005). Chemical characterization of fog and rain water collected at the eastern Andes cordillera. *Hydrol. Earth Syst. Sci. Discuss.*, **2**, 863–885. 160

BEYSENS, D., OHAYON, C., MUSELLI, M. AND CLUS, O. (2006). Chemical and biological characteristics of dew and rain water in an urban coastal area (bordeaux, france). *Atmos. Environ.*, **40**, 3710 – 3723. 160

BIGGERSTAFF, M.I., AND LISTEMAA, S.A. (2000). An improved scheme for convective/stratiform echo classification using radar reflectivity. *J. Appl. Meteorol.*, **39**, 2129–2150. 111

BLANCHARD, D.C. AND SPENCER, A.T. (1970). Experiments on the generation of raindrop-size distributions by drop breakup. *J. Atmos. Sci.*, **27**, 101–108. 130

BOHREN, C.F. AND HUFFMAN, D.R. (1983). *Absorption and Scattering of Light by Small Particles*. John Wiley & Sons, Inc, New York. 24, 25, 27, 32, 176

BRANDES, G.Z., E.A. AND VIVEKANANDAN, J. (2002). Experiments in rainfall estimation with a polarimetric radar in a subtropical environment. *J. Appl. Meteorol.*, **41**, 674–685. 18, 19, 20, 122

BRINGI, V. AND CHANDRASEKAR, V. (2001). *Polarimetric Doppler Weather Radar: Principles and Application*. Cambridge Univ. Press, United Kingdom. 22, 29, 32

BRINGI, V.N., CHANDRASEKAR, V., HUBBERT, J., GORGUCCI, E., RANDEU, W.L. AND SCHOENHUBER, M. (2003). Raindrop size distribution in different climatic regimes from disdrometer and dual-polarized radar analysis. *J. Atmos.Sci.*, **60**, 354–365. 111, 118, 128, 131, 132, 142

BRUSSAARD, G. (1974). Rain-induced crosspolarisation and raindrop canting. *Electron. Lett.*, **10**, 411–412. 21

BRUSSAARD, G. (1976). A meteorological model for rain-induced cross polarization. *IEEE Trans. Antennas Propag.*, **24**, 5–11. 21

CAO, Q., ZHANG, G., BRANDES, E., SCHUUR, T., RYZHKOV, A. AND IKEDA, K. (2008). Analysis of video disdrometer and polarimetric radar data to characterize rain microphysics in Oklahoma. *J. Appl. Meteorol. Climatol.*, **47**, 2238–2255. 50, 133

CARACCIOLO, C., PRODI, F., BATTAGLIA, A. AND PORCU, F. (2006). Analysis of the moments and parameters of a gamma dsd to infer precipitation properties: A convective stratiform discrimination algorithm. *Atmos. Res.*, **80**, 165–186. 2, 56, 75

CARTER, D.A., GAGE, K.S., ECKLUND, W.L., ANGEVINE, W.M., JOHNSTON, P.E., RIDDLE, A.C., WILSON, J. AND WILLIAMS, C.R. (1995). Developments in UHF lower tropospheric wind profiling at NOAA's aeronomy laboratory. *Radio Sci.*, **30**, 997–1001. 52

CHANDRASEKAR, V. AND BRINGI, V.N. (1987). Simulation of radar reflectivity and surface measurements of rainfall. *J. Atmos. Oceanic Tech.*, **4**, 464–478. 15

CHANDRASEKAR, V., COOPER, W.A. AND BRINGI, V.N. (1988). Axis ratios and oscillations of raindrops. *J. Atmos. Sci.*, **45**, 1323–1333. 126

CHEBIL, J. AND RAHMAN, T.A. (1999). Worst-month rain statistics for radio wave propagation study in Malaysia. *Electron. Lett.*, **35**, 1447–1449. 173

CHOI, Y.S., LEE, J.H., PARK, S.K., LEE, H.S., AND PACK, J.K. (1999). The effect of size distribution of rain-drops on the specific rain attenuation. *Proceedings of ICT'99*. 182

CHUANG, C.C. AND BEARD, K. (1990). A numerical model for the equilibrium shape of electrified raindrops. *J. Atmos. Sci.*, **47**, 1374–1389. 17

COLE, K.S. AND COLE, R.H. (1941). Dispersion and absorption in dielectrics-i, alternating current characteristics. *J. Chem. Phys.*, **9**, 341–351. 158

COLLIE, C.H., HASTED, J.B. AND RITSON, D.M. (1948). The dielectric properties of water and heavy water. *Proc. Phys. Soc. (London)*, **60**, 145–160. 5, 157

COOK, H.F. (1952). A comparison of the dielectric behavior of pure water and human blood at microwave frequencies. *Brit. J. Appl. Phys.*, **3**, 249–255. 5, 157

COUTINHO, M.A. AND TOMS, P.P. (1995). Characterization of raindrop size distributions at the Vale Formoso Experimental Erosion Center. *CATENA*, **25**, 187 – 197. 2

CRANE, R.K. (1975). Attenuation due to rain-A mini review. *IEEE Trans. Antennas Propag.*, 750–752. 182

CRANE, R.K. (1980). Prediction of attenuation by rain. *IEEE Trans. Commun.*, **28**, 1717–1733. 34

DAVIDSON, D.W. AND COLE, R.H. (1950). Dielectric relaxation in glycerine. *J. Chem. Phys.*, **18**, 1417–1417. 159

DEBYE, P. (1929). *Polar Molecules*. The Chemical Catalog Company, New York. 158

DEMIRAK, A., BALCI, A., KARAOG, H. AND TOSMUR, B. (2006). Chemical characteristics of rain water at an urban site of south western Turkey. *Environ. Monit. Assess.*, **123**, 271–283. 161

DONNADIEU, G. (1980). Comparison of results obtained with the VIDIAZ spectropluviometer and the Joss–Wadvogel rainfall disdrometer in a rain of a thundery type. *J. Appl. Meteorol.*, **19**, 593–597. 2, 3, 39, 108

DOVIAK, R.J. AND ZRNIC, D. (1984). *Doppler Radar and Weather Observations*. Academic Press, San Diego. 22, 31

ERPUL, G., D. GABRIELS, D. AND JANSSENS, D. (1998). Assessing the drop size distribution of simulated rainfall in a wind tunnel. *Soil Tillage Res.*, **45**, 455–463. 152

ERPUL, G., D. GABRIELS, D. AND JANSSENS, D. (2000). Effect of wind on size and energy of small simulated raindrops: a wind tunnel study. *Int. Agrophys.*, **14**, 1–7. 152

FEINGOLD, G. AND LEVIN, Z. (1986). The lognormal fit to raindrop spectra from frontal convective clouds in Israel. *J. Clim. Appl. Meteorol.*, **25**, 1346–1363. 2, 15, 88

FIEBIG, U.C. AND RIVA, C. (2004). Impact of seasonal and diurnal variations on satellite system design in V band. *IEEE Trans. Antennas Propag.*, **52**, 923 – 932. 170

FOOTE, G.B. AND TOIT, P.S.D. (1969). Terminal velocity of raindrops aloft. *J. Appl. Meteorol.*, **8**, 249–253. 120

FUJIWARA, M. AND YANASE, T. (1971). On raindrop-size distribution on warm rain. *Meteorol. Geophys.*, **22**, 61–68. 143

FUKAO, S. (2006). Coupling processes in the equatorial atmosphere (CPEA): A project overview. *J. Meteorol. Soc. Japan*, **84A**, 1–18. 4, 109

FUKAO, S., WAKASUGI, K., SATO, T., MORIMOTO, S., TSUDA, T., HIROTA, I., KIMURA, I. AND KATO, S. (1985). Direct measurement of air and precipitation particle motion by VHF doppler radar. *Nature*, **316**, 712–714. 53

FUKAO, S., HASHIGUCHI, H., YAMAMOTO, M., TSUDA, T., NAKAMURA, T., YAMAMOTO, M.K., SATO, T., HAGIO, M. AND YABUGAKI, Y. (2003). Equatorial atmosphere radar (EAR): System description and first results. *Radio Sci.*, **38**, doi:10.1029/2002RS002767. 4, 53

GAGE, K.S. AND WILLIAMS, C.R. (2005). Use of radar profilers in multi-sensor ground validation for TRMM and GPM. *Proc. Geosci. Remote Sensing Symp (IGARSS '05)*, **6**, 4116– 4119. 92

GAGE, K.S., WILLIAMS, C.R. AND ECKLUND, W.L. (1994). UHF wind profilers: A new tool for diagnosing tropical convective cloud system. *Bull. Am. Meteorol. Soc.*, **75**, 2289–2294. 52

GRANT, E.H. AND SHACK, R. (1967). Complex permittivity measurements at 8.6 mm wavelength over the temperature range 1-60°C. *Brit. J. Appl. Phys.*, **18**, 1807–1814. 5, 157

GRANT, E.H., BUCHANAN, T.J. AND COOK, H.F. (1957). Dielectric behavior of water at microwave frequencies. *J. Chem. Phys.*, **26**, 156–161. 5, 157

GRAY, W.R., UDDSTROM, M.J. AND LARSEN, H.R. (2002). Radar surface rainfall estimates using a typical shape function approach to correct for the variations in the vertical profile of reflectivity. *Inter. J. Remote Sens.*, **23**, 2489–2504. 32

GREEN, A.W. (1975). An approximation for the shape of large raindrops. *J. Appl. Meteorol.*, **14**, 1578–1583. 17

GUNN, R. AND KINZER, G. (1949). The terminal velocity of fall for water droplets in stagnant air. *J. Meteorol.*, **6**, 243–248. xvi, xvii, xxiii, 20, 21, 39, 40, 41, 119, 120

GUPTA, R. AND KUNDU, D. (2003). Closeness of gamma and generalized exponential distribution. *Comm. Stat.Theor. Methods*, **32**, 705–721. 65

HADDAD, Z.S., DURDEN, S.L. AND IM, E. (1996). Parameterezing the raindrop size distribution. *J. Appl. Meteorol.*, **35**, 3–13. 61

HAN, G. AND LIU, C.Q. (2006). Strontium isotope and major ion chemistry of the rainwaters from guiyang, guizhou province, china. *Sci. Total Environ.*, **364**, 165 – 174. 160

HAUSER, D., AMAYENC, P. AND NUTTEN, B. (1984). A new optical instrument for simultaneous measurement of raindrop diameter and fall speed distributions. *J. Atmos. Oceanic Technol.*, **1**, 256–269. 2, 3, 39, 108

HOLT, A.R. (1984). Some factors affecting the remote sensing of rain by polarization diversity radar in the 3-to-35 GHz range. *Radio Sci.*, **19**, 1399–1412. 21

HONG, Y., KUMMEROW, C.D. AND OLSON, W.S. (1999). Separation of convective and stratiform precipitation using microwave brightness temperature. *J. Appl. Meteorol.*, **38**, 1195–1213. 111

HOSKING, J.R.M. (1990). L-moments: Analysis and estimation of distributions using linear combinations of order statistics. *J. R. Stat. Soc., Ser. B*, **52**, 105–124. 63

HOUZE, R. (1993). *Cloud Dynamics*. Academic Press, San Diego. 9, 13

HOUZE, R. (1997). Stratiform precipitation in regions of convection: A meteorological paradox? *Bull. Amer. Meteorol. Soc.*, **78**, 2179–2196. 13

HOWARD, J. AND GEROGIOKAS, M. (1982). A statistical raindrop canting angle model. *IEEE Trans. Antennas Propag.*, **30**, 141–147. 21

HUANG, G.J., BRINGI, V.N., SCHÖNEHUBER, M., THURAI, M., SHIMOMAI, T., KOZU, T., MARZUKI, M. AND HARJUPA, W. (2007). Drop shape and canting angle distribution in rain from 2-D video disdrometer. *Proc. 33rd Conf. on Radar Meteorol. Cairns, Australia.* 123, 124

HUGGEL, A., SCHMID, W. AND WALDVOGEL, A. (1996). Raindrop size distributions and the radar bright band. *J. Appl. Meteorol.*, **35**, 1688–1701. 138, 146

ILLINGWORTH, A., ed. (2004). *Polarimetric Measurements*, vol. 2 of *In: Weather Radar, P. F. Meischner*. Springer, Germany. 22, 31

ITU-RECOMMENDATIONS (1990). *The concept of worst month*. P.581-2, Geneva. 172

ITU-RECOMMENDATIONS (2001). *Characteristics of precipitation for propagation modelling*. P.837-3, Geneva. xxvi, 34, 170, 172, 173

ITU-RECOMMENDATIONS (2002). *Specific attenuation model for rain for use in prediction methods*. P.838-3, Geneva. xxvi, xxvii, 34, 177, 178, 179

ITU-RECOMMENDATIONS (2005). *Conversion of annual statistics to worst-month statistics*. P.841-4, Geneva. xxvi, 173, 174, 175

ITU-RECOMMENDATIONS (2007). *Propagation data and prediction methods required for the design of earthspace telecommunication systems*. P.618-9, Geneva. 182, 184

JIRIES, A. (2001). Chemical composition of dew in Amman, Jordan. *Atmos. Environ.*, **57**, 261–268. 161

JONES, D.M. (1959). The shape of raindrops. *J. Meteorol.*, **16**, 504–510. 126

JOSS, J. AND GORI, E.G. (1978). Shapes of raindrop size distributions. *J. Appl. Meteorol.*, **17**, 1054–1061. 14, 73, 84, 86

JOSS, J. AND WALDVOGEL, A. (1969). Raindrop size distribution and sampling size errors. *J. Atmos. Sci.*, **26**, 566–569. 2, 3, 45, 48, 91, 108

JOSS, J. AND WALDVOGEL, A., eds. (1990). *Precipitation measurements and hydrology*, vol. 14 of *In: Radar in Meteorology, D. Atlas Ed.*. Amer. Meteorol. Soc., Boston. 32

KAATZE, U. (1989). Complex permittivity of water as a function of frequency and temperature. *J. Chem. Eng. Data*, **34**, 371–374. xxv, 162, 163

KAWASHIMA, M., FUJIYOSHI, Y., OHI, M., HONDA, T., KOZU, T., SHIMO-MAI, T. AND HASHIGUCHI, H. (2006). Overview of doppler radar observations of precipitating cloud systems in Sumatera island during the first CPEA campaign. *J. Meteorol. Soc. Japan*, **84A**, 33–56. 116, 152

KEENAN, T.D., CAREY, L., ZRNIC', D. AND MAY, P. (2001). Sensitivity of 5-cm wavelength polarimetric radar variables to raindrop axial ratio and drop size distribution. *J. Appl. Meteorol.*, **40**, 526–545. 18, 122, 123

KITCHEN, M., BROWN, R. AND DAVIES, A. (1994). Real-time correction of weather radar data for the effects of bright band, range and orographic growth in widespread precipitation. *Q. J. R. Meteorolog. Soc.*, **120**, 1231–1254. 32

KLICHE, D., SMITH, P. AND JOHNSON, R. (2008). L-moment estimators as applied to gamma drop size distributions. *J. Appl. Meteorol. Climatol.*, **47**, 3117–3130. 56, 75

KOOL, P.S., TRAN, V.N., LEONG, M.S. AND YEO, T.S. (1992). Microwave complex permittivity of rainwater in the 26-40-GHz band. *Microwave Opt. Technol. Lett.*, **5**, 198–201. 161

KOZU, T. AND NAKAMURA, K. (1991). Rainfall parameter estimation from dual-radar measurements combining reflectivity profile and path-integrated attenuation. *J. Atmos. Oceanic Tech.*, **8**, 259–271. 2, 15, 55, 75, 77

KOZU, T., SHIMOMAI, T., AKRAMIN, Z., MARZUKI, SHIBAGAKI, Y. AND HASHIGUCHI, H. (2005). Intraseasonal variation of raindrop size distribution at Koto Tabang, West Sumatra, Indonesia. *Geophys. Res. Lett.*, **60**. 3, 38, 91, 92, 108, 109, 150

Kozu, T., Reddy, K.K., Mori, S., Thurai, M., Ong, J.T., Rao, D.N. and Shimomai, T. (2006). Seasonal and diurnal variations of raindrop size distribution in Asian monsoon region. *J. Meteorol. Soc. Japan*, **84A**, 195–209. 109, 135, 137, 140, 142

Kruger, A. and Krajewski, W.F. (2001). Two-dimensional video disdrometer: a description. *J. Atmos. Oceanic Tech.*, **19**, 602–617. 37, 108

Kubesh, R.J. and Beard, K. (1993). Laboratory measurements of spontaneous oscillations for moderate-size raindrops. *J. Atmos. Sci.*, **50**, 1089–1098. 17

Kulshrestha, U.C., Kulshrestha, M.J., Sekar, R., Sastry, G.S.R. and Vairamani, M. (2003). Chemical characteristics of rainwater at an urban site of south-central India. *Atmos. Environ.*, **37**, 3019 – 3026. 160

Kundu, D., Gupta, R. and Manglick, A. (2006). A convenient way of generating normal random variables using generalized exponential distribution. *J. Modern Appl. Stat. Meth.*, **5**, 266–272. 65

Lacaux, J.P., Delmas, R., Kouadio, G., Cros, B. and Andreae, M.O. (1992). Precipitation chemistry in the mayombe forest of equatorial africa. *J. Geophys. Res.*, **97**, 6195 – 6206. 160

Lang, S., Tao, W., Simpson, J. and Ferrier, B. (2003). Modeling of convectivestratiform precipitation processes: Sensitivity to partitioning methods. *J. Appl. Meteorol.*, **42**, 505–527. 111

Lee, G. and Zawadzki, I. (2005). Variability of drop size distributions : Noise and noise filtering in disdrometric data. *J. Appl. Meteorol.*, **44**, 634–652. 45, 47, 48, 50, 133, 176

Liebe, H.J., Hufford, G.A., and Manabe, T. (1991). A model for the complex permittivity of water at frequencies below 1Thz. *Int. J. Infrared and Millimeter Waves*, **12**, 659–674. xxv, 4, 5, 157, 159, 162, 163, 176

LIEBE, H.J., HUFFORD, G.A. AND COTTON, M. (1993). Propagation modeling of moist air and suspended water/ice particles at frequencies below 1000 GHz. *Proc. NATO/AGARD Wave Propagation Panel, 52nd Meeting*. 159

LIST, R., DONALDSON, N. AND STEWART, R.E. (1987). Temporal evolution and drop spectra to collisional equilibrium in steady and pulsating rain. *J. Atmos. Sci.*, **44**, 362–372. 130

LÖFFLER-MANG, M. AND JOSS, J. (2000). An optical disdrometer for measuring size and velocity of hydrometeors. *J. Atmos. Oceanic Technol.*, **17**, 130–139. 2, 3, 92, 108

MADDEN, R.A. AND JULIAN, P.R. (1972). Description of global-scale circulation cells in the tropics with a 40-50 day period. *J. Atmos. Sci.*, **29**, 1109–1123. 109

MAEKAWA, Y., FUJIWARA, T., SHIBAGAKI, Y., SATO, T., YAMAMOTO, M., HASHIGUCHI, H. AND FUKAO, S. (2006). Effects of tropical rainfall to the Ku-band satellite communications links at the equatorial atmosphere radar observatory. *J. Meteorol. Soc. Japan*, **84A**, 211–225. 169, 180, 181, 184

MAGONO, C. (1954). On the shape of water drops falling in stagnant air. *J. Atmos. Sci.*, **11**, 77–79. 16

MAITRA, A. AND GIBBINS, C.J. (1995). Inference of raindrop size distributions from measurements of rainfall rate and attenuation at infrared wavelengths. *Radio Sci.*, **30**, 931–941. 20

MAKI, M., PARK, S. AND BRINGI, V. (2005). Effect of natural variations in raindrop size distributions on rain rate estimators of 3 cm wavelength polarimetric radar. *J. Meteorol. Soc.Japan*, **83**, 871–893. 6

MARSAGLIA, G. AND TSANG, W.W. (2000). A simple method for generating gamma variables. *CM Trans.Math. Software*, **26**, 363–372. 66

MARSHALL, J.S. AND PALMER, W.M.K. (1948). The distribution of raindrops with size. *J. Meteorol.*, **5**, 165–166. 2, 14

Marzuki (2005). *Vertical structure of precipitation over west Sumtra as inferred from zenith looking radars*. Master's thesis, Interdisciplinary Faculty of Scince and engineering, Shimane University. 150, 151

Marzuki, Kozu, T. and Shimomai, T. (2006). Raindrop size distribution of tropical precipitation over west sumatera. *Proc. of 2006 International Symposium on Antennas and Propagation, Singapore, 1-4 November 2006*. 39

Marzuki, Kozu, T., Shimomai, T., Randeu, W.L., Hashiguchi, H. and Shibagaki, Y. (2009). Diurnal variation of rain attenuation obtained from measurement of raindrop size distribution in equatorial indonesia. *IEEE Trans. Antenas and Propag.*, **57**, 1191–1196. 170, 180

Marzuki, Kozu, T., Shimomai, T., Hashiguchi, H., Randeu, W.L. and Vonnisa, M. (2010). Raindrop size distributions of convective rain over equatorial indonesia during the first cpea campaign. *Atmos. Research*, **96**, 645 – 655. 116, 150, 151

Mätzler, C. (2002). Matlab functions for mie scattering and absorption version 2, IAP Research Report No. 2002-11, Institut für angewandte Physik, Universität Bern. 27

McFarquhar, G.M. and List, R. (1991). The raindrop mean free path and collision rate dependence on rainrate for three-peak equilibrium and marshall-palmer distributions. *J. Atmos. Sci.*, **48**, 1999–2003. 130

Mishchenko, M., Hovenier, J. and Travis, L. (2000). *Light Scattering by Nonspherical Particles: Theory, Measurements, and Applications*. Academic Press, San Diego. 24, 28

Mitchell, D.L. (1996). Use of mass- and area-dimensional power laws for determining precipitation particle terminal velocities. *J. Atmos. Sci.*, **53**, 1710–1723. 120

Moisseev, D.N. and Chandrasekar, V. (2007). Examination of the $\mu - \lambda$ relation suggested for drop size distribution parameters. *J. Atmos. Oceanic Technol.*, **24**, 847–855. 66

MORI, S., HAMADA, J., YUDI, I.T., YAMANAKA, M.D., OKAMOTO, N., MU-RATA, F., SAKURAI, N., HASHIGUCHI, H. AND SRIBIMAWATI, T. (2004). Diurnal landsea rainfall peak migration over Sumatra Island, indonesian maritime continent observed by TRMM satellite and intensive rawinsonde soundings. *Mon. Wea. Rev.*, **132**, 2021–2039. 135, 137, 139, 143

MPHEPYA, J.N., GALY-LACAUX, C., LACAUX, J.P., HELD, G. AND PIEN-AAR, J.J. (2006). Precipitation chemistry and wet deposition in Kruger National Park, South Africa. *J. Atmos. Chem.*, **53**, 169–183. 5, 157, 161

NEŠPOR, V., KRAJEWSKI, W. AND KRUGER, A. (2000). Wind-induced error of raindrop size distribution measurement using a two-dimensional video disdrometer. *J. Atmos. Oceanic Technol.*, **17**, 1483. 45

OGUCHI, T. (1983). Electromagnetic wave propagation and scattering in rain and other hydrometeors. *Proc. IEEE*, **71**, 1029–1078. 2, 33, 156

OKAMOTO, N., YAMANA, M.D., OGINO, S.Y., HASHIGUCHI, H., NISHI, N., SRIBIMAWATI, T. AND NUMAGUTI, A. (2003). Seasonal variations of tropospheric wind over indonesia: Comparison between collected operational rawinsonde data and ncep reanalysis for 1992-99. *J. Meteorol. Soc. Japan*, **81**, 829–850. 139, 140

OLSEN, R.L., ROGERS, D.V. AND HODGE, D.B. (1978). The ar^b relation in the calculation of rain attenuation. *IEEE Trans. Antennas Propag.*, **26**, 318–329. 34, 180

POLKOWSKA, Z., ASTEL, A., WALNA, B., MALEK, S., MEDRZYCKA, K., GRECKI, T., SIEPAK, J. AND NAMIESNIK, J. (2005). Chemical composition of dew in Amman, Jordan. *Atmos. Environ.*, **39**, 837 – 855. 160, 161

PRUPPACHER, H. AND BEARD, K.V. (1970). A wind tunnel investigation of the internal circulation and shape of water drops falling at terminal velocity in air. *Q. J. R. Meteorolog. Soc.*, **96**, 247–256. xvii, 16, 17, 19, 20, 40, 41, 122

PRUPPACHER, H. AND PITTER, R. (1971). A semi-empirical determination of the shape of cloud and rain drops. *J. Atmos. Sci.*, **28**, 86–94. 16, 17, 20

Pruppacher, H.R. and Klett, J.D. (1998). *Microphysics of clouds and precipitation*. Kluwer Academic, New York. 120

Puxbaum, H., Simeonov, V. and Kalina, M.F. (1998). Ten years trends (1984-1993) in the precipitation chemistry in central Austria. *Atmos. Environ.*, **32**, 193–202. 5, 157, 160, 161

Raghavan, S. (2003). *Radar Meteorology. Atmospheric and Oceanographic Sciences Library*. Springer-Verlag, New York, vol. 27 edn. xxix, 22, 23

Ralph, M.F. (1995). Using radar-measured radial vertical velocities to distinguish precipitation scattering from clear-air scattering. *J. Atmos. Oceanic Tech.*, **12**, 257–267. 114

Rao, T.N., Radhakrishna, B., Nakamura, K. and Rao, N.P. (2009). Differences in raindrop size distribution from southwest monsoon to northeast monsoon at Gadanki. *Q. J. R. Meteorolog. Soc.*, **135**, 1630 – 1637. 142

Ray, P.S. (1972). Broadband complex refractive indices of ice and water. *Appl. Optics*, **11**, 1836–1844. 4, 5, 157, 159, 176

Renggono, F., Hashiguchi, H., Fukao, F.S., Yamanaka, M.D., Ogino, S.Y., Okamoto, N., Murata, F., Sitorus, B.P., Kudsy, M., Kartasasmita, M. and Ibrahim, G. (2001). Precipitating clouds observed by 1.3-Ghz boundary layer radars in equatorial Indonesia. *Ann. Geophys.*, **19**, 889–897. 4, 53, 137, 171

Roger, R. and Yau, M. (1996). *Radar Meteorology. Atmospheric and Oceanographic Sciences Library*. Butterworth-Heinemann, United State of America, 3rd edn. 9, 11, 12

Rosenfeld, D. and Ulbrich, C.W. (2003). Cloud microphysical properties, processes, and rainfall estimation opportunities. *Meteorol. Monographs*, **30**, 237–237. 143, 152

Rosenfeld, D., Wolff, D.B. and Atlas, D. (1993). General probability-matched relations between radar reflectivity and rain rate. *J. Appl. Meteorol.*, **32**, 50–72. 134

ROTSTAYN, L.D. (1997). A physically based scheme for the treatment of stratiform clouds and precipitation in large-scale models. i: Description and evaluation of the microphysical processes. *Q. J. R. Meteorolog. Soc.*, **123**, 1227–1282. 1

SANDUS, O. AND LUBITZ, B. (1961). Dielectric relaxation of aqueous glycine solutions at 3.2 centimeter wave length. *J. Phys. Chem.*, **65**, 881–885. 5, 157

SATO, T., DOJI, H., IWAI, H. AND KIMURA, I. (1990). Computer processing for deriving drop-size distributions and vertical air velocities from VHF doppler radar spectra. *Radio Sci.*, **25**, 961–973. 53

SAUVAGEOT, H. AND LAUCAUX, J.P. (1995). The shape of averages drop size distributions. *J. Atmos. Sci.*, **52**, 1070–1083. 77

SCHÖNHUBER, M. (1987). *Ueber Methoden und Algorithmen zur Berechnung der elektromagnetischen Streuparameter von Niederschlagspartikeln (Frequenzbereich ueber 3 GHz)*. Master's thesis, Graz, Techn. Univ., Inst. f. Nachrichtentechnik u. Wellenausbreitung. 29

SCHÖNHUBER, M. (1998). *About interaction of precipitation and electromagnetic waves.*. Ph.D. thesis, Graz University of Technology. 2, 3, 38, 108

SCHÖNHUBER, M., URBAN, H.H., BAPTISTA, J.V.P.P., RANDEU, W.L. AND RIEDLER, W. (1997). Weather radar vs. 2D-video-distrometer data. weather radar technology for water resources management. *B. Braga Jr. and O. Massambani, Eds., UNESCO Press*. xvi, xxix, 36, 37, 38

SCHONHUBER, M., RANDEU, W., URBAN, H. AND BAPTISTA, J. (2000). Field measurements of raindrop orientation angles. *Proc. AP Milleneum Conf Ant. Prop., Davos, Switzerland*. 21

SCHUMACHER, C. AND HOUZE, R.A. (2003). Stratiform rain in the tropics as seen by the TRMM precipitation radar. *J. Climate*, **16**, 1739–1756. 192

SCHUUR, T.J., RYZHKOV, A., ZRNIC̀, D. AND SCHÖNHUBER, M. (2001). Drop size distributions measured by a 2D video disdrometer: Comparison with dual-polarization radar data. *J. Appl. Meteorol.*, **40**, 1019–1034. 45, 47

SEKHON, R. AND SRIVASTAVA, R. (1971). Doppler radar observations of drop-size distributions in a thunderstorm. *J. Atmos. Sci.*, **28**, 983–994. 15, 20, 117

SEKINE, M., CHEN, C. AND MUSHA, T. (1987). The lognormal fit to raindrop spectra from frontal convective clouds in israel. *IEEE Trans. Antennas Propag.*, **35**, 358–359. 15

SELIGA, T. AND BRINGI, V. (1976). Potential use of radar differential reflectivity measurements at orthogonal polarizations for measuring precipitation. *J. Appl. Meteorol.*, **15**, 6976. 28, 29

SHIBAGAKI, Y., KOZU, T., SHIMOMAI, T., MORI, S., MURATA, F., FU-JIYOSHI, Y., HASHIGUCHI, H. AND FUKAO, S. (2006). Evolution of a super cloud cluster and the associated wind fields observed over the Indonesian maritime continent during the first CPEA campaign. *J. Meteorol. Soc. Japan*, **84A**, 19–31. 152

SHIMAZAKI, H. AND SHINOMOTO, H. (2007). A method for selecting the bin size of a time histogram. *Neural Comput.*, **19**, 1503–1527. 3, 92

SIMPSON, J., KUMMEROW, C., TAO, W.K. AND ADLER, R. (1996). On the tropical rainfall measuring mission (TRMM). *Meteorol. Atmos. Phys.*, **60**, 1936. 1

SMITH, P.L. (2003). Raindrop size distributions: Exponential or gammadoes the difference matter? *J. Appl. Meteorol.*, **42**, 1031–1034. 55

SMITH, P.L. AND KLICHE, D.V. (2005). The bias in moment estimators for parameters of drop size distribution functions: sampling from exponential distributions. *J. Appl. Meteorol.*, **40**, 1195–1205. 2, 56, 75

SMITH, P.L., KLICHE, D.V. AND JOHNSON, R. (2009). The bias and error in moment estimators for parameters of drop size distribution functions: sampling from gamma distributions. *J. Appl. Meteorol. Climatol.*, **48**, 2118–2126. 66

SPILHAUS, A. (1948). Raindrop size, shape and falling speed. *J. Atmos. Sci.*, **5**, 108–110. 16, 17

SRIVASTAVA, R.C. (1988). On the scaling of equations governing the evolution of raindrop size distributions. *J. Atmos. Sci.*, **45**, 1091–1092. 130

STEINER, M. AND SMITH, J.A. (2004). Scale dependence of radar-rainfall rate-san assessment based on raindrop spectra. *J. HydroMeteorol.*, **5**, 1171–1180. 134

STOUT, G.E. AND MUELLER, E.A. (1968). Survey of relationships between rainfall rate and radar reflectivity in the measurement of precipitation. *J. Appl. Meteorol.*, **7**, 465–474. 143

STRAKA, J., ZRNIC', D. AND RYZHKOV, A. (2000). Bulk hydrometeor classification and quantification using polarimetric radar data: Synthesis of relations. *J. Appl. Meteorol.*, **39**, 1341–1372. 31

STUTZMAN, W. AND DISHMAN, W. (1982). A simple model for the estimation of rain-induced attenuation along earth-space paths at millimeter wavelengths. *Radio Sci.*, **17**, 1465–1476. 182

TESTUD, J., OURY, S. AND AMAYENC, P. (2000). The concept of "normalized" distribution to describe raindrop spectra: A tool for hydrometeor remote sensing. *Phys. Chem. Earth Part B*, **25**, 897 – 902. 16, 117

TESTUD, J., OURY, S., BLACK, R.A., AMAYENC, P. AND DOU, X. (2001). The concept of normalized distributions to describe raindrop spectra: A tool for cloud physics and cloud remote sensing. *J. Appl. Meteorol.*, **40**, 1118–1140. 2, 16, 71, 111, 117, 129

THURAI, M. AND BRINGI, V. (2005). Drop axis ratios from a 2D video disdrometer. *J. Atmos. Oceanic Technol.*, **22**, 966–978. 18, 19, 122

THURAI, M., BRINGI, V.N. AND SCHONHUBER, M. (2006). Drop shape probability contours in rain from 2-D video disdrometer: implications for the self consistency method at C-band. *Proc. Fourth European Conf. on Radar in Meteorology and Hydrology, Barcelona, Spain*. 18, 20

THURAI, M., HUANG, G., BRINGI, V. AND SCHONHUBER, M. (2007). Calculations of XPD spread for 20 GHz fixed satellite systems using 2-D video disdrometer data. *IET Seminar Digests*, 364–364. 22, 122, 124

TOKAY, A. AND BEARD, K.V. (1996). A field study of raindrop oscillations. part I: Observation of size spectra and evaluation of oscillation causes. *J. Appl. Meteorol.*, **35**, 1671–1687. 125

TOKAY, A. AND SHORT, D.A. (1996). Evidence from tropical raindrop spectra of the origin of rain from stratiform versus convective clouds. *J. Appl. Meteorol.*, **35**, 355–371. 1, 77, 129, 134, 135

TOKAY, A., SHORT, D.A., WILLIAMS, C.R., ECKLUND, W.L. AND GAGE, K.S. (1999). Tropical rainfall associated with convective and stratiform clouds: Intercomparison of disdrometer and profiler measurements. *J. Appl. Meteorol.*, **38**, 302–320. 109, 114, 116, 184

TOKAY, A., KRUGER, A. AND KRAJEWSKI, W.F. (2001). Comparison of drop size distribution measurements by impact and optical disdrometer. *J. Appl. Meteorol.*, **40**, 2083–2097. 3, 38, 39, 77, 91, 92, 122

UIJLENHOET, R., PORR, J., SEMPERE-TORRES, D. AND CREUTIN, J.D. (2006). Analytical solutions to sampling effects in drop size distribution measurements during stationary rainfall: Estimation of bulk rainfall variables. *J. Hydrol.*, **328**, 65–82. 4, 31

ULBRICH, C.W. (1983). Natural variations in the analytical form of raindrop size distributions. *J. Clim. Appl. Meteorol.*, **22**, 1764–1775. 2, 4, 14, 15, 108

ULBRICH, C.W. AND ATLAS, D. (1998). Rainfall microphysics and radar properties: Analysis methods for drop size spectra. *J. Appl. Meteorol.*, **37**, 912–923. 2, 56, 75, 117

ULBRICH, C.W. AND ATLAS, D. (2002). On the separation of tropical convective and stratiform rains. *J. Appl. Meteorol.*, **41**, 188–195. 135

VAN DE HULST, H. (1957). *Light scattering by small particles*. Wiley & Sons, New York. 24

WAKASUGI, K., MIZUTANI, A., MATSUO, M., FUKAO, F. AND KATO, S. (1986). A direct method for deriving drop-size distribution and vertical air velocities from VHF doppler radar spectra. *J. Atmos. Oceanic Technol.*, **3**, 623–629. 53

WALDVOGEL, A. (1974). The N_0 jump in raindrop spectra. *J. Atmos. Sci.*, **31**, 580–590. 67, 129

WILLIAMS, C.R. (2008). Influence of sample volume on disdrometer and radar reflectivity estimates. *American Geophysical Union, Fall Meeting 2008*, H13D–0964. 48

WILLIAMS, C.R., ECKLUND, W.L. AND GAGE, K.S. (1995). Classification of precipitating clouds in the tropics using 915-MHz wind profilers. *J. Atmos. Oceanic Tech.*, **12**, 996–1011. 52, 111, 112, 113, 114, 116

WILLIS, P. (1984). Functional fits to some observed drop size distributions and parameterization of rain. *J. Atmos. Sci.*, **41**, 1648–1661. 16, 117

WILLIS, P.T. AND TATTELMAN, P. (1989). Drop-size distributions associated with intense rainfall. *J. Appl. Meteorol.*, **28**, 3–15. 130

WRIEDT, T. (1998). A review of elastic light scattering theories. *J. Part. & Part. Systems Charact.*, **15**, 67–74. 29

ZENG, Y. AND HOPKE, P. (1989). A study of the sources of acid precipitation in Ontario, Canada. *Atmos. Environ.*, **23**, 1499 – 1509. 160

ZIPSER, E.J. AND LUTZ, K.R. (1994). The vertical profile of radar reflectivity of convective cells: A strong indicator of storm intensity and lightning probability? *Mon. Wea. Rev.*, **122**, 1751–1759. 13